STRUCTURE PROPERTY RELATIONSHIPS IN POLYETHYLENE BLOWN FILMS

A Thesis
Presented to
The Academic Faculty

by

Abhiram S Kannan

In Partial Fulfillment
of the Requirements for the Degree
Doctor of Philosophy in the
School of Materials Science and Engineering

Georgia Institute of Technology
December 2015

STRUCTURE PROPERTY RELATIONSHIPS IN POLYETHYLENE BLOWN FILMS

Approved by:

Professor David Bucknall, Advisor
School of Materials Science and Engineering
Georgia Institute of Technology

Dr. Aaron Eberle
Senior Scientist
ExxonMobil Research and Engineering

Professor Meisha Shofner
School of Materials Science and Engineering
Georgia Institute of Technology

Professor Donggang Yao
School of Materials Science and Engineering
Georgia Institute of Technology

Professor Kyriaki Kalaitzidou
School of Mechanical Engineering
Georgia Institute of Technology

Date Approved: October 31, 2015

To my parents, Shri. Kannan and Smt. Anupama

ACKNOWLEDGEMENTS

I would like to sincerely thank my research advisor, Dr. David G. Bucknall. His insight and guidance in matters of research have been priceless and his opinions on academia and life in general have been rather timeless. I am indebted to him for teaching me the art of channelizing one's thoughts and enthusiasm towards a concentrated research effort. Most of all, I am grateful for his boundless patience without which this dissertation would not come to fruition.

I would like to express my deepest gratitude to our industry collaborators ExxonMobil Chemical Company and ExxonMobil Research and Engineering for providing financial backing to this project. I want to especially thank Dr. David Fiscus, Dr. Timothy Schaffer, Dr. Alexander Norman and Dr. Aaron Eberle for contributing whole heartedly towards my development as a researcher and presenter over these last four years. I would also like to thank Dr. Jeffery Butler and Dr. Sergey Yakolev for constructive criticism on the analysis of X-ray scattering data as well as useful discussion on the microscopy of polyethylene films.

The 10 week internship at the National Institute of Standards and Technology (NIST) will remain amongst my most cherished experiences. This internship would not be possible without the support of Dr Aaron Eberle, Dr. Steven Kline and Dr. Paul Butler. The exposure to neutron research and life at a national lab have greatly broadened my research interests. A special thank you to the Argoti family for letting me into their home and lives during my brief stint at NIST.

I would also like to mention Nabankur, Prateek, Yimin, Chinmay, Dibyajat, James, Drew, Cornelia, Alyssa, Paul and Graham for making my time at GT worth cherishing for ever. A special thanks is due to Susan, Teresa and Mechelle for making my administrative issues their own and ensuring that I settled in well when I first arrived in Atlanta.

This acknowledgement is complete without thanking my parents Shri. S. Kannan and Smt. Anupama Kannan and my sister Smt. Aditi Kannan. This dissertation is the result of

their hard work, their guidance and their perseverance; I am merely the conduit. Needless to say, this dissertation belongs almost as much to Sharvari Bhagwat as it does to me, for I would be lost without her.

TABLE OF CONTENTS

LIST OF TABLES

LIST OF FIGURES

LIST OF SYMBOLS OR ABBREVIATIONS

BUR	Blow Up Ratio
MD	Machine Direction
TD	Transverse Direction
ND	Normal Direction
TUR	Take Up Ratio
HDPE	High Density Polyethylene
LDPE	Low Density Polyethylene
LLDPE	Linear Low Density Polyethylene
SCB	Short Chain Branching
CCD	Chemical Composition Distribution
c	Velocity of Light (3 x 10^8 ms^{-1})
ν	Frequency of Electromagnetic Radiation
λ	Wavelength of Electromagnetic Radiation
E	Energy of Electromagnetic Radiation
h	Plank's Constant (6.623 x 10^{-34} Joule-sec)
s or q	Scattering Vector
$I(s)$ or $I(q)$	Intensity of Scattered X-rays
$J(s)$ or $J(q)$	Flux of Scattered X-rays
$A(s)$ or $A(q)$	Amplitude of Scattered X-rays
$\rho(r)$	Scattering Length Density Distribution
$\Gamma_\rho(r)$	Autocorrelation Function of $\rho(r)$

SAXS	Small Angle X-ray Scattering
WAXS	Wide Angle X-ray Scattering
d_c	Ensemble Average Lamellar Thickness
d_a	Ensemble Average Amorphous Spacing
d_{ac}	Ensemble Average Characteristic Repeat Dimension
L_{SAXS}	Ensemble Average Lateral Width of Lamellae
ε	Tensile Strain
$g(x)$	Gaussian Distribution
a_g	Amplitude of Gaussian
w_g	Half Width at Half Maximum of Gaussian
q^*	Location of Gaussian Peak Maxima
$l(x)$	Lorentzian Distribution
a_l	Amplitude of Lorentzian
w_l	Half Width at Half Maximum of Lorentzian
χ	Tilt Angle
LAR	Lamella Alignment Ratio
γ	1D Correlation Analysis
Xc	Percentage Crystallinity
$L(x)$	Area Normalized Lorentzian Distribution
A_L	Area under $L(x)$
$V(x)$	Area Normalized Voigt Distribution
A_V	Area under the Voigt Distribution

W_L	Full width at Half Maximum of the Lorentzian Distribution contained within $V(x)$
W_G	Full width at Half Maximum of the Gaussian Distribution contained within $V(x)$
n	Mixing fraction describing the relative proportion of a Lorentzian and a Gaussian contained within $V(x)$
F_i	Herman's Orientation Parameter for i where i represents any axis of interest the orientation of which is under investigation. Correspondingly, F_a, F_b and F_c represent the Herman's Orientation Parameter for the a, b and c axes respectively, of a crystal lattice. F_{am} represents the Hermans Orientation Parameter for the Amorphous chains in a semicrystalline system.
ϕ	Angle between the reference axis and the axis of interest i in the computation of F_i
ψ	Azimuthal Angle
a_v	Amplitude of an area normalized Voigt distribution
C_{ij}	Number of Carbon atoms between the i^{th} and j^{th} carbon where i and j are consecutive locations of branching along a single backbone. This quantity is also referred to as run length.

SUMMARY

The fabrication of blown films is a complex industrial process that has received some attention in the past from both industry and academia with the intention to establish detailed property-structure-processing linkages between polymers and their resulting blown films. Unfortunately, a clear understanding of the molecular level architectural variables which control important properties of blown films such as resistance to tear and the resistance to puncture are not fully developed. The current work uses powerful synchrotron based *in situ* X-ray scattering techniques to explore the morphologies of blown films as well as morphological evolution under uniaxial strain, for a series of polyethylenes whose architectures are well understood. Firstly, a number of protocols based on traditional analyses of X-ray scattering are developed which aid in the quantification of both the crystalline and non crystalline phases of the overall semicrystalline morphology of films. The analysis protocols developed allow the parametrization of dimensionality and orientation for both these phases at atomistic and mesoscopic length scales. Secondly, emperical relationships are established between the pertinent extracted parameters and molecular architectures of the polyethylenes under investigation. This enables the elucidation of those aspects of the molecular architecture of polyethylene the targeted manipulation of which is likely to result in the attainment of desired tear and puncture properties in blown films. Thirdly, quantitative relationships relating the dimensional and orientational parameters to the tear and puncture resistance properties are developed to determine the origin of these properties. Complementing the central theme of this dissertation are studies on the modeling of semicrystalline microstructures and the theoretical simulations of X-ray scattering from the same. Supplementing the analyses protocols developed from the traditional understanding of scattering phenomena are statistical analyses of scattering based on concepts borrowed from the realm of *big-data analytics*.

CHAPTER I

INTRODUCTION AND OBJECTIVES

This dissertation provides insight into the relationships between the structure and properties of blown films of polyethylene. This work uses synchrotron based X-ray scattering in a time resolved *in situ* experimental environment to explore the morphology of blown films from a series of architecturally well understood polyethylenes. This experimental methodology is selected because it allows visualization of the evolution of blown film morphology at the atomistic scale (1-10 Å) and the mesoscopic scale (10-1000 Å) under externally applied strains. It is shown in this dissertation that such an approach permits a detailed understanding of film deformation from a morphological standpoint. Detailed architectural information about the polyethylenes is made available by a combination of Nuclear Magnetic Resonance (NMR) and Cross Fractionation (CFC) based experiments on the polyethylenes. The mechanical properties of the blown films are measured by the *tear* and *dart* drop tests which are the standard tests for performance evaluation in the packaging and sheeting industry.

It is hypothesized that the combined analysis of film morphology along with molecular level architectural design of the polyethylenes and mechanical properties of films will instruct future efforts in the performance enhancement of polyethylene blown films. In order to test this hypothesis the following objectives are identified and achieved.

1. **Morphological Domain:** Quantify from X-ray scattering measurements, the dimension parameters and orientation parameters of crystalline and non crystalline components of the semicrystalline morphology of films at the atomistic scale (1-10 Å) and the mesoscopic scale (10-1000 Å).

2. **Molecular Level Architectural Design:** Investigate the molecular architecture of polyethylene from CFC and NMR data and determine how different architectural features manifest in the morphology of films.

3. **Mechanical Performance of Films:** Investigate the tear and puncture resistance of different polyethylene blown films and identify correlations between scattering derived dimension and orientation parameters

4. **Structure - Property Relationships:** Establish quantitative relationships between the architectural information describing various polyethylenes and the tear and puncture resistance of films

In order to achieve these objectives a series of experiments and theoretical studies are conducted. Following Chapter 3 which introduces and discusses the relevant literature, Chapter 4 describes the experimental procedures that enabled the collection of synchrotron based X-ray scattering data. Details of the analyses procedures, which enable parameter quantification central to objective 1 are discussed in Chapter 5. In Chapter 6, preliminary analysis of mesoscopic scattering data obtained in combination with uniaxial tensile testing is undertaken. The results of these are discussed in Chapter 7 in relationship to the molecular architecture of the polyethylenes with relevance to objective 2. In Chapter 8, the atomistic scale morphology and its evolution under tensile strain is investigated. In addition to the experimental approaches, a complementary study of real space modeling and simulation of X-ray scattering is undertaken and the tools necessary for this are presented in the Chapter 9 along with some novel scattering measurements which prompted the modeling initiative. The findings from Chapters 6, 7, 8 and 9 are relevant to objectives 3 and 4 which pertain to the origin of tear and puncture properties of films within the context of the molecular architecture of the polyethylenes. These are discussed in chapter 10.

CHAPTER II

BACKGROUND AND LITERATURE REVIEW

2.1 The Basics of Blown Films

Blown film extrusion is an efficient and economical method of producing a vast array of film products including shrink films, multilayer films, industrial packaging and agricultural film. Many of these products are indispensable in day to day activities and are ubiquitous. Typically, the polyethylene family consisting of high density polyethylene (HDPE), low density polyethylene (LDPE) and linear low density polyethylene (LLDPE) form the largest subset of commercial polymers that are processed into films by blown film extrusion. Polypropylene (PP) and ethylene vinyl alcohol (EVOH) are some of the other polymers that might also be converted into blown films. A variety of possible end applications demand that the optical, mechanical and barrier properties of blown films be tailored toward their particular application. Polymer manufacturers that routinely supply the blown film market therefore adopt a strategy by which market penetration is possible via a number of different grades or polymer families intended to serve different end applications.

2.1.1 The Fabrication of Blown Films

In the manufacture of blown films of polyethylene, polymer melt is fed to a horizontally situated annular die with an outer diameter R_0 and a fixed annular gap known as the die gap. The extruded melt emerges from the die gap as a tubular parison with diameter R_0 and is pulled upwards against the direction of gravitational force with a vertical velocity gradient exerted by a take up device. Simultaneously, air is introduced through the die center subjecting the tubular parison to radial expansion as it cools from the melt. As the melt moves upwards away from the die it solidifies above the die exit at a height commonly known as the *frost line height*. A schematic showing the process of blown film extrusion is provided in Figure 1. The pressure created by blowing air through the tubular parison increases the parison diameter by a factor known as the 'Blow Up Ratio (BUR)' such that

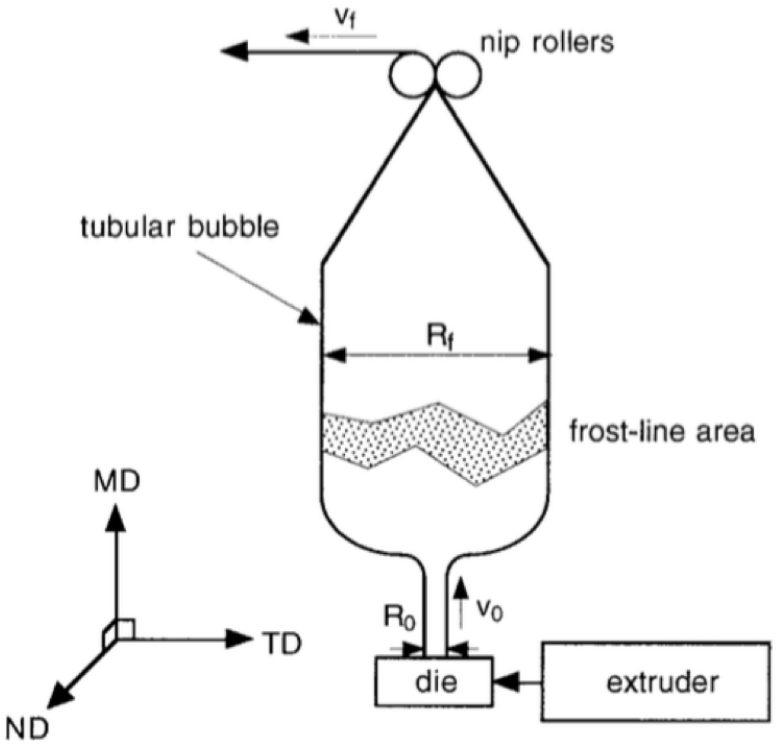

Figure 1: Schematics of the operation of blown film fabrication. Machine Direction, Transverse Direction and Normal Direction are the three directions of orientation imported to the blown film and are abbreviated as MD, TD and ND respectively. Figure reproduced from reference [1]

the original diameter of the parison i.e. R_0 and the diameter of the expanded parison R_f are related by Equation 1. Typical BURs encountered in film blowing operations might range from 1.5 to 4 depending on the end use application of the film.

$$BUR = \frac{R_f}{R_0} \tag{1}$$

The dual action of pulling the parison vertically as well as subjecting it to radial expansion occurs while the parison cools from the melt into solidified tubular film. The polymer melt is therefore understood to form a solid film by undergoing crystallization in the region just below the frost line from the melt where chains are oriented [2]. The blown film, now solidified, is collapsed into flat film by passing it through nip rollers. In addition, the nip rollers exert a tensile drawing force on the film pulling it upwards. The film thickness, or gauge, is dictated by the velocity gradient applied between the die exit and the take up of

film by the nip rollers [2]. If V_0 is the velocity of the melt at the die exit and V_f is the velocity exerted on the film at the nip rollers, then a factor known as the 'Take Up Ratio (TUR)' can be described by Equation 2. The TUR and gauge values are inversely related wherein large values of TUR produce thinner films than lower values of TUR [3].

$$TUR = \frac{V_f}{V_0} \tag{2}$$

The processes of biaxial stretching of the parison from the melt and its simultaneous solidification into a cylindrical film via oriented crystallization collectively comprise the blown film manufacturing process. As a consequence of the film blowing process, preferred orientation can be imparted to the produced films. Three mutually orthogonal preferred orientation directions are known to exist in blown films and are conventionally known as the Machine Direction (MD), the Transverse Direction (TD) and the Normal Direction (ND). The MD lies along the draw direction in the plane of tubular film, TD lies in the plane of the film and is orthogonal to MD. The ND is orthogonal to both MD and TD and is perpendicular to the film surface. MD, TD and ND are highlighted in Figure 1. It is accepted that the morphology produced in any blown film is influenced by the choice of polymer involved in the blowing operation. In addition, the frost line height, BUR, TUR and the temperature of the melt at the die exit are also factors that contribute to the morphology [2]. Due to the commercial importance of PE blown films, a number of authors have investigated the process-structure-property relationships in these films [3–19].

2.1.2 Benchmarking the Performance of Blown Films

The main application of blown films is packaging, an application that often necessitates films to possess a combination of flexibility, toughness and ductility. Improving the balance of these mechanical properties in films is often the goal of the product development efforts made by suppliers of polymers or by blown film manufacturers. The mechanical characteristics and therefore performance quality of blown films are most often measured by two industry wide standard characterization methods namely the puncture resistance test and the tear resistance test [2]. Physically these tests subject a film specimen to a complex stress field in which the film can plastically deform before it fails. Puncture resistance is measured by the

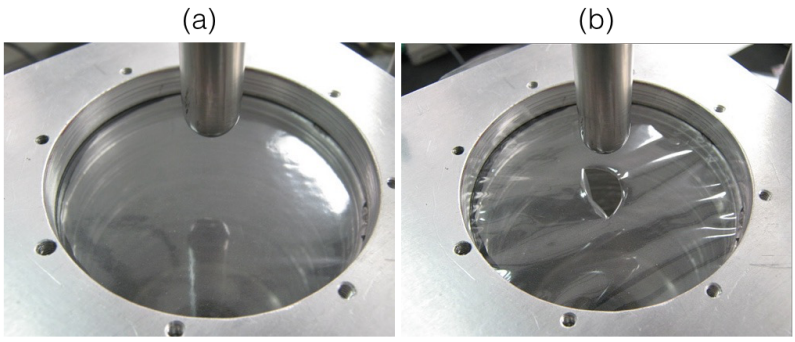

Figure 2: Puncture test to determine mechanical performance of blown films (a) a specimen ready for testing (b) the ruptured i.e. failed specimen after testing. Figure adapted from from [2]

standard dart drop test. In this test, a hemispherical weight or dart is released from a fixed height onto the plane of a single film that has been clamped in a taut manner. Depending on the inherent strength of the film, the weight of the dart may or may not cause the film to tear. This test of dropping a dart from a fixed height is repeated iteratively with incrementally higher weight until a dart of a particular weight is determined to penetrate the film with a certain degree of statistical significance. Figure 2a shows the placement of the film sample relative to the dart whereas Figure 2b shows a puncture in the tested sample indicating film failure. Tear resistance is measured by the Elmendorf Tear apparatus which is shown in Figure 3a while the sample geometry is illustrated in Figure 3b. Films are loaded into the apparatus and the pendulum of the apparatus is released. The kinetic energy of the pendulum propagates a tear along the notch in the specimen. An orientational influence on the tear strength of blown films is usually measured by propagating the tear along MD or along TD.

While the tear and puncture properties are both useful to benchmark the quality of films, these tests fail to provide the feedback that can be directly instructive towards the optimization of the mechanical properties. Indeed studies of the mechanical performance

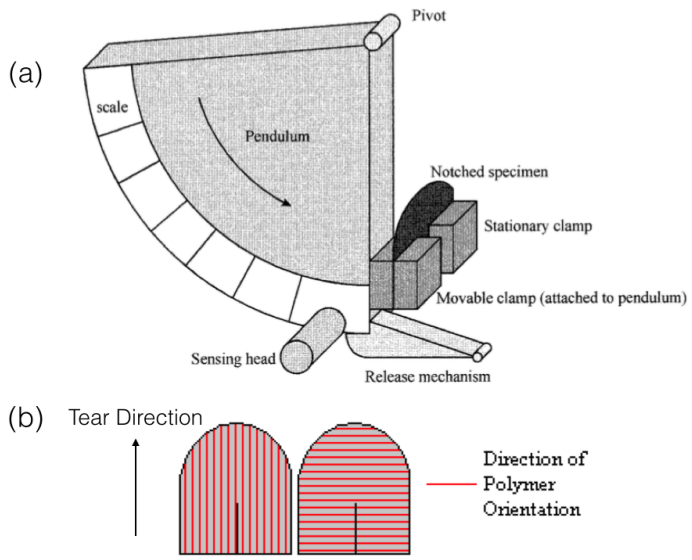

Figure 3: Elmendorf tear test to determine orientational tear properties of Blown Films. (a) shows the testing apparatus. (b) shows the typical test specimen geometry. Figure adapted from [2]

of films, i.e. tear [4, 10, 17, 20, 21] and puncture [17, 21] identify some of the elements that influence these properties, but do not provide actionable recommendations based on the chemical architecture of the polymers which might be directly improve these properties. The mechanical performance of films is dictated by the architecture of the polymer used in making the film as well as the structure of the film itself. Specifically, the architecture is dependent on the various conditions of synthetic chemistry that drive the polymerization process while the structure of the film i.e. film morphology is dependent on the processing conditions employed during the film fabrication process. The term *morphology* refers to the hierarchical multi scale features present within the film and occuring as a direct result of the oriented crystallization from the melt during the film blowing process. It is now understood that morphology produced during film blowing influences the tear and puncture properties [4, 6, 7, 10, 14, 17, 20–22]. Work by Maddams and Preedy [6, 7] suggests that tear properties are related to the crystalline morphology of films, specifically to the arrangements of polymer crystalline unit cells relative to the MD, TD and ND. The findings of Register *et al.* [10] and Chum *et al.* [17] examined this claim and found some correlations between the tear properties and the orientation of the unit cell axes relative to MD and

TD in blown film of HDPE, LLDPE and LDPE respectively. The work of Sherman [20] investigated blown films of HDPE and suggested that a higher degree of randomness in the arrangements of crystalline lamella were responsible for the improvement in tear properties. Patel *et al.* [21] theorized that tear and dart properties were controlled by the same morphological parameters that controlled shrinkage along MD and TD, by performing film shrinkage measurements. The authors suggested that this morphological parameter was molecular orientation. Seguela *et al.* [14] explained that imbalance in MD tear and TD tear was observed in various LLDPEs due to the differences in the kinetics of chain relaxation between the different types of LLDPEs during the film blowing process. The work of Zhang *et al.* [4] agreed with the findings of Seguela and also suggested that architectural variations between LDPE, LLDPE and HDPE were responsible for differences in tear and puncture properties of the corresponding blown films.

While these studies provide some understanding and establish qualitative relationships between morphology and film properties, they don't provide the framework which permits the architecture of a polymer to be quantifiably evaluated in the context of film performance. Therefore, a lack of understanding between the molecular design variables that determine the architecture of PE and the film performance exists. A detailed investigation of the morphology of blown films for a series of controlled architectures it is hypothesized, might provide key insights into the various aspects of molecular design of a polymer, which might then be manipulated to modify film properties.

2.2 Fundamental Concepts in Polyethylene

2.2.1 Molecular Architecture

Polyethylene (PE) in its simplest form consists of -CH_2-CH_2- repeat units along the length of the backbone chain. A number of developments over the last five decades have resulted in various non-linear/branched PE architectures capable of providing a wide range of properties while still utilizing the same monomeric building blocks [23, 24]. PE classification and hence nomenclature is based on its architecture and by association density into the three conventional types of PE i.e. High Density (HDPE), Low Density (LDPE) and Linear Low

Density (LLDPE). The architectures of these polymers are schematically illustrated in Figure 4. HDPE consists of long linear chains of unbranched polyethylene. LDPE is comprised of highly branched architectures of polyethylene whereas LLDPE possesses limited short chain branching distributed along the length of long linear sections.

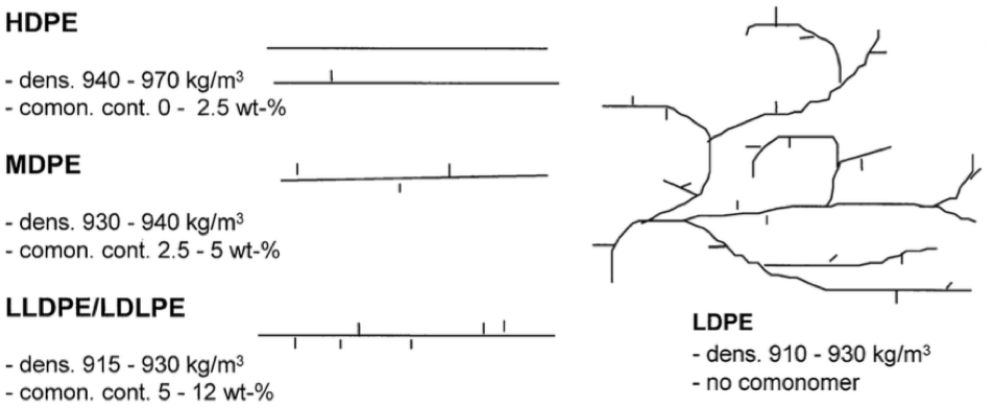

Figure 4: The different types of polyethylenes available in the current market. Figure reproduced from [25]

2.2.1.1 Linear Low Density Polyethylene

LLDPEs are the latest members of the PE family, their synthesis having been made possible by the discovery of copolymerization of ethylene with an α-olefin by Ziegler and Natta [23, 24]. LLDPE architectures as Figure 4 suggests are realized primarily by incorporating short chain branching (SCB) along the length of the carbon chain. This seemingly trivial incorporation of SCB has had a profound impact on the global PE market. Indeed the global demand for LLDPE currently exceeds nearly 70 million tons annually with a 5% annual growth rate [25]. In the current scientific environment, branch incorporation can

exhibit statistical states between complete randomness and precise control [26–35].

2.2.1.2 Bivariate Distribution

The molecular architecture in LLDPE polymers is influenced by the following molecular design variables: [2]

(a) Molecular Weight Distribution (MWD) of the LLDPE

(b) The type and content of α-olefin comonomer incorporated during copolymerization

(c) The distribution of comonomer content into backbone chains of varying molecular weight i.e. inter chain comonomer distribution

(d) The uniformity/non-uniformity of comonomer distribution within individual chains i.e. intra chain comonomer distribution

These design variables can be classified into two groups based on their effects to modify the MWD of the LLDPE or the chemical composition distribution (CCD) of the LLDPE. The combination of MWD and CCD is collectively known as the bivariate distribution of an LLDPE polymer [22]. The CCD component of the bivariate distribution depends on the incorporation of SCB whereas the MWD component depends more on the length of backbone in LLDPE chains. The inherent complexity of achievable structures due to variations in bivariate distributions of LLDPEs is illustrated by Figure 5. The mechanical performance of LLDPE blown films is expected to be influenced by the bivariate distribution of the LLDPE polymer. Consequently, any effort to determine relationships between mechanical performance of LLDPE films and the molecular architecture of LLDPEs characterized by the bivariate distribution, will only be successful if the linkages between solid state morphology of the films and the bivariate distribution can be uniquely established. This proposition is complicated by the knowledge that the tear and puncture tests provide little insight into the film morphology and less still into the architectural control on mechanical performance.

It is also relevant to note that the effects of MWD and CCD on mechanical properties have seldom been jointly investigated in studies reported in literature. A general understanding for the the MWD has been well established and rightly suggests that higher values

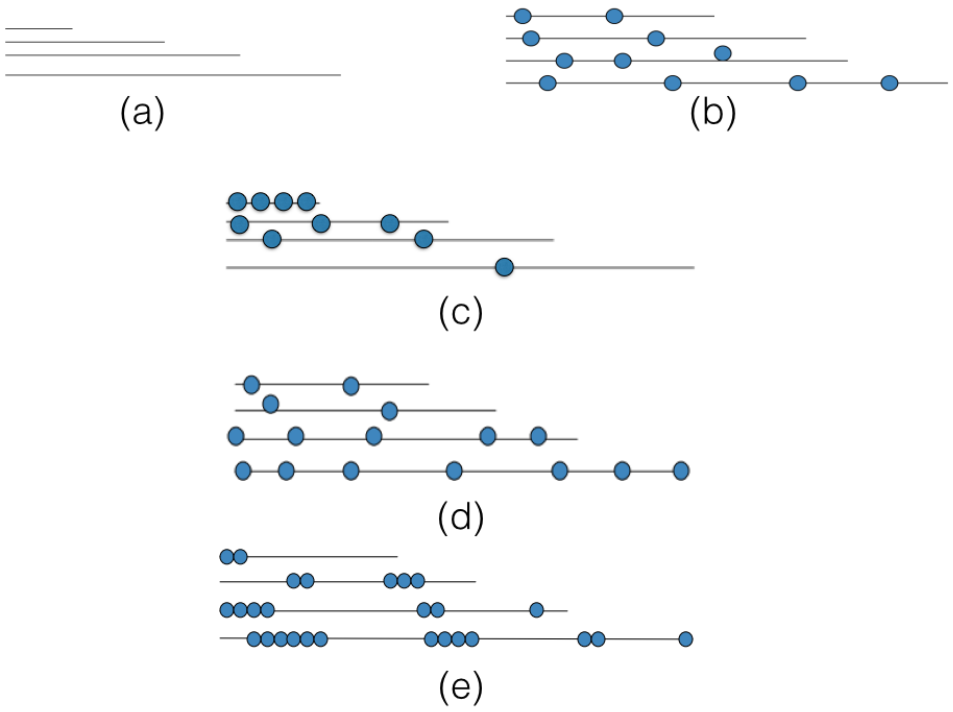

Figure 5: Illustrations showing the various configurations of polymers achievable by tuning the bivariate distribution. Straight lines represent the polymer backbone while blue circles represent branch points (a) MWD in a homopolymers (b) bivariate distribution (c) bivariate distribution in Ziegler Natta LLDPE (d) bivariate distribution in metallocene LLDPE and (e) bivariate distribution in a blocky LLDPE. Figure adapted from [36]

of molecular weight result in an increased polymer density, which also improves the yield stress and provides a higher tensile modulus [2]. Contributions from the CCD tend to be less robustly investigated with most studies restricted to investigations of comonomer type and an average value of comonomer distribution (see Figure 9) [37–40]. These studies were undertaken on samples crystallized isothermally and devoid of significant orientational influence in the form of melt compressed plaques possessing isotropic morphology. The results from these studies are unlikely to be representative of CCD effects in blown films. In order to create a workflow that prevents disconnected investigations of the MWD and the CCD of a single LLDPE polymer, characterization workflows should be necessarily inclusive of contributions from both MWD and CCD effects. A combined approach of this type is achieved by cross fractionation studies [22, 41–44].

2.2.2 Crystallization from Oriented Melt

Crystallization of PE from the melt always results in a lamellar superstructure consisting of alternating crystalline and amorphous regions. Lamellae can be visualized as regions of confined ordering of chain segments formed by the aggregation of crystalline unit cells. At longer length scales, a structure composed of the juxtaposition of crystalline lamellae and amorphous arrangements of chains creates a stacked lamellar morphology. These features are illustrated in Figure 6a. A spherulitic structure is formed comprised of the stacked arrangement of lamella-amorphous repeats in melts crystallized in the absence of orientation. [45–47]. When a melt is subjected to extensional flow such as in extrusion and film blowing the crystallization proceeds in such a way so as to create a cylindritic morphology comprised of the same lamellar-amorphous repeats [2]. Structures formed during the oriented crystallization process are often modeled as shish-kebabs. The shish-kebab structure consists of extended chain cores or shish which permit crystallization to occur radially in the form of kebabs as shown in Figure 6b. The origin of the shish-kebab morphology has been investigated by a number of authors using X-ray and neutron scattering studies as well as through computations. [48–55]. The general morphology formed from the crystallization of a melt irrespective of its shear field always exhibits an average interlamellar distance since lamellae are separated by interlamellar amorphous domains. Tang *et al*. [56] have defined the lamellar morphology in extruded PE specimens in terms of three average length scales namely the average thickness of lamellae (d_c), the average repeat dimension in the extrusion direction (d_{ac}) consisting of a single lamella-amorphous repeat and the average lateral dimension of a lamella (L_{SAXS}). The physical representation of these three parameters is provided in Figure 6c.

2.2.2.1 Morphology at the Mesoscopic Scale (10-1000Å)

The mesoscale morphology in PEs crystallized under orientation comprises of lamellae and amorphous features typically ranging in dimensions between 100-1000Å,. In blown films lamellae tend to arrange in such a way that the lamellar planes tend to be perpendicular to the direction in which the film was maximally drawn i.e. MD [1, 10, 17, 18]. Average

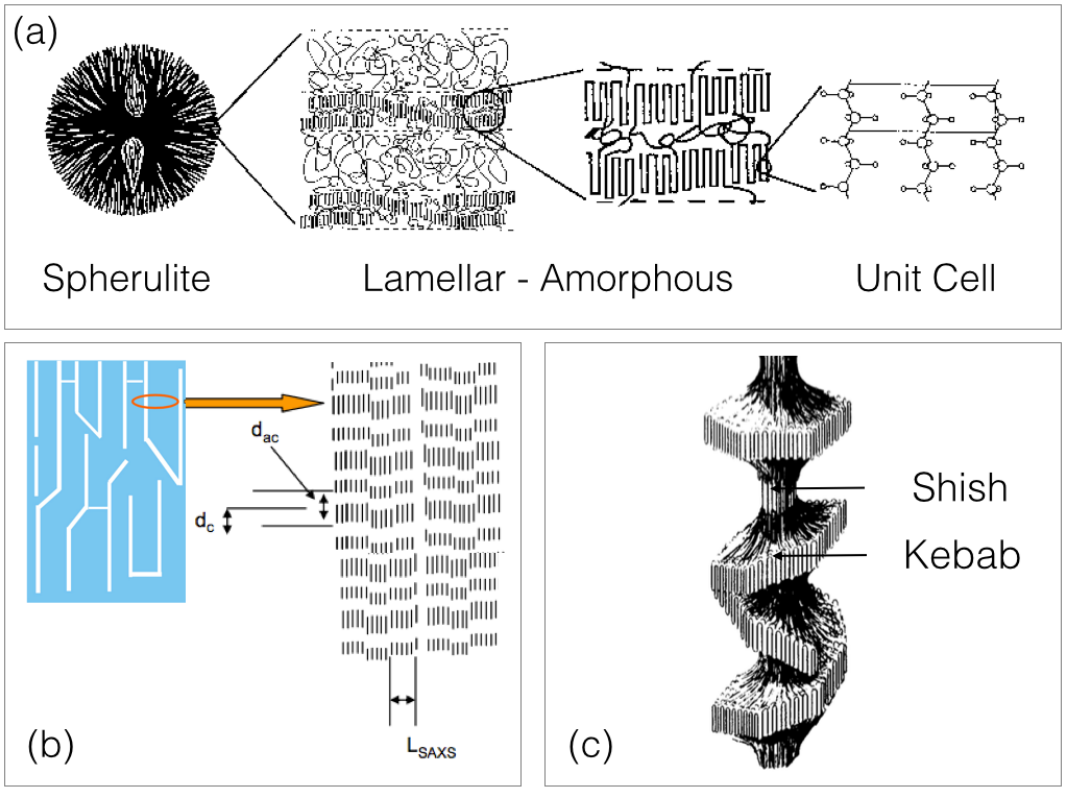

Figure 6: (a) The hierarchical morphology of polyethylene consisting of spherulites at macroscopic scales down to the unit cell structure in crystallographic scales. (b) schematic showing the lamellar structure in polyethylene crystallizing from an extruded melt (c) the shish-kebab morphology seen in ultra drawn polyethylene fires

values of d_c reported for PEs in blown films typically vary between 20-200Å depending on the type of PE. Typical investigations have been undertaken by transmission electron microscopy (TEM), Raman spectroscopy, differential scanning calorimetry (DSC), Nuclear Magnetic Resonance (NMR) and Small Angle X-ray scattering (SAXS) [57–59]. Each of these techniques is sensitive to different aspects of the distribution of lamellar thicknesses [60]. Each of these techniques provides a measure of the lamella thickness, spacing and in some cases distributions. The presence of periodic crystalline and amorphous structures is a prerequisite in the application of SAXS and TEM towards quantifying the mesoscopic morphology of PE. TEM is more sensitive to the presence of large uniformly shaped lamellae. The contrast necessary for TEM to be effective as a technique is provided by staining of species with Ruthenium Tetraoxide [45]. This method is not free from measurement unambiguity since staining the specimen might alter the sample or non uniform staining

might also occur. DSC methods do not require a periodic structure since these are dependent purely on the enthalpy of fusion of the various lamellae. DSC can therefore account for lamellae of all sizes but is most effective for monitoring of homopolymers such as HDPE. The accuracy of this technique in determining the size scales of the different semicrystalline features is severely affected when a wide distribution of lamellar sizes is encountered as is the case typically with LLDPEs.

Typically, d_c measured by TEM is greater than for SAXS which is in turn greater than DSC [34, 57–59, 61]. In LLDPE specifically, a wide distribution of lamellar thicknesses is generally observed [62, 63]. Lamellae of a range of thicknesses when distributed in an amorphous matrix result in a range of values for the lamella - amorphous repeat which in turn results in an overall average value of d_{ac}. Considering d_c to be the average lamellar thickness and d_a to be the average amorphous length scale distribution, d_{ac} can be separated into its constituents given by the sum of d_c and d_a as shown shown in Equation 3.

$$d_{ac} = d_c + d_a \tag{3}$$

The mesoscopic morphology in blown films of LLDPE has been described as a shish-kebab structure as discussed previously in section 2.2.2.1. The proposed mechanism for the formation of shish-kebabs suggests that elongation of the melt during the film blowing causes a preferential extension of high molecular weight chains. These chains in their elongated, low entropy state, are capable of initiating homogeneous nucleation events along their elongated length. The shish corresponds to these chains elongated in their entirety or more probably to elongated sections of the high molecular weight chains. Kebabs correspond to those crystalline lamellae that grow radially outwards from the shish following nucleation and subsequent crystallization of lower molecular weight chains. [49, 51–55]. The shape of the kebabs has been greatly debated in the past, with general consensus supporting the views of Keller and Machin [64, 65] who suggest that kebabs can form flat plates or twisted ribbons depending on the stresses developed in the melt. Keller and Machin [64, 65] suggested that in HDPE, higher shear stresses developed during oriented crystallization caused the growth of flat kebabs radially outwards from the shish while in LLDPE lower shear stresses resulted

in more relaxed chains in the melt which resulted in allegedly twisted kebabs. The second model of twisted kebabs has been schematically represented in Figure 7.

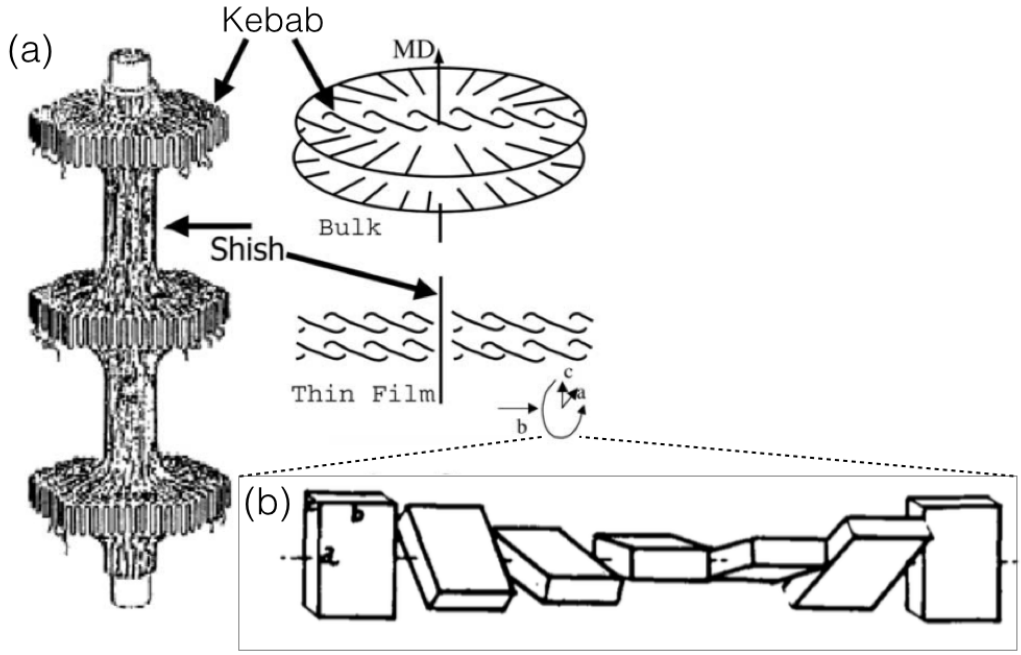

Figure 7: Kellers suggested morphology for low stress LLDPE morphology formed from oriented melts showing (a) shish-kebab morphology and (b) rotation of the unit cell in kebabs about the b axis. Figure adapted from [49] and [66]

2.2.2.2 Crystallographic Scale Morphology

The geometry of the unit cell in polyethylene is predominantly orthorhombic in undeformed specimens possessing a, b and c axes that are orthogonal to each other but are unequal in length. An orthorhombic unit cell of PE is shown in figure 8b. The c axis of the orthorhombic cell is defined as the axis along the molecular axis of a PE chain. Under mechanical loading an orthorhombic to monoclinic transformation is possible [67–70]. The monoclinic unit cell of PE is illustrated in Figure 8c. The transition itself causes the tri-axes orthogonality from the orthorhombic cell to be lost. In the monoclinic cell, the c axis is perpendicular to a and b and the a and b axis subtend an angle of 107.9. Figure 8a overlays monoclinic cells over orthorhombic cells illustrating the three relative positions of

the orthorhombic and transformed monoclinic cells. The monoclinic cell is stable only under an applied load reverting back to the orthorhombic form at the cessation of load [71].

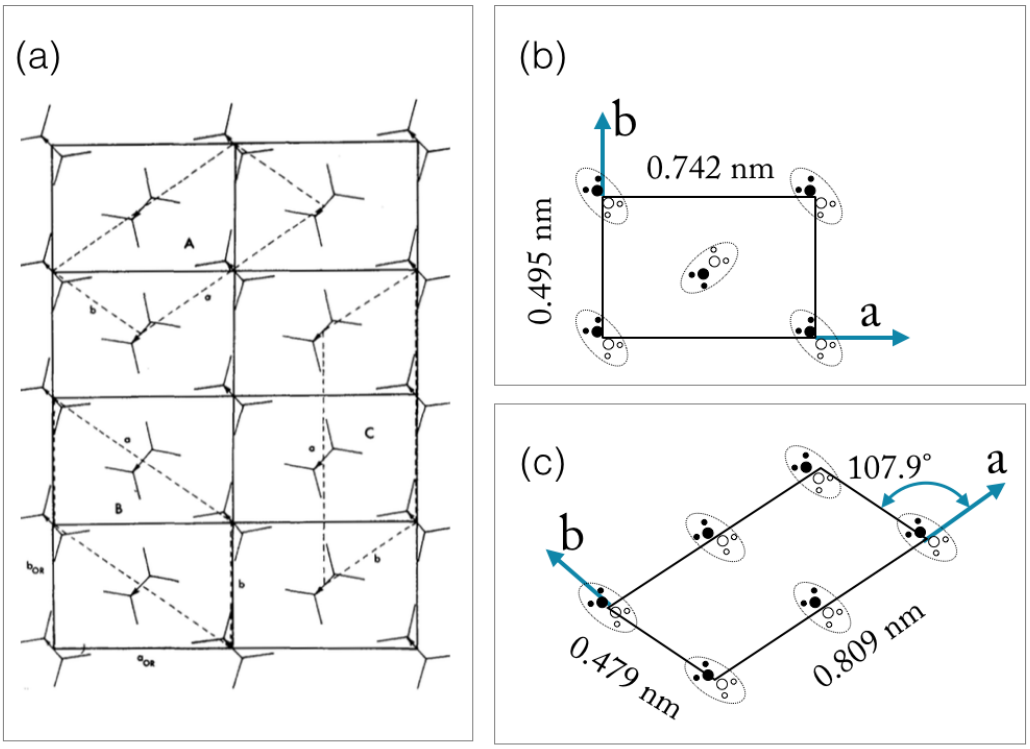

Figure 8: (a) Overlayed unit cell structure of polyethylene showing the placement of monoclinic cells relative to the orthorhombic cells. Figure adapted from [72] (b) & (c) Dimensions of the a and b axes for orthorhombic and monoclinic cells respectively. The c axis has a length of 0.255 nm in both and is perpendicular to the plane of the paper.

Keller's model of low melt stress structures in LLDPE suggested that the a axis was preferentially aligned along the processing direction i.e. MD and the b axis was aligned along the TD of films. A number of studies via Wide Angle X-ray Scattering (WAXS) have confirmed the presence of this kind of an orientation distribution in LLDPE blown films as well as suggested the rotation of the a-c plane about the b axis. [6, 8, 10, 15, 17, 18]. Schematically, the rotation of the unit cells around the b axis in LLDPE blown films following Keller's structural model are shown in Figure 7b.

2.3 Tensile Deformation in Polyethylene

2.3.1 Stress Strain Behavior

The typical stress strain plots of room temperature deformation of LLDPEs made from hexene and butene comonomers are presented in Figure 10. The plots show the existence of a linear Hookean region at small strains, followed by the occurrence of one or two yield points depending on the comonomer content. Subsequently to the yielding a plateau region is observed in some specimens. At the end of the plateau region, the the stress rises non-linearly with strain in the regime of strain known conventionally as strain hardening.

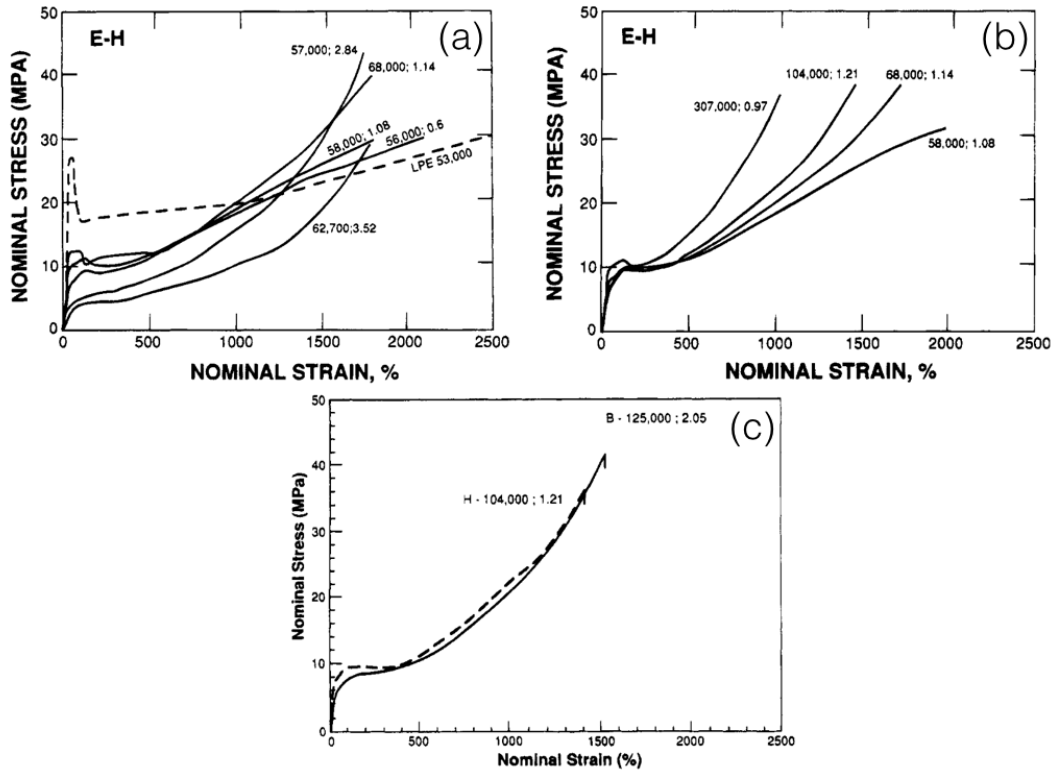

Figure 9: Typical Stress Strain Behavior of LLDPE showing (a) the effect of similar molecular weights but different hexene contents in ethylene hexene LLDPEs (b) the effect of similar hexene contents but different molecular weights (c) Similar stress strain behavior exhibited by a butene based LLDPE and a hexene based LLDPE. Reproduced from references [37, 39, 40]

2.3.2 Historical Understanding of Deformation

Physically, the linear Hookean response in semicrystalline polymer systems above the glass transition temperature, is driven by affine deformation of non-crystalline or amorphous arrangements of chains within the solid state morphology [73]. Within the confines of this linear regime, crystalline arrangements of chains are likely to be unperturbed by mechanical loading. The sequence of events is shown in Figure 10a is illustrative of affine deformation.

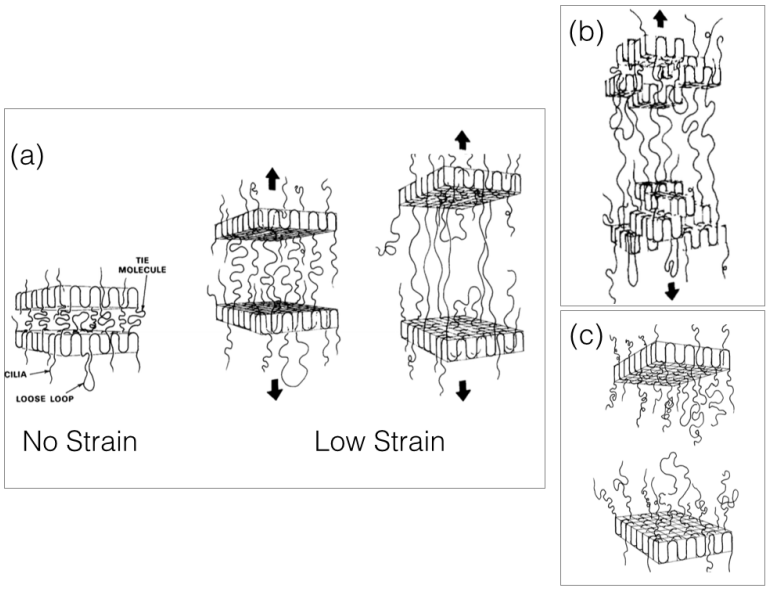

Figure 10: (a) Stages of affine deformation in an LLDPE. The third stage represents the Hookean limit (b) Initiation of stepwise deformation during ductile failure (c) Deformation during brittle failure. Figure adapted from [74]

The first comprehensive molecular model of deformation in PE was suggested by Peterlin in the 1970s [75–80]. Peterlin's model suggested that tensile drawing first caused slippage to occur along the crystal planes of lamellae and subsequently disrupted the lamellar structure. The crystallite blocks under further draw rearranged to form fibrils. The underlying assumptions of this model included a dominance of strictly adjacent chain reentry at the surface of lamellae as well as a spherulitic morphology within which existed a number of lamellar stacks. The first of these assumptions is more appropriate for solution crystallized tensile specimens than for melt crystallized ones. Nevertheless, certain aspects of this model

are accepted by the scientific community [81, 82] and are discussed here. Peterlin's model of cold drawing of semicrystalline polymers comprised of three stages namely

(a) The initiation of irreversible deformation in the original spherulitic morphology at low strains

(b) A stepwise transformation of the spherulitic morphology into a fibrillar structure at intermediate strain

(c) Sustained plastic deformation of the fibrillar morphology at high strains

Peterlin identified that the low strain region occurred prior to the formation of a neck in tensile specimens, the intermediate strain regime was observed at strains at which necking occurred and high strain regions as those where the neck propagated through the entire tensile specimen. In the first stage, crystalline unit cells, i.e. the building blocks of all lamellae present within the spherulitic morphology, underwent crystal transformations although the shapes of individual lamellae were preserved. In these initial stages of deformation, transformations occur within lamellae resulting in twinned orthorhombic crystals, as well as orthorhombic to monoclinic phase transitions. Yield points in the stress strain plots of semicrystalline polymers, such as those seen in LLDPEs signify a perturbation of the previously stable crystalline fractions. The crystal lamellae present before deformation undergo restructuring at strains beyond the limit of affine extensibility. At higher strains when the deformation was no longer affine, the increasing collective influence of crystal unit cell transformations in all lamellae resulted in the initiation of crystalline fragmentation which acted towards lowering lamellar stability. Fragmentation was possible largely due to a combination of longitudinal and transverse slip.

Slip behavior in crystalline lamellae has been recently investigated within the framework of double yield phenomena. Schrauwen *et al.* [83] suggested that the first yield occurred due to fine (small scale) slip within crystalline lamellae while the second yield was a result of coarse (large scale) slip of the lamellae in specimens of PP, HDPE and polyethylene terephthalate. Seguela and coworkers [84, 85] ascribed the first and second yield in LLDPE to temperature dependent thermally activated slip processes. At room temperature, they

suggested that the first yield point was a manifestation of homogeneous slip of the individual mosaic crystalline blocks that comprise a lamella. The second yield point manifested in the stress-strain plot due to a heterogeneous slip of the individual components of the mosaic block structure resulting in permanent destruction of the original crystalline morphology. Additionally, Seguela and coworkers suggested that the slip processes had a greater likelihood of nucleating at defects on the surface of the lamellae prior to propagating through a crystalline lamella. Consequently fragmentation of lamellae occured and the resulting fragments could rotate into the strain direction. In the third and final stage, a fibrillar morphology was obtained by sustained draw of chains from their previously folded state to a now extended state.

Peterlin's model also assumed existence of limited tie chains connecting adjacent crystallites. In LLDPE, a branch point serves as a defect in the crystallization process preventing otherwise long crystallizable ethylene sequences from forming a single chain folded lamella. Instead, crystallizable sequences of single chains containing SCBs can form multiple lamellae upon crystallization. The entire length of such a single chain can thus traverse multiple lamellae wherein, branch points are forced towards the crystalline-amorphous interphase region. The incorporation of branches can therefore facilitate physical linking between crystalline lamellae in the form of interlamellar tie chains. Tie chains provide stability to the lamellar superstructure and contribute towards improving mechanical properties of the polymer system. Tie chains are shown in Figure 10a and b which highlights a mechanism that forces ductile deformation in lamellar-amorphous systems containing tie chains.

2.4 The Theory of Scattering

The family of X-ray scattering and neutron scattering techniques are amongst the most central tools in the study of polymers. This section focuses on the basic theories of scattering that are common to both. While the similarities between the two techniques are extensive, more importance is provided to the former since the entirety of this dissertation deals in the application of X-ray scattering to challenges based on morphological considerations. The derivations shown in the following section are explained in greater detail in the books

by R.J. Roe [86] and N. Stribeck [87]. Another useful resource for non-specialists is the introduction to scattering studies collated in the ACS proceedings [88].

2.4.1 Scattering by X-Rays and Neutrons

2.4.1.1 Scattering Vector

The scattering of monochromatic and coherent X-rays from a sample on which the X-rays are incident is due to the combination of two sets of effects. The first set is due to the scattering of incident X-rays by the collection of all the electrons within the sample that the X-rays interact with. The second can be attributed to the interference between X-rays scattered in the above described manner. Effects of wave interference affect the flux of the spherically scattered X-rays where $flux$ is a term describing the number of photons (or neutrons for that matter) passing through a unit area per second. Interference effects typically cause the flux in different scattering directions to be different. The effects of interference arising particularly from differences in geometrical path length are investigated to setup the theoretical framework of X-ray scattering. The connection between the scattered waves specifically their intensity and the spatial structure of the matter which causes the scattering is of relevance in scattering studies.

Consider a wave with *amplitude* A, frequency ν and a wavelength λ propagating in the positive x direction. Mathematically, such a wave can be expressed as

$$A(x,t) = \mathcal{A}cos[2\pi(\nu t - \frac{x}{\lambda})] \tag{4}$$

where $\mathcal{A}$ represents the absolute value of $A(x,t)$. The $\frac{2\pi x}{\lambda}$ term represents the change in phase for the wave. In complex notation, the above equation 5 can be rewritten as follows

$$A(x,t) = \mathcal{A}e^{i2\pi(\nu t - \frac{x}{\lambda})} \tag{5}$$

Figure 11 illustrates the scattering by two particles located respectively at the two points O and P from a plane traveling along the direction of the unit vector S_0. A detector conveniently located in the direction go the unit vector S records the scattering at a large distance away from the points of scattering. Under the assumption of coherent scattering where no phase change takes place from the scattering itself, the phase difference $\Delta\phi$ depends solely

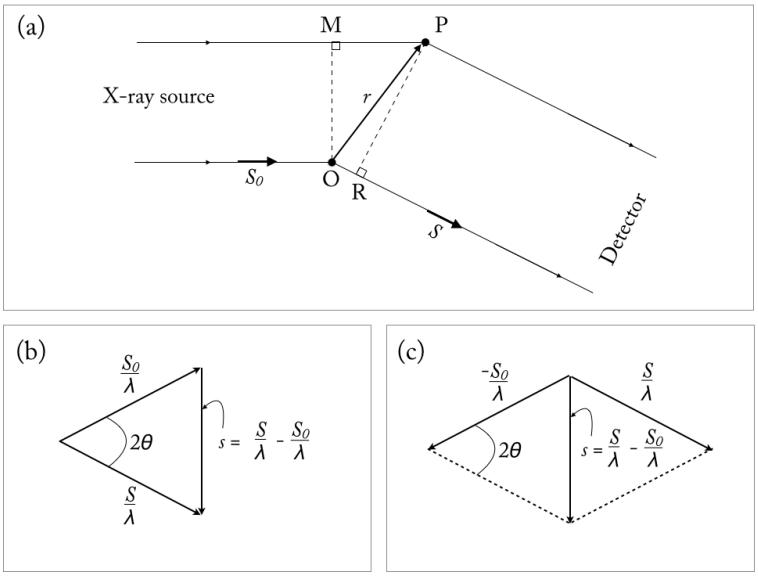

Figure 11: (a) Geometry of the scattering Path Length (b) and (c) Definition of scattering vector s. Figure adapted from [86]

on path length difference δ between the two rays such that

$$\Delta\phi = \frac{2\pi\delta}{\lambda} \tag{6}$$

If the relative position of the two scatterers differs by r, geometrically, $MP = S_0 \cdot r$ and $OR = S \cdot r$ and as a result the phase difference is

$$\Delta\phi = \frac{2\pi}{\lambda}(S_0 \cdot r - S \cdot r) = -2\pi s \cdot r \tag{7}$$

where s is defined as

$$s = \frac{S - S_0}{\lambda} \tag{8}$$

The vector s is defined as the scattering vector. The scattering vector encompasses all the information pertaining to the scattering geometry including the directions of incident and scattered beams and the wavelength. The magnitude of s is related to the scattering angle 2θ by the relationship

$$|s| = s = \frac{2sin\theta}{\lambda} \tag{9}$$

In a number of studies by different groups another quantity q is defined as the scattering vector. The relationship between q and s is as follows.

$$q = 2\pi s \tag{10}$$

In this equation, the vector q can be defined as

$$q = k - k_0 \tag{11}$$

where $k_0 = \frac{2\pi S_0}{\lambda}$ and $k = \frac{2\pi S}{\lambda}$ are the analogous wave vectors that are descriptive of the incident and scattered X-rays respectively. In essence, all equations involving s and q are interchangeable. Depending on the purpose of end analyses, either of these may be used. In this dissertation, both terms are featured with the reasons for the specific choice provided. The scattering vector q is also known as the momentum transfer vector in certain articles.

2.4.1.2 Scattering Intensity ($I(q)$)

Considering the original case of scattering from two identical scatterers as described in Figure 11, specifically if the wave scattered at O by the first particle is represented as $A_1(x,t)$ then

$$A_1(x,t) = A_0 b e^{i2\pi(\nu t - \frac{x}{\lambda})} \tag{12}$$

where A_0 represents the amplitude of incident radiation and b is the scattering length indicative of the scattering efficiency of the particle 1. The magnitude of b depends on factors such as the nature of the incident wave and the particle causing the scattering. Accordingly, the wave scattered at particle 2 i.e. at point P can be expressed in terms of the wave scattered at O as follows

$$A_2(x,t) = A_1(x,t) e^{i\Delta\phi} \tag{13}$$

$$A_2(x,t) = A_0 b e^{i2\pi(\nu t - \frac{x}{\lambda})} e^{-2\pi s \cdot r} \tag{14}$$

The wave that reaches the detector i.e. $A(x,t)$ is a combination of $A_1(x,t)$ and $A_2(x,t)$. This combination is expressed as follows

$$A(x,t) = A_1(x,t) + A_2(x,t) \tag{15}$$

$$A(x,t) = A_0 b e^{i2\pi(\nu t - \frac{x}{\lambda})}(1 + e^{-2\pi s \cdot r}) \tag{16}$$

It can be shown that the flux $J(s)$ of such a wave can be calculated by the square of the amplitude [88]. Therefore

$$J(s) = A(x,t) \star A(x,t) \tag{17}$$

$$J(s) = {A_0}^2 b^2 (1 + e^{-i2\pi s \cdot r})(1 + e^{i2\pi s \cdot r}) \tag{18}$$

The terms in parentheses cancel each other out allowing Equation 16 to be rewritten as

$$A(s) = A_0 b(1 + e^{-i2\pi s \cdot r}) \tag{19}$$

which describes the scattered wave from two identical point scatterers purely in terms of the scattering geometry represented by s. In the general case of N scattering events, 19 can be generalized to

$$A(s) = A_0 b \sum_{j=1}^{N} e^{-i2\pi s \cdot r_j} \tag{20}$$

where r_j denotes the location of the jth scatterer relative to a chosen origin. Using the consideration that the flux (J) is proportional to the square of the Amplitude A of the wave i.e. $J = |A|^2$, the incident flux J_0 and the flux of the scattered radiation $J(s)$ can be expressed in terms of the squares of the magnitudes of their respective amplitudes $A(s)$ and A_0. The ratio of the flux of the scattered X-rays and incident X-rays can be defined as the intensity of scattering as follows

$$I(s) = \frac{J(s)}{J_0} = \frac{|A(s)|^2}{|A_0|^2} = b^2 \Big| \sum_{j=1}^{N} e^{-i2\pi s \cdot r_j} \Big|^2 \tag{21}$$

The summation may be replaced with an integration over a complete scattering volume V which encompasses a volume element $dr = dxdydz$ where $n(r)dr$ is representative of

all the scatterers distributed within the V. This modified version of Equation 20 can be expressed as

$$A(s) = A_0 b \int_V n(r) e^{-i2\pi sr} dr \tag{22}$$

In the above Equation 22 $A(s)$ is proportional to the three-dimensional Fourier Transform of the local numerical density of scattering centers in the sample determined by $n(r)$. The quantity $A(s)/A_0$ can be defined as a *normalized amplitude* of scattering and in combination with Equation 10 the Equation 22 can be rewritten as

$$A(q) = b \int_V n(r) e^{-iqr} dr \tag{23}$$

Since b represents the scattering length of a single particle, the quantity $b{\cdot}n(r)$ is representative of a *scattering length density distribution* within the volume V of the sample under investigation. Equation 23 therefore takes the form

$$A(q) = \int_V \rho(r) e^{-iqr} dr \tag{24}$$

where $\rho(r)$ is the scattering length density distribution. Applying the same treatment valid in Equation 21, 24 can therefore be rewritten to determine the intensity of scattered X-rays as

$$I(q) = |A(q)|^2 = \Big| \int_V \rho(r) e^{-iqr} dr \Big|^2 \tag{25}$$

The quantity measured experimentally is the intensity of scattered radiation, $I(q)$ or $I(s)$. If the scattering length density distribution i.e. $\rho(r)$ is known then the intensity of the scattered wave can be directly calculated. In the world of X-ray scattering, $\rho(r)$ represents more specifically the *electron density distribution* function. Hence in the ideal case, if the electron density distribution is known then the scattering might be calculated. However, the reverse problem is the one that is most often under investigation i.e. Can we determine the morphology characterized by $\rho(r)$ given the experimental scattering data i.e$I(q)$? While the specifics of how this challenge might be tackled are discussed in detail

in appendix A, the most pertinent aspects of this problem can be succinctly summarized for the non-expert by a construction called the 'magic square of scattering' [87]. This construction concisely describes the interdependence of the electron density distribution $\rho(r)$, the autocorrelation function $\Gamma_\rho(r)$, the amplitude of scattering $A(q)$ and the intensity of scattered radiation $I(q)$. This construction is presented in Figure 12. The autocorrelation function describes how the distribution of scattering centers separated by a distance r are correlated. For a detailed understanding of Fourier Transforms and the autocorrelation function readers are directed to appendix A. The first key learning from the magic square is that the path from $\rho(r)$ via the Fourier Transform to obtain $A(q)$ and then $I(q)$ is conducted experimentally in a single step by scattering studies. This path is non-reversible i.e. $\rho(r)$ cannot be obtained by a square root treatment of $I(q)$ followed by inverse Fourier Transform as well as unique (For details see Appendix A). The second key learning is that the experimental scattering may be accurately described by the autocorrelation and subsequent Fourier Transform of a hypothesized $\rho(r)$ but this mathematical treatment is trivially non-unique. The understanding from both these key learnings is that, while a hypothesized morphology ($\rho(r)$) might perfectly describe the experimental scattering, it may not accurately represent the true morphology. In fact, it is entirely plausible for the experimental scattering to be accurately described by a multitude of hypothesized $\rho(r)$s.

2.4.1.3 Characteristics of X-rays

X-rays are electromagnetic radiation possessing a wavelength range from approximately 10^-2 to 10^2 Å . The X-rays used in experiments to resolve the structure of materials however are carefully restricted to a narrower window of wavelength between 0.5 to 2.5Å . Based on the Plank-Einstein equation which determines the energy of electromagnetic radiation (E) given its characteristic frequency the ν via the Plank's constant (h) we have

$$E = h\nu \tag{26}$$

Since the wavelength (λ) of electromagnetic radiation is related to ν via the velocity of electromagnetic radiation which is identical to the velocity of light (c) Equation 26 can be

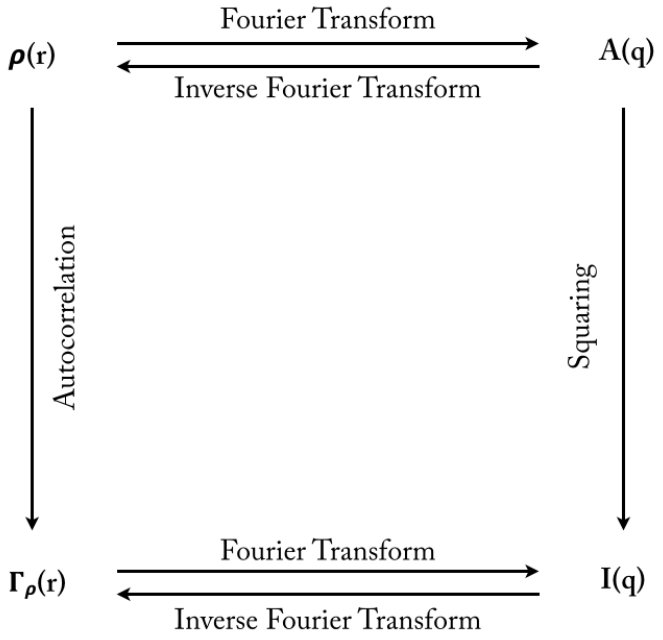

Figure 12: The relationships between $\rho(r)$, $\Gamma_\rho(r)$, $A(q)$ and $I(q)$. Figure reproduced from reference [86]

re-written as

$$E = \frac{hc}{\lambda} \tag{27}$$

The conversion of energies, often measured in terms of Electron-Volts (eV) and wavelengths in Å can be easily established on the basis of Equation 27.

CHAPTER III

MATERIALS AND METHODS

3.1 Materials

Three LLDPE resins ($LLDPE_1$, $LLDPE_2$ and $LLDPE_3$) were synthesized on a common metallocene catalyst platform and subsequently converted into blown films were supplied by ExxonMobil Chemical Company (EMCC). The resins were ethylene/$\alpha-$olefin copolymers where the $\alpha-$olefin comonomer was hexene. The short chain branching (SCB) incorporated into each of the three resins was predominantly butyl although trace amounts of ethyl and methyl branching were known to be present in the resin. The comonomer content incorporated into the three resins was different[1] and correspondingly, there existed a difference in the average branch content[2] along the length of the average chain. The differences in SCB content measured by NMR number of butyl branches per 1000 carbon atoms along the near backbone resulted in subtle differences in the density for the three resins. The SCB incorporation was tailored however to prevent significant differences in the molecular weight distribution across the resins. Indeed the gel permeation chromatography (GPC) measured values of M_n and M_w for the three resins were similar. The melt flow indices of the three polymers were also the same and had a value of 1.0 (measured for 10 min of flow under 2.16 kg load as prescribed by ASTM-D 1238). The characteristics detailed above are listed in table 1. Each of the three resins was processed into two series of monolayer blown films. The first series of films had a BUR of 2.5 while the second series had a BUR of 3.0. Within each series, three films were fabricated with average thicknesses of 20μm, 30μm and 75μm thereby totaling eighteen films. The sample labelling scheme followed in the current work is $LLDPE_{Resin}$.[BUR condition][thickness]. A list of labels is provided in Table 2.

[1]Determined by NMR as average mole % comonomer

[2]Determined by NMR as average number of butyl branches per 1000 backbone carbons (BBC)

Table 1: Description of the three LLDPE resins studied in this thesis along with their relevant physical and chemical characteristics. Data supplied by ExxonMobil Chemical Company

Resin	Density (g/cc)	M_n x 10^3 (g/mole)	M_w x 10^3 (g/mole)	Comonomer Content (mole %)	Branch Content (Butyls per 1000 BBC)
$LLDPE_1$	0.912	46.3	113.5	3.50	20
$LLDPE_2$	0.918	53.4	117.5	2.45	14
$LLDPE_3$	0.923	40.3	113.7	1.75	10

Table 2: Labelling of tensile specimens made from blown films of the three LLDPE resins

Resin	Film Label	BUR	Thickness(μm)
$LLDPE_1$	$LLDPE_1$.1a	2.5	20
	$LLDPE_1$.1b	2.5	30
	$LLDPE_1$.1c	2.5	75
	$LLDPE_1$.2a	3.0	20
	$LLDPE_1$.2b	3.0	30
	$LLDPE_1$.2c	3.0	75
$LLDPE_2$	$LLDPE_2$.1a	2.5	20
	$LLDPE_2$.1b	2.5	30
	$LLDPE_2$.1c	2.5	75
	$LLDPE_2$.2a	3.0	20
	$LLDPE_2$.2b	3.0	30
	$LLDPE_2$.2c	3.0	75
$LLDPE_3$	$LLDPE_3$.1a	2.5	20
	$LLDPE_3$.1b	2.5	30
	$LLDPE_3$.1c	2.5	75
	$LLDPE_3$.2a	3.0	20
	$LLDPE_3$.2b	3.0	30
	$LLDPE_3$.2c	3.0	75

3.2 Uniaxial Tensile Testing

Uniaxial tensile testing was either performed on a standard load frame apparatus or on a portable table top tensile tested. The choice of tensile testing apparatus depended on the specific synchrotron beamline where *in situ* measurements were performed.

3.2.1 Standard Uniaxial Testing on an Instron

A dual head Instron model 8500 Materials Testing System henceforth referred to as Instron, was used for *in situ* uniaxial measurements performed at beamline 5ID-D of the Argonne

Photon Source (APS). The Instron had dual servo hydraulic actuators that permitted a total of 406.4 mm of travel (203.2 mm per actuator). The dual actuators allowed the centre of a tensile specimen to remain fixed during a stretching experiment. The Instron could deliver upto 2.5 MN of force.Load, position and strain variables could be independently controlled. In the experiments conducted as part of the current work, the Instron was always operated at a uniform deformation rate of 25.4 mm per minute (12.7 mm per minute per actuator in opposite directions).

3.2.2 Tensile Testing on a Linkam Stage

A portable tensile and heat stage model Linkam TST350, developed specifically for *in situ* measurements was procured from Linkam Scientific Instruments, UK and is henceforth referred to as Linkam. The Linkam was used for tensile measurements conducted at beamline 12 IDC-C of the APS. It permitted uniaxial tensile stretching in opposite directions. The Linkam had a maximum tensile travel of 80 mm and had a force limit of 200 N. A minimum sample length of 26 mm was required and a range of sample thickness of between 1μm to 1mm were permissible. Width of specimens was required to be less than 22mm. The temperature range of the Linkam was -196 to 350°C applicable between rates of 0.01 to 60C per minute although these features were not utilized in this work. The Linkam was controlled by the Linksys 32 AV software provided by the vendor with capabilities to save stress-strain data to a spreadsheet. The Linkam was operated at a uniform deformation rate of 25.4 mm per minute (12.7 mm per minute per actuator in opposite directions) to match Instron data.

3.2.3 Preparation of Tensile Specimens

For the preparation of *in situ* specimens, it was recommended by EMCC that optically clear sections of film free from haze, be preferentially selected as these clear sections were free from inhomogeneities that were known to be present in sections of the stock film which were not haze free. A haze free region continuously appeared along the length of the supplied stock film at a distance of 6 inches to the left of one of the two fold lines specifically fold-line 'A'. Fold-line 'A' is that which lies on the left of the stock film spool provided the

film is being pulled off the spool by an individual towards himself or herself. Appropriate sections of the films were cut, folded, creased and stored for 24 hours suppressed between a flat clean surface and a free weight of two kilos. This action prevented the stacked films from separating during subsequent tensile specimen preparation.Tensile specimens were prepared from these specimen precursors with their axes parallel or perpendicular to the MD. Specimens were prepared by careful cutting with an Xacto scalpel. *In situ* tensile tests were not performed according to strict ASTM standards. Instron specific specimens were rectangular in shape having a gauge length of 152.4 mm and a width of 2.54 mm. The width of the specimens was less than the width of the specimen clamps. Linkam specific samples were also rectangular and had a gauge length of 16 mm and a width of 7 mm. Care was taken to ensure that the edges along the gauge length were free from notches by visually inspecting the edges using a magnifying glass. The slicing itself was performed on a foam backed board. Specimens once prepared were handled by plastic tweezers for loading and unloading into tensile grips of the Linkam/Instron. Preliminary scattering measurements revealed that single ply of the monolayer films weakly scattered incident X–rays. In order to maximize the scattering intensity multilayer stacks of films were used in X-ray experiments. These stacks contained 8 ply of monolayer film. *Ex situ* tensile measurements comparing the stress strain response between single ply and multi-ply film were also performed to validate that mechanical testing remained unaffected by using multiply film stacks. These tests revealed that the stress strain response remained largely unaffected by the choice of monolayer films per stack. See Figure 13.

3.3 In Situ X-Ray Scattering Measurements

The general experimental procedure involved in an *in situ* experiment can be described as follows. The tensile testing apparatus (Instron or Linkam) was first mounted in the path of X-ray beam prior to calibration of the X-ray beam. The standard scattering geometry was achieved wherein the plane of the tensile specimen under investigation was orthogonal to the incident X-ray beam as illustrated in Figure 14. At the start of a every new test, a prepared specimen was loaded into the tensile testing apparatus. The load cell and strain

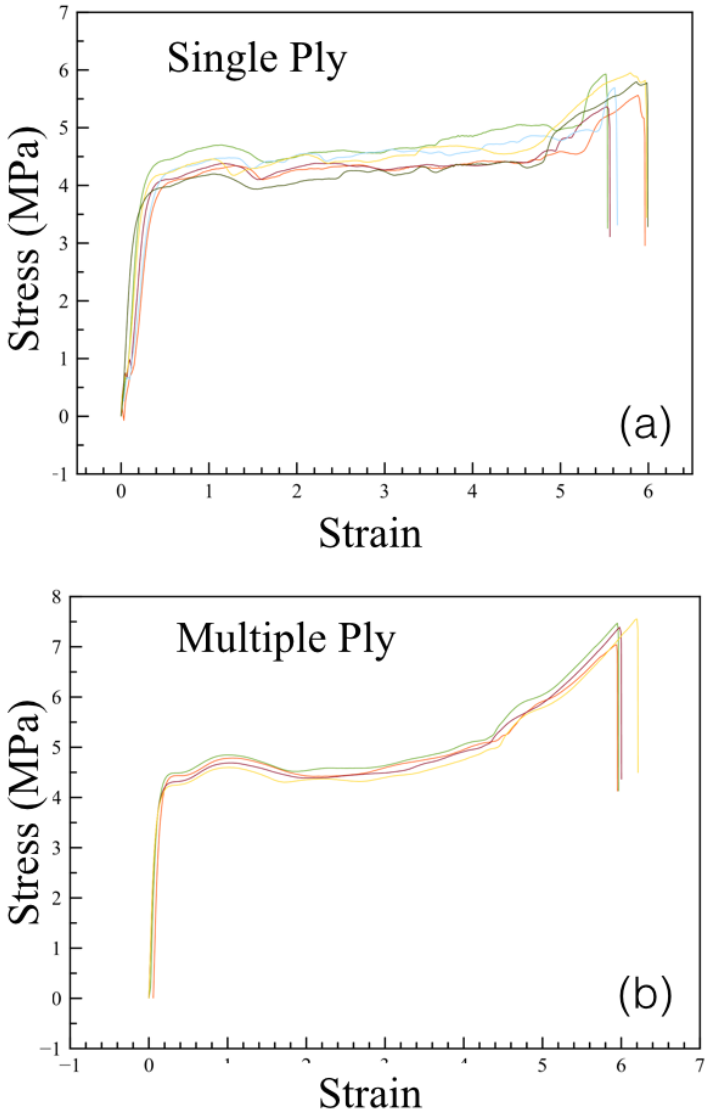

Figure 13: Stress strain comparison between tensile specimens made from a) single ply films b) 8 ply films. The data shown here are from the repeat measurements of specimens of $LLDPE_2$.1a

gauges were set to zero. X-ray data and tensile data were collected simultaneously and the start of data collection for both was synchronized. X-ray scattering measurements were conducted at the Argonne Photon Source (APS), Chicago. Two beamlines were used and the details of the experimental setup, data collection and reduction procedures are provided in the following section.

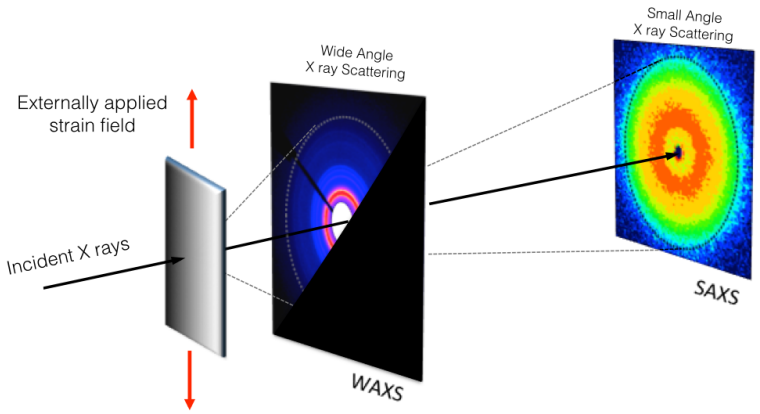

Figure 14: Standard *in situ* setup with simultaneous SAXS & WAXS capabilities combined with tensile testing

3.3.1 Beamline 12-IDC

Beamline 12-IDC is a single detector beamline where a MAR CCD detector can be moved on a translation stage further or closer to a sample to perform SAXS or WAXS experiments respectively. In these experiments, the collimated incident X-ray beam had an energy of 12 keV (corresponding to a wavelength 1.0332Å) and its dimensions were 200 μm x 200 μm. X-rays scattered by the tensile specimens were detected by the detector placed at a fixed distance of 2426 mm from the tensile specimen. The detector had a square pixel size of 175 μm.

SAXS patterns were collected with a time interval of 3 seconds. This was the minimum time interval between consecutive SAXS patterns and was dictated by the time required for detector readout from one pattern. This readout time is the factor limiting the deformation rates utilized in the tensile measurements. Faster rates of deformation in the tensile measurements can be investigated without a loss in strain resolution only when lower intervals between consecutive detector readouts are possible.

A constant exposure time of 0.1 seconds was continually maintained for all the tensile measurements. This short exposure time ensured that specimens could be continually

strained unlike previous studies [1,70,89,90] where one order of magnitude increase in exposure time necessitated strain to be applied discontinuously. Effects related to discontinuous strain are highlighted in Figure 15 through *ex situ* stop-go measurements comparable to those by Butler and Donald [1, 70, 89, 90] where strain was arrested for 30 seconds during collection of SAXS data. Figure 15a shows elongation-time profiles for different ex situ tensile specimens. Elongation was arrested at specific strains as shown by Figure 15b at varying hold times. At the completion of the hold time, elongation of the sample was resumed. The effects of holding and stretching in this way are clearly noticeable for hold times corresponding to the data collection times in the work of Butler and Donald. These preliminary 'strain-hold' experiments show that while the work of Butler and Donald was instructive, it was not free from effects of relaxation which is likely to affected the morphology development during their '*in situ*' studies.

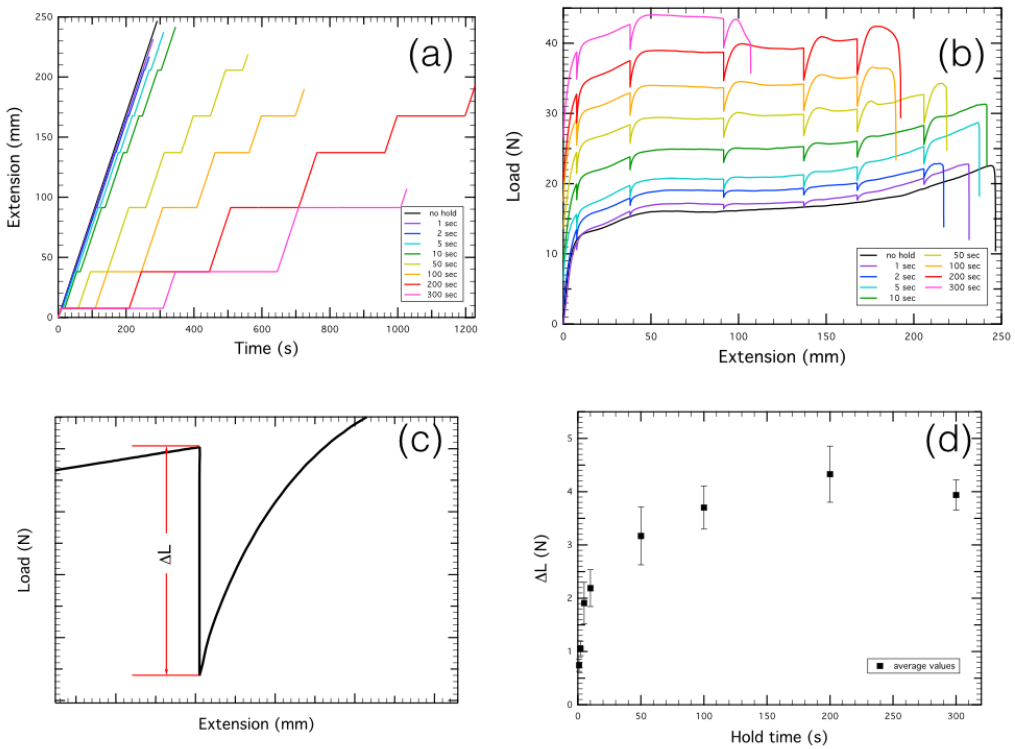

Figure 15: (a) Elongation is arrested for different hold times at various strain points during tensile testing (b) The load strain plots of corresponding strain hold measurements (c) Defines load relaxation during the period of strain arrest (d) Load relaxation as a function of hold times averaged over various strain points. The data shown here are for $LLDPE_2$.1b

Prior to data collection, the sample-to-detector distance was calibrated by the beamline scientist using silver behenate as the standard reference. Silver behenate has a number of well defined scattering peaks in the SAXS range (0.01^{-1}Å to 0.40^{-1}Å). Knowing the peak positions and widths of these scattering peaks it was possible to accurately calibrate the sample to detector distance. Background scattering from air was measured at the same exposure time and was subtracted from the SAXS data.

3.3.2 Beamline 5-IDD DND CAT

Beamline 5-IDD is a triple detector beamline capable of simultaneous SAXS, WAXS and MAXS (Medium Angle X-ray Scattering) measurements. Each of the three detectors are CCD detectors made by Rayonix LLC. At experiments performed at this beamline the beam characteristics were as follows. The incident X-ray beam had an energy of 18 keV (0.7293Å) and its dimensions were 200 μm x 200 μm. X-rays scattered by the tensile specimens were detected by the SAXS detector placed at a distance of 7496 mm from the tensile specimen, which had a pixel size of 177.2 μm x 177.2 μm. The WAXS detector was placed at a distance of 198 mm from the tensile specimen and had a square pixel size of 88.6 x 88.6 μm. The schematic in figure 16 shows the arrangement of the three detector system. The shapes of the detectors and their arrangement provide coverage over a wide azimuthal and reciprocal space range. Further details about the experimental setup at this beamline can be found elsewhere. [91]. Prior to data collection, the apparatus was calibrated by the beamline scientist using silver behenate as the standard to determine sample-to-detector distance. SAXS patterns were collected at a time resolution interval of 3 seconds. A constant exposure time of 0.1 seconds was continually maintained during the tensile measurements. The rate of deformation was once again limited by the detector readout time[3] Background scattering from air was measured at the same exposure and was subtracted from the SAXS data.

[3]This limitation is likely to be short lived as software upgrades to the system at DND CAT are expected in the near future.

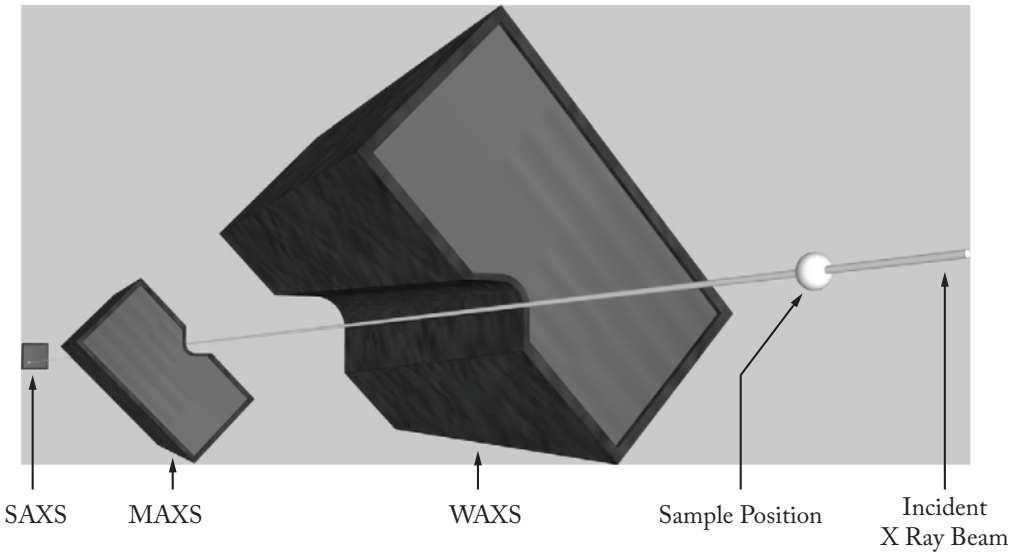

Figure 16: The triple detector system recently acquired by beamline 5-IDD at APS. Figure adapted from [91]

CHAPTER IV

DATA EXTRACTION PROTOCOLS

While the 2D scattering data are visually instructive, a prerequisite for the detailed analysis presented in subsequent chapters is the availability of reduced 1D scattering data. This chapter provides details image processing techniques and workflows that enable the conversion of 2D data to the more useful 1D data. An integral aspect of this conversion and one that is routinely utilized in both SAXS and WAXS data is the extraction of line profiles from the 2D data. For the sake of brevity, the process of extracting line profiles is referred to as a 'line cut' in the remainder of this dissertation. A line cut provides a sampling of the intensity from the 2D data along an arbitrary user specified q-dependent path. The path takes the form of a segment between two pre-selected vertices. The line cut calculates the intensity at each point between the vertices while maintaining the sampling density in the 2D data. The calculation itself must be performed by averaging over several pixels that are orthogonal to the specified line segment path in order to improve the sampling statistics. Clearly, line cuts can be obtained along a number of paths examples of which include but are not limited to vertical lines (i.e. meridian), horizontal lines (i.e. equator) and circular (i.e. at a fixed value of q). The choice of line cut must therefore depend on the intended analysis.

To fully analyze the X-ray data it is necessary to apply a number of models requiring curve fitting. In the current work non-linear curve fitting is undertaken on software package known as MagicPlot. This software is preferred over a number of other useful software because of its ability to perform iterative fitting repetitively via its graphical interface. This capability is particularly useful when working with time resolved datasets such as those obtained as part of this dissertation. The scattering software package 'Nika' based on the IgorPro software platform is used to convert 2D data into 1D line cuts. A detailed description of Nika's capabilities can be found elsewhere [92].

4.1 Extraction of 1D SAXS data

4.1.1 Characteristic Dimension (d_{ac})

Extracting the value of the characteristic dimension d_{ac} is typically the first step in analyzing SAXS data from polymer systems that exhibit a semicrystalline morphology. Once background subtracted data are obtained, the next step is to acquire the appropriate line cuts from the 2D data. Since tensile specimens in the current work were strained either along MD or TD, an investigation into d_{ac} was conducted along the strain direction. Line cuts were therefore selectively obtained along the strain direction. The width of the line paths was varied systematically between 1 pixel and 8 pixels to identify an optimal width for statistical averaging. Between 1 and 8 pixels there was no change in the profile of the line cuts, of course, sampling error was lower for the larger width. Therefore, a width of 8 pixels was chosen for the line profile analysis.

Figure 17 shows the various steps involved in calculating d_{ac} from MD strained specimens and is consistent with the methods described in references [56, 93]. In Figure 17a the pink dotted line segments vertically placed along q_y illustrate the line path along which line cuts were obtained. The solid pink lines represent the width of the line path over which the 2D data were averaged. The intensity profiles from these line cuts are displayed in 17b for the four strains. The peak maxima observed here are directly related to the scattering from lamellar - amorphous repeats in the specimen. Once the line cuts are obtained, the Lorentz treatment can be applied. The Lorentz treatment entails a further correction by a weighting factor dependent upon the geometry of the scattering sample [94]. When considering an isotropic system and considering s as the scattering vector, the intensity is scattered in reciprocal space over spheres of surface area $4\pi s^2$. In order to compare intensities that are spread over spheres whose radii are different, a treatment factor of $4\pi s^2$ used.

Traditionally when q is used as the definition for scattering vector, [95, 96] the corresponding $\frac{1}{\pi}$ factor is dropped and the Lorentz treatment involves suppressing the large scattering intensities at zero q by converting $I(q)$ to $I(q)q^2$. This technique improves the contribution to the scattering maxima from large scale periodic lamellar amorphous repeats whose contribution might otherwise be overlooked as these are visually hard to distinguish

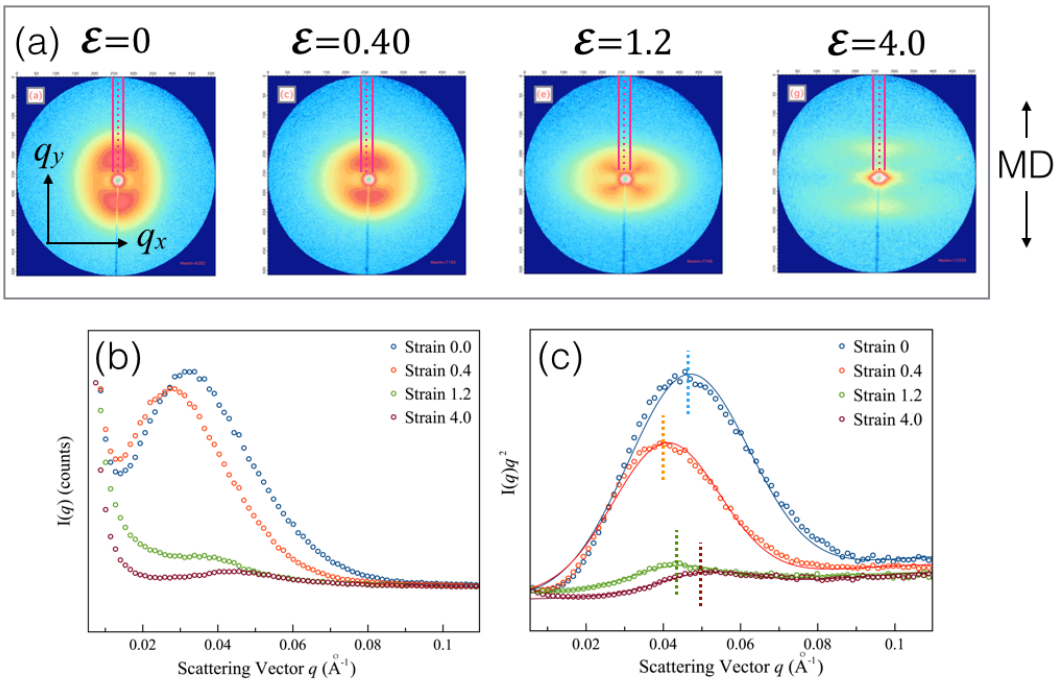

Figure 17: a) Vertical line paths of fixed width, indicated by the pink segmentized zones are used to extract intensity line profiles. Line paths have a width of 8 pixels but are highly exaggerated in the schematic b) Extracted intensity line profiles c) Data are Lorentz corrected and subsequently fit with a gaussian distribution. Solid lines represent best fit curves and dotted lines indicate the location of the peak maxima q^*. The details of the fitting are provided in the text. The data shown here are obtained for the specimen $LLDPE_2$.1a strained along its MD.

especially in the low q regime [95, 96]. Additionally it also eradicates the contribution of dispersed particle scattering that is concentrated at zero q. The Lorentz correction should only be applied in cases where a distinct scattering maxima is observed. Applying the correction when no maxima is observed in the scattering results in the appearance of an artificial maxima which might be erroneously attributed to the morphology [95].

Lorentz treated values of intensity from figure 17b are displayed in 17c. Lorentz corrected intensity profiles can now be analyzed by peak fitting. The lamellar-amorphous peak was fit in the q range 0.02Å^{-1} - 0.08Å^{-1} using a single gaussian function described by the Equation 28. In this fitting range, q^* represents the position of the peak maxima, w_g represents the

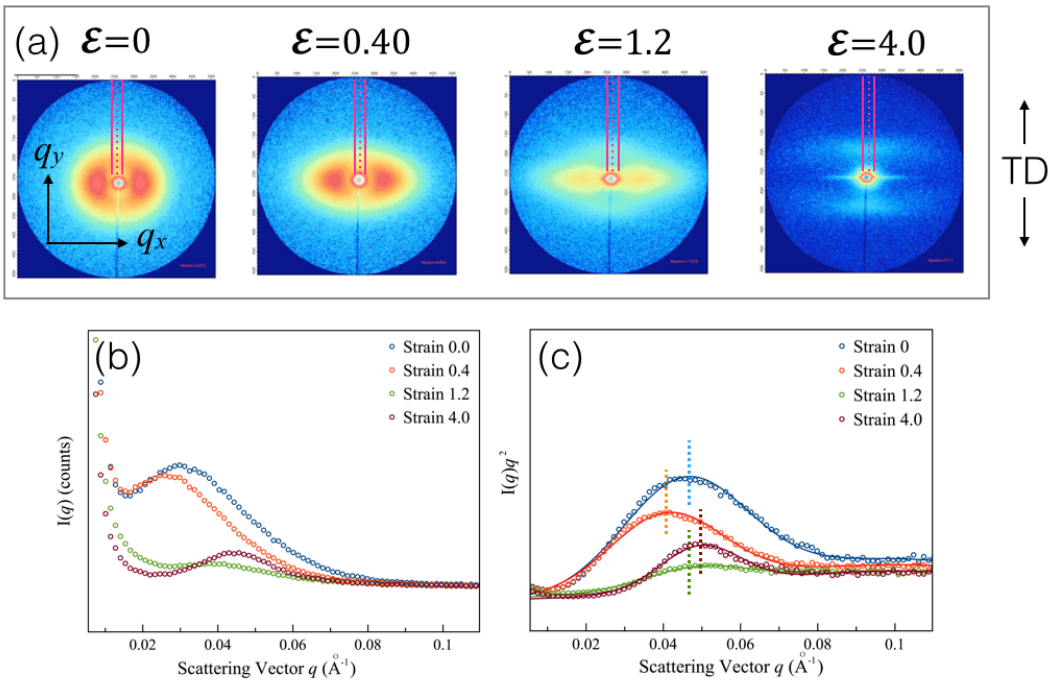

Figure 18: a) Vertical line paths of fixed width, indicated by the pink segmentized zones are used to extract intensity line profiles. Line paths have a width of 8 pixels but are highly exaggerated in the schematic b) Extracted intensity line profiles c) Data are Lorentz treated and subsequently fit with a gaussian distribution. Solid lines represent best fit curves and dotted lines indicate the location of the peak maxima q^*. The details of the fitting are provided in the text. The data shown here are obtained for the specimen $LLDPE_2$.1a strained along its TD.

half width at half maximum and a_g represents the amplitude of the gaussian at q^*.

$$g(x) = a_g e^{\frac{-\ln 2(x-q^*)^2}{w_g{}^2}} \tag{28}$$

Since the scattering vector q measured in Fourier space and dimensions in real space are inversely related the location of the peak maxima i.e. q^* is an accurate measure of d_{ac}. The value d_{ac} can be predicted by Equation 29. In Figure 17c solid lines are the best fit profiles, and the dotted lines correspond to q^*.

$$d_{ac}(\varepsilon) = \frac{2\pi}{q^*(\varepsilon)} \tag{29}$$

Similar to the specimens strained along MD, d_{ac} can also be extracted from TD strained specimens. The entire process of d_{ac} extraction from TD strained specimens is summarized

in figure 18 where 18c represents the position of q^* for the chosen strains via the dotted vertical lines. Although in the current work d_{ac} is measured along the strain direction, in principle d_{ac} can be measured in any radial direction.

4.1.2 Lamellar Width (L_{SAXS})

L_{SAXS} is extracted from 2D SAXS data from strained specimens following the method of Tang et al [56]. Figure 19 shows the steps involved in calculating L_{SAXS} from strained specimens. In figure 19a the pink dotted line segments placed parallel to q_x and illustrate the line path along which line cuts were obtained. The placement of the horizontal line path at a fixed q_y and parallel to q_x is however a non-trivial task. The method of Tang et al dictates that line cuts must only be acquired from regions on the 2D SAXS pattern where a distinct peak maxima exists. Therefore, in the determination of L_{SAXS}, the value of q_y at which the line path is constructed is always made to coincide with q^* for individual values of strain. The solid pink lines represent the width the of the line path over which the 2D data were averaged. The intensity profiles from these line cuts are displayed in 19b at four values of strains. The peak maxima observed here are directly related to ensemble average width of crystalline lamellae. Once the line cuts are obtained the peak maxima were fit using a distribution consisting of two Lorentzians. The standard form of a Lorentzian distribution centered at x_c, having an amplitude a_l and half width at half maximum w_l is given by the Equation 30. The fitting routine implemented in this work was manipulated so as to ensure that the amplitudes, widths and therefore areas under the curve for both the Lorentzians were identical but not constant. This resulted in two identical Lorentzians possessing amplitudes A, half widths at half maximum w_l and centered at x_{c1} and x_{c2}, respectively. The horizontal separation between these peak maxima i.e. Δq_x was then calculated as using Equation 31 and allowed the value of L_{SAXS} as a function of strain to be determined using Equation 32 [56].

$$l(x) = \frac{A}{\frac{(x-x_c)^2}{{w_l}^2} + 1} \tag{30}$$

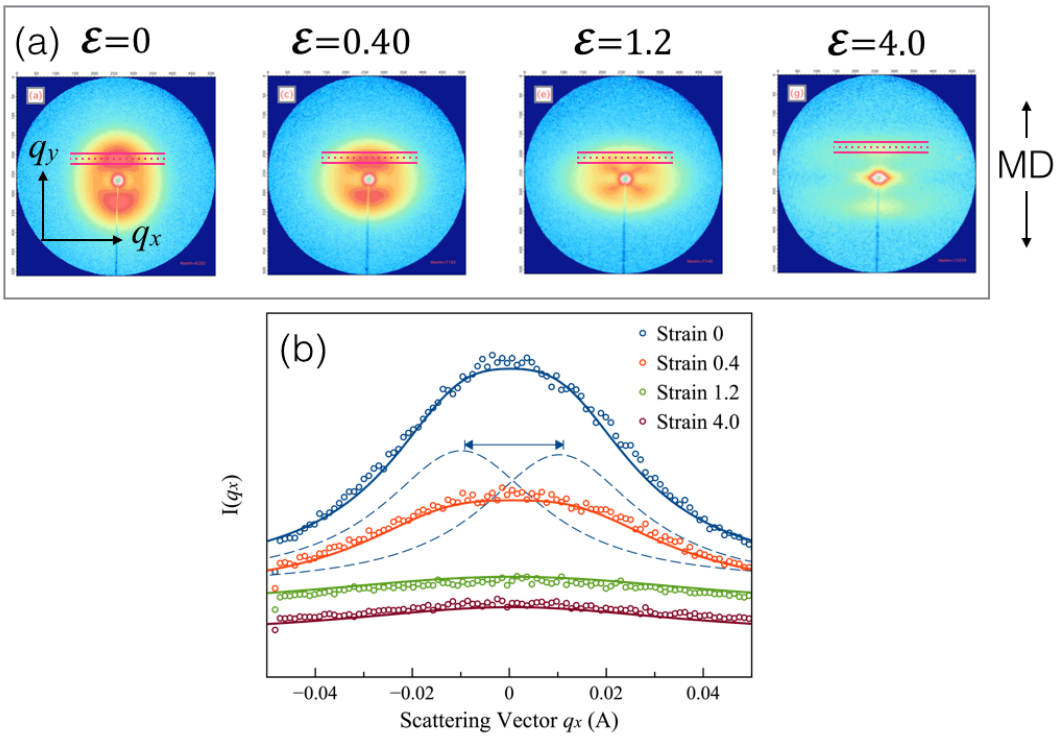

Figure 19: a) Horizontal line paths of fixed width, indicated by the pink segmentized zones are used to extract intensity line profiles. Line paths are uniquely placed parallel to q_x at $q_y = q^*$. Width of the path is fixed at 8 pixels. q_y position and pixel width are exaggerated and are not to scale. b) Extracted intensity line profiles at the four strain points. Data are fit with two identical Lorentzian distributions. The separation between the locations of the two Lorentzians provides a measure of L_{SAXS}. Solid lines represent best fit curves and dotted lines indicate the double Lorentzian distributions which for the sake of clarity are only shown at zero strain. The details of the fitting are provided in the text. The data shown here are obtained for the specimen $LLDPE_2$.1a strained along its MD and have been vertically translated.

$$\Delta q_x(\varepsilon) = \mid x_{c1}(\varepsilon) - x_{c2}(\varepsilon) \mid \tag{31}$$

$$L_{SAXS}(\varepsilon) = \frac{2\pi}{\Delta q_x(\varepsilon)} \tag{32}$$

4.1.3 Tilt Angle (χ)

A peculiar feature in the MD strained films, particularly at intermediate values of strain is the appearance of a four lobe pattern. The four lobe pattern has been observed previously

and has been linked to the deformation of lamellae by different groups of researchers [1,30]. An example of a four lobe pattern observed in the current work is presented in figure 20b. The tilt angle χ measured in degrees, is also defined with respect to this four lobe pattern as the positive value of the angle subtended between the dotted arrows. A quick examination of the 2D SAXS patterns in 20a suggests that the tilt angle is strain dependent. prompting an investigation into the phenomenon of the four lobe pattern and the tilt angle χ subtended by it is investigated.

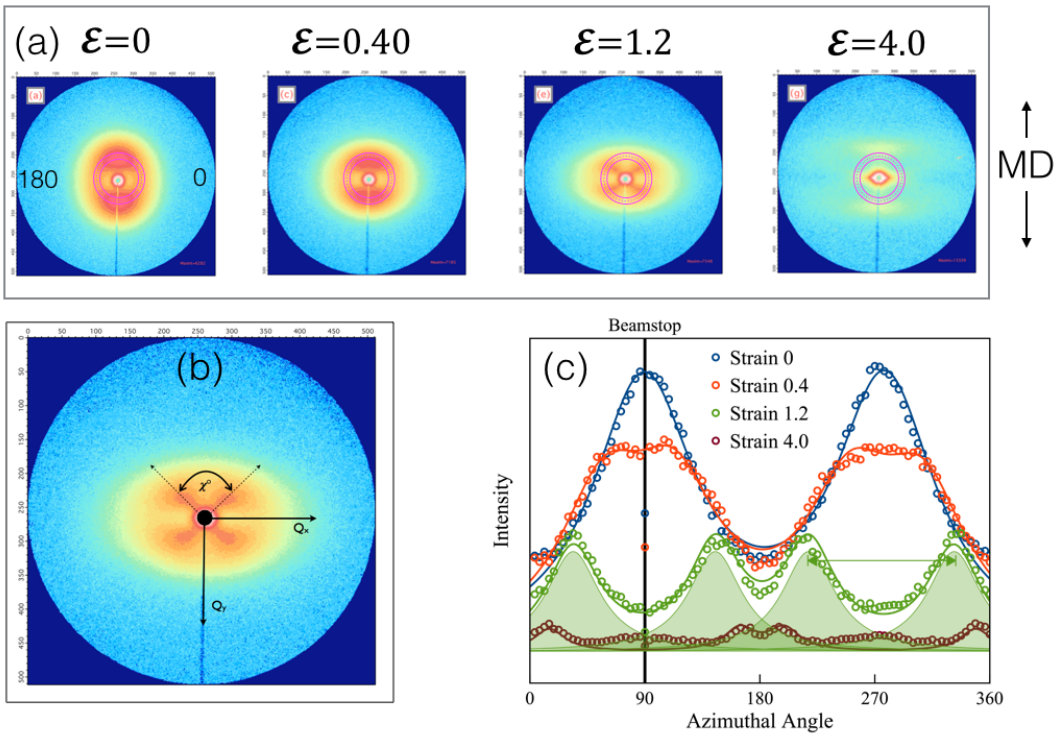

Figure 20: a) Azimuthal line paths of fixed width, indicated by the pink segmentized zones are used to extract intensity line profiles. Width of the path is fixed at 8 pixels and its radius is 45 pixels. Width and radius are are exaggerated and are not to scale. b) Graphical definition of the tilt angle c) Extracted intensity line profiles at the four strain points. Data are fit with four identical Lorentzian distributions. The separation between the locations of first second or third fourth Lorentzians provides the a measure of χ, the latter is marked by the solid green arrow. Solid lines represent best fit curves and dotted lines indicate the double Lorentzian distributions which for the sake of clarity are only shown at strain 1.2. The details of the fitting are provided in the text. The data shown here are obtained for the specimen $LLDPE_2$.1c strained along its MD

While the usefulness of straight line paths in determining d_{ac} and L_{SAXS} is obvious,

similar protocols cannot be used to investigation of the tilt angle phenomenon due to the circular nature of its evolution. Correspondingly a different line path must be used for data extraction. The straightforward choice in this case, is to make use of a circular line path (i.e. constant q_y=q_x) in order to extract properties 2D SAXS patterns that exhibit azimuthal angle dependence. An example of such circular or azimuthal line paths is highlighted in figure 20a by the pink annular segmentation. Again, a path width of 8 pixels is chosen for statistical averaging. In the previous section, the importance of correct placement of the line path with respect to peak maxima in the 2D SAXS patterns was discussed. In this particular case, the radius of the chosen azimuthal path, i.e. the fixed radial distance measured outward from the center of the scattering pattern is of utmost importance as it must be ensured that the azimuthal path always bisects the peak maximum.

The line cuts obtained at four representative values of strain for MD strained specimens from azimuthal line paths are shown in Figure 20c. In order to extract the tilt angle, angular separation between the peak maxima are calculated using peak fitting routines. Four distributions are shown in Figure 20c corresponding to the four strains shown in Figure 20a. Four lobes were clearly visible at only out of four chosen strain points. Nevertheless, each of the strains were fit with four Lorentzian functions, one for each of the four lobes. The fit Lorentzians are shown on figure 20c for that strain value where the four lobes are clearly visible without ambiguity. The overall fit curve for each of the strain points is provided in the figure. The fitting routine is manipulated as in the previous section, such that all Lorentzians possess the same amplitude, half width at half maximum and area under the curve. The only difference between the four functions is then their peak centers i.e. x_{c1}, x_{c2}, x_{c3} and x_{c4} respectively where $x_{c1} < x_{c2} < x_{c3} < x_{c4}$. The Equation 33 then describes the value of the tilt angle at an instantaneous value of strain.

$$\chi(\varepsilon) = \mid x_{c2}(\varepsilon) - x_{c1}(\varepsilon) \mid = \mid x_{c4}(\varepsilon) - x_{c3}(\varepsilon) \mid \tag{33}$$

4.1.4 Lamella Alignment Ratio (LAR)

The Lamella Alignment Ratio (LAR) is a factor that provides an understanding of the relative fraction of MD and TD oriented lamellae in a specimen by simultaneously comparing

the intensities along the meridian q_y and along the equator q_x such that the origin coincides with the beamstop. The LAR is extracted from a 2D SAXS pattern as follows. First, a 2D SAXS pattern is subjected to two line cuts, one along the MD ($I(q)_y$) and one along the TD ($I(q)_x$). The line cuts are obtained using an 8 pixel slice as has previously been described. If n represents the number of pixels at which intensity data are obtained from the line cuts, then the LAR can be defined as follows.

$$LAR = \frac{1}{n} \sum_{i=1}^{n} \frac{I(q)_{y,i}}{I(q)_{x,i}} \tag{34}$$

An isotropic specimen would have an equal distribution of intensity along the q_x & q_y thus resulting in an LAR of 1 [97].

4.2 Extraction of 1D WAXS data

4.2.1 Percentage Crystallinity (Xc)

The extraction of percentage crystallinity from 2D WAXS data is possible by evaluating the ratio of peak areas of the crystalline peaks and the total area under the scattering curve. This is conventionally achieved by first obtaining 1D line cuts of the circularly averaged 2D data and subsequently subjecting the line cuts to profile fitting. The line cuts are expected to contain crystalline peaks distributed over a broad amorphous scattering. The standard process involves fitting the individual crystalline peaks with appropriately sharp Lorentzian distribution functions and the amorphous scattering with a Voigt distribution function.

In the current work, the 2D WAXS data corrected for air scattering are first subjected to azimuthal averaging thus providing a 1D WAXS plot in the form $I(q)$ vs q. Guinier [98] suggested that the representing the scattering vector q in the form s where $s = \frac{q}{2\pi}$ during crystallinity extraction is beneficial[1]. Therefore, the appropriate replotting of data into $I(s)$ vs s is performed. The 1D WAXS patterns are subjected to a peak fitting routine wherein the crystalline peaks are fit with Lorentzian distributions having an area A_L such that the Equation 30 originally in terms of amplitude a_l can be modified to be area normalized.

[1]Full width half maximum (FWHM) of a crystalline peak in the WAXS measured in s can be converted to a domain sizing using the relationship Domain Size = $\frac{1}{FWHM}$ thus circumventing Scherrer Analysis

$$L(x) = (\frac{A_L}{w_l \pi}) \frac{1}{\frac{(x-x_c)^2}{{w_l}^2} + 1} \tag{35}$$

The amorphous scattering is peak fitted with a Voigt distribution. The equation of a Voigt curve $V(x)$ whose area is A_V can be described by a fractional mixture of a Gaussian distribution of full width at half maximum W_G and Lorentzian distribution of full width at half maximum W_L and distributions commonly centered at position x_c. If n is the fractional content of the Lorentzian i.e. mixing fraction of the mixture, then $V(x)$ is given by

$$V(x) = y_0 + \frac{A_V n^2 W_L}{4\pi(x-x_c)^2 + {W_L}^2} + \frac{A_V(1-n)\sqrt{4\,ln\,2}\,e^{\frac{-4\,ln\,2(x-x_c)^2}{{W_G}^2}}}{\sqrt{\pi} W_G} \tag{36}$$

A correct approximation of an amorphous Voigt might only be made if a fully amorphous sample is analyzed first. WAXS data from the amorphous melts of each of the three LLDPE resins was therefore measured in a Linkam heat stage combined with a lab based WAXS device[2]. 2D patterns were obtained by half hour exposures at temperatures above the melt temperature T_m for all resins. A Voigt distribution was fitted to the 1D WAXS dataset of the completely amorphous structure (see Figure 21) and the following ranges of parameters were obtained for which the adjusted coefficient of determination (R^2) was 0.999:

- $x_c = 0.2066$ Å^{-1}
- $A_V = 36$ to 50
- $n = 0.92$ to 0.97
- $W_L = 0.1$ to 0.2 Å^{-1}
- $W_G = 0.06$ to 0.08 Å^{-1}
- $y_0 = 0$

Figure 21 shows the Voigt fits to 1D isotropic WAXS measured from the melt of resin $LLDPE_3$ and film $LLDPE_3$.1c respectively.

[2]Device Located at ExxonMobil Research and Engineering (EMRE)

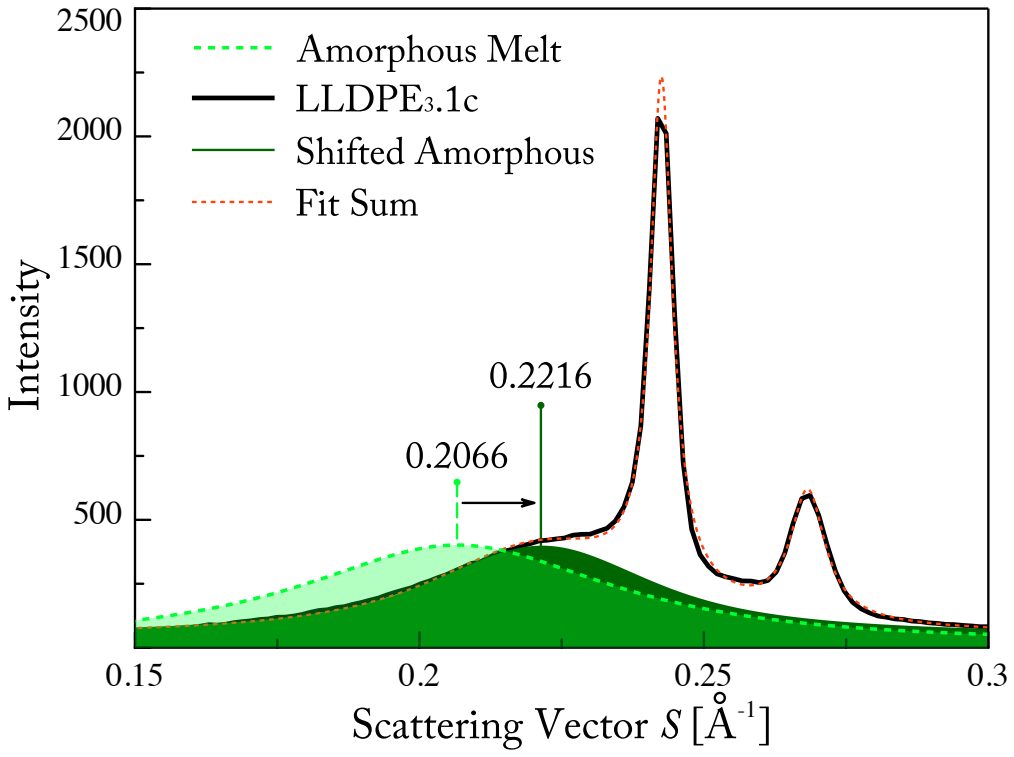

Figure 21: Voigt distribution fits of the amorphous contribution in 1D WAXS for as made film and melt of resin $LLDPE_3$

Once the template for the amorphous scattering is obtained, fitting the 1D WAXS data from the semicrystalline film is a straightforward exercise. The fitting routine is shown in figure 22 for data collected as a function of strain. A fitting window is identified between s values of 0.18 and 0.3Å^{-1}. The fitting window represents that range of s within which significant changes in the WAXS patterns are observed. Ideally, the value of crystallinity would be most accurate provided the fitting was performed on the entire range of s. However outside of the fitting window, the total intensity of the scattering is consistently low across all samples. By systematically neglecting this contribution, it is expected that deviations from absolute crystallinity will be consistent across all films.

The orthorhombic (110 and 200) peaks are the most intense in the 1D data measured for as made films since orthorhombic polyethylene is the stable crystalline form. These are visible clearly in the fitting window in Figure 22 and are fitted with Lorentzian distributions. At increasing values of strain a monoclinic (010) peak appears very close to the centre of

the Voigt. The monoclinic peak is therefore included in the fitting as a Lorentzian function but its area is held at zero until the fit from the amorphous is no longer able to sufficiently describe the data. Equation 37 where a_{hkl} and $hkl = (110), (200), (010)$ represent the areas under the crystalline peaks and A_V represents the area under the amorphous scattering i.e. Voigt Distribution determines the percentage crystallinity for the specimen

Crystallinity is extracted by the equation 37.

$$Xc(\varepsilon) = \frac{a_{110}(\varepsilon) + a_{200}(\varepsilon) + a_{010}(\varepsilon)}{a_{110}(\varepsilon) + a_{200}(\varepsilon) + a_{010}(\varepsilon) + A_V(\varepsilon)} \tag{37}$$

4.2.2 Herman's Orientation Parameter

The Herman's orientation parameter provides a single parameter quantification of orientation between an axis of interest and a specific reference axis of orientation. The standard formula for calculating a Herman's Orientation Parameter (F_i) for an axis of interest i can be given by the following equation where ϕ represents the angle between i and the reference axis of orientation.

$$F_i = \frac{3\cos^2\phi_i - 1}{2} \tag{38}$$

Figure 23 shows the variation of the Herman's Orientation Parameter as a function of the angle ϕ between a reference axis and an axis of interest.

This definition implies that F_i can have a theoretical maximum of 1 and a theoretical minimum of -0.5. The physical interpretation of these values is as follows. When F_i is unity, i is aligned parallel to the reference axis of orientation. When F_i is -0.5, the entity i is aligned perpendicular to the reference axis. A value of zero indicates that the entity i has no preferential alignment with respect to the to reference axis of. In the current work, the behavior of blown films is observed as a function of strain applied along the vertical direction and hence the appropriate values of F_i are calculated with the vertical direction set as a reference. Depending on whether the the MD is held vertical or the TD is held vertical, the Herman's orientation parameters will provide insight into the the orientation various morphological entities relative to MD or TD.

4.2.3 Orientation of the Crystalline a, b and c axes

An analysis of Herman's orientation parameters from the WAXS data quantifies the relative orientations of the normals to the hkl planes in the system i.e. normals to the 110 and 200 orthorhombic crystal planes. However since an azimuthal distribution of intensities is always obtained for these, the $\cos^2\phi$ term is not a unique value but rather a distribution that is more appropriately designated as $\langle\cos^2\phi\rangle$. The value of this distribution is obtained by the Equation 39.

$$\langle\cos^2\phi\rangle_{hkl} = \frac{\int_0^{2\pi} I(\phi)\, sin(\phi)\, \cos^2(\phi)\, d\phi}{\int_0^{2\pi} I(\phi)\, sin(\phi)\, d\phi} \tag{39}$$

In this equation $I(\phi)$ represents the intensity at azimuthal angle ϕ, and the vertical direction i.e. the strain direction is taken as having an azimuthal angle equal to ninety. Using equations 39 and 38 the values of F_{110} & F_{200} can be readily determined. Typically, the Herman's orientation parameters for the a,b and c axes i.e. F_a,F_b and F_c are determined from the Hermans orientation parameters for the pure $h00$, $0k0$ and $00l$ planes corresponding to each of the three axes. In the case of LLDPE blown films, the only pure peak obtained is the (200) orthorhombic. Therefore a different route must be used to extract the values of F_a,F_b and F_c. Wilchinsky's relationships [99] provided in equations 40 to 42 enable the conversion of F_{110} & F_{200} to the Herman's orientation parameters for the a,b and c axis are abbreviated to F_a, F_b and F_c, respectively. These relationships are used when pure peaks corresponding to the three axes a,b and c

$$F_a = F_{200} \tag{40}$$

$$F_b = 1.445(F_{110}) - 0.445(F_{200}) \tag{41}$$

$$F_c = -(F_a + F_b) \tag{42}$$

4.2.4 Orientation of the Amorphous Chains

The orientation of the amorphous chains is not trivial to extract and is rarely attempted due to the difficulties in extracting this information. One of the significant developments from the current body of work is the ability to extract from the 2D WAXS patterns in an

organized manner, a quantifiable orientation parameter of amorphous chains. The analyses described in this section will establish the methodology to quantitatively separate the contribution from the crystalline and amorphous phases to the WAXS. Figure 24 schematically shows the steps involved in deconvoluting the experimentally measured WAXS pattern into its crystalline and amorphous fractions. The expected results of the deconvolution are qualitatively shown in Figure 24a. The quantitative analysis protocol to obtain Herman's orientation factors for the deconvoluted amorphous peak from the 1D WAXS data are shown in Figure 24b.

Deconvolution is carried out by a combination of sector and azimuthal cuts. First, a WAXS pattern at a fixed strain, typically at ε_0 was azimuthally sectioned into several sectors having a width of 10°. A total of nine sectors were obtained between the orthogonal axes subtended by the MD and TD i.e. between 0 and 90°at 10°intervals. Each of the 1D WAXS datasets at ε_0 obtained by such azimuthal sectioning were fitted with amorphous and crystalline peaks at fixed s within the fitting window described in the subsection 4.2.1. Crystalline peaks were fit with Lorentzian distributions while amorphous scattering in the scattering were fit with Voigt distributions as described in subsection 4.2.1. Thus nine Voigt fits each representing the amorphous contribution to the scattering were obtained between the MD and TD axes at intervals of 10°for a single WAXS pattern. The equation 36 is area normalized i.e. A_V represents the area under the Voigt; in order to acquire the amorphous intensity however the amplitude of the Voigt a_v must be determined.

At values of n i.e. mixing fraction close to unity, the area under the Voigt becomes predominantly Lorentzian and therefore the assumption that W_L is representative of the width of the Voigt is viable. Since areas under the Voigt and the Lorentzian are now nearly equal, the amplitude of the Voigt a_v which also happens to be the amorphous intensity I_{am} can be calculated at any fixed strain ε and azimuthal angle ψ by the following equation

$$a_v(\varepsilon, \psi) = I_{am}(\varepsilon, \psi) = \frac{2A_V(\varepsilon, \psi)}{\pi W_L(\varepsilon, \psi)} \tag{43}$$

Accordingly the error propagation can be determined to be

$$\Delta I_{am}(\varepsilon,\psi) = \pm \frac{2|I_{am}(\varepsilon,\psi)|}{\pi}\sqrt{\frac{\Delta {A_V}^2}{{A_V}^2} + \frac{\Delta {W_L}^2}{{W_L}^2}} \tag{44}$$

In the above described approach, 1D Voigt fits representative of the amorphous contributions in the 1D WAXS data at ε_0 serve as the fitting template for amorphous contributions at higher strains. Therefore the appropriate choice of fitting parameters for the Voigt template are made by first examining the LLDPE resins in their purely amorphous state as described in subsection 4.2.1. Due to the symmetric nature of distribution of WAXS in biaxially oriented systems, a reflection of azimuthal intensities about the strain direction provided a 180°azimuthal window of the amorphous intensity. An example of this is provided in figure 25. The total number of points at which the amorphous intensity is obtained are not sufficient to implement the determination of $\langle \cos^2 \phi \rangle$ by equation 39. A more straightforward method is implemented wherein the amorphous intensity distribution with ϕ is fitted using a standard Gaussian distribution described in equation 28. The full width at half maximum of this Gaussian i.e. $(2w_g)$measured in degrees can be utilized in place of ϕ in equation 38 to provide the value of F_{am} at an instantaneous strain. This procedure was then repeated iteratively for WAXS patterns obtained at higher strains and therefore orientational changes in the amorphous domains could be studied. Figure 25 illustrates the change in the full width at half maximum of the gaussians fit to the amorphous intensity over a range of applied strains.

4.3 1D Correlation Analysis (γ): Scattering from Lamellar Systems

1D correlation functions of 2D SAXS patterns are calculated following the method of Strobl and coworkers [62, 63, 100]. An implementation of this protocol is a feature of the software package 'Corfunc' developed within the framework of the collaborative Computational Project for Fibre Diffraction (CCP13) Project. In the current work Corfunc is operated via Matlab to perform the 1D correlation on line cuts obtained along the strain direction.

1D correlation analysis is a data extraction protocol that first transforms 1D line cuts such as those in Figure 17c into 1D correlation functions such as those in Figure 26a-d. In this process, the morphology under investigation is assumed to resemble the lamellar

stack described in Figure 26d by the schematic on the left and the resulting parameters extracted from Figure 26d by the schematic on the right describe the features of this assumed morphology. The initial basis for the 1D correlation analysis is the ideal lamellar stack the electron density distribution $\rho(r)$ for which is described by a unit step function having ρ_c and ρ_a as the crystalline and amorphous electron densities respectively considering the lamellar system to form in a semicrystalline virgin polymer.

The 1D correlation analysis is formally designed for isotropic scattering in which case the necessary 1D line cut is obtained by performing a circular averaging since the scattering maxima appears in all directions. However, anisotropic scattering can be studied using this approach provided the line cuts are obtained from a specific direction of interest. The primary requirement of the correlation analysis is that the scattering and therefore the line cuts always provide a scattering maxima. The correlation analysis is useful because it provides a methodology approach to determine d_{ac} as well as deconvolute the value of d_{ac} into d_a and d_c. This deconvolution is not possible by fitting the peak maxima as described in subsection 4.1.1.

Mathematically, the correlation function $\Gamma(r)$ is the Fourier transform of the 1D scattering curve $I(q)$ as defined by the following equation. The normalized correlation function $\gamma(r)$ is used when $I(q)$ is measured in arbitrary units, where $\gamma(r)$ is defined in Equation 45.

$$\Gamma(r) = \frac{1}{2\pi}\int_{-\infty}^{+\infty} q^2\, I(q)\, e^{i(qr)}\, dq = \frac{2}{2\pi}\int_{0}^{\infty} q^2\, I(q)\, cos(qr)\, dq \tag{45}$$

$$\gamma(r) = \frac{\int_0^\infty q^2\, I(q)\, cos(qr)\, dq}{\int_0^\infty q^2\, I(q)\, dq} \tag{46}$$

Based on the geometrical interpretation of $\gamma(r)$, a number of parameters can be extracted from 1D line cuts the most important of which are the characteristic dimension d_{ac} and the crystalline and amorphous contributions to the characteristic dimension i.e. d_c and d_a respectively. In addition, a minimum value of the crystal thickness can be extracted in terms of the average core thickness d_0 as well as the interface thickness d_{tr}. The former is very useful since it represents the average size of the thinnest crystal lamellae. Since 2D SAXS data are measured between finite values of the scattering vector q, the resulting 1D

line cuts must be extrapolated to values between 0 and ∞ before performing the Fourier transform. The extrapolation is possible by selecting an appropriate low q tail region of $I(q)$ to extrapolate to $q = 0$ and a high q head region of $I(q)$ to extrapolate to $q = \infty$. The extrapolation process is the most crucial step in performing the transform as both overfitting and undercutting the head or tail might lead to erroneous values of extracted parameters. In the current work the head and tail region were judged by trial and error until some convergence between peak fit values of d_{ac} matched correlation function values of d_{ac}. A built-in self checking feature of 'Corfunc' is that it performs an inverse Fourier transform of the extrapolated data to ensure that the original data can be perfectly described by the extrapolated data with the head and tail. For more detail regarding the extraction of the 1D correlation itself readers are directed to the book chapter by P.Cebe [88]. Figure 26 shows the differences in $\gamma(r)$ for subtle changes in the assumed ideal lamellar morphology.

The denominator of the normalized 1D correlation function determined by Equation 46 at $r = 0$ is called the scattering invariant Q. The invariant represents the total area under the scattering curve. Subsequent to the normalization by the invariant performed as part of Equation 46 the 1D correlation ranges between +1 and -1. The average separation between lamellae or amorphous regions previously defined as d_{ac} is extracted from $\gamma(r)$ by the location of the first maximum of $\gamma(r)$ for $r > 0$. The horizontal line that can be drawn tangent to the very first minimum of $\gamma(r)$ is the experimental baseline and is represented in Figure 26d by the horizontal dashed line marked γ_{min}. The value of γ_{min} is given by $\chi_c^2(\rho_c - {\rho_a}^2)$ where χ_c represents the linear crystallinity within a single lamellar stack. The slope of $\gamma(r)$ prior to the first minimum is related to the values of average core thickness d_0 as well as the interface thickness d_{tr}.

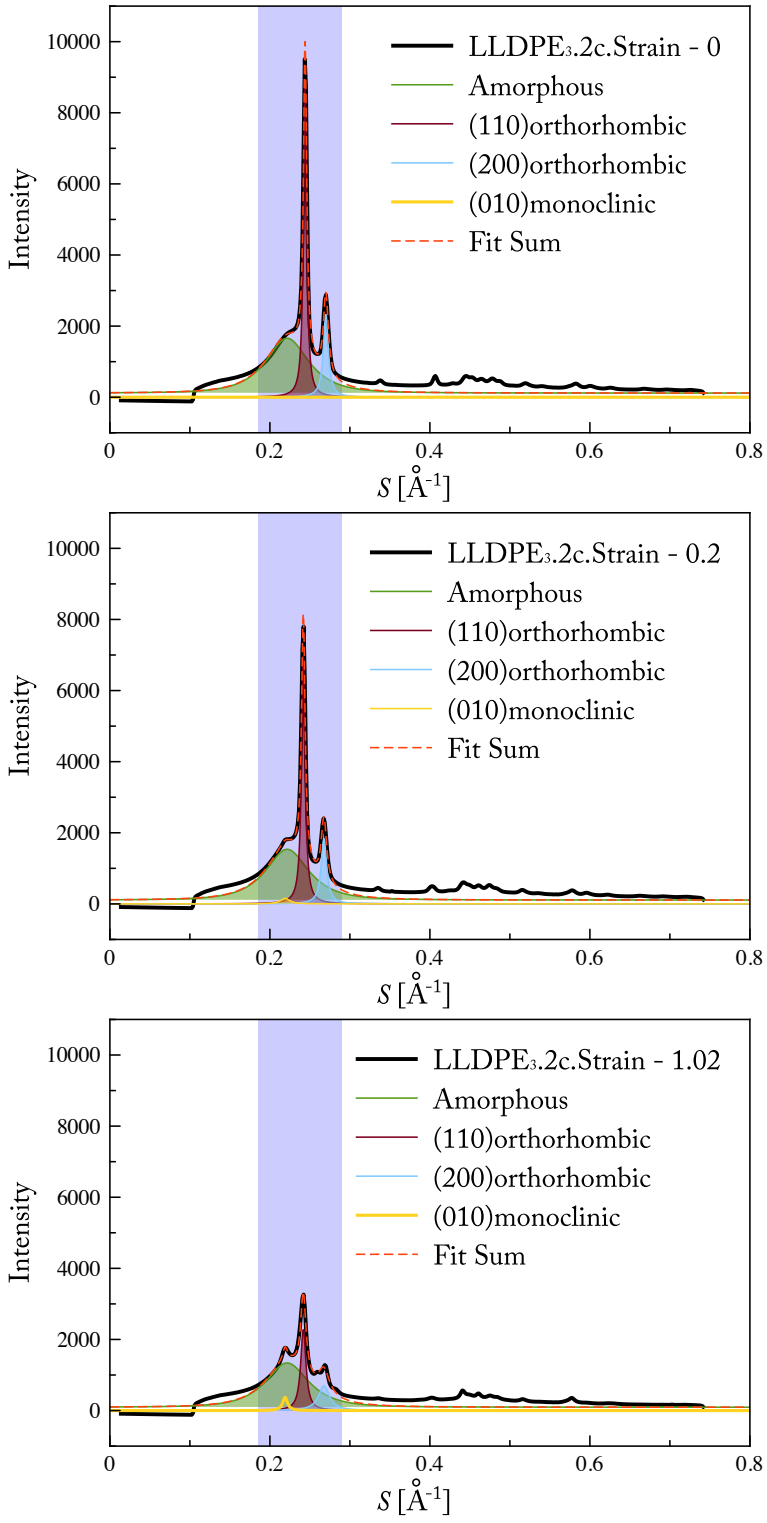

Figure 22: Use of the fitting window for deconvoluting the crystalline and amorphous contributions in the 1D WAXS data under strain. The window is the lilac region where convolution of the sharpest crystalline peaks and amorphous halo exists. The fitting is performed in reverse order of strain as the low intensity monoclinic peak is highly conspicuous at high strain

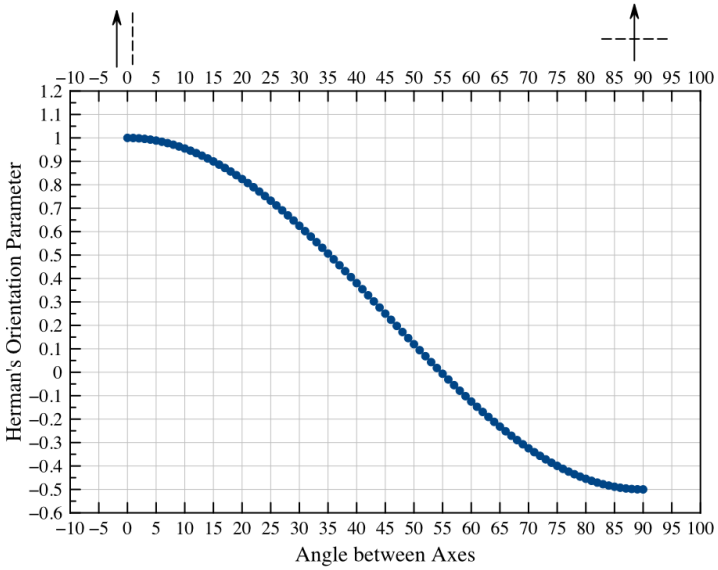

Figure 23: The variation of Herman's orientation parameter between values of -0.5 and 1 is dependent on the angle between the reference axis and the axis of interest i. The solid arrow represents the reference axis and the dotted line represents the axes of interest. The angle ϕ is the positive angle between the two.

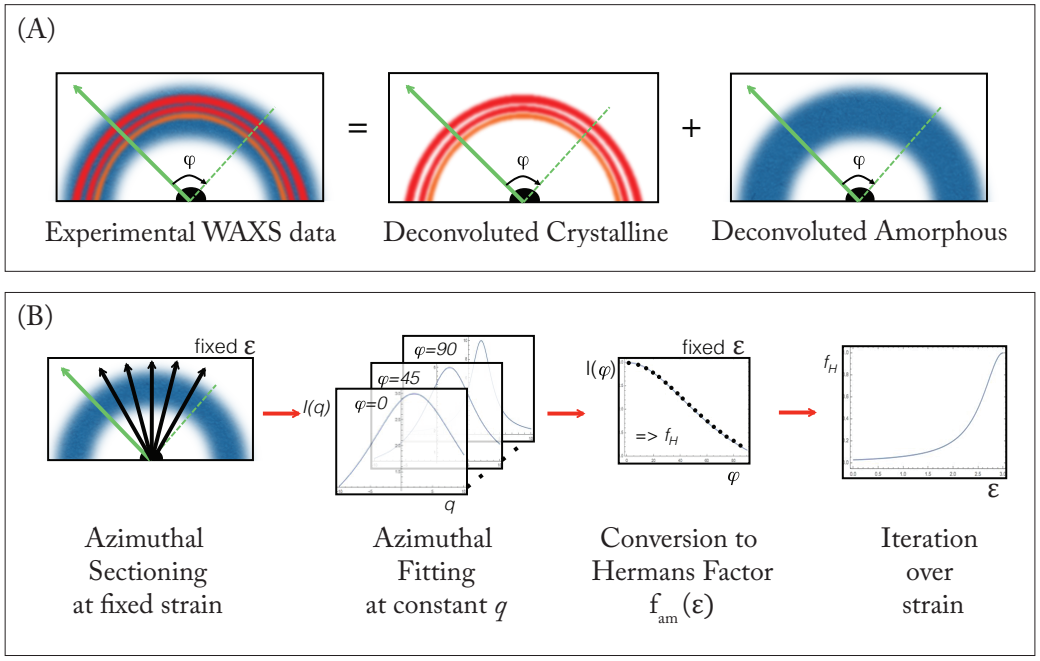

Figure 24: (A) Qualitative description of experimental WAXS data and its deconvoluted crystalline and amorphous components. (B) Stepwise workflow to obtain Herman's orientation factors from 1D WAXS data

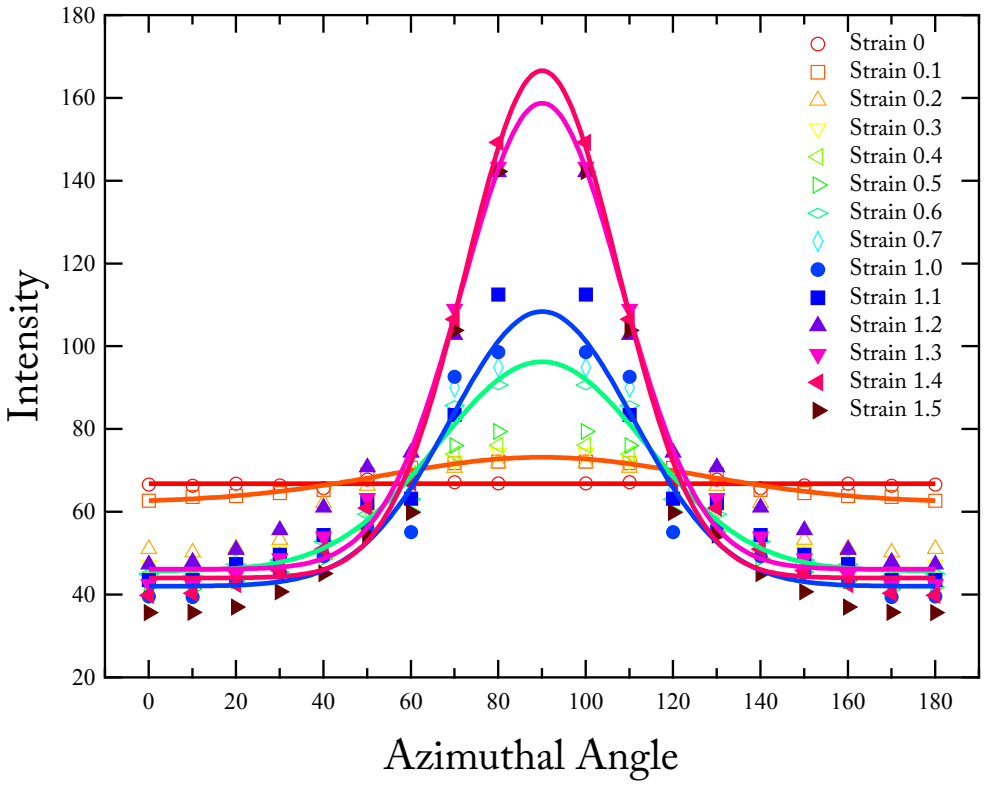

Figure 25: Evolution of the azimuthal distribution of amorphous intensity under strain is shown by colored symbols for the film $LLDPE_3$ strained along TD. The solid lines represent best fit gaussians at the chosen strains.

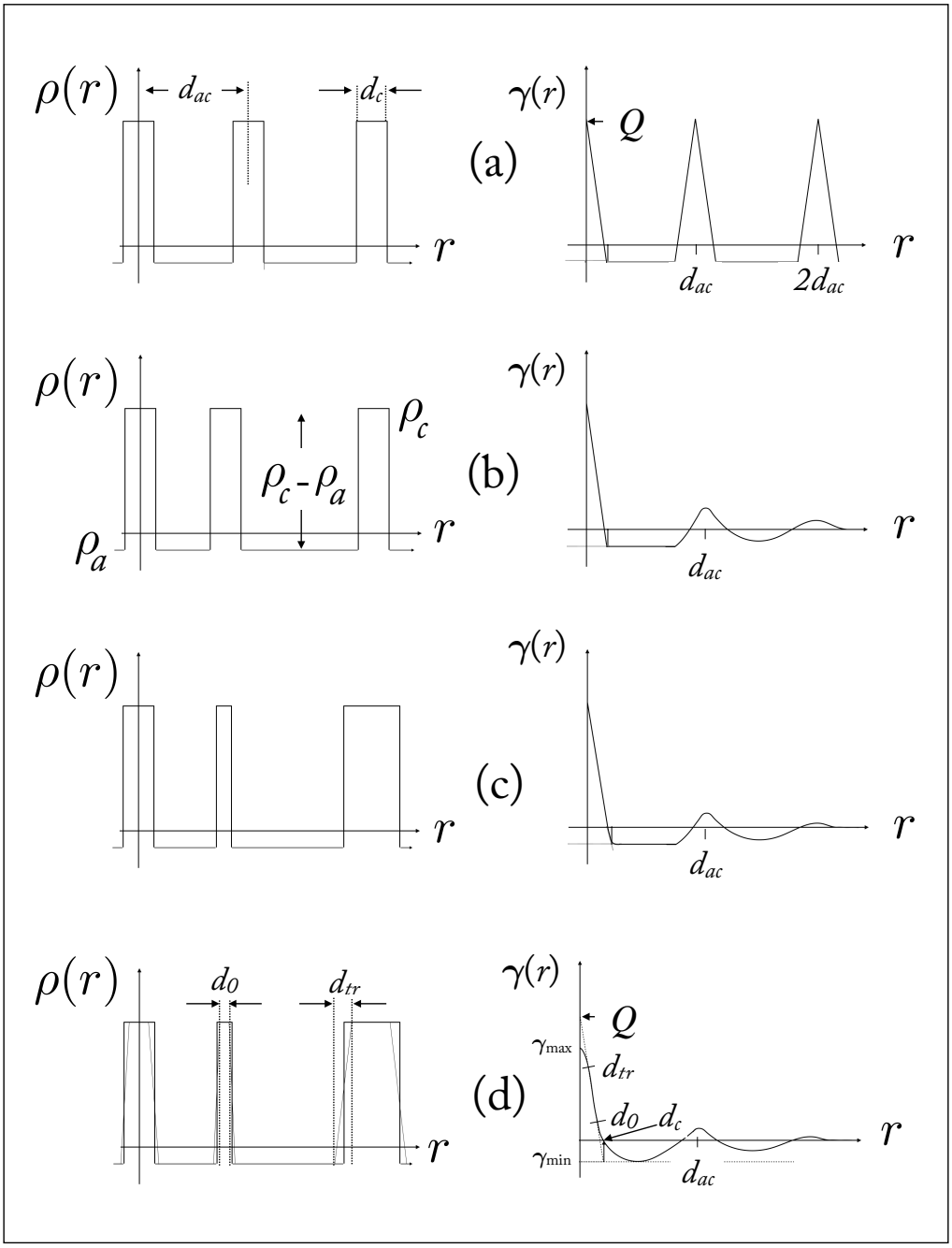

Figure 26: Electron Density Distribution (left hand column) and Its effects on the 1D Correlation (right hand column) are shown for (a) an ideal periodic lamellar morphology with sharp interfaces between amorphous and crystalline regions (b) an ideal aperiodic lamellar morphology with sharp interfaces (c) an ideal aperiodic lamellar morphology with sharp interfaces but non-uniform crystal lamellae thickness (d) an aperiodic lamellar morphology with non-uniform crystal lamellae thickness and an interfacial transition region. Figure adapted from [62]

CHAPTER V

MESOSCALE DEFORMATION: MD - TD COMPARISON

In this chapter the effect of processing derived orientation on the uniaxial deformation behavior of films is investigated for a single blown film series. Films from only one resin were utilized since any occurrence of orientational dependence on deformation, would also occur in the remaining series of films since the processing conditions utilized during fabrication were common across all resins. Films of resin $LLDPE_2$ were preferentially selected based on the recommendation of collaborators at EMCC, because this particular series of films has been extensively investigated by different characterization techniques and therefore provides additional information about the polymer.

5.1 Stress Strain Behavior

Figure 27 shows the typical behavior in MD and in TD deformation for samples of the resin $LLDPE_2$. The data displayed herein were supplied by EMCC and were collected under the appropriate ASTM standards. The overall response of the $LLDPE_2$ series of blown films over a large strain range is comprised of an initial Hookean region between ε_0 and $\varepsilon_{0.1}$ where stress rises linearly with strain, followed by the occurrence of two yield points at $\varepsilon_{0.1}$ and $\varepsilon_{0.48}$ respectively. Subsequent to the second yield point, strain increased without significant changes in stress between $\varepsilon_{0.48}$ and $\varepsilon_{2.0}$. Beyond $\varepsilon_{2.0}$ however, a non-linear rise in the stress with strain was observed up to the point of failure. The strain range beyond which the stress increases non-linearly with strain is referred to as the strain hardening regime. In this study, deformation along the MD, as well as the TD, exhibited two distinct yield points in the low strain regime. Double yield points have previously been reported and investigated by other researchers in LLDPE resins [38–40, 83–85, 101, 102]. Figure 27 also shows clearly that MD specimens are particularly influenced by film thickness in the strain hardening regime. TD strained specimens show more uniformity in their stress-strain behavior in the strain hardening regime remaining largely unaffected by film thickness or

blow up ratio.

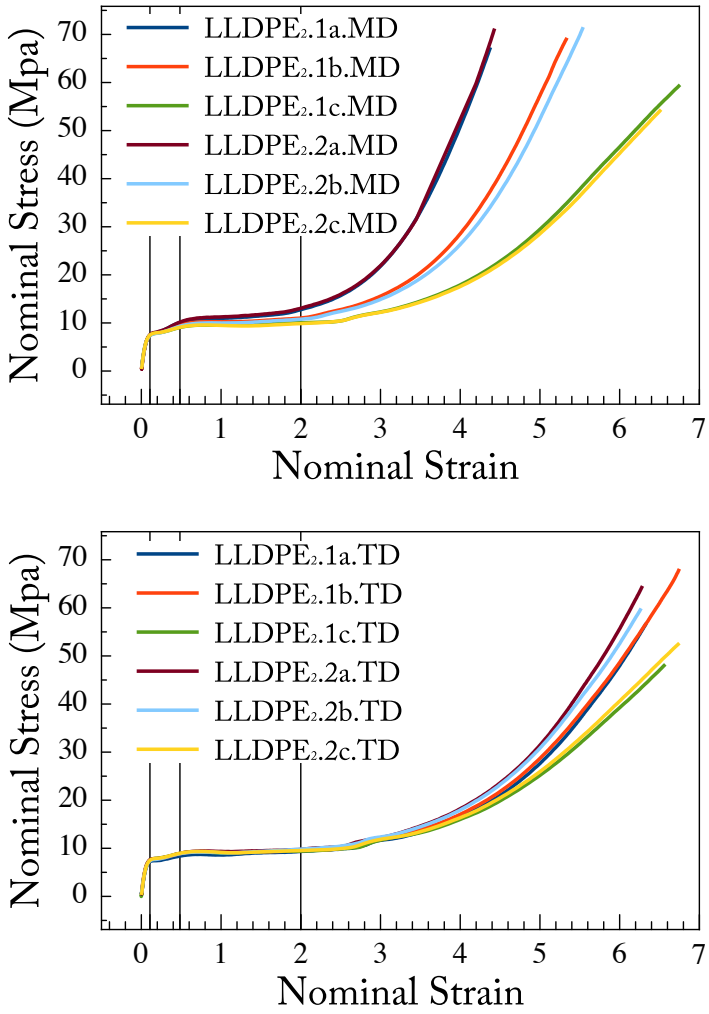

Figure 27: Stress-Strain behavior exhibited by $LLDPE_2$ films under MD (upper figure) and TD (lower figure) strain. TD strained films appear to be less influenced by thickness and BUR variations than corresponding MD strained films particularly in the strain hardening regime. These data were captured in *ex situ* measurements on monolayer films. Vertical black lines indicate the strains at which the first yield, second yield occur and onset of strain hardening occur at $\varepsilon_{0.1}$, $\varepsilon_{0.48}$ and $\varepsilon_{2.0}$, respectively. Data supplied by EMCC.

5.2 In situ Meausrements

The tensile data reported in this chapter were collected using a Linkam stage therefore appropriate samples were prepared as described in Section 3.2.3. Two sets of specimens were prepared having their tensile axes aligned along the MD and TD of the films respectively.

A total of twelve tensile specimens were tested, as listed in Table 3. *In situ* measurements were conducted at beamline 12 ID-C of the APS, wherein a Linkam TST 350 tensile stage was mounted in the path of the incident X-ray beam. Tensile testing was conducted using the standard procedure for Linkam based specimens as previously detailed in Section 3.2.2. Scattering data were collected using procedures listed in Section 3.3.1. 2D SAXS data were subjected to the image analyses procedures described in Section 4.1.

Table 3: Resin and Corresponding Film Specimens

Resin	Film Label	BUR	Thickness(μm)	Direction
$LLDPE_2$	$LLDPE_2$.1a	2.5	20	MD & TD
	$LLDPE_2$.1b	2.5	30	MD & TD
	$LLDPE_2$.1c	2.5	75	MD & TD
	$LLDPE_2$.2a	3.0	20	MD & TD
	$LLDPE_2$.2b	3.0	30	MD & TD
	$LLDPE_2$.2c	3.0	75	MD & TD

5.2.1 SAXS Results

The inset of Figure 28 shows selected 2D SAXS patterns from the *in situ* tensile experiments on two of the films stretched along MD and TD at the indicated values of strain. A number of key 2D SAXS patterns are enlarged and annotated in Figure 29 to highlight significant features of the scattering that might otherwise not be immediately obvious.

In specimens where strain was applied along TD, the SAXS evolved from a distribution of lobe-like intensity observed equatorially at zero strain, to a diffuse meridional scattering accompanied by equatorial streaking at high strains. While the first and second yield points were not clearly distinguished, strains beyond the second yield were marked by a distinctive scattering pattern featuring the combination of diffuse scattering and equatorial streaking. This combined feature persistently appeared over a strain range of a 180% at minimum at an apparently fixed q_y position until the sample failed. Further inspection of the diffuse intensity was conducted by observing the 1D plots of $I(q)$ vs q. These data for specimen $LLDPE_2.1a$ are shown in Figure 30. The intensity at high strains which in the figure is shown by the peak at $q = 0.45\text{nm}^{-1}$ pertains to the diffuse meridinal intensity. This intensity of this peak subsequent to its appearance, increases with increasing strain.

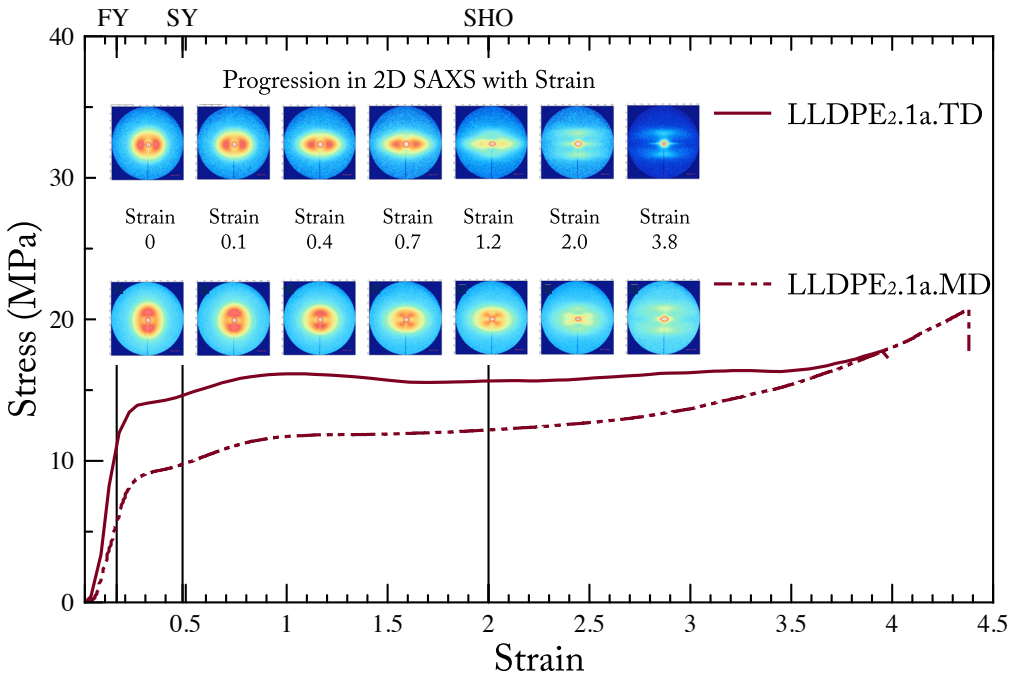

Figure 28: Typical 2D SAXS patterns observed during MD and TD tensile measurements as represented by specimens of $LLDPE_2$ films of 2.5 BUR and 20μm thickness. *In situ* tensile measurements were performed on a Linkam TST350 stage with 8 ply multilayer specimens. Intensities are represented on a logarithmic color scale between minimum and maximum intensity. Specific patterns are selected as they are representative of the general behavior in the SAXS data.

This increase of intensity during continuous straining is only possible if the structures that give rise to the scattering are increasing in number. This points to a morphology that is actively growing in the specimen at high strains and not one that is simply uncovered at high strains.

In contrast, when the strain was applied along MD, the pathway of SAXS evolution was noticeably different than in TD, although the final scattering patterns were similar. In the MD strained sample, the dual lobes were not surprisingly observed along the meridian i.e. the strain direction, since MD and the TD are orthogonal axes of orientation. In contrast to TD, a transformation from the dual lobe scattering to a quadralobe, i.e. a four lobe, scattering pattern was visually observed at strains beyond the second yield point. The quadralobes were clearly visible for strain values greater than $\varepsilon_{0.4}$. With increasing strain the central angles subtended by the lobes also increased. In addition to the obvious visual

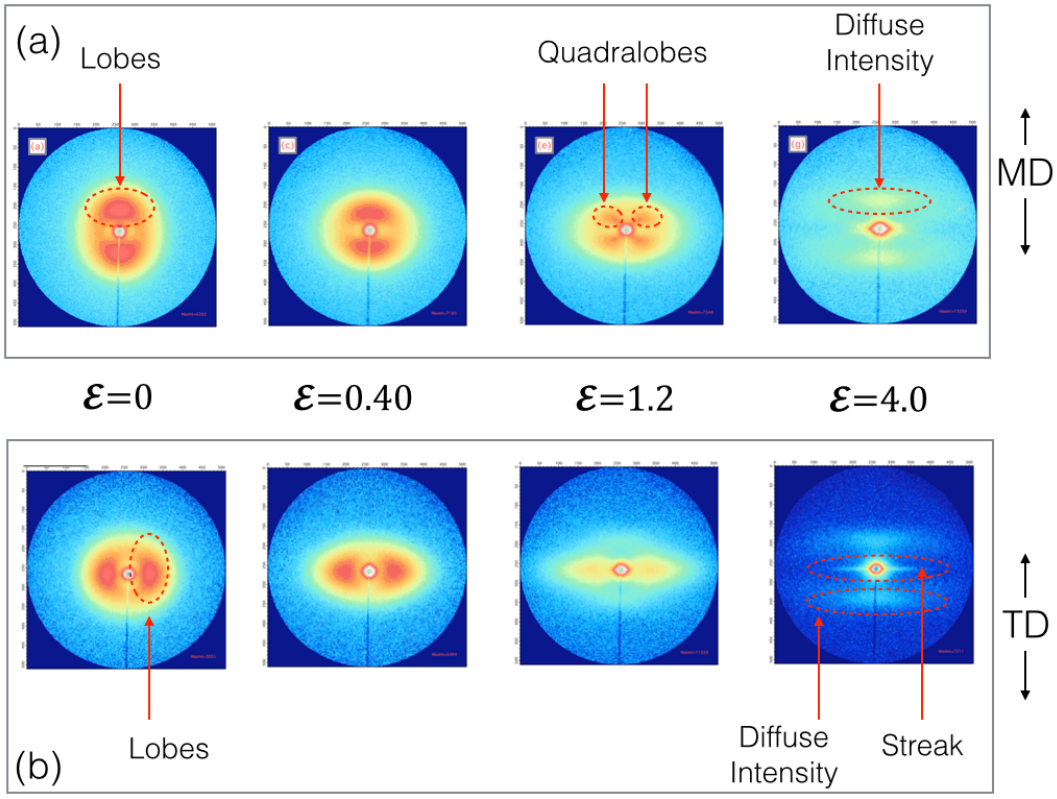

Figure 29: Representative SAXS patterns from Figure 28 are enlarged to highlight significant features in the scattering for a) MD strain and b) TD strain. Annotated features are continually referred to in the text by the indicated nomenclature

differences between the SAXS data from MD and TD strained specimens, some similarities were also observed particularly at increased strain values. The meridional diffuse scattering observed in TD was also present in MD specimens at strains greater than $\varepsilon_{2.0}$, which also coincides with the strains where the quadralobes were no longer visible. As observed for MD strained samples, the diffuse intensities in the TD strained samples appeared persistently in the strain hardening regime of the stress-strain plot of the specimen. The equatorial streak observed in TD specimens was never fully observed in MD although some scattering artifacts were observed around the beamstop. Semicrystalline polymer morphologies consisting of arrangements of crystalline lamellae and non-crystalline amorphous regions that are locally periodic, but globally random, result in the appearance of an isotropic SAXS pattern best described as a ring of intensity around the beamstop [89, 96, 97]. In the work of Lee at al [96], ring like intensities in SAXS patterns were ascribed to globally isotropic spherulites

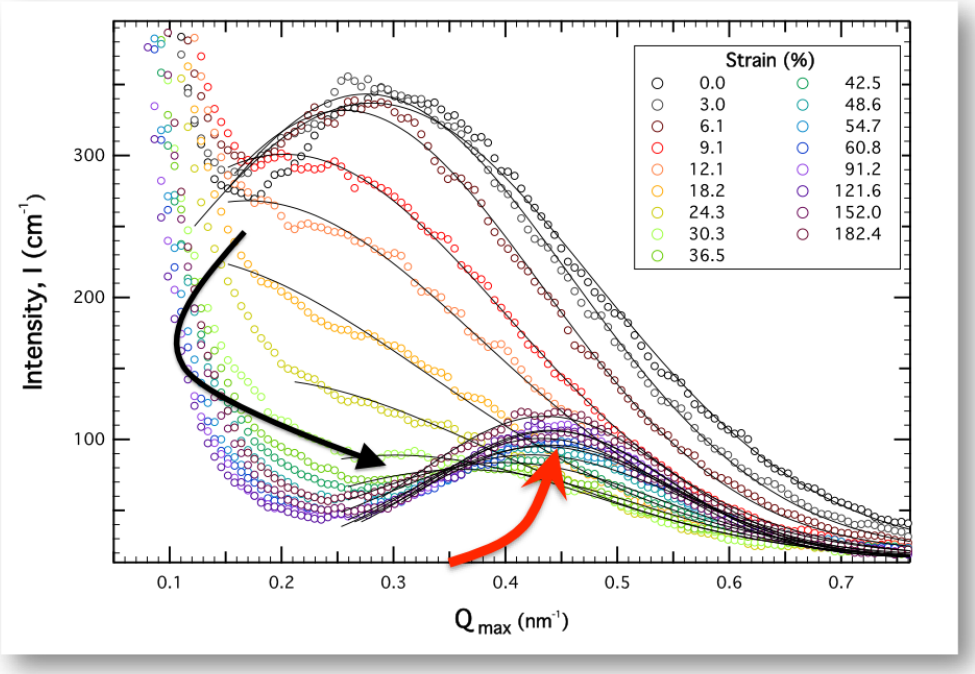

Figure 30: The strain driven evolution of $I(q)$ as a function of q_y for a film of LLDPE$_2$.1a shows two regions. In the first region marked by the black arrow, the intensity moves towards $q = 0$. At high strains the diffuse intensity for a highly TD strained is evidenced by the peak at $q = 0.45\text{nm}^{-1}$ which is marked by the red arrow. The intensity of this peak increases with increasing strain and this is evidence for 'growth' of a new structure. If the structure was present from the start and was simply 'unravelled' the increase in intensity with increasing strain would not be observed.

that possessed locally lamellar semicrystalline morphologies. Such spherulitic morphologies were observed by the authors in heat compressed plaques of HDPE, LDPE and LLDPE resins. The work of Dalton et al [97] on HDPE and LDPE was in full agreement with these findings.

In contrast, the scattering patterns observed in this work were anisotropic and a ring-like intensity was not observed indicating that the morphology was unlikely to be spherulitic. Similar anisotropic patterns have been observed in unstrained blown film specimens of HDPE, LDPE and LLDPE in the work of several authors where the morphology was described as lamellar [1,6,14,103]. Anisotropic scattering has also been observed in specimens of semicrystalline polymers crystallized from the melt state under externally applied shear

stresses [49,53,55]. Indeed, blown film fabrication can be considered as a subset of the latter case, wherein oriented crystallization of the polymer chains in the melt under extensional flow fields is encountered.

Experimental studies such as those by the work of Hsiao and coworkers [49,53,55] suggest that under extensional flow fields, polymer chains crystallize to form lamellae that orient with their long axis orthogonal to the flow direction. An extension of this finding is that an ideal case of perfect alignment would result in alternating lamellar and amorphous phases forming along the flow direction, which in the case of blown film fabrication is the processing direction i.e. in MD. An idealized morphology of this type can be described by a perfectly aligned system of infinitely wide and periodically alternating crystalline and non-crystalline regions. A step function would best describe the electron density distribution along MD, wherein crystalline regions have higher electron density than non-crystalline regions. The interface separating crystalline and non-crystalline regions is assumed be perfectly sharp (Figure 26a). The 2D SAXS pattern of such an ideal morphology with a periodic step function would consist of two point intensities equally spaced about the beamstop and along the MD. The radial spacing between the centre of the beamstop and either of the point intensities then accurately represents the most probable value of a single lamella-amorphous repeat [62, 63, 100].

In order to describe the dual lobe scattering a more realistic morphology of loosely aligned crystalline and non-crystalline regions can be invoked wherein, crystalline lamellae of finite, but polydisperse dimensions, are separated by non-crystalline or amorphous regions. In this case, orientation distribution of the characteristic amorphous-lamellae repeat structure is expected, where lamellar normals are on average oriented along the MD, and the long axis of any lamellae is on average orthogonal to MD. In such a morphology the electron density distribution along MD diverges from the previously described ideal periodic step function to a damped aperiodic step function. This divergence from ideal behavior occurs firstly, due to the existence of differently sized populations of lamella-amorphous repeats causing aperiodicity, and secondly, due to separation of lamella-amorphous regions

by a finite interphase causing a broadening of the sharp transition interfaces of the idealized electron density distribution. Unlike in the ideal case, a smooth transition of electron density between lamellae and amorphous regions cannot be described by a sharp interface and hence an interphase must be included in the model [62,63,100] as shown in Figure 26d. In the SAXS patterns from such morphologies, q^*, i.e. the radially obtained peak position of the lobe maxima, represents the ensemble average of combined length scale contributions from all lamella-amorphous repeats illuminated by the X-ray beam. This experimentally measurable ensemble average is known as the characteristic dimension d_{ac}. The value of d_{ac} can easily be determined from SAXS patterns by profile fitting methodologies established in Section 4.1.1.

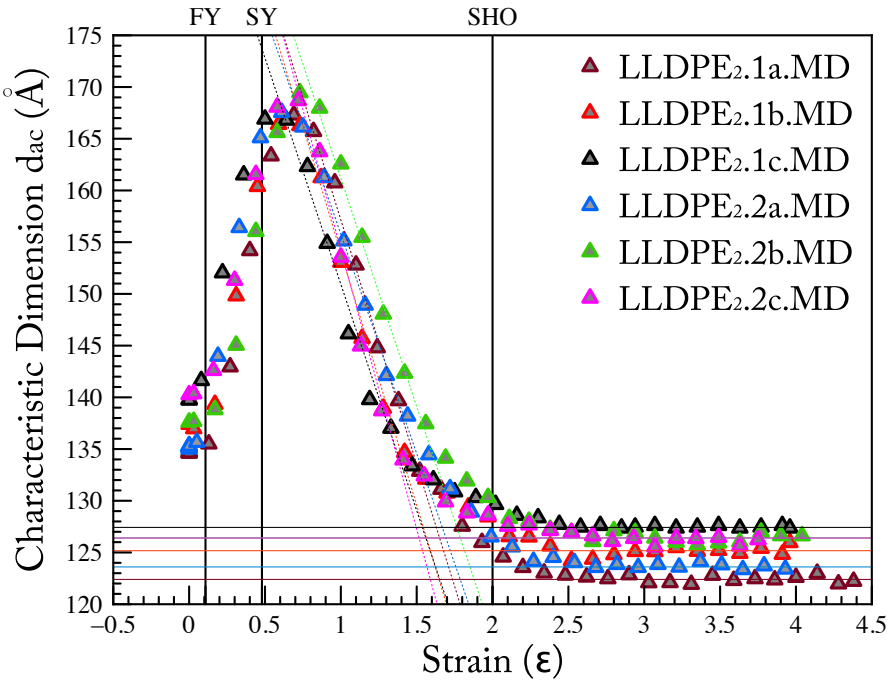

Figure 31: Characteristic dimension changes in $LLDPE_2$ (BUR =3.0) films under MD strain. Dotted lines represent the best fits to the slope in the strain regime after the maximum value of characteristic dimension is attained. Solid lines represent the best fits in the strain regime where constant values of characteristic dimension are persistently observed.

The evolution of the characteristic dimension in the strain direction measured for the series of specimens strained along MD is displayed in Figure 31. The tensile specimens display a similar trend, wherein the characteristic dimension experiences an initial increase

from zero strain reaching a maxima at $\varepsilon_{0.7}$ across all MD strained films. At values of strain between $\varepsilon_{0.8}$ and $\varepsilon_{2.5}$ the characteristic dimension decreases consistently in all specimens. Linear fits to the data within this strain range represent the rate of change of characteristic dimension with strain between the second yield point and the onset of strain hardening. For all the polymers the absolute value of the average slope from the MD strained films is 47 $\pm$ 4 Å. At values of strain above $\varepsilon_{2.5}$ the characteristic dimension appears to reach an asymptotic value between $\varepsilon_{2.5}$ and $\varepsilon_{4.0}$. In this strain range, best fit lines are seen to be parallel to the strain axis, showing that the value of the characteristic dimension remains constant after the onset of strain hardening. In this regime, the characteristic dimension arises from structural features represented by the diffuse meridian scattering. Although for any one of the films, d_{ac} in this strain hardening region is remains constant, the characteristic dimension for different films under MD strain, is different. The variation in d_{ac} of 122Å to 128Å was observed for the different LLDPEs.

The corresponding characteristic dimension variation with strain for TD strained samples is plotted in Figure 32. Changes in the characteristic dimension display trends similar to those observed in MD strain. The characteristic dimension increases from zero strain experiencing a maxima at $\varepsilon_{0.6}$ before decreasing in value and plateauing between $\varepsilon_{2.5}$ and $\varepsilon_{4.0}$. Additionally, the absolute value of the slope which is representative of the rate of change of characteristic dimension with strain between the second yield point and the onset of strain hardening is 51 $\pm$ 2Å for all six films. This value is nearly equivalent to corresponding values observed in MD strained specimens suggesting that morphology changes due to both TD and MD strain between $\varepsilon_{0.48}$ and $\varepsilon_{1.5}$, i.e. between the second yield point and prior to the onset of strain hardening, occur at a similar rate.

The behavior of the long period at high strains particularly in the strain hardening regime for each of the six films strained along TD displays a rather interesting phenomena that is not observed in the corresponding strain regime for MD specimens. Best fit lines in this plateau region of the characteristic dimension at high strains yield an average d_{ac} value of 126 Å. Unlike in MD strain where a 6Å spread was observed between the six films, the spread in d_{ac} values for TD strained specimens is negligible in this strain regime. While the

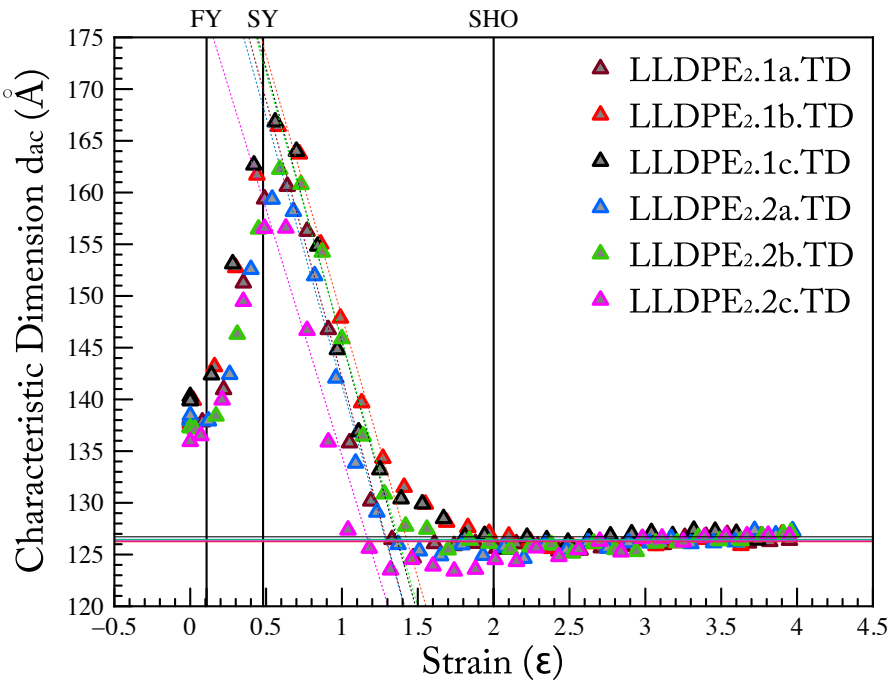

Figure 32: Characteristic dimension changes in $LLDPE_2$ (BUR =3.0) films under TD strain. Dotted lines represent the best fits to the slope in the strain regime after the maximum value of characteristic dimension is attained. Solid lines represent the best fits in the strain regime where where constant values of characteristic dimension are persistently observed. A feature of TD deformation is the apparent convergence to a common value of characteristic dimension at high strains irrespective of BUR or film thickness.

mean values of d_{ac} in the strain hardening regime are comparable between MD and TD, the spread of values are not. This observation is important as it implies that at large values of strain above $\varepsilon_{2.0}$ processing conditions i.e. BUR and film thickness have a negligible effect on the characteristic dimension in TD strain. In MD strained samples in a similar strain range, the effect of processing history cannot be neglected. Consequently, straining any film of $LLDPE_2$ series along the TD causes the internal structure to converge to a single specific value of d_{ac} that must be related to some processing independent factor. It is highly plausible that this factor which governs the high strain value of d_{ac} is directly related to and is characteristic of the molecular architecture of resin $LLDPE_2$.

A similar SAXS study on deformation in blown films of LLDPE made with different types of $\alpha-$olefin comonomers such as hexene, octene, butene and 4-methyl-1-pentene by Butler and Donald [1] investigated the effects of deformation parallel and perpendicular to

MD. However not all features described in the current work were observed in the scattering data of Butler and Donald. While dual lobes, quadralobes and streaking were observed at similar values of strain in the appropriate MD and TD strained samples, the diffuse intensity which is characteristic of the current work were not observed in [1]. More recent *in situ* studies [30,104] on blown films of LLDPE have observed the formation of the diffuse intensity at high strains. In the work of Romo-Uribe et al [30] tensile specimens of LLDPE at high strains produced SAXS patterns with the diffuse intensity persisting over a strain range of 50% in the strain hardening regime. However the characteristic dimension persistence due to the structural feature at high strains was not investigated. The more detailed work of Liu et al [104] on ethylene-propylene copolymers showed a structural feature at high strains similar to that observed in the current work with a corresponding characteristic dimension value of 180Å over a strain range from 100 - 200 % strain. Strain induced crystallization was invoked by these authors to explain the persistent behavior. However, a link between the architecture of the resins involved in these studies could not be made to the high strain characteristic dimension since the processing variables such as BUR and thickness were not considered in the design of experiments in these prior studies [30, 104].

The changes to the relative orientations of lamellae in the MD-TD plane was determined from the SAXS data via calculations for the tilt angle χ for MD strained specimens in which quadralobes are observed. The instantaneous value χ at any value of strain then represents the ensemble average orientation for a fragmented lamellar block in the MD-TD plane. The protocol to extract values of χ are described in detail in Section 4.1.3. Lamellar width L_{SAXS} is also extracted from the SAXS data as described by the procedure in Section 4.1.2.

The variation of the tilt angle and change in lamellar width for an MD strained sample of $LLDPE_2$ under strain was calculated and the results are displayed in Figure 33. Prior to the first yield point, L_{SAXS} values do not change suggesting that lateral dimensions of lamellae are preserved at small strains. Subsequently to the first yield point, lamellae experience a reduction in the value of L_{SAXS} before reaching an asymptotic value beyond $\varepsilon_{2.5}$. The plateau region corresponds to the diffuse intensity in MD specimens. The tilt angle has a value of 0 prior to the first yield point. The value of χ begins to increase

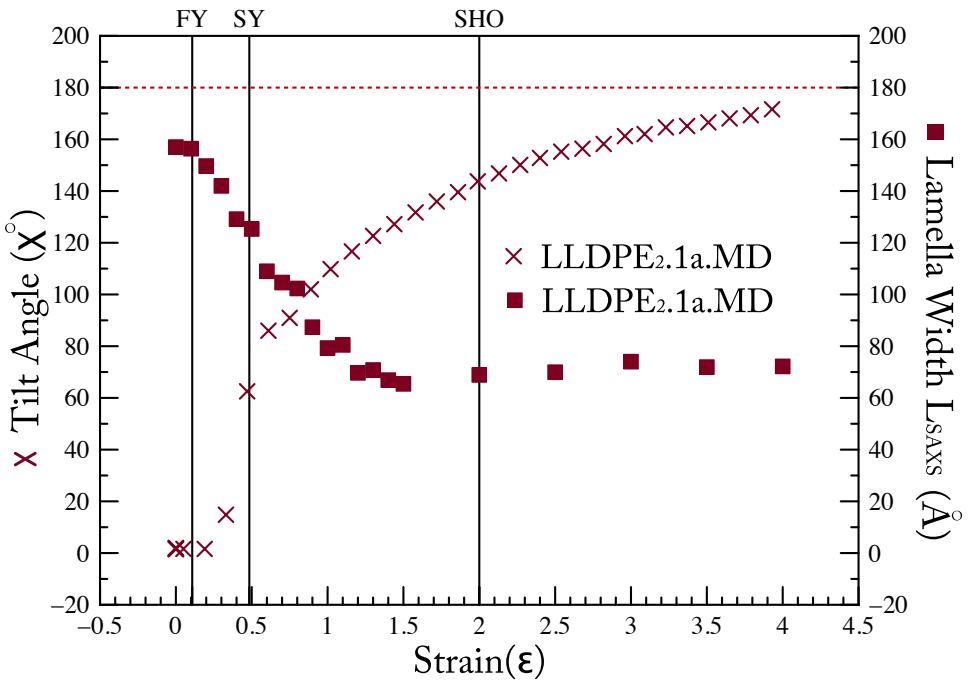

Figure 33: Lamellar width and tilt angle changes in BUR =2.5 $LLDPE_2$ film of 20μm thickness under MD. Closed squares represent the change in lamellar width due to MD strain. Tilt angle measurements are obtained from only MD strained specimens as a quadralobe pattern in the SAXS is required to extract these values. Black dotted lines represent the first and second yield point respectively. The red dotted line represents the theoretical maximum value of tilt angle for fragmented lamellae.

at strains coinciding with the reduction in L_{SAXS} values. This behavior suggests that changes in lateral width of lamellae and their orientations are initiated simultaneously. The magnitude of changes in the values of L_{SAXS} and χ is large between the first and second yield points but progressively reduce with increasing strain.

5.2.2 Physical Interpretation of the SAXS data

In situ deformation and SAXS studies in the recent past have successfully captured some components of Peterlin's model of deformation [79] described in detail in subsection 2.3.2. The 2D SAXS data in Figure 29 shows the response of the initial morphology to small strain perturbations and agrees well with stage one of Peterlin's model. The dual lobe intensity in MD and TD is largely preserved at low strains indicating preservation of the original lamellar scheme in the first stage prior to yielding. The increase in the characteristic dimension

prior to the first yield point occurs due to affine extension of amorphous domains. The possibility of lamellae being displaced relative to each other is however not excluded. During deformation along MD, analysis shows that d_{ac} changes continuously between between ε_0 - $\varepsilon_{0.1}$. L_{SAXS} only begins to decrease beyond strains greater than $\varepsilon_{0.1}$ and coincides with increase in χ. Between ε_0 and $\varepsilon_{0.1}$ the lamellae remain structurally unaffected indicating that in the strain range ε_0 - $\varepsilon_{0.1}$ affine deformation of the inter lamellar amorphous domains occurs.

At higher strains corresponding to the second yield point in MD strained specimens, the scattering shows a discontinuous change from the dual lobe to the quadralobe pattern. Four point SAXS patterns observed in the work of Butler and Donald and Romo-Uribe et al as have been ascribed to the restructuring of original lamellae. Butler and Donald [1] argue that the four point pattern appears at the macroscopic yield point and corresponds to corrugation and bending of the original lamellae which is then succeeded by lamellar fragmentation at higher strains. By comparison, Romo-Uribe et al [30] observe the four point pattern appearing between the first and second yield points in PE due to the formation of a 'staggered roof' structure. Both structural models could explain the appearance of a four point pattern in the scattering. While the two groups of researchers provide little evidence for either of the two hypotheses to explain quadralobe scattering, the suggestion that values of strain beyond the macroscopic yield are accompanied by fragmentation of the lamellae is highly plausible. In our data, deformation is no longer affine beyond $\varepsilon_{0.2}$ as the structural integrity of the lamellae is affected as indicated by the reduction of L_{SAXS}.

This implies that lamellae fragment beyond $\varepsilon_{0.2}$ and the fragmentation is accompanied by orientational changes as strain increases above $\varepsilon_{0.2}$. The morphology of the lamellae between $\varepsilon_{0.1}$ - $\varepsilon_{0.2}$ cannot be resolved by SAXS data alone. Indeed it is in this strain regime, that the morphology of the lamellae is ambiguous as it can be mathematically described as either staggered or corrugated. Additional data from WAXS can resolve this ambiguity by providing information about chain slips or unit cell transformation. Based on Peterlin's [79] model, tensile drawing beyond values of strain associated with fragmentation of lamellae is accompanied by a continuous change in lamellar orientations. In the current

work, between $\varepsilon_{0.2}$ and $\varepsilon_{4.0}$ lamellae on average are shown to change their orientation by nearly 90° as they rotate into the strain direction from their initial position perpendicular to the MD. Since the orientational change can occur in a clockwise or an anti clockwise manner, the average tilt angle value at the highest strains is nearly 180°. From Figure 33 it appears as though the tilt angle asymtotically approaches this theoretical value in MD strained films.

The inherent difference between lamellar fragmentation schemes in MD and in TD is captured through the SAXS pattern differences between $\varepsilon_{0.3}$ and $\varepsilon_{4.0}$. MD samples show clearly the phenomenon of rotating fragmentized lamellae through the observation of a quadralobe pattern. With increasing strain the quadralobe pattern collapses into a feature that resembles a streak but is not as well defined. TD samples in contrast show a clear equatorial streak but not the quadralobe behavior. The equatorial streak has been observed in the work of other groups and is most often ascribed to the formation of extended chain crystals [49, 52–54]. These extended chain crystals have been referred to as the shish in a shish kebab structure (see Figure 6) and result from the formation of fibre like structures due to aggregation of fibrils. The formation of shish or extended chain crystals at high strains is consistent with Peterlin's molecular model at high strains. At high strains in TD, samples show clearly identifiable equatorial streaking suggesting that extended chain crystals form and are well oriented along the strain direction. MD strained films, at the highest strains are incapable of forming well aligned extended chain crystals along the strain direction. This effect is likely due to the pathway of morphology evolution in MD strained films. Indeed the tilt angle never attains the theoretical maximum, suggesting that at the highest strains, the cessation of rotation of highly fragmented lamellar blocks prevents the tilt angle maximum of 180 degrees from being attained. Moreover, the distinct differences in strain hardening regime between MD strained films of different thickness points to a molecular model where the process for reorientation of fragmentized lamellar blocks is influenced by film thickness.

CHAPTER VI

MESOSCALE MORPHOLOGY: POLYMER ARCHITECTURE

On the basis of *in situ* deformation studies on films of $LLDPE_2$ it was determined in Section 5.2.1 that the high strain mesoscale morphology in TD strained specimens was characterized by a constant value of d_{ac} that is independent of processing effects. At high strains in the strain hardening regime, the mesoscale morphology therefore depended only on contributions of molecular architecure of the polymer $LLDPE_2$ to the morphology of films. In this chapter, TD strain experiments on blown film series made from the two additional polymers viz $LLDPE_1$ and $LLDPE_3$ are discussed. SAXS data obtained from the additional *in situ* experiments is analyzed using the same methods discussed in Section 4.1. A number of morphological parameters are extracted from the SAXS data and compared between the as made state and high strain state of films. These are tabulated at the end of this chapter. The bivariate distribution of $LLDPE_1$, $LLDPE_2$ and $LLDPE_3$ is compared to observations in the SAXS data in an attempt to construct relationships between molecular architecture and film morphology.

6.1 In Situ *SAXS measurements*

The set of films studied by SAXS measurements simultaneously with strain testing are listed in Table 2. In situ measurements were performed at beamline 5-IDD at the APS using a a dual head Instron as described in Section 3.2.1. The preparation of tensile specimens for use with the Instron is described in Section 3.2.3.

6.2 SAXS: Results and Discussions

The 2D SAXS patterns from as made samples of selected films is shown in Figure 34. The films were held with the TD vertical in the strain direction and hence the lobe intensities from preferentially oriented lamellae are equatorial. Interestingly, the shapes of the lobes showed subtle variations across the polymers, and are discussed below.

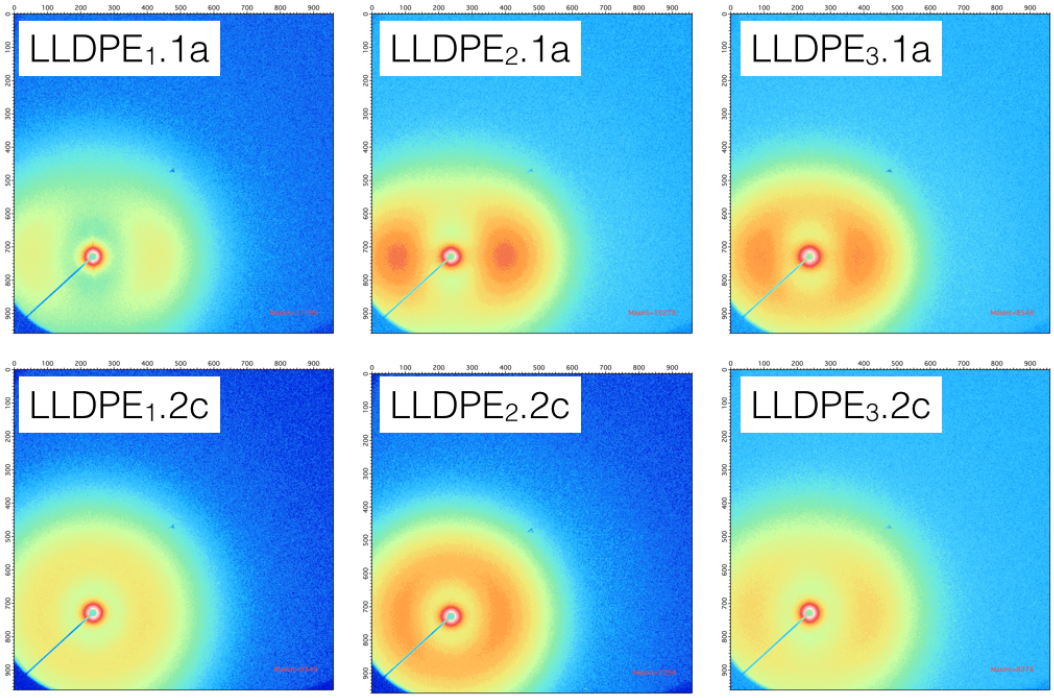

Figure 34: 2D SAXS patterns measured at APS for as made films. Selected films are chosen to highlight visually, the effects of film thickness and BUR on the 2D patterns. The top row represents 20μm films made at a 2.5 BUR. The bottom row represents 75μm films made at a 3.0 BUR. Images are plotted on a color scale between minimum and maximum intensities to emphasize changes in the distributions of the SAXS intensities.

Prior to the analysis of strain resolved data, a detailed investigation into the as made morphology of blown film series from all three polymers was first conducted to identify effects of these subtle variations on the standard SAXS parameters defined in Section 4.1. Table 5 lists the values of d_{ac} and L_{SAXS} obtained by peak fitting, $d_{ac\gamma}$, $d_{c\gamma}$, and $d_{a\gamma}$ obtained via 1D correlation analysis and also values for LAR and F_{lam} (MD). The parameters determined by the 1D correlation analyses are highlighted using the subscript γ. In this chapter, the values of characteristic dimension and its deconvoluted amorphous and crystalline contributions along with lamella width are preferentially discussed in relationship to the molecular architecture of the polymers. The analysis of the remaining parameters is conducted in chapter 9 in the context of the mechanical properties of the films.

The application of TD strain, as described previously in Section 3.2.1 resulted in changes

to the 2D SAXS similar to those observed in section 5.2.1. The general behavior in films of $LLDPE_1$ and $LLDPE_3$ obeyed the same trends observed in films of $LLDPE_2$. These were described previously in detail in Section 5.2.1 and highlighted in Figure 29. The characteristic feature in the 2D SAXS patterns at high strains along TD, i.e. the diffuse intensity accompanied by equatorial streaking, was observed in all of the films. A similar analysis of characteristic dimension d_{ac}, as a function of strain could therefore be conducted.

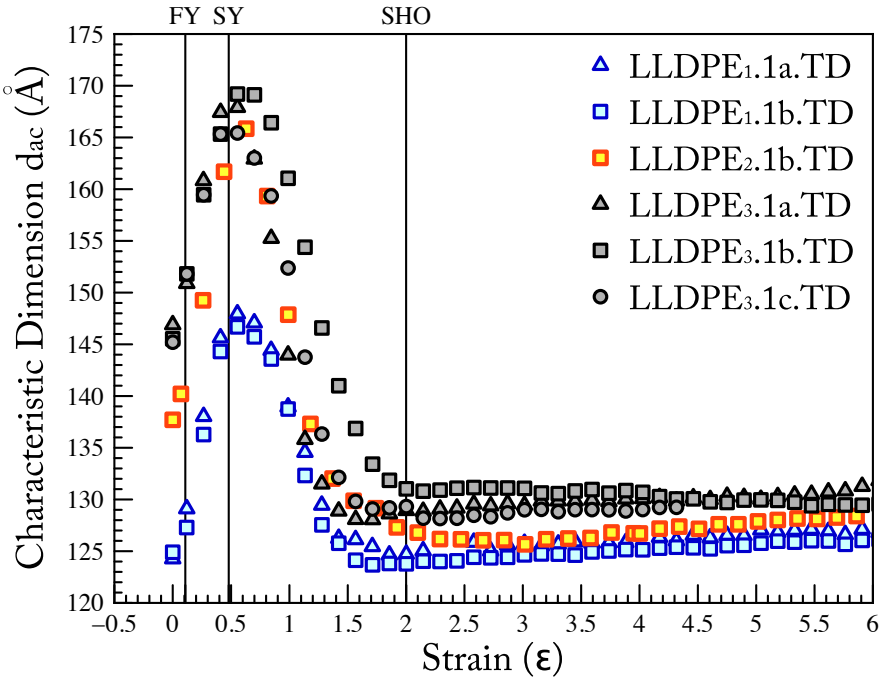

Figure 35: Changes in the d_{ac} of selected films of $LLDPE_1$, $LLDPE_2$ and $LLDPE_3$ films due to TD strain. At $\varepsilon_{0.0}$ i.e. for as made films, the d_{ac} follows the trend of film density. Solid vertical lines correspond to the first yield, second yield and strain hardening onset

Figure 35 displays the d_{ac} variation under applied TD strain in selected films of the three LLDPE polymers with a 2.5 BUR. The d_{ac} in the as made films increases with increasing density of the LLDPEs, i.e. the lowest density polymer $LLDPE_1$ produces films having the lowest value of d_{ac} and the highest density polymer $LLDPE_3$, produces films having substantially higher values of d_{ac}. With increasing strain the same general behavior is observed for the strain driven evolution of the d_{ac} in all three polymers. The value of d_{ac} initially increases and reaches a maximum value at approximately $\varepsilon_{0.5}$ for all films, before subsequently decreasing. In the region of strain between $\varepsilon_{2.5}$ and $\varepsilon_{6.0}$ i.e. when the films

break, the d_{ac} values for all films remain approximately constant as shown in Figure 35. A result of conducting tensile experiments on the Instron is the ability to attain larger values of strain thereby extending the strain range for $LLDPE_2$. For consistency, additional measurements on films of $LLDPE_2$ were undertaken and the values of d_{ac} between $\varepsilon_{3.0}$ and $\varepsilon_{6.0}$ were obtained. For clarity, only one of these data sets is displayed in Figure 35.

The average values of d_{ac} in the high strain region between $\varepsilon_{2.5}$ and $\varepsilon_{6.0}$ are obtained by a linear fit the values of which for the three polymers in order of ascending density are 124.5 $\pm$ 0.83 Å, 127.83 $\pm$ 0.40 Å and 131.33 $\pm$ 1.03 Å , respectively. Interestingly, the high strain d_{ac} values for both $LLDPE_2$ and $LLDPE_3$ films are much lower than their corresponding as made values. $LLDPE_1$ films however exhibit similar values of d_{ac} in the as made sample and at break. The difference between values of d_{ac} at the low and high strains especially in films of $LLDPE_2$ and $LLDPE_3$ points towards morphology in the as made films that is a result of the combination of the polymer architecture and the processing conditions. The fact that d_{ac} remains essentially constant under large tensile strains is indicative of morphology control by the polymer architecture alone.

Dimensionally, average crystalline ($d_{c\gamma}$) and amorphous ($d_{a\gamma}$) length scale contributions to d_{ac} are calculated from analysis using one-dimensional correlation functions and are presented in Table 5 for as made films along with the $d_{ac\gamma}$. The one-dimensional correlation functions for the different films themselves, measured at zero strain and high strain conditions are presented in Figure 36.

The deconvoluted values of $d_{c\gamma}$ might help elucidate the effects of polymer architecture on lamellar thickness. $LLDPE_1$ films exhibit noticeably thinner lamellae than corresponding $LLDPE_2$ or $LLDPE_3$ films. Interestingly, dc_γ values in $LLDPE_2$ and $LLDPE_3$ are nearly the same. This suggests that the lengths of average crystallizable ethylene sequences, i.e. between branch points are smaller in $LLDPE_1$ than those in either $LLDPE_2$ or $LLDPE_3$ thereby affecting the average lamellar thickness when chains in each of the three polymers crystallize. Films from the higher density polymers exhibit very similar lamellar thicknesses suggesting that these polymers probably contain similar distributions of crystallizable ethylene sequences. Corresponding values of the average amorphous spacing i.e. $d_{a\gamma}$ increase

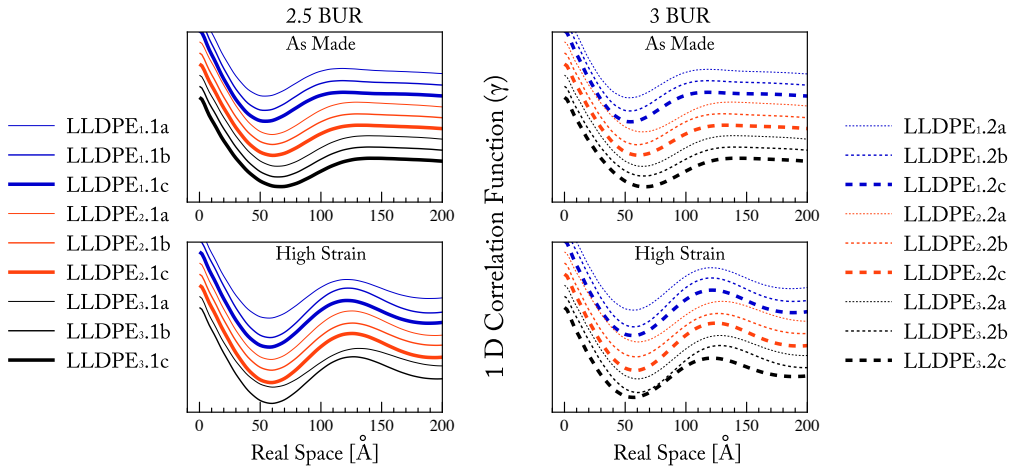

Figure 36: One-dimensional correlation functions for each of the films in their original as made condition as well as the high strain condition. Analysis of these data provides the quantification for $d_{c\gamma}$ and $d_{a\gamma}$ which are listed in Table 5 and Table 6

systematically by nearly 10Å between polymers as the content of SCB is reduced. These observations suggest that the d_a and d_c are both controlled by the extent of SCB incorporation and by association, SCB content controls d_{ac}.

The values of L_{SAXS} for the eighteen films are shown in Table 5. An examination of these values indicates that L_{SAXS} displays dependence on processing conditions as well as dependence on SCB content. The effect of processing conditions specifically BUR suggests that L_{SAXS} at higher BUR values tends to be lower in value than for lower BURs. For instance, $LLDPE_2$ specimens having a 2.5 BUR show L_{SAXS} values of 157Å, 139Åand 123Årespectively for film thicknesses 20, 30 and 75 μm while $LLDPE_2$ specimens having a 3.0 BUR show L_{SAXS} values of 149Å, 125Åand 121Årespectively for film thicknesses 20, 30 and 75 μm. This also suggests that film thickness is inversely related to values of L_{SAXS}. In order to isolate effects of polymer architecture from effects of processing conditions L_{SAXS} values are averaged within each polymer and over processing conditions. The values of L_{SAXS} averaged over thickness and BUR for $LLDPE_1$, $LLDPE_2$ and $LLDPE_3$ are 110.7 $\pm$ 2.45 Å, 136.1 $\pm$ 14.84 Å and 158.2 $\pm$ 14.42 Å respectively. These values suggest that the width of lamellae experiences a systematic increase with reduction in SCB incorporation. A generic construct of morphology for a film blown from any of the three polymers can now be understood based purely on the average dimensions of lamellae and interlamellar domains

obtained from SAXS data. $LLDPE_1$ produces films with thin closely spaced lamellae and $LLDPE_2$ and $LLDPE_3$ produce films with systematically thicker less closely spaced lamellae.

In addition to the dimensional analysis performed on as made films, the values of d_{ac}, L_{SAXS}, $d_{c\gamma}$ and $d_{a\gamma}$ determined in the high strain region are reported in Table 6. This strain range which equates with the plateau and strain hardening regime, is characterized by the near uniformity of values for each of the reported dimensional variables. The values reported were averaged between $\varepsilon_{2.5}$ and ε_6 for all films. The average values of d_{ac}, $d_{c\gamma}$ and $d_{a\gamma}$ for $LLDPE_2$.1b in the Figure 37 are obtained from the strain regime highlighted by the dashed lines. Average values for L_{SAXS} were also determined within this same strain regime. The trends described in Figure 37 are representative of the behavior at high strains for all the films.

Remarkably, over a macroscopic strain regime of nearly 400% the values of d_{ac}, $d_{c\gamma}$ and $d_{a\gamma}$ are constant. These values even across the three polymers are very similar which is in contrast to the corresponding as made state values. A comparison of $LLDPE_1$ with $LLDPE_2$ and $LLDPE_3$ at the entire strain range extremes is therefore indicative of two significant features. First, the as made morphology of $LLDPE_1$ is significantly different from $LLDPE_2$ and $LLDPE_3$. Second, the high strain morphology of the three films is very similar. Since the only underlying factor that is common to the as made and high strain morphologies is the architecture of each polymer, a hypothesis is proposed wherein the architecture of the polymer is an intrinsic factor which in combination with extrinsic factors dictates the film morphology. For the as made films, the extrinsic factor is the range of processing conditions while for highly (TD) strained films, strain is the extrinsic factor. An important inference which is relevant to the discussion can be made at this stage by observing the 2D SAXS patterns for as made and high strain conditions. In the as made films, even under the same processing conditions the patterns are visually different for the three polymers. In the strained films, however these visual differences are significantly subdued. Specifically in the as made state, even though the three polymers are subjected to the same film processing conditions the morphology is different suggesting that architectural differences i.e. intrinsic differences between the three polymers account for the observed

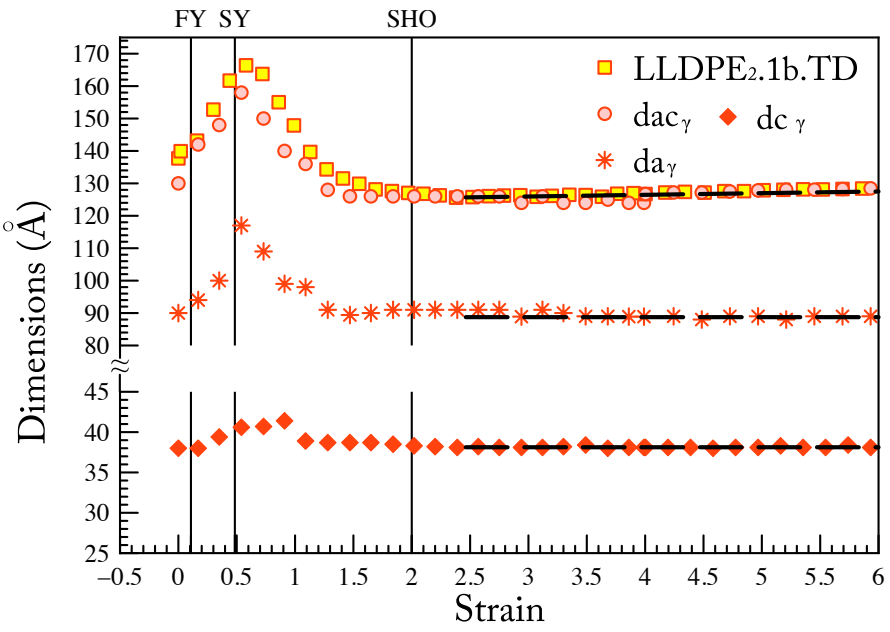

Figure 37: d_{ac}, $d_{c\gamma}$ and & $d_{a\gamma}$ are averaged between $\varepsilon_{2.5}$ and ε_6 for film LLDPE$_2$.1b. Dashed lines serve as a guide to the eye illustrating the general tendency of the parameters to plateau. Solid lines indicate the first yield, second yield and onset of strain hardening. Averaged values for the 18 films are calculated and reported in Table 6

morphology differences between the films. Under TD strain the morphology is visually very similar, suggesting that architectural similarities between the three LLDPEs could account for the high strain morphology. Clearly, the similarities and differences between the architectures of the three LLDPE polymers are of importance to the morphologies of films and their evolution. It is anticipated that the common and uncommon features between the three LLDPE architectures will be captured via a characterization of their bivariate distribution.

6.3 Connecting the Morphology of Films to Polymer Architecture

6.3.1 Bivariate Distribution

The bivariate distributions of the three polymers were obtained by cross fractionation (CFC) enabled by an instrument that fractionates an LLDPE according to crystallinity and subsequently measures the molecular weight distribution of each fraction. Fractionation based

on crystallinity is achieved by a Temperature Rising Elution Fractionation (TREF) process. As a fraction elutes, it is injected into an adjacent GPC column where its molecular weight distribution can be determined. The bivariate distribution was characterized by a CFC apparatus at EMCC and the data were subsequently supplied. The molecular weight distributions for the three unfractionated polymers are measured by GPC and is displayed in Figure 38[1]. The three GPC curves indicate that the molecular weight distribution of the polymers is very similar. The TREF results for the three polymers is shown in Figure 39. The TREF data for the three polymers are bimodal indicating that the MWD consists of at least two populations of chains that elute in different temperature ranges. A fit of the TREF data with two Gaussian distributions suggests that a population of chains, i.e. population A, elutes from the polymer between 90 - 110°C while another population i.e. population B, elutes in a temperature range from 0 - 90°C. It is interesting to note that the concentration of A and B are unique for each polymer.

In a TREF experiment, the temperature of a fixed weight of the LLDPE polymer is raised slowly from a low temperature in a stepwise manner. At each temperature step, the mobility of polymer chains will change depending on their branch content i.e. crystallinity. With consecutive incremental temperature steps, populations of chains with progressively lower branching can be mobilized and subsequently eluted in a solvent. Population B elutes at lower temperatures when compared to A as the average SCB content in the chains of B is expected to be larger than that for A. Comparing the three polymers, the TREF data show that the concentration of chains with a high SCB content is greatest in $LLDPE_1$ and lowest in $LLDPE_3$. Conversely, the concentration of chains with low SCB content increases from $LLDPE_1$ to the highest value in $LLDPE_3$. This behavior agrees with the densities of the three polymers since decreasing the SCB content causes an increase in the polymer density.

For each polymer, fractions were obtained by TREF and subsequently the M_w and MWDs of each fraction were determined by GPC.Next, the SCB content for each fraction was measured by NMR studies[1]. The bivariate distribution of SCB in the MWD of each

[1]Data supplied by EMCC

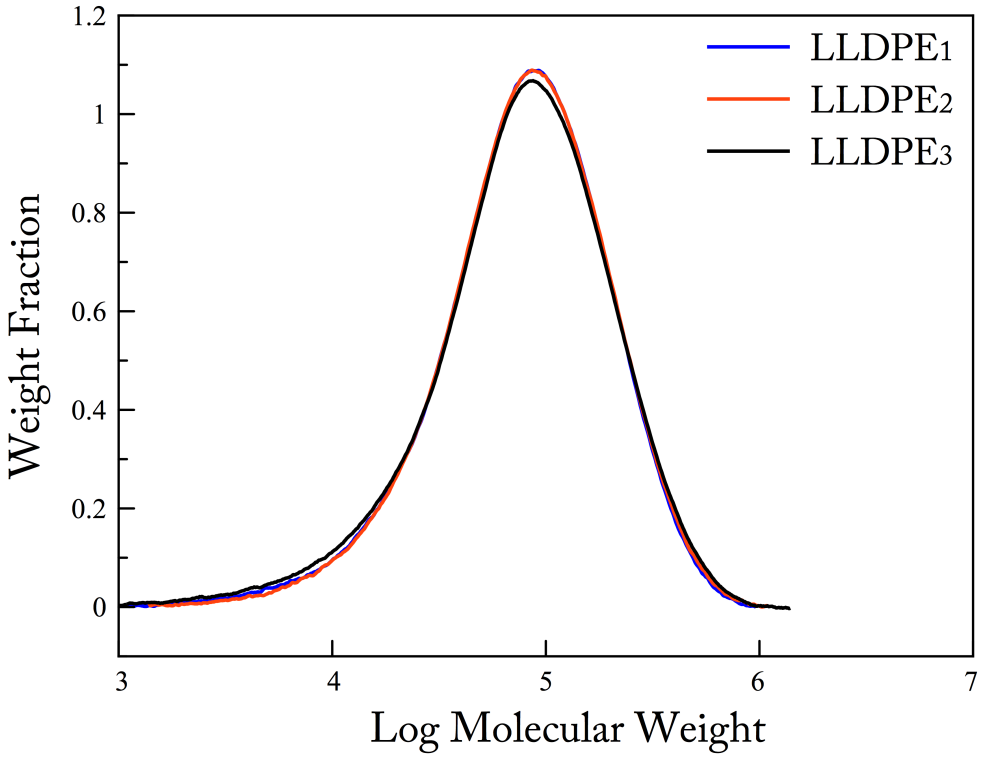

Figure 38: GPC data for the three polymers

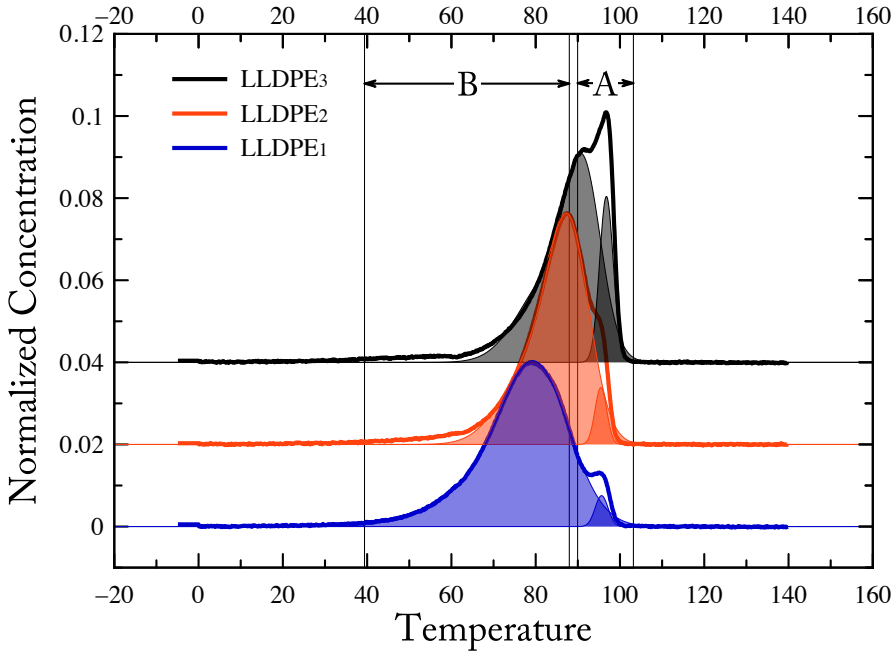

Figure 39: TREF data for the three polymers

polymer could thus be extracted and is shown in Figure 40 in the form of a contour plot displaying the distribution of SCB as a function of the MWD.

Considering the bivariate distribution for $LLDPE_3$ is first, is shows that $LLDPE_3$ has between 0 and 6% comonomer incorporated into the polymer chains yielding an average comonomer incorporation of 1.75% at a mean molecular weight of 113,500 g/mole. The bivariate distribution for $LLDPE_2$ has between 0 and 7% comonomer incorporated into the polymer yielding an average comonomer incorporation of 2.45% at a mean molecular weight of 117,500 g/mole. Lastly, $LLDPE_1$ has between 0 and 9% comonomer incorporated into the polymer yielding an average comonomer incorporation of 3.50% at a mean molecular weight of 113,700 g/mole. While the shape of the bivariate distribution of the three polymers is similar, the most striking feature observed from the contour plots is the increased incorporation of comonomer content in $LLDPE_3$ compared to $LLDPE_1$. It is also clear that the bivariate distribution in $LLDPE_3$ and $LLDPE_2$ exhibits a bimodal nature. This bimodality has been ascribed to the two populations A and B.

Additional information about the nature of the distribution of SCB is obtained by plotting the temperature dependency obtained from TREF data and shown in the inset to Figures 40a, b and c. In each of the insets, dark colored regions correspond to the temperature regime in which population A elutes while the light colored regions correspond to the regime in which population B is eluted. For $LLDPE_3$ and $LLDPE_2$, the temperature dependence equates to populations A and B. However for $LLDPE_1$ this is not the case because the two populations are not isolated.

In the case of $LLDPE_3$, the inset of Figure 40a suggests that the population B consists of branched chains whose molecular weights are between 10,000 and 1,000,000 g/mole and possess between 2 and 6% comonomer incorporation. Population A consists of lightly branched chains incorporating less than 2% comonomer into chains whose molecular weights lie between 10,000 and 1,000,000 g/mole.

The distribution in $LLDPE_2$ is similar to $LLDPE_3$ wherein population B consists of branched chains whose molecular weights are between 10,000 and 1,000,000 g/mole and possess between 2 and 7% comonomer incorporation. Population A consists of lightly

branched chains incorporating less than 2% comonomer into chains whose molecular weights lie between 10,000 and 1,000,000 g/mole. The concentration of chains of population A is higher in $LLDPE_3$ than in $LLDPE_2$.

$LLDPE_1$ consists of a bivariate distribution where the chains have a molecular weights between 10,000 and 1,000,000 g/mole and between 1 and 9% comonomer incorporation. While the behavior in bivariate distribution for $LLDPE_1$ is similar to the other two polymers, population A and population B are not isolated groups with respect to comonomer incorporation. The inset in Figure 40c suggests that population A and population B in $LLDPE_1$ are well distributed throughout the polymer unlike in $LLDPE_2$ and $LLDPE_3$. In addition to A and B having the same distribution of molecular weights between 10,000 and 1,000,000 g/mole in molecular weight, both incorporate similar percentages of SCB.

6.3.2 Morphology in As Made Films

The behavior seen in Figure 35 can now be explained in the context of the bivariate distribution. The work of Kornfield et al [52, 105] and Hsiao et al [49, 53, 55] suggest that chains of the highest molecular weight with the least number of branches are the most elongated prior to crystallization from an oriented melt. At the onset of crystallization, these oriented chains promote crystal growth from the melt by aggrandizing shorter but highly branched chains from their immediate vicinity to form crystal lamellae. These lamellae are likely to originate from near the location of branches on the nucleating chain and grow radially outwards from the elongated length of the long chains. As crystallization proceeds, shorter chains capable of crystallization are incorporated to the evolving crystals. The instantaneous state of morphology produced by the longest chains at the crystallization onset thus serves as a template which facilitates subsequent crystallization processes and thereby enables the development of the semicrystalline film morphology. An implication of this hypothesis, is that the morphology produced in films at the very end of the film blowing process i.e. the as made film morphology is directly dependent on the morphology at the instant of crystallization onset. Naturally, the concentration of the long linear unbranched chains that elongate prior to crystallization, their average elongated length and

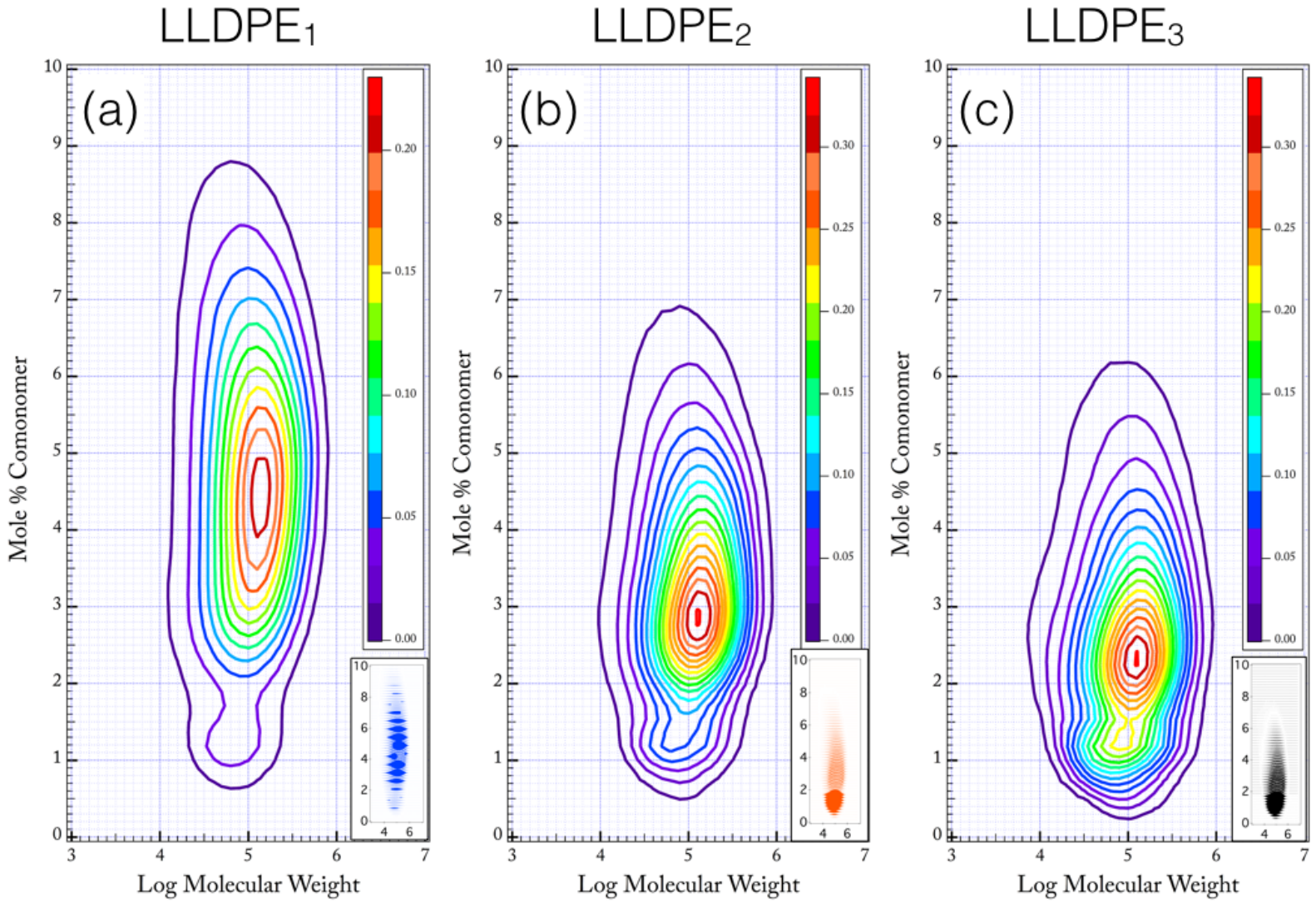

Figure 40: Bivariate distribution for the three polymers shown in contour form where each contour represents a normalized concentration of LLDPE chains of particular molecular weight and comonomer content. The inset plots highlight the distribution of the two populations A and B within the bivariate distribution.The axes on these inset figures are the same as those for the contour plots.

their branching characteristics would affect the instantaneous morphology attained at the onset of crystallization and therefore the morphology in the as made films.

Based on the TREF data, it is reasonable to associate population A of the three polymers with those chains that initiate crystallization process i.e.nucleation and population B with the fraction of chains that are recruited by A during crystal growth. This delineation explains why the as made films of polymer $LLDPE_3$ exhibit on average the highest d_a values. During the initial stages of nucleation, population A for each of the three polymers serves as a template. In comparison with $LLDPE_2$ and $LLDPE_1$, $LLDPE_3$ possesses a larger fraction of poorly branched chains in population A, which is evident from the contour plot in Figure 40c. The higher concentration of these types of chains combined with a smaller distribution in comonomer content in population B suggests that $LLDPE_3$ eventually forms films where the d_a is controlled by the branching of polymer chains in population A. Lowering the number of branches in the long chains is likely to increase the value of d_a and therefore d_{ac}. This is particularly true for the case of $LLDPE_2$ and $LLDPE_3$.

Trends between $LLDPE_3$ and $LLDPE_1$ can be similarly explained. Population A in $LLDPE_1$ consists of similar lengths of chains as population A of $LLDPE_3$, but with a much larger incorporation of comonomer content. Prior to the onset of crystallization, population A in $LLDPE_3$ is capable of forming longer elongated sequences of backbone ethylene units. In contrast, $LLDPE_1$ at the onset of crystallization will possess shorter sections of elongated ethylene sequences that are capable of nucleating lamellae. In addition, population B in $LLDPE_1$ has broad comonomer incorporation that forces the formation of thinner crystal lamellae. The average values of d_a for $LLDPE_1$ are the smallest which also suggests that this polymer produces films with a greater population of thinner lamellae, which is observed in the SAXS data as a lower average value of d_{ac} in as made films of $LLDPE_1$.

6.3.3 Morphology in highly strained films

In the high strain regime the spread in d_{ac} values across films of the three polymers are much smaller than in the as made films. The application of strain particularly along TD as discussed in Section 5.2.1, shows that effects associated with processing and therefore

oriented crystallization of the chains are destroyed at the high strains. This is because lamellae at high strains typically greater than $\varepsilon_{2.0}$ are new lamellae that were originally not present in the original as made morphology. As previously discussed, the morphology at high strain is primarily associated with the structure of the polymer itself and independent of the processing. Clearly at high strains, the framework provided initially by chains from population A is destroyed and a new persisting structure is formed. The lack of significant variation in the d_{ac} values for the three polymers strongly suggest that a similar population of chains in all three polymers is responsible for the behavior observed at high strains. It is likely that the chains in question form part of population B. The common feature across the three polymers is that population B comprises of more than half the chains in the entire polymer. It is therefore plausible that structural features at high strains are dominated by these smaller more heavily branched chains. At high strains, chains from population A possess no significant influence over the morphology unlike in the case of the as made films, since deformation events particularly at high strains affect crystal lamellae of all sizes equally. It is therefore conceivable that the high strain structures are directly related to the characteristics of chains in population B. The similarities in population B across the three polymers might account for the nearly uniform values of d_{ac} at high strains in the three polymers. The increased comonomer content in population B from $LLDPE_3$ to $LLDPE_2$ and $LLDPE_1$ are likely to be responsible for larger values of high strain d_{ac} in $LLDPE_3$ than in $LLDPE_2$ and $LLDPE_1$.

6.3.3.1 Theoretical Considerations

Based on the analyzed NMR data provided by EMCC on the three polymers, the average branch distribution is known as a function of the number of butyl branches present for every thousand backbone carbon atoms. If the assumption that branches larger than methyl groups are omitted from the lamella holds true [26, 33, 35, 106, 107] then theoretically, the average dimension of a crystal - of which the entire crystallizable length between branch locations is a part - is dictated by the average number of carbon atoms between consecutive branch points, i.e. C_{ij}, where C_i and C_j are branch subtending carbon atoms of the

backbone chain and i and j are consecutive branches. Since C_{ij} is known, the theoretical lamellar thickness for the ideal case of a chain extended crystal where the entire crystallizable length of a polymer chain between branch points crystallizes can be calculated as the *fully extended length of chain between branch points* i.e. R where $R = NLcos\frac{\theta}{2}$. Here, N represents the number of C-C bonds between branch points i.e. $C_{ij} - 1$, L is the C-C bond length i.e. 1.54 Å and θ is the C-C bond angle in polyethylene i.e. 68°. Moreover, it is understood from both theoretical [108–113] and experimental studies [114–116] that the packing of crystalline unit cells within a lamella is characterized by a 35° tilt of the c axis with respect to the lamellar normal. Therefore, the theoretically obtained value R is corrected by a value of $sin\,35°$ giving a corrected theoretical crystal thickness $\bar{R} = R \cdot sin\,35°$. Figure 41 shows the relationship between R, $\bar{R}$ and the electron density distribution $\rho(r)$. Table 4 lists the theoretically obtained values for $\bar{R}$ for the three polymers. These values are compared to the average $d_{c\gamma}$ values obtained across the films.

Table 4: Theoretically obtained lamellar thickness dimensions based on EMCC supplied NMR data on average Butyl Branching

Polymer	B4/1000 BBC	C_{ij} (NMR)	R (Å)	$\bar{R}$ (Å)	$d_{c\gamma}$ (Å)
$LLDPE_1$	20	50	64	37	33
$LLDPE_2$	14	71	91	52	40
$LLDPE_3$	10	100	128	73	40

The values of $\bar{R}$ are higher than corresponding $d_{c\gamma}$ for all three polymers. A stepwise increase in C_{ij} does not seem to affect the average lamellar thickness determined from the scattering. This suggests that the average thickness of lamellae in the blown films are not dictated by the NMR derived average spacing values between branches, but are clearly more sensitive to shorter crystallizable ethylene sequences in all three polymers. This phenomenon is qualitatively illustrated in Figure 42. The corresponding morphology in films can be visualized as a distribution of different lamellar thicknesses. Indeed this is captured in the SAXS data as the width of the distribution of the scattering maxima. The fraction of lamellae formed from short crystallizable sequences might outnumber the fraction of lamellae formed from longer crystallizable sequences thus causing the weighted average

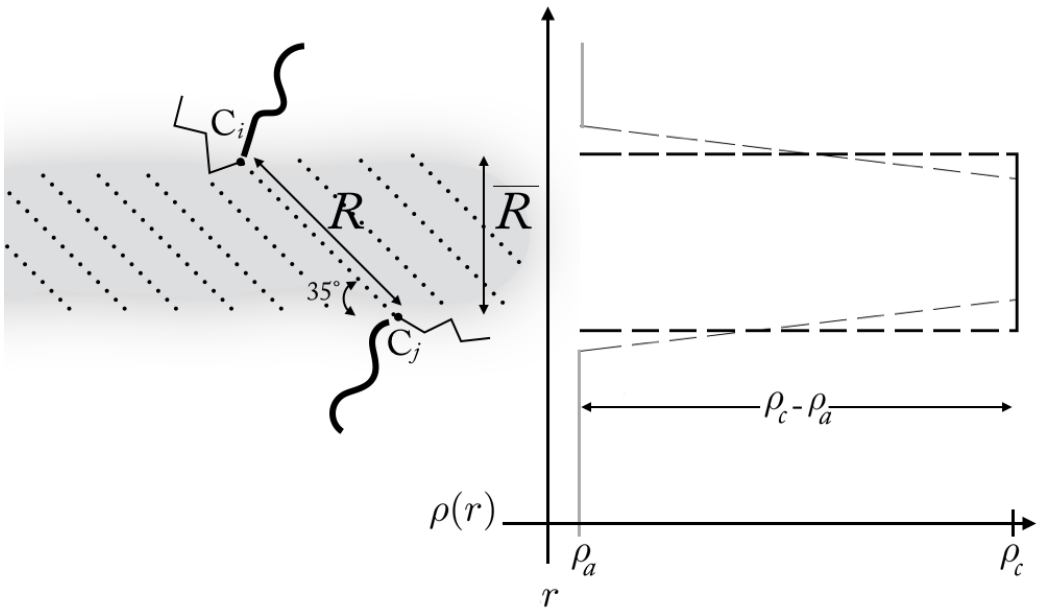

Figure 41: The electron density distribution $\rho(r)$ and its variation along r for a lamella present in an amorphous matrix is shown. The electron density for the crystalline region is represented by ρ_c and for the amorphous region by ρ_a. The contrast for scattering is provided by the difference of electron density i.e. ρ_c-ρ_a. The lamellar region is highlighted by the darker grey area with ordered chains. The amorphous regions are white and the separation between the lamella and amorphous region i.e. interphase is shown as a diffuse grey region. The relationship between C_{ij}, R and $\bar{R}$ are visually demonstrated

lamellar thickness d_c to be lower than the theoretical values obtained from considering an average value of branch spacing. This hypothesis explains why the lamellar thickness does not increase by a 100% between LLDPE_1 and LLDPE_3 even though the corresponding value of $\bar{R}$ rises from 37Å to 73Å , nearly double the value. Correspondingly the systematic 10Å increase in the values of d_a $\text{LLDPE}_1 \langle \text{LLDPE}_2 \langle \text{LLDPE}_3$ suggests that the longer crystallizable sequences i.e. chains where C_{ij} is greater than the reported NMR based average may impact the size of amorphous domains. The maximum value of d_{ac} attained under strain which systematically changes with $\text{LLDPE}_1 \langle \text{LLDPE}_2 \langle \text{LLDPE}_3$ also supports the theory that the amorphous domain sizes are dominated by those chains where the C_{ij} is greater than the reported NMR based average i.e. to the right of the blue, orange and black solid vertical lines respectively for the three polymers in the Figure 42.

sq

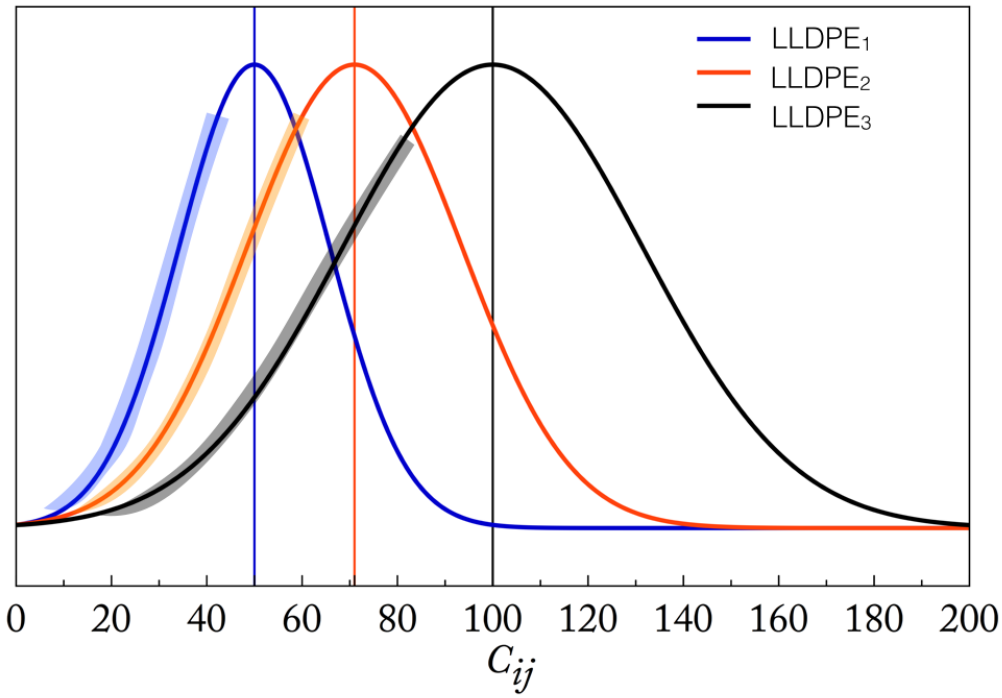

Figure 42: The three distributions represent the distributions of crystallizable sequences of ethylene in the backbone of the three polymers. Solid vertical lines represent the NMR derived average number of backbone carbons between consecutive branch points i.e. C_{ij}. Shorter sequences are highlighted by shaded regions. The shaded portions of the three distributions are likely to feature heavily in the lamellae thus dominating $d_{c\gamma}$ determined from the SAXS. Longer sequences represented by the unshaded portion of the distributions to the right of the three solid lines respectively are likely to feature in the amorphous domains separating lamellae thus dominating $d_{a\gamma}$ determined from the SAXS. Distributions here are modeled as Gaussians but this may not be truly representative of the behavior

Table 5: Variables descriptive of the as made mesoscale morphology across all three polymers and their film series

Film	Density (g/cc)	BUR	Thickness (μm)	d_{ac} (Å)	$d_{ac\gamma}$ (Å)	$d_{c\gamma}$ (Å)	$d_{a\gamma}$ (Å)	L_{SAXS} (Å)	LAR	F_{lam} (MD)
LLDPE1.1a	0.912	2.5	20.0	124	118	35	83	112	1.56	0.073
LLDPE1.1b	0.912	2.5	30.0	124	118	35	83	114	1.60	0.068
LLDPE1.1c	0.912	2.5	75.0	126	118	35	82	109	1.22	0.030
LLDPE1.2a	0.912	3.0	20.0	124	118	30	87	108	1.55	0.062
LLDPE1.2b	0.912	3.0	30.0	125	118	36	82	111	1.37	0.046
LLDPE1.2c	0.912	3.0	75.0	126	118	36	82	108	1.11	0.018
LLDPE2.1a	0.918	2.5	20.0	135	128	40	87	157	3.70	0.18
LLDPE2.1b	0.918	2.5	30.0	137	130	39	90	139	2.16	0.100
LLDPE2.1c	0.918	2.5	75.0	139	130	39	90	123	1.37	0.039
LLDPE2.2a	0.918	3.0	20.0	143	138	40	97	149	2.58	0.127
LLDPE2.2b	0.918	3.0	30.0	136	130	39	90	125	1.89	0.084
LLDPE2.2c	0.918	3.0	75.0	139	130	39	91	121	1.23	0.024
LLDPE3.1a	0.923	2.5	20.0	145	140	40	99	181	3.36	0.177
LLDPE3.1b	0.923	2.5	30.0	145	140	41	98	162	2.20	0.113
LLDPE3.1c	0.923	2.5	75.0	146	140	39	100.	146	1.25	0.032
LLDPE3.2a	0.923	3.0	20.0	144	140	41	99	166	2.58	0.137
LLDPE3.2b	0.923	3.0	30.0	147	140	39	100	148	1.78	0.081
LLDPE3.2c	0.923	3.0	75.0	149	140	39	100	144	1.17	0.024

Table 6: Variables descriptive of the high strain mesoscale morphology across all three polymers and their film series

Film	Density (g/cc)	BUR	Thickness (μm)	d_{ac} (Å)	$d_{ac\gamma}$ (Å)	$d_{c\gamma}$ (Å)	$d_{a\gamma}$ (Å)	L_{SAXS} (Å)
LLDPE1.1a	0.912	2.5	20.0	124	122	36	86	56
LLDPE1.1b	0.912	2.5	30.0	125	122	37	85	66
LLDPE1.1c	0.912	2.5	75.0	125	122	38	84	68
LLDPE1.2a	0.912	3.0	20.0	123	120	37	83	51
LLDPE1.2b	0.912	3.0	30.0	125	120	36	83	67
LLDPE1.2c	0.912	3.0	75.0	125	122	36	85	69
LLDPE2.1a	0.918	2.5	20.0	128	126	38	88	64
LLDPE2.1b	0.918	2.5	30.0	128	126	38	88	60
LLDPE2.1c	0.918	2.5	75.0	128	126	37	90	67
LLDPE2.2a	0.918	3.0	20.0	127	130	40	90	56
LLDPE2.2b	0.918	3.0	30.0	128	126	37	89	56
LLDPE2.2c	0.918	3.0	75.0	128	126	39	88	72
LLDPE3.1a	0.923	2.5	20.0	133	132	39	93	63
LLDPE3.1b	0.923	2.5	30.0	131	126	39	89	72
LLDPE3.1c	0.923	2.5	75.0	132	129	39	100	63
LLDPE3.2a	0.923	3.0	20.0	131	128	41	88	63
LLDPE3.2b	0.923	3.0	30.0	131	128	38	89	61
LLDPE3.2c	0.923	3.0	75.0	130	122	36	86	75

CHAPTER VII

ATOMIC SCALE DEFORMATION

WAXS captures a range of morphological features at the crystallographic scale. Commonly extracted parameters from WAXS of semicrystalline systems includes the size and type of the unit cell, its orientation with respect to the processing direction as well as an estimate of crystallinity. In the case of LLDPE blown films, studies by various groups [3, 4, 10, 11, 14, 17, 19] have suggested the prevalence of crystalline unit cells that obey to a certain extent Keller's model of low stress crystallization described in Section 2.2.2.2. Tensile deformation studies on LLDPEs by Butler and Donald [1, 70, 89, 90], both in isotropic heat compressed specimens and anisotropic blown film specimens found that an orthorhombic to monoclinic transformation occurred prior to plastic deformation. In this section, we examine first, the as made crystalline morphology of films of the three resins and subsequently its evolution under tensile strain.

7.1 As Made films

7.1.1 Crystallinity

The degree of crystallinity (Xc) is extracted from the WAXS data as described in Section 4.2.1 and reported in Table 7. Xc varies between approximately 30-50% across all of the as made films. The 75μm thick films for all the LLDPEs exhibit the highest levels of crystallinity. Films of $LLDPE_1$ display on average lower crystallinity values than either $LLDPE_2$ or $LLDPE_3$ which is consistent with the density of the polymers while a comparison of the degree of crystallinity between $LLDPE_2$ and $LLDPE_3$ shows very similar values suggesting that the effect of density on Xc is diminished for these two polymers. The trends in L_{SAXS} and d_c values reported in Table 5 suggests that the crystallinity in $LLDPE_3$ stems from a larger population of thicker and wider crystal lamellae. It is interesting to note that although $LLDPE_1$ films possess lower average values of L_{SAXS}, d_c and d_{ac} certain films show nearly the same crystallinity as films of $LLDPE_2$ and $LLDPE_3$. This suggests that

the crystallinity in $LLDPE_1$ is affected by the presence of large populations of thin and narrow width crystal lamellae.

Table 7: Variables descriptive of the as made crystallographic morphology across all three resins and their film series

Film	Density (g/cc)	BUR	Thickness (μm)	Xc (%)	F_a (MD)	F_b (MD)	F_c (MD)	F_a (TD)	F_b (TD)	F_c (TD)
$LLDPE_1$.1a	0.912	2.5	20	38.48	0.033	-0.055	0.022	-0.037	0.087	-0.050
$LLDPE_1$.1b	0.912	2.5	30	39.17	0.038	-0.045	0.007	-0.032	0.062	-0.030
$LLDPE_1$.1c	0.912	2.5	75	45.22	0.012	-0.018	0.006	-0.002	0.033	-0.0311
$LLDPE_1$.2a	0.912	3.0	20	33.31	0.023	-0.030	0.007	-0.037	0.086	-0.049
$LLDPE_1$.2b	0.912	3.0	30	40.34	0.023	-0.031	0.008	-0.032	0.061	-0.029
$LLDPE_1$.2c	0.912	3.0	75	40.43	0.010	-0.015	0.005	-0.001	0.025	-0.0240
$LLDPE_2$.1a	0.918	2.5	20	42.03	0.163	-0.185	0.022	-0.120	0.312	-0.192
$LLDPE_2$.1b	0.918	2.5	30	40.92	0.101	-0.124	0.023	-0.078	0.193	-0.115
$LLDPE_2$.1c	0.918	2.5	75	47.82	0.035	-0.058	0.023	-0.022	0.048	-0.026
$LLDPE_2$.2a	0.918	3.0	20	38.24	0.083	-0.167	0.083	-0.103	0.2729	-0.170
$LLDPE_2$.2b	0.918	3.0	30	39.73	0.073	-0.099	0.027	-0.065	0.148	-0.083
$LLDPE_2$.2c	0.918	3.0	75	46.29	0.016	-0.025	0.009	-0.018	0.035	-0.017
$LLDPE_3$.1a	0.923	2.5	20	39.62	0.143	-0.213	0.070	-0.076	0.187	-0.111
$LLDPE_3$.1b	0.923	2.5	30	42.75	0.092	-0.148	0.055	-0.070	0.170	-0.100
$LLDPE_3$.1c	0.923	2.5	75	47.30	0.017	-0.042	0.025	-0.062	0.152	-0.090
$LLDPE_3$.2a	0.923	3.0	20	38.26	0.076	-0.178	0.101	-0.061	0.150	-0.089
$LLDPE_3$.2b	0.923	3.0	30	37.93	0.063	-0.109	0.045	-0.057	0.141	-0.084
$LLDPE_3$.2c	0.923	3.0	75	47.33	0.010	-0.032	0.022	-0.025	0.051	-0.026

7.1.2 Crystal Orientation

Herman's orientation parameters of the a, b and c axes given by F_a, F_b and F_c were determined with respect to the MD and the TD as described in Section 4.2.2. The values F_a, F_b and F_c in the as made films are reported in Table 7. An examination of the parameters relative to MD indicates that F_a is always positive. This suggests that all the films have their a axis on average aligned along MD. A negative value of F_b with respect to MD suggests that the b axis is orthogonal to the MD i.e. parallel to TD. With respect to MD, F_c possesses a near zero value in most cases suggesting isotropy in the c axis orientation.

Films with an ideal MD orientation i.e. where the a axis of the PE unit cell is perfectly aligned parallel to the MD axis are characterized by a value of F_a value of unity. The investigation of F_a, F_b and F_c with respect to the TD, confirmed that MD and TD were indeed orthogonal axes of orientation. The b axis appears to be preferentially aligned

along TD as suggested by the positive values of F_b for the individual polymers. The a axis orientation was negative for all films with respect to TD suggesting once again that the a axis was aligned along MD. Figure 43 is a graphical representation of the F_i values observed for the individual polymers under MD and TD configuration respectively. The general behavior of the films is immediately obvious from Figure 43, which suggests that the orientation exhibited by the films in this work are in agreement with the low stress model of Keller and Machin (see Section 2.2.2.2) where the a and b axis tend to orient preferentially along the MD and the TD respectively.

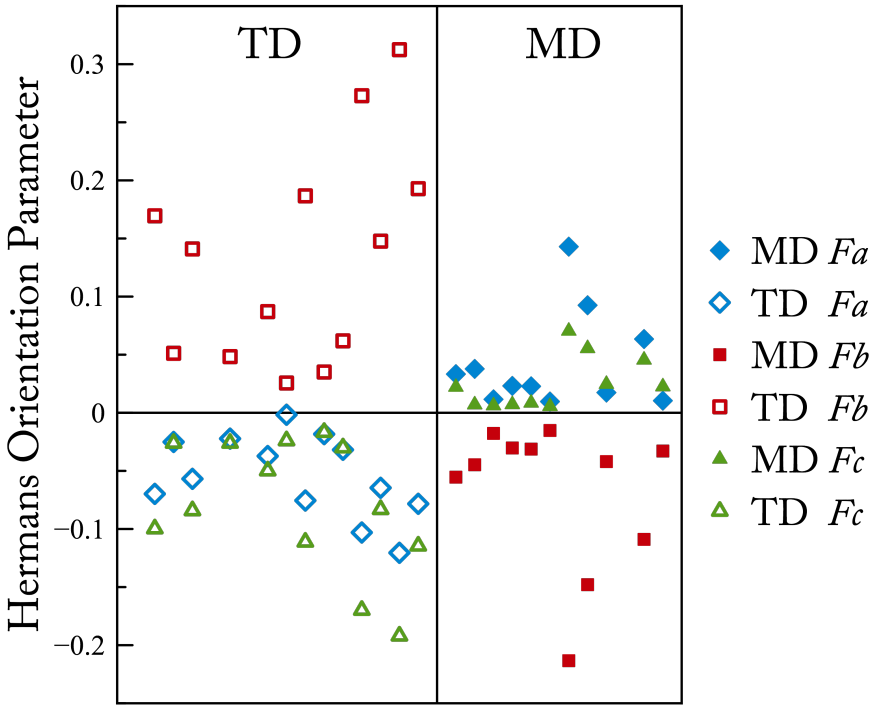

Figure 43: Scatter plot of the Herman's orientation factors F_a, F_b and F_c measured for all films. Solid symbols represent film specimens that were held with the MD in the vertical direction while open symbols represent film specimens with the TD in the vertical direction. The films all show the b axis orienting along TD and the a axis orienting along MD

Taking the data in the TD Section of Figure 43 and replotting in Figure 44 it highlights the influence of film thickness and BUR on the initial blown film orientation (see Figure 44). In general the following trends are observed. The thinnest films exhibit greatest degree of orientation and the alignment of the unit cell axes becomes less ordered as the film thickness

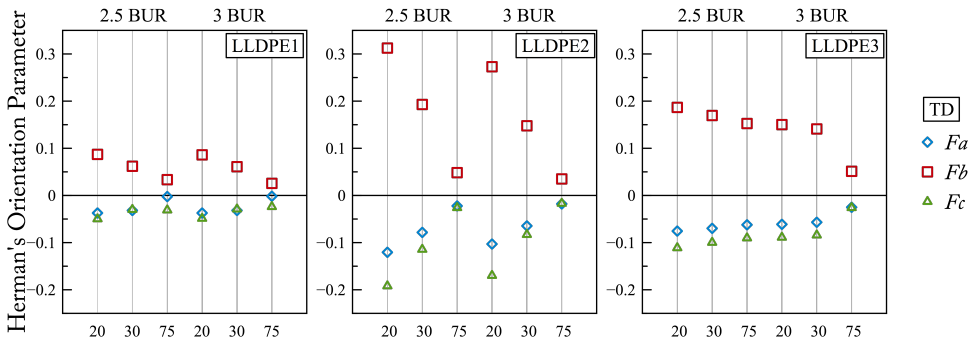

Figure 44: F_a, F_b and F_c measured with the TD as the reference axis for films of the three resins. The X axis indicates film thickness in mils where 0.75 mil = 20μm, 1.2 mil = 30μm and 3 mil = 75μm

increases. Films made with a 2.5 BUR show slightly better orientation that films made with the 3 BUR. An idealized model of the alignment of polyethylene chains in the orthorhombic crystal cell within a lamella in melt blown films with respect to the MD and TD is shown in Figure 45. In this idealized model, the c, a and b axis are perfectly oriented relative to the ND, MD and TD film processing directions respectively and the lamella normal is the MD. The corresponding F_c values relative to MD and TD are therefore expected to be -0.5 since the c axis is orthogonal to MD and TD in the idealized case. In reality however the unit cell is expected to slant relative to the lamellar normals i.e. the unit cell is tilted relative to MD [108]. Rutledge et al [108] show via molecular simulations that a stable c axis tilt of 35° to the lamellar normal is to be expected. A range of tilting values between 19 to 45° have been experimentally observed and reported by other authors in polyethylene and similarly structured polymers using single crystal diffraction or electron microscopy studies on solution crystallized specimens [116, 116–119].

The tilting phenomenon can be directly evidenced based on the appearance and behavior of the (001) reflection of the c axis particularly in single crystals. In melt crystallized specimens, such as the films in this work however, this reflection was not observed in the 2D WAXS data. Therefore, an indirect approach of determining c axis tilt is discussed. Firstly, the values of F_c relative to TD (see Table 7) lie between 0 and -0.2 which equates to an angular spread of ∼55° to ∼65° between the TD and the c axis. Secondly, due to

the MD-TD orthogonality, the the c axis on average subtends an angular spread of $\sim 25^\circ$ to $\sim 35^\circ$ relative to MD. Since the MD also coincides with the direction of the lamellar normal, our results indicate that the c axis does indeed experience a tilting in the range of $\sim 25^\circ$ to $\sim 35^\circ$ relative to the lamellar normal which is consistent with the reported values of the c axis tilting discussed in the literature.

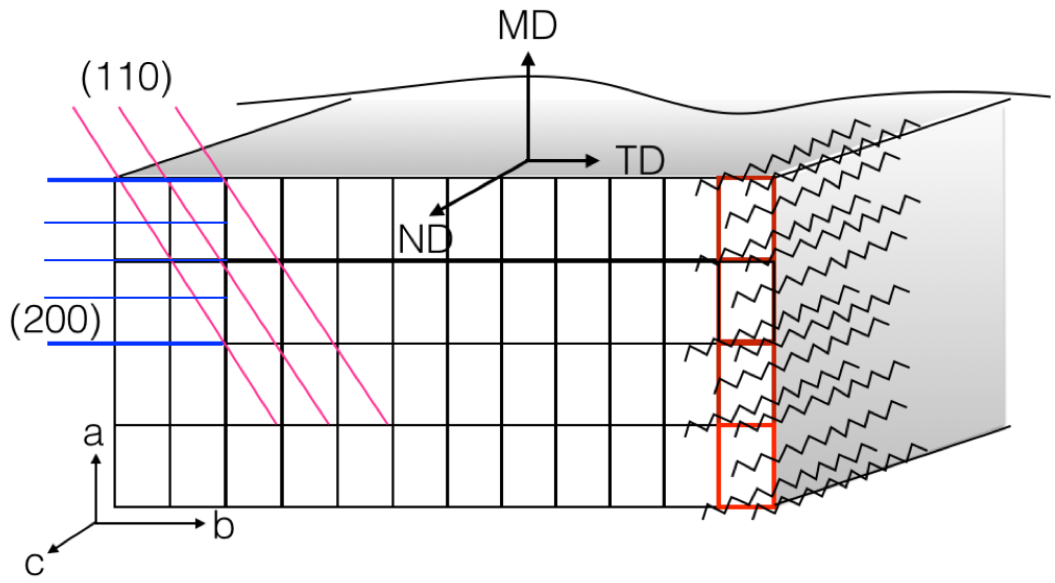

Figure 45: Schematic for the arrangement of PE chains in an orthorhombic crystal within a lamella for a melt blown film. The orientations of the a, b and c axes with respect to the MD and TD of films are exaggerated to show ideal alignment behavior

7.2 Tensile Deformation of Films

7.2.1 Crystallinity

The crystallinity variation as a function of strain is captured by the fitting routine described in Section 4.2.1. While the onset of an orthorhombic to monoclinic transformation is observed in all specimens beyond the first yield point by the appearance of a faint (010) monoclinic peak, the fraction of monoclinic content can be accurately determined closer to the second yield point when the (010) monoclinic peak is clearly visible. Indeed, the

monoclinic content attains a maximum beyond the second yield point. In general, the total crystallinity is shown to decrease by ∼10% during the tensile deformation particularly at low to intermediate strains. The loss in crystallinity can be reconciled with the drop in L_{SAXS} values at the same strains. The onset of strain hardening at approximately $\varepsilon_{2.0}$ is coincident with an apparent slight rise in the crystallinity values. At corresponding strains, the diffuse intensity appears in the 2D SAXS which is associated with the formation of a new lamellar superstructure from the fragmented remnants of the original lamellar structure in blown films. The rise of crystallinity that accompanies the formation of this new lamellar superstructure suggests that a strain induced recrystallization indeed takes place in the large strain regime. The plots shown in Figures 46 and 47 captures the variation of crystalline orthorhombic and monoclinic content in two different films. Figures 48, 49 and 50 show the variation in crystallinity, orthorhombic and monoclinic content as well as the change in domain size for the (110) and (200) orthorhombic planes. The latter are obtained by calculating the reciprocal of the full width at half maximum of the Lorentzian profiles utilized in the fitting of the (110) and (200) planes, provided the scattering vector is defined as s (see footnote in Section 4.2.1). The crystalline domain size captured here is expectantly larger than the average value of L_{SAXS} but the trend with regards to the dimensional evolution with strain is consistent particularly for the (200) reflection showing firstly, a rapid decrease in domain size from ε_0 to $\varepsilon_{1.0}$ and secondly, a gradual decrease in domain size beyond $\varepsilon_{1.0}$.

7.2.2 Crystalline Orientational Changes

Figures 51 and 52 show the change in the orientation of the a, b and c axes as a function of strain in MD and TD strained films. Irrespective of the deformation direction, i.e. MD or TD F_a, F_b and F_c show similar trends. The application of strain causes the c axis to orient into the strain direction and at large strains, the c axis is always parallel to the applied strain with the a and b axes existing in cylindrical geometry about the c axis. This behavior is entirely consistent with the model of orientation proposed by Keller in his high stress model and is typically observed in blown films of HDPE specimens [6, 8, 64, 65].

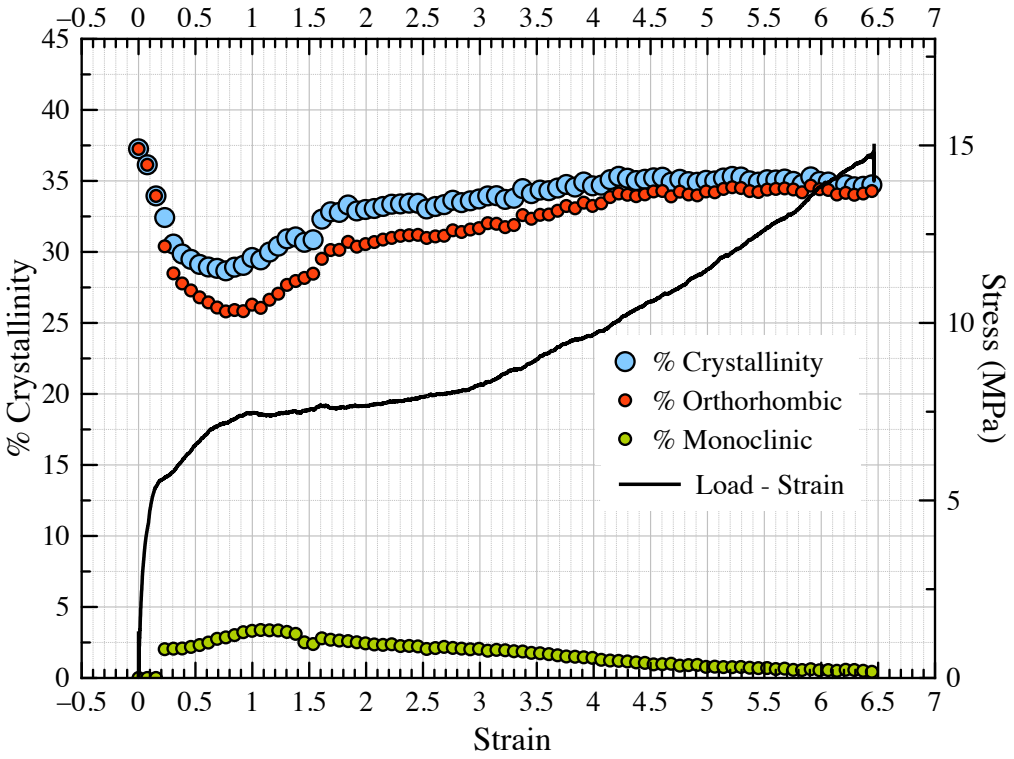

Figure 46: Crystallinity variation under strain for LLDPE$_1$.1a resolved into contributing orthorhombic and monoclinic fractions. Crystalline lamellae are initially comprised of orthorhombic unit cells which experience an orthorhombic to monoclinic transition after the first yield point

On closer inspection of the variation of F_a, F_b and F_c with strain (Figures 51 and 52) some interesting features are observed. It is seen that in TD strained specimens, specifically at high strain, the values of F_c are higher than the corresponding values for MD strained samples. To understand this it is also important to take into account the mesoscale changes occurring during the deformation from the SAXS data (discussed in Section 5.2.1 and Section 6.3.3.1). It is shown that TD deformation at high strains produced a strain induced recrystallized lamellar morphology that was independent of the morphology in the as made films, which was not the case in MD deformation. Similar to obtaining a spread in d_{ac} values at high MD strains from the SAXS data, a distribution of F_c values is obtained for corresponding MD strains in the WAXS. The lower F_c values during MD strain might might ultimately explain the absence of a clear equatorial steak in the MD specimens. When F_c values are low at the highest strains it suggests poor alignment of the molecular axis

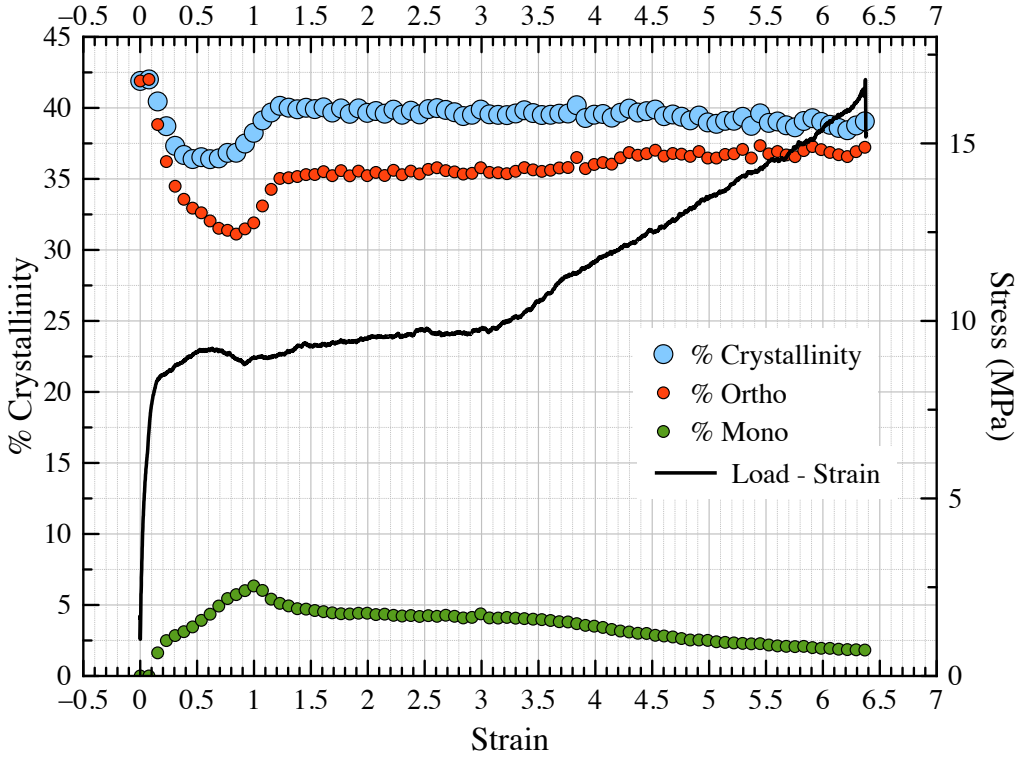

Figure 47: Crystallinity variation under strain for LLDPE$_3$.1b resolved into contributing orthorhombic and monoclinic fractions. Crystalline lamellae are initially comprised of orthorhombic unit cells which experience an orthorhombic to monoclinic transition after the first yield point

in the strain direction. Since the formation of shish is permissible only by elongation of chains [49, 55], it is plausible that incomplete elongation and therefore poor alignment of the molecular axis prevents the successful formation of well defined shish. The inverse is true when drawing along TD. Higher values of F_c suggest better alignment of the molecular axis along the strain direction which might aid the formation of shish. The complete set of findings suggest that the LLDPEs investigated in this work, depending on the strain imparted to the material are compatible with both of Keller's models - in the as made conditions, blown films of LLDPE are consistent with Keller's low stress model while at high strains they are consistent with Keller's high stress model. This is the first time that a single polyethylene has exhibited a tendency to exist in both configurations. The finding is important because it suggests that a suitably tailored architecture can allow access to properties exhibited by both the Keller models.

7.2.3 Amorphous Orientational Changes

The variation of F_{am}, i.e. the Herman's orientation factor of the amorphous chains, as a function of applied strain is shown in Figure 53. F_{am} was extracted from the WAXS data for two films i.e. LLDPE$_1$.1$_a$ and LLDPE$_3$.1$_a$ using methods described in Section 4.2.4.

The plot of F_{am} as a function of the applied strain indicates that at zero strain the non-crystalline chains are arranged isotropically. As may be anticipated following the onset of strain below the first yield point, the non crystalline chains begin to align into the strain direction.

This initial alignment is shown in Figure 53 as the rise of F_{am} between ε_0 and $\varepsilon_{0.15}$. This initial ordering is observed in the SAXS data particularly by the initial rise of d_{ac} between ε_0 and $\varepsilon_{0.11}$ as shown in Figures 31, 32 and 35. Within this affine deformation range, local ordering of amorphous chains between lamellae due to strain explains the rise in values of F_{am}. The rate of increase of F_{am} with respect to strain i.e. the slope of the linear rise between ε_0 and $\varepsilon_{0.15}$ is however different between the two polymers being compared here. In previous discussions in Section 6.2, it is shown that lamellae formed from LLDPE$_3$ and LLDPE$_1$ polymers respectively differ in their average dimensions due to architectural differences between the polymers. Firstly, LLDPE$_1$.1a and LLDPE$_3$.1a have nearly the same degree of total crystallinity $\sim$39%. However, LLDPE$_1$.1a has an average L_{SAXS} value of 112Å while LLDPE$_3$.1a has an average L_{SAXS} value of 181Å(see Table 5). Similarly the d_a values for LLDPE$_1$.1a and LLDPE$_3$.1a are 83Å and 99Å respectively while the d_c values for the two films are 35Å and 40Å respectively. Also, the LAR value which characterizes the relative proportions of MD and TD ordered lamellae is 1.56 for LLDPE$_1$.1a while it is 3.36 for LLDPE$_3$.1a (see Table 5). This indicates that for the same degree of crystallinity, lamellae in LLDPE$_1$.1a are smaller, more closely spaced and highly disordered than corresponding lamellae in LLDPE$_3$.1a which are larger, less closely spaced and well ordered. During the low strain affine regime, amorphous chains in LLDPE$_3$.1a can orient into the strain direction at a faster rate than amorphous LLDPE$_1$.1a as the amorphous domains in LLDPE$_3$.1a are likely to be less entangled. These subtle differences in morphology of the two films which are themselves driven by the architectural differences

in the polymers represent the most plausible reason for the different rates of change of F_{am}.

Between $\varepsilon_{0.15}$ and $\varepsilon_{0.48}$ i.e. the first and second yield point, F_{am} shows a conspicuous local minimum for LLDPE$_3$.1a but not for LLDPE$_1$.1a. This local minimum appears at $\varepsilon_{0.2}$ for LLDPE$_3$ and coincides with the strain at which L_{SAXS} begins to decrease and χ begins to increase. These simultaneously occurring events point to a model of lamellar rotation and fragmentation that is initiated after the first yield point. The fragmentation itself is likely to initiate at defect sites on the lamellar surface during the sustained application of strain beyond the affine limit. The drop in crystallinity beyond the first yield point also provides justification for the lamellar fragmentation hypothesis. It is hypothesized that the instantaneous disorder of polymer chains at the edges of the fragmented lamellae combined with the loss in alignment of previously ordered interlamellar amorphous chains in the strain regime between $\varepsilon_{0.15}$ and $\varepsilon_{0.2}$ is captured by the 2D WAXS data in the form of the observed local minima.

Subsequently to the local minima, application of strain up to $\varepsilon_{0.6}$ results in further improvement in amorphous chain orientation relative to the strain direction. As deformation continues, the fragmented lamellae quickly rotate into the direction of strain. This is inferred from the rapid changes in χ values after the first yield point. Under sustained tensile strain an ordering of the amorphous domains can take place again. This reordering can explain the rise of F_{am} after the local minima between the first and second yield point. In LLDPE$_1$.1a however, since the semicrystalline morphology is highly disordered to start with, any instantaneous change in ordering of the non-crystalline domains is unlikely to be captured by the 2D WAXS data. Instead, F_{am} continues to increase at gradually till $\varepsilon_{0.6}$ (It is possible however to test this hypothesis by performing similar measurements on annealed specimens of LLDPE$_1$.1a. If the hypothesis is correct, annealing will increase the rate of change of F_{am}). Between $\varepsilon_{0.6}$ and $\varepsilon_{1.0}$, F_{am} increases gradually for LLDPE$_3$.1a while it marginally reduces in value for LLDPE$_1$.1a.

Towards the end of this strain regime the process of lamellar fragmentation is nearly completed. Beyond $\varepsilon_{1.0}$, no significant changes in lamellar dimensions or crystallinity occurs. At strains greater than $\varepsilon_{1.1}$ for LLDPE$_3$.1a and $\varepsilon_{1.6}$ for LLDPE$_1$.1a respectively, the

process of strain induced crystallization propagates through the entire specimen and the full extent of amorphous orientation along the strain direction is achieved shortly thereafter. At these strains, typically in the plateau region of the stress-strain plot, the crystallinity begins to increase. This crystallinity increase coincides with the appearance off the diffuse meridinal scattering in the SAXS i.e. the persistent lamellar structure that grows from of the fragmented remnants of the original lamellae. At still higher strains the F_{am} values rise as amorphous chains orient along the strain direction. This is captured by the values of $F_{am} = 0.8$ that are asymptotic to the strain axis.

It is interesting to note that the changes in the amorphous orientation are observed at values of strain that are greater than similarly expected changes in the stress-strain plots of the polymers. In the stress-strain plots, the first and second yield point occur at $\varepsilon_{0.11}$ and $\varepsilon_{0.48}$ respectively, while changes in F_{am} that are likely to accompany the first and second yield occur at $\varepsilon_{0.15}$ and $\varepsilon_{0.6}$ respectively. This suggests that while the multiscale physical processes occurring in an LLDPE film under strain are represented in the stress-strain plots by the single point values of first and second yield respectively, these physical processes in reality, occur over a strain range. In the case of $LLDPE_3$.1a, $\varepsilon_{0.11}$ to $\varepsilon_{0.20}$ represents the initiation and completion of the first yield processes while $\varepsilon_{0.48}$ to $\varepsilon_{1.1}$ represents initiation and completion of the second yield processes. In the case of $LLDPE_1$.1a, $\varepsilon_{0.11}$ to $\varepsilon_{0.20}$ represents the initiation and completion of the first yield processes while $\varepsilon_{0.48}$ to $\varepsilon_{1.6}$ represents initiation and completion of the second yield processes.

Amorphous orientation in semicrystalline polymers has been probed by a variety of characterization techniques such as Positron Annihilation Lifetime Spectroscopy (PALS) [120], infra-red dichroism (IR dichroism) [**?**] and birefringence measurements [46]. The IR dichroism work of Read et al utilized the absorbances of IR radiation polarized along the stretching direction and perpendicular to the stretching direction for LDPE specimens in order to quantify the amorphous orientation F_{am} as a function of strain inside spherulitic microstructures. The strain applied on these specimens was much lower in the work of Read et al. ($\sim\varepsilon_{0.8}$) than in the current work. F_{am} was quantified for a number of different IR bands for which the absorbances were measured. These bands are assigned to the different

conformations of a sequence of CH_2 groups along the backbone of an amorphous chain. Of the various bands measured, the bands at 2016 cm^{-1} and 1078 cm^{-1} were directly related to the sequence of *trans* and *gauche* conformations. F_{am} from *trans* conformations were found to be greater in value than for *gauche* conformations. The *trans* conformation expectedly showed the highest values of F_{am}. The F_{am} values obtained by these IR measurements are lower in magnitude than our corresponding data at similar strains. However the initial trend in F_{am} is similar showing a rise with applied strains. Due to the lack of *in situ* measurements, only a few data points exist for the IR work and as a result the work of Read et al is unable to capture salient features such as local minima in F_{am} that are related to the physical processes corresponding to the first and second yield points.

Birefringence measurements performed by Petraccone et al [46] on LDPE specimens also enables the quantification of F_{am}. In this work, specimens were strained to different elongations and the total birefringence was measured. The crystalline contribution to the birefringence was calculated using diffraction measurements and the amorphous contribution was obtained by subtraction. In this work it was assumed that the crystallinity remained constant in the strain range which was ∼40%. This is however inconsistent with our data where a drop of 10% at minimum is expected in the same strain range. The equation listed below (Equation 47) is used to determine F_{am} from birefringence data at any strain.

$$\triangle n = \triangle {n_a}^{\circ}(1 - X_c)F_{am} + \triangle {n_c}^{\circ}(X_c)F_c + \triangle n_f \tag{47}$$

In Equation 47 $\triangle n$ is the measured birefringence from an optically transparent specimen of a uniaxially oriented semicrystalline polymer. The exhibits birefringence due to the alignment of crystals and amorphous chains. $\triangle {n_a}^{\circ}$ and $\triangle {n_c}^{\circ}$ are the intrinsic birefringences of the crystalline and amorphous phases respectively. $\triangle n_f$ is the form birefringence which in the case of semicrystalline polymers is related to the shape and structure of the crystalline component (in the form of rods or spheres or cuboids) with one refractive index suspended in amorphous media with a second refractive index. F_{am} and F_c represent the Herman's orientation functions for the amorphous and crystalline phases respectively and X_c is the

degree of crystallinity. There is poor accuracy in the measurement of the Herman's parameters by birefringence methods because of the lack of certainty in intrinsic birefringences. The form birefringence depends on the shape and size of crystalline lamellae but in the work of Petraccone et al, the assumption that $\triangle n_f$ is independent of crystal size and disorder was made. The corresponding values of F_{am} obtained by the authors are therefore inconsistent with the IR work of Read et al as well as the values reported here. The approach outlined in the current work using WAXS to calculate F_{am} can be easily and consistently applied to all polymers provided the WAXS data is two dimensional. From an experimental standpoint It does not require transparent specimens like in birefringence experiments nor does it necessitate the need for assumptions about the shape, size and ordering of crystals. While it might be more time intensive to extract the values of orientation, it is clear that the WAXS method is better equipped to handle *in situ* measurements.

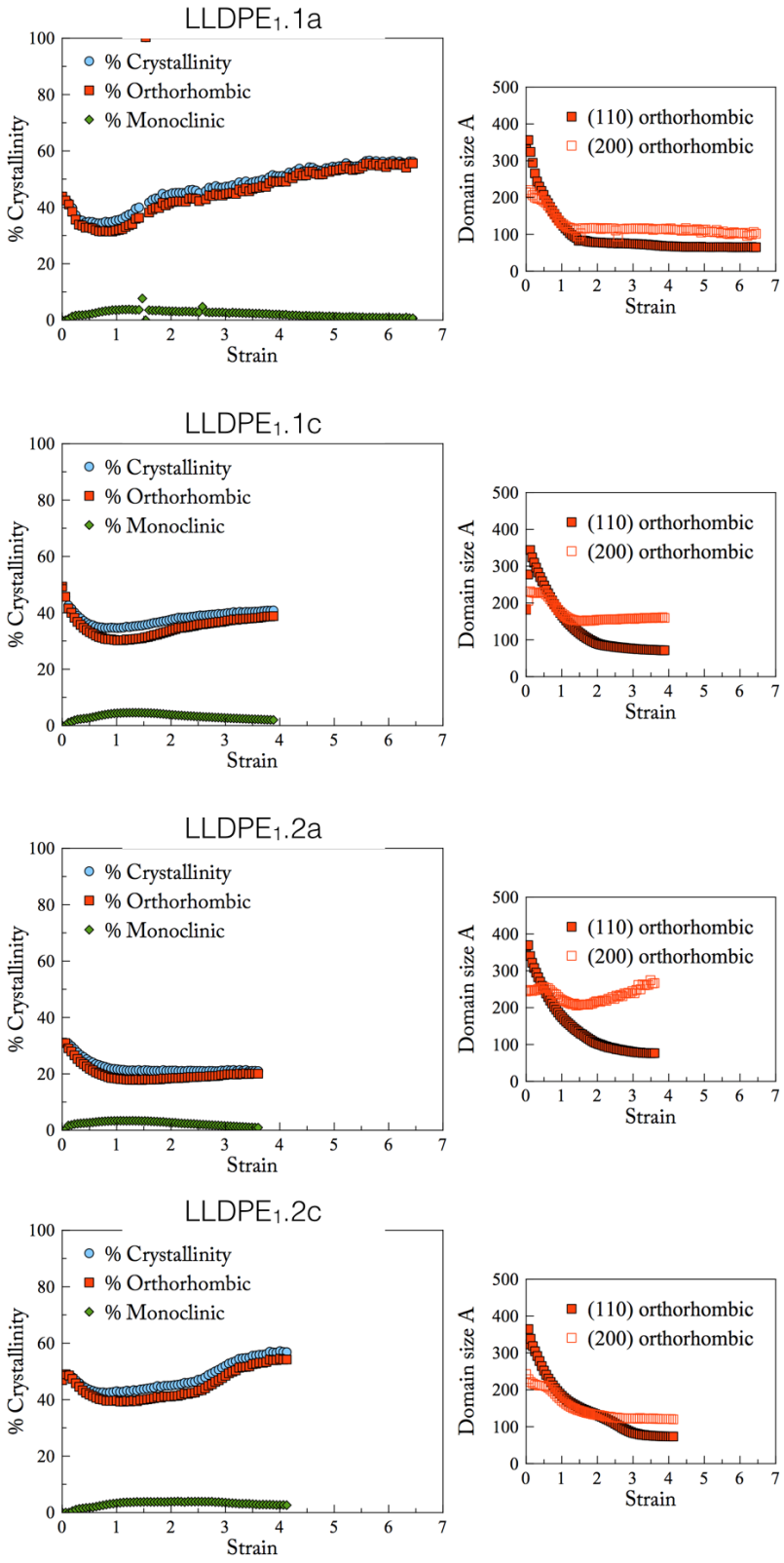

Figure 48: Crystallinity variation under strain for $LLDPE_1$ resolved into contributing orthorhombic and monoclinic fractions. Crystalline lamellae are initially comprised of orthorhombic unit cells which experience an orthorhombic to monoclinic transition after the first yield point

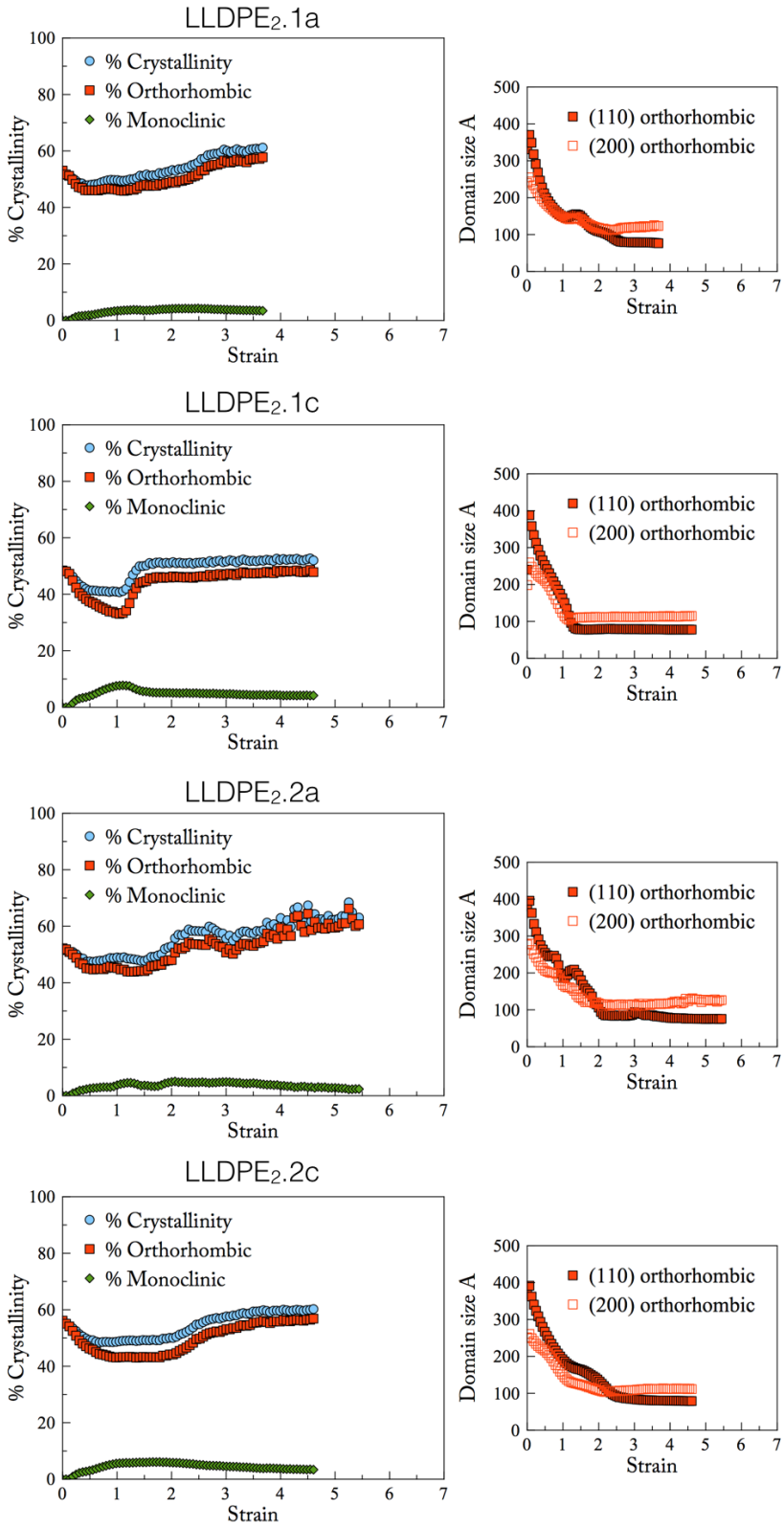

Figure 49: Crystallinity variation under strain for $LLDPE_2$ resolved into contributing orthorhombic and monoclinic fractions. Crystalline lamellae are initially comprised of orthorhombic unit cells which experience an orthorhombic to monoclinic transition after the first yield point

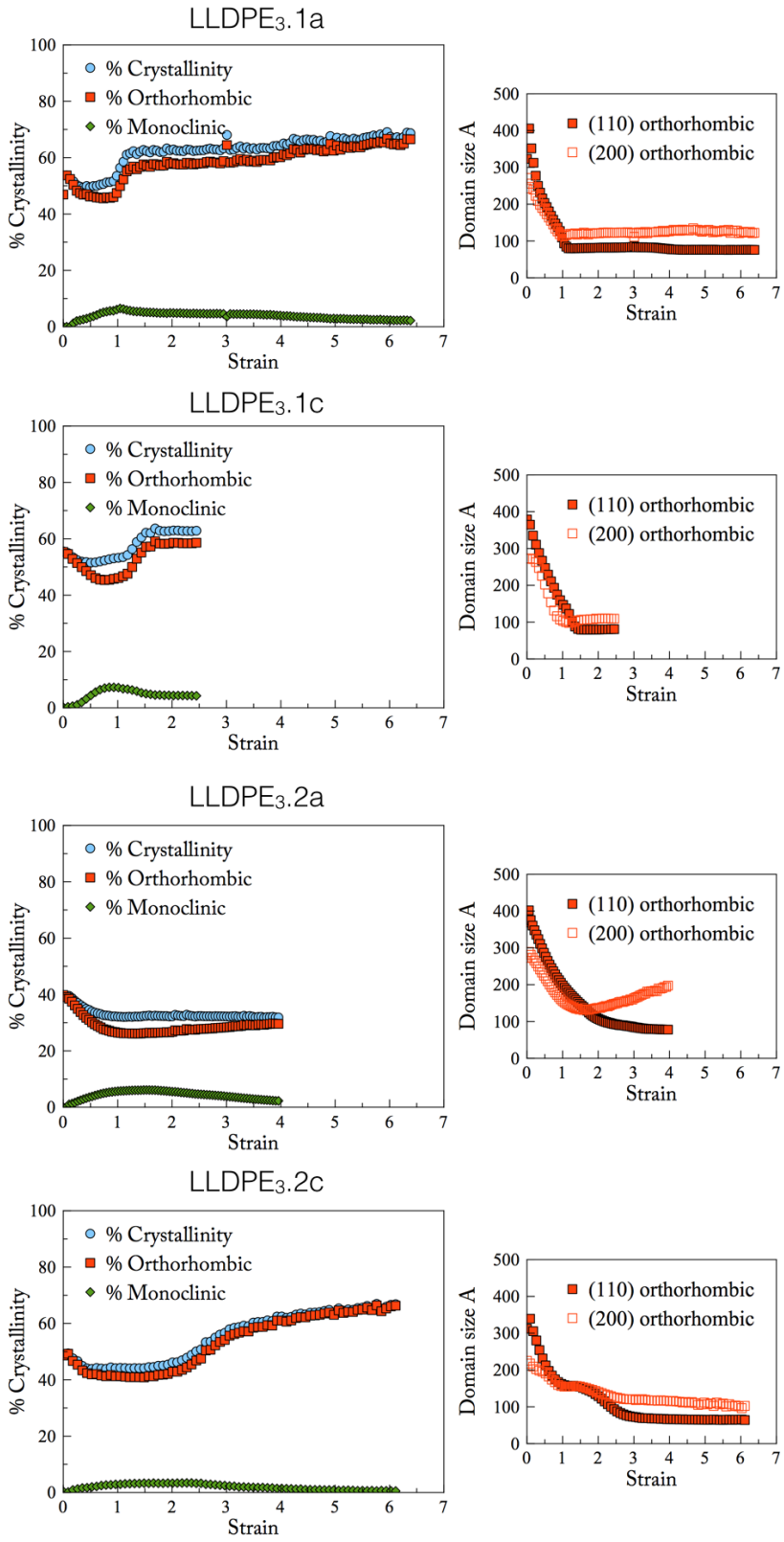

Figure 50: Crystallinity variation under strain for $LLDPE_3$ resolved into contributing orthorhombic and monoclinic fractions. Crystalline lamellae are initially comprised of orthorhombic unit cells which experience an orthorhombic to monoclinic transition after the first yield point

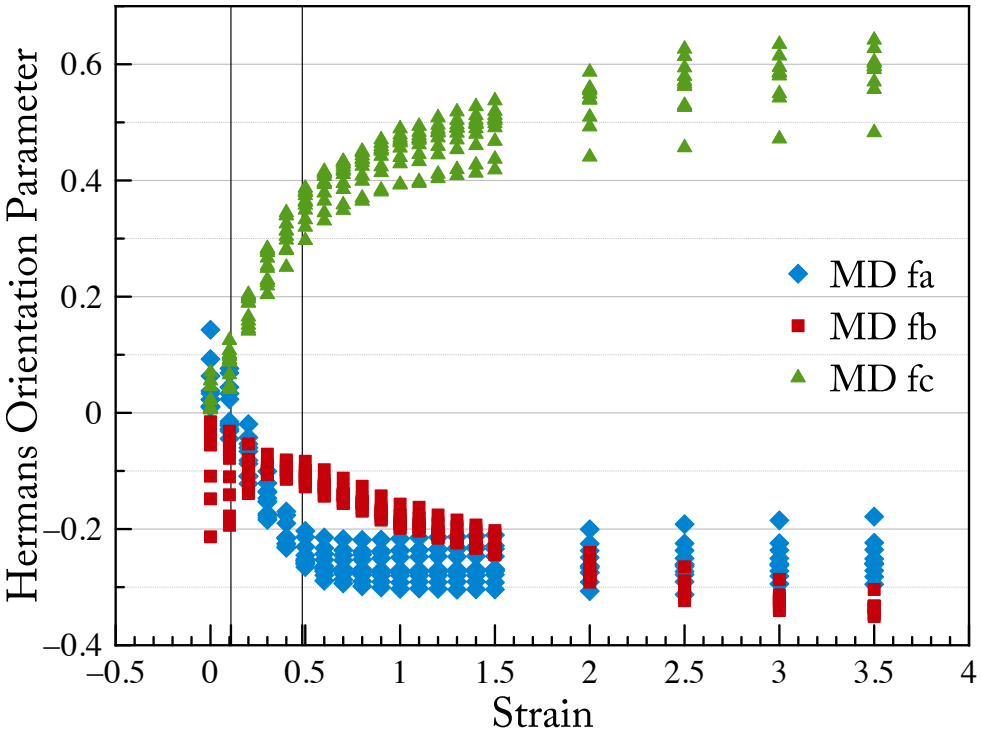

Figure 51: Changes in F_a, F_b and F_c under strain for MD strained films. At high strains the c axis is along the strain direction while the a axis is perpendicular to it. The solid lines at $\varepsilon_{0.11}$ and $\varepsilon_{0.48}$ represent the first and second yield point respectively.

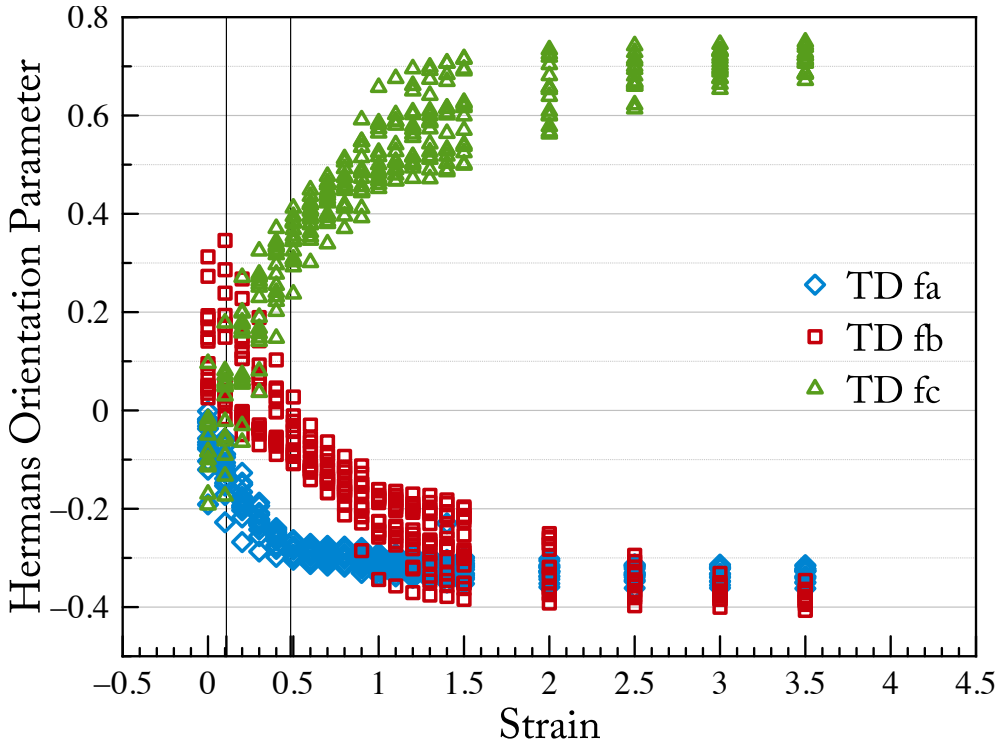

Figure 52: Changes in F_a, F_b and F_c under strain for TD strained films. At high strains the c axis is along the strain direction while the a axis is perpendicular to it. The solid lines at $\varepsilon_{0.11}$ and $\varepsilon_{0.48}$ represent the first and second yield point respectively.

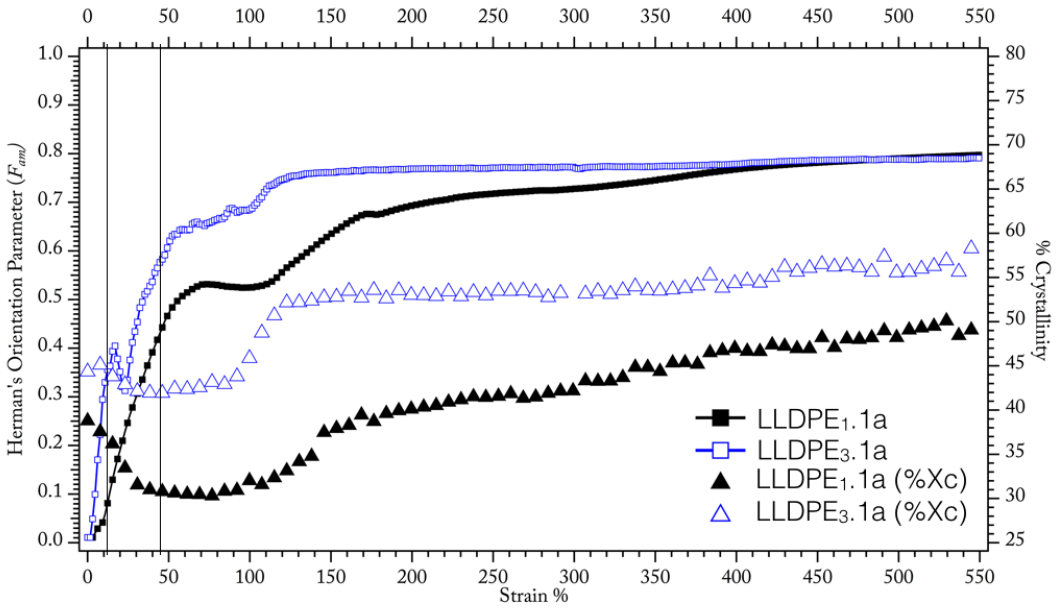

Figure 53: Variation of F_{am} under applied strain for films LLDPE$_1$.1a, and LLDPE$_3$.1a. F_{am} is calculated with respect to the strain direction.The first and second yield point in the strain are marked by black vertical lines at $\varepsilon_{0.11}$ and $\varepsilon_{0.48}$

CHAPTER VIII

INVESTIGATION OF THROUGH THICKNESS FILM STRUCTURE

8.1 β Rotation Measurements

The standard geometry for measuring SAXS and WAXS data is one where the X-ray beam is normal to the plane of a film specimen. Since however, the scattering only captures an ensemble average 2D projection of a 3D structure on the detector, features of film morphology through the thickness of the films cannot be properly investigated in the 'standard' geometry. Therefore, experiments are performed where the film specimen is rotated relative to the incident X-ray beam and the scattering is measured as a function of rotation angle. By rotating the specimen, more of the structure through the thickness of the films contributed to the scattering than in experiments where the films were investigated in the standard configuration. These experiments were labelled as β rotation measurements where β represented the non-orthogonal angle. The value of β is zero when in the normal scattering geometry. A schematic of β rotation measurements is shown in Figure 54.

β rotation WAXS and SAXS were conducted in separate measurements by staff at EMCC at β angles 0°, 10°, 20°, 30°, 40°and 50°for two films of the $LLDPE_2$ series. The experiments were first performed with the MD held vertical, second with MD held at 45°and third with the MD held horizontally i.e. TD vertical. The pertinent results from WAXS and SAXS are shown in Figure 55.

The measured WAXS data was converted to F_a, F_b and F_c with respect to MD and these are presented in the Figure 55. When MD is held vertically and the film is rotated systematically in β in steps of 10° up to a final β value of 50°, the F_a, F_b and F_c values remain unchanged with only a small increase in orientation observed. When the TD is held vertically the behavior of F_a, F_b and F_c with increasing rotation is different. At $\beta = 0°$,F_b is positive suggesting alignment along TD while F_a and F_c are both negative. The absolute values of F_a, F_b and F_c are greater for the thinner films. At a value of $\beta =$

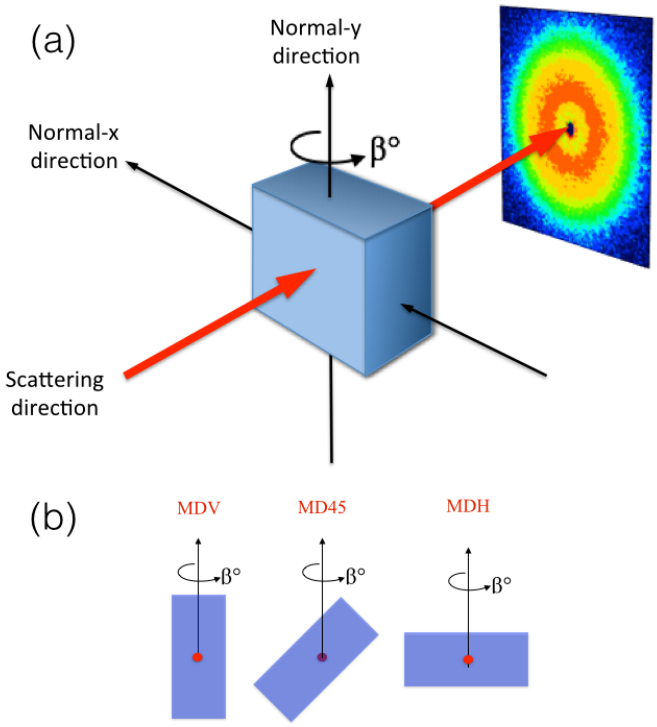

Figure 54: β rotation schematic showing (a) experiment geometry (b) orientation of the β rotation specimens where MDV represents the MD held vertical and MDH represents the MD held horizontal i.e. TD vertical and MD45 represents the MD held at a 45° angle.

50° and TD vertical, the F_a, F_b and F_c behavior reverses entirely with F_a and F_c becoming increasingly positive and F_b becoming increasingly negative (see Figure **??**). This implies that a distribution of orientations of the a, b and c axis exists within the film specimen which are only obvious when the through thickness structure of the films is investigated. Since, scattering captures a 2D projection on the detector of the 3D structure in real space, rotating the film allows the internal structure to be more accurately probed. The data show that for both thin and thick films the internal structure of films is non-trivial because the structural features that contribute to the results in MDV geometry must also contribute to the results in MDH geometry. An attempt is therefore made to explain the two sets of data i.e. MDV and MDH, separately before attempting a combined explanation of the two (MD45 is ignored here because the behavior is intermediate between MDV and MDH).

Firstly, by rotating the specimen around MDV, projections from those unit cells that

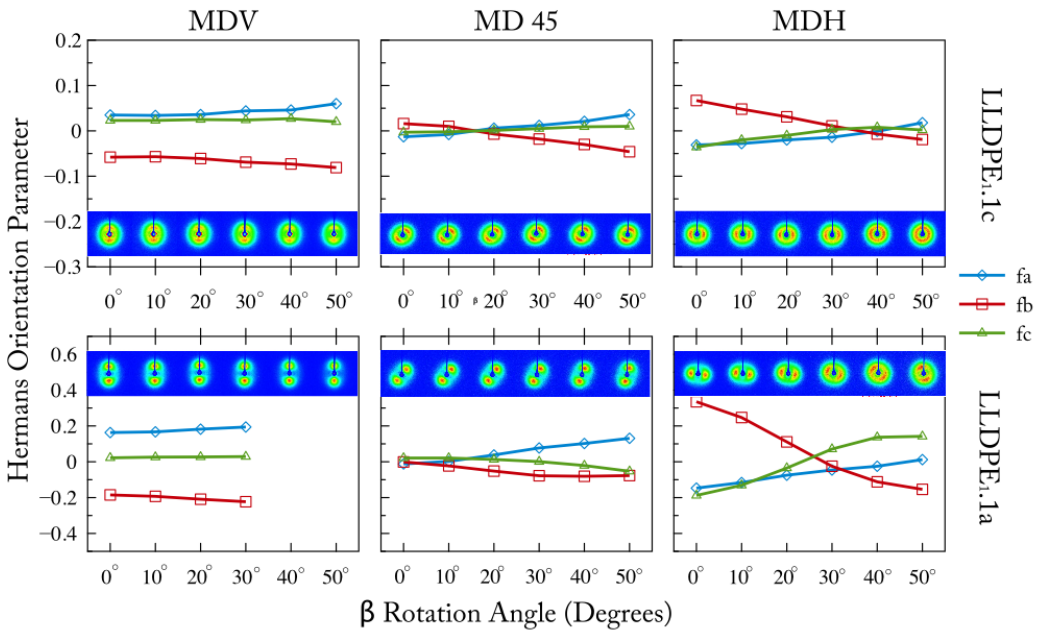

Figure 55: β rotation WAXS and SAXS measurements conducted on two sets of films of $LLDPE_2$. MDV, MD45 and MDH represent films that were held with their MD in along the vertical direction, at 45° to the vertical direction and perpendicular to the vertical direction. The values of F_a, F_b and F_c are examined as a function of β. Insets show 2D SAXS patterns at the corresponding β angles.

were absent in the standard scattering geometry are measured and they are consistent with the standard Keller model at low stress i.e. a axis orientation along MD and b axis orientation along TD. At higher rotation angles, more of these unit cells can contribute to the scattering and hence the overall orientation increases.

Secondly, rotating the specimen in MDH mode, implies that we are rotating around the b axis and the expectation is that at higher rotation angles, the F_b should increase and F_a and F_c should decrease. However, the inverse is observed such that F_b decreases from a positive value eventually becoming negative at high β while both F_a and F_c increase from negative values eventually becoming positive. This means that by rotating around the MDH, those unit cells that contribute to the original WAXS patterns in the standard geometry are no longer present in the MDH β rotation measurements.

The two contradicting sets of data i.e. from MDV and MDH must necessarily be reconciled by a single model of the internal structure of the films. The hypothesis of twisted kebab structures growing radially outward from a shish and following cylindrical geometry (based on Keller's low stress model [64, 65]) (see section 2.2.2.2) might correctly explains these results by suggesting that the a and c axis twists uniformly around the b axis. If such a structure truly exists then rotating around MDH i.e. the a axis, will bring populations of unit cells oriented with their a axis along MD into the path of the X-ray beam without changing the overall orientation. This explains why in MDV geometry, β rotation does not significantly affect the orientation. In the MDH geometry and under β rotation, the WAXS detector captures once again, the scattering from all those unit cells whose contributions to standard WAXS measurements were lost due to the projection problem. Specifically projections from the a, b and c axes in unit cells arranged in the cylindrical geometry around the shish are now 'visible'. The b axes of these unit cells will approach orthogonality to the TD (i.e MDH) under β rotation in the MDH geometry. This phenomenon causes F_b to become progressively more negative as β approaches 50°. Clearly, having twisted kebabs accounts for the results of the β rotation WAXS measurements.

The SAXS patterns measured at the corresponding β angles are intriguing because they suggest a change in orientation of the lamellae in the mesoscopic regime as a function of β. For the specimens where MD was held vertically, SAXS patterns did not change appreciably during the experiment. It appeared as though the width of the SAXS lobes in MDV narrowed as the β angle was increased suggesting an improvement of lamellar orientation relative to the MD. This is consistent with the WAXS data. When MD was held at 45° and the SAXS was captured in the standard geometry, the azimuthal position of the lobe centers changed. The SAXS pattern at $\beta = 0$ showed a positioning of lobes between typical MD and TD SAXS patterns. Interestingly, at $\beta = 50°$ it appeared as though there was a shift in the azimuthal position of the lobes. The most significant difference was however observed in the case of specimens where MD was held horizontal and the sample was rotated through β. At $\beta = 0°$ the standard anisotropic TD SAXS pattern with two lobes was observed. On rotation to $\beta = 50°$, LLDPE$_2$.1c showed a complete loss of the anisotropic

scattering. This was replaced by a clear isotropic ring. The behavior in the thin film viz $LLDPE_2$.1a was even more surprising. While at $\beta = 0°$, the typical two lobe SAXS pattern was clearly observed along the equator, at $\beta = 50°$ the specimen displayed the same two lobe pattern but now distributed about the meridian. The behavior is surprising for two reasons. Firstly, this is quite different from the behavior observed in $LLDPE_2$.1c which upon rotation showed an isotropic morphology through its thickness. Secondly, this phenomenon suggested that morphology through the film thickness consisted of lamellae that were preferentially oriented orthogonal to MD and these could only be probed in the MDH configuration of β rotation. The change in the orientation of lamellae as measured by β rotation SAXS and the orientation distribution of the a and c axes points towards the presence of a twist like morphology through the thickness. However this does not wholly suggest the existence of a continuous twisted ribbon like lamellae. Our findings are in agreement with the low stress model developed by Keller [64]. However, the observations only partially support the hypothesized description of kebabs as continuous twisted structures. There is no evidence to support the claim of mono-directional rotation of the a and the c axis around the b axis within a single isolated kebab such that the kebab forms a continuous twist in melt crystallized specimens.

Furthermore, in experiments where $LLDPE_2$.1a was strained at $\beta = 50°$ in an *in situ* measurement, The morphology evolution through the thickness did not follow the standard observed pathway for either MD or TD strain. Selected images from the 2D SAXS detector of these measurements are shown in Figure 56. MD strain does not show the characteristic four lobe pattern at medium strains such as those shown in Figure 29. At high strains close to failure, neither the diffuse scattering intensity in the meridian direction nor the streak-like artifacts close to the beamstop are observed. Specimens held with the TD along the strain direction at $\beta = 50°$ do however show the behavior described above, where the dual lobes are rotated and present along the meridian and not along the equator as is the case with traditional $\beta = 0°$ measurements. Strain in such a specimen shows clearly the presence of four lobe scattering at strains greater than the first yield along with the increase in the angle subtended by the four lobes with increasing strain. Unlike

the MD strained specimen at $\beta = 50°$, the diffuse intensity and the equatorial streak do indeed appear. The results of the β rotation studies strongly suggest that the internal structure in blown films and its evolution is more complicated than suggested in literature by various authors [1,30,50,70,76,78–80,90,104,121–125] and cannot be completely resolved by standard SAXS-WAXS studies. The complexity arises due to preferential ordering of lamellae through the thickness of the films that is not captured in the scattering when the specimens are held normal to the incident X-ray beam. To understand the origin of this behavior we have applied the Fourier Transform method (FFT) as described below.

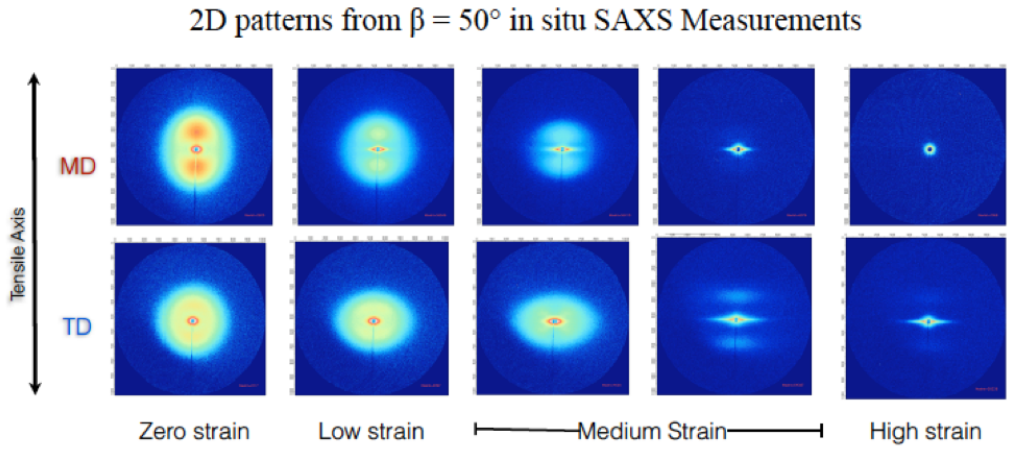

Figure 56: β rotation *in situ* SAXS measurements conducted on LLDPE$_1$.1a for MD and TD strained specimens

8.2 Simulation of 2D SAXS patterns

Since the results of the β rotation measurements could not be accurately explained by the model of morphology accurately, a modeling effort was undertaken in a complementary study to understand the through thickness structure of films. The current work focussed on

modeling structures in 2D and 3D and simulating the SAXS patterns from these structures. The mathematical relationship between the real space structure and scattering is obtained through the Fourier transform function (FFT) (see Appendix A). The FFT explains that shows that the SAXS pattern (or indeed any scattering pattern) from a mathematically defined structural model can be simulated once the Fourier Transform or more specifically the Fast Fourier Transform of the structure is computed. To understand our SAXS data model structures were synthesized in 2D and 3D and the theoretical scattering from these structures were computed.

8.2.1 2D SAXS Simulation from 2D Structures

Structural models of lamellae distributed in an amorphous matrix were synthesized in Matlab. The following boundary conditions were applied. Lamellae were modeled as either polydisperse rectangular or polydisperse ellipsoidal objects possessing a defined aspect ratio. The aspect ratio i.e. the ratio of length to breadth of the object, was varied between 1 and 100. A minimum separation between lamellar objects existed and was analogous to the d_a. The separation itself was modeled using a Poisson point process [126]. This method allows isolated centers to be identified without any lattice restrictions such that the overall distribution of points within a volume is pseudo-random. Lamellae were constructed with a length and breadth around the various identified Poisson centers and distributed in an amorphous matrix and lacked an ordered lattice structure. In addition, lamellae were assigned an orientation distribution that permitted the generation of isotropic and anisotropic morphologies. The orientation was randomly assigned with a self checking process that prevented the overlap of multiple oriented objects.

The 2D patterns are constructed on a cartesian grid of 128 by 128 pixels. The fill factor or volume fraction to be filled is the primary input along with an average aspect ratio and its normal distribution. Based on these two quantities an estimate of the total number of Poisson centers to be drawn is determined allowing the image to be constructed. The Fourier transform of the image is calculated within Matlab to give the amplitude of the scattering as a function of reciprocal dimension and subsequently the amplitude can be

squared in order to compute the 2D scattering. Some examples of 2D structural models and their 2D FFT patterns, i.e. simulated SAXS patterns, are shown in Figures 60 to 61.

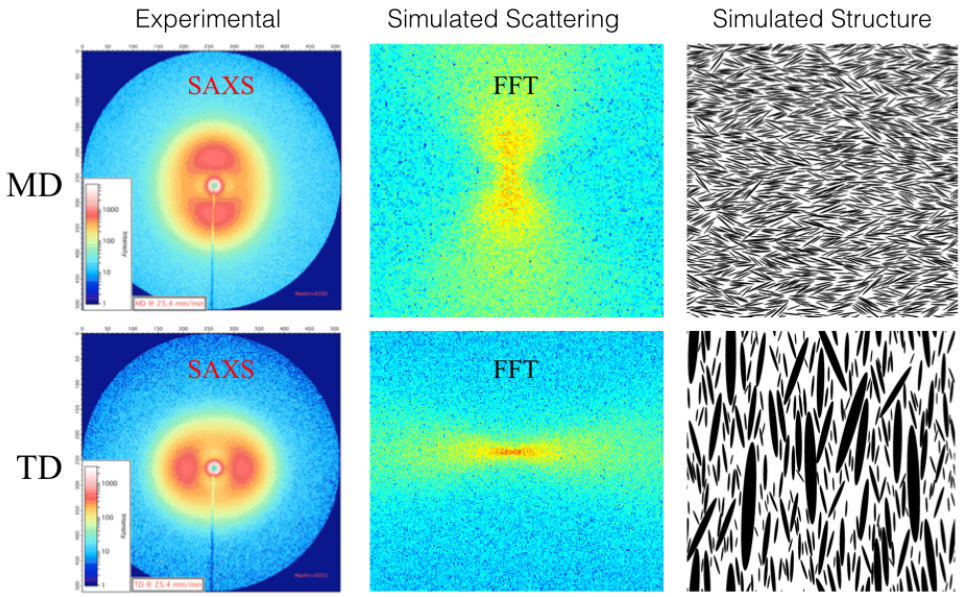

Figure 57: Polydisperse ellipsoidal lamellae (filled black objects) are simulated within an amorphous matrix (unfilled white background) along with an orientation distribution to explain the MD-TD scattering maxima in the as made films. The FFTs capture the salient features present in the experimentally collected data. The degree of crystallinity in the simulated structures i.e. ratio of black to total area is 0.4 in the MD case and 0.25 in the TD case.

Firstly, we tried to emulate the scattering patterns for the as made condition in MD and TD modes. In order to do this, microstructures were simulated as per the basic lamellar model comprising of lamellae distributed in an amorphous matrix. Orientational dependence was provided to the lamellae and a spread of distributions was made possible. The upper rows of Figure 60 show the attempt made to recreate the MD type scattering while the lower row shows how the TD type scattering might occur. In the recreation of MD type scattering, the simulated structure consists of lamellar objects with low polydispersity whereas the in the TD recreation, the polydispersity is much higher as is obvious from the clearly distinguishable large and small objects. Although the experimental MD and TD

scattering are related by a simple translation of the sample and therefore arise from the same morphology we show that similar salient features (two lobes in the scattering with appropriate orientation effects) can be obtained using different microstructures. This highlights the non triviality of the scattering simulation discussed in Section 2.4.1.1 i.e. although experimentally obtained scattering patterns and simulated scattering patterns are visually similar, the real (true) microstructure and the simulated microstructure need not be similar. A large number of simulated microstructures might provide exactly the same scattering pattern. This is especially true where dimensions and orientations of the microstructure being described are in fact broad discrete distributions. Nevertheless, it is important to note that provided there is convergence the scattering pattern and the simulated pattern for an exhaustive series of simulations, the true microstructure is necessarily part of the simulated subset.

Secondly, the quadralobe behavior in MD strained specimens was examined and similar patterns were simulated by the FFT approach. Figure 62 shows that the simulated scattering visually matches the experimentally measured scattering at strain values of 0.9 and 2.25 respectively. The microstructures here are visually quite different from those in Figure 60 in the upper row. Specifically, the L_{SAXS} is lower and the orientation of the lamellae is less random although a distribution of the orientation does exist. The microstructures are however linked because under strain, the microstructure in the upper row of Figure 60 evolves in to the microstructures shown in 62.

Thirdly, the β rotation measurements described in Section 8.1 are examined from the point of view of the through thickness microstructure. Specifically, we capture the change in the orientation of SAXS patterns under β rotation for specimens of $LLDPE_2$.1a (see Figure 61). This is achieved by changing the mean orientation direction of the lamellar arrangement scheme. At $\beta = 0^\circ$ the average lamellar normal is oriented along the TD. With each increment in β, the orientation of the lobes in SAXS changes with the lobes eventually displaying MD type of behavior at $\beta = 50^\circ$. In order to account for this change in the azimuthal positions of the lobes measured experimentally, the direction of the average lamellar normal is also tweaked relative to the azimuth during the simulation of microstructures. The

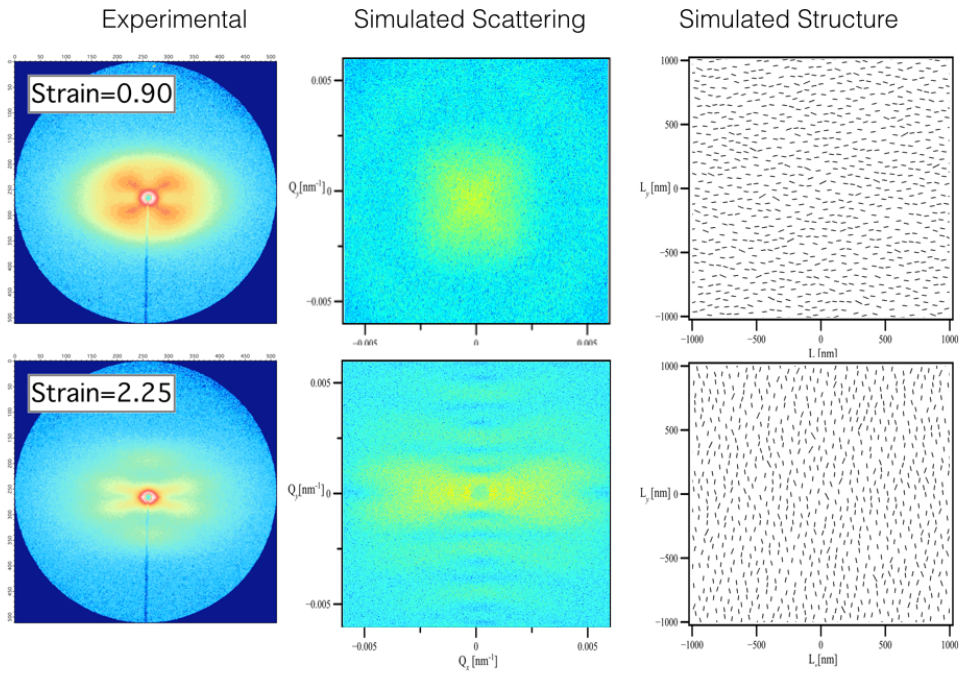

Figure 58: Polydisperse rectangular lamellae (filled black objects) are simulated within an amorphous matrix (unfilled white background) along with an orientation distribution to explain the four lobe scattering in MD strained specimens. The FFTs capture the salient features present in the experimentally collected data. The degree of crystallinity in the simulated structures i.e. ratio of black to total area is 0.05.

resulting simulated scattering patterns capture the SAXS behavior at the different β angles and are shown in Figure 61. In reality, a single microstructure under observation at different β positions should necessarily explain the scattering. What is presented here instead are separate microstructures that. Therefore, the six two-dimensional images shown in the uppermost row of Figure 61 must be reconciled into a single three-dimensional structure which under investigation by β rotation shows the observed experimental behavior. While our model fails in this respect, the 2D simulation is extremely useful because it allows some visualization of real space structures that pertain to the observed scattering patterns. For instance, If we were to visually superimpose the six images over each other, the incremental change in the average orientation of the lamellar normal might be explained as a twisting of lamellae through the thickness of films. In order to test whether such a hypothesis is

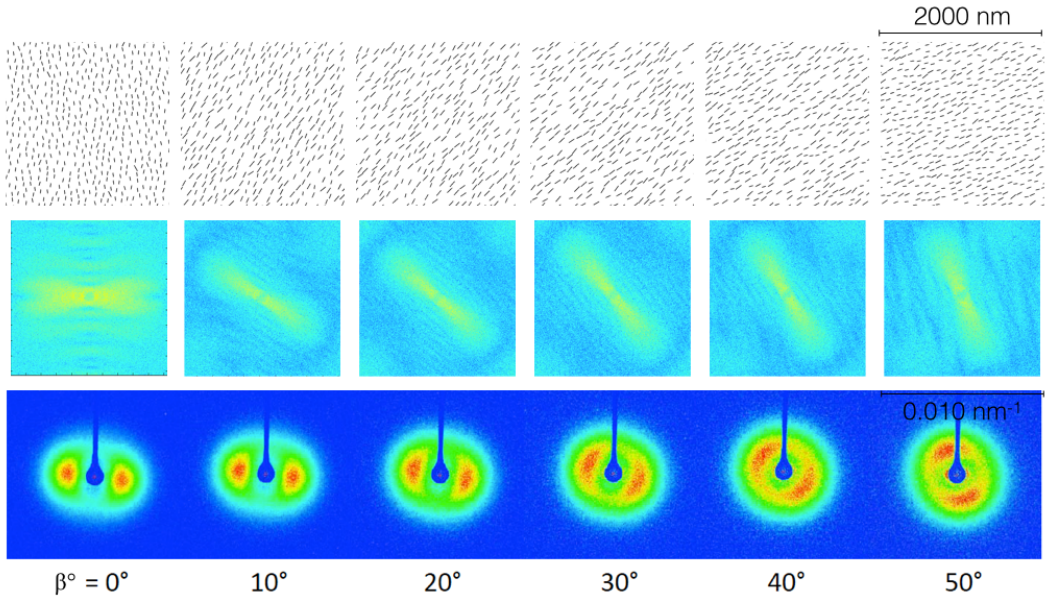

Figure 59: Polydisperse rectangular lamellae (filled black objects) are simulated within an amorphous matrix (unfilled white background) along with an orientation distribution. The mean orientation angle is increased systematically to capture trends of the β rotation. The FFTs capture the salient features present in the experimentally collected data. The degree of crystallinity in the simulated structures i.e. ratio of black to total area is 0.05.

correct, the simulation environment must capture information the thickness direction as well. In the following section modeling studies on 3D structural models and accompanying scattering simulations are discussed.

8.2.2 2D SAXS Simulation from a 3D Structure

While the 2D simulations are visually instructive, they do not provide an accurate representation of the lamellar morphology since structural information from the crucial third dimension, i.e. the thickness, is not accounted for in these studies. Modeling of 3D structures was therefore undertaken in Matlab followed by the 3D FFT of these structures in IgorPro. The simulation of scattering was made possible by the exploiting the 'Real Space

Modeling' package written by Steve Kline [127] and distributed freely on the National Institute of Standards and Technology (NIST) website. This package was originally intended for use by the neutron scattering community, but since the essence of small angle scattering phenomena remain the same between X-rays and neutrons it could be suitably modified with minimal effort. The advantage of this software package is the ability to provide an input model in the form of a 3D box and calculate the scattering patterns from the box at various user defined angles thus mirroring the β rotation experiments.

The assumptions from 2D structural modeling (see Section 8.2) are carried forward into models generated in 3D as well. In addition to the ellipsoidal and rectangular lamellae used in 2D models more complex architectures were simulated in 3D models. These include two types structures that resemble the shish kebab morphology. In the first type, kebabs were modeled as flat plates following Keller's high stress model. In the second type kebabs were modeled with regular periodic as well as aperiodic twists. Structural modeling was performed using computational geometry algorithms such as the poisson disc sampling algorithm [128]. Some examples of 3D structural models and their 2D FFT patterns i.e. simulated SAXS patterns are provided below.

The above Figures **??** to **??** show that the complex morphology of blown films can be constructed via modeling of 3D structures and subsequently the calculation of scattering patterns can be calculated. While absolute convergence between the experimental patterns and simulated patterns were not achieved here an important conclusion was made nonetheless. The order in which a simulation volume is filled with different sized lamellar populations is more important than the number of lamellae or their sizes and distributions. This finding is in line with the hypotheses that a large number of thin crystals which dominate the scattering are formed last during the crystallization process.

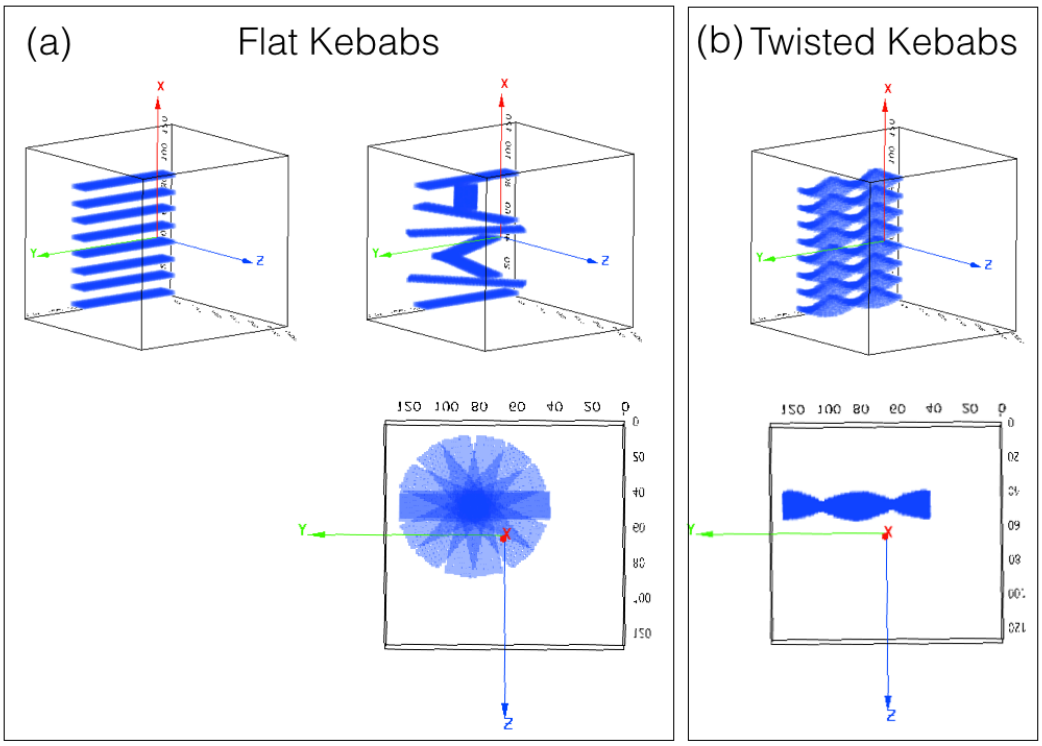

Figure 60: Monodisperse lamellar kebabs of two types are geometrically described in (a) showing flat sheet like kebabs either as perfectly stacked systems and as a stack with a 180° rotation along the X axis and (b) as a perfectly ordered system consisting of twisted kebabs

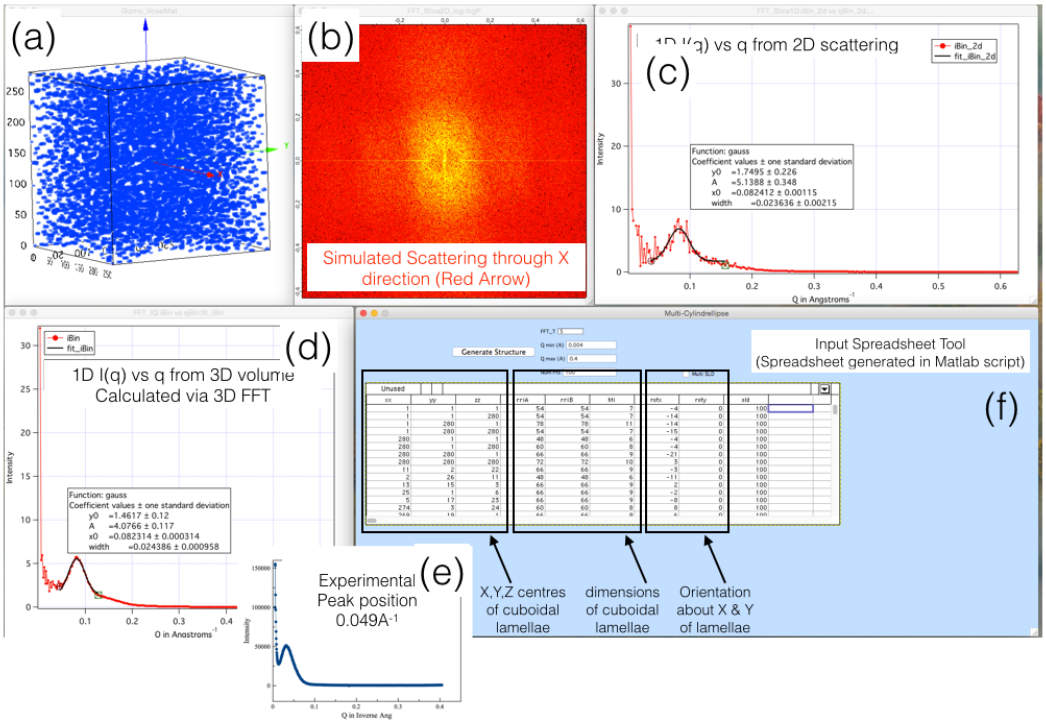

Figure 61: Figure(a) shows rectangular lamellae (filled blue objects) simulated within an amorphous matrix (unfilled white background) in a 3D box with a volume of $2500\mathring{A}^3$. The lamellae have an orientation, size and aspect ratio distribution. (b) SAXS pattern simulated from the 3D box in the direction of the red line in (a). Figure (c) shows the 1D scattering intensity $I(q)$ as a function of the scattering vector q calculated from the SAXS pattern in (b). Black line is a best fit Gaussian to the simulated data. Figure (d) shows $I(q)$ vs q calculated via a 3D FFT over the full volume in the modeling box. Figure (e) is an experimentally obtained $I(q)$ vs q plot which shows that the simulation captures the correct q position for the scattering maxima. Figure (f) shows the inputs required for modeling of the real space structure in (a)

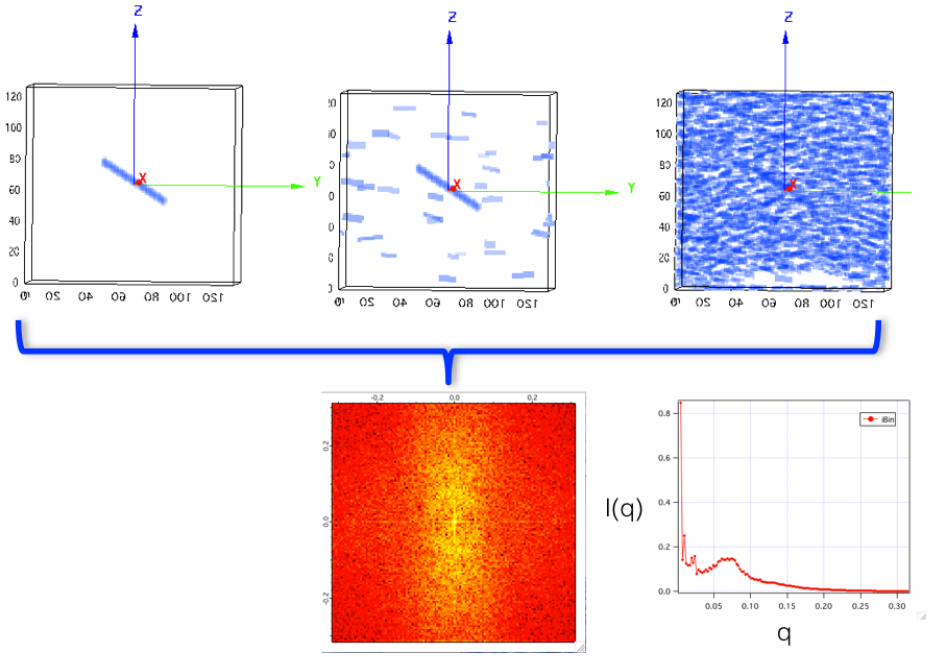

Figure 62: Three size distributions of lamellae are incorporated into the scattering volume. The largest lamellae are incorporated into the box first followed by progressively larger populations of smaller lamellae. The $I(q)$ vs q plot captures the correct scattering maxima position when compared with Figure 61e.

CHAPTER IX

STRUCTURE PROPERTY RELATIONSHIPS

9.1 Structural Features of Blown Film Morphology

9.1.1 Generalized Morphological Model in Blown Films

The LLDPEs investigated in the current work have a bimodal distribution of comonomer content i.e. short chain branching in PE chains (see Section 6.3.1). The first component of the polymer architecture is a high density fraction consisting of long relatively unbranched chains. The second component is a low density fraction comprised of more highly branched chains.

When a melt of such LLDPEs experience shear flow, such as in the process of film blowing, the high density component elongates preferentially as it undergoes a coil-stretch transition [49]. The low density component does not undergo this transition due to the combination of its lower molecular weight and presence of branching. Consequently when the melt cools under extensional flow, the high density elongated component is expected to crystallize first. The collapse of these chains from their elongated state might however be restricted due to the presence of the coiled chains in the immediate vicinity. As the temperature of the melt falls, co-crystallization can occur wherein the low molecular weight and branched chains also begin to crystallize. Oriented crystallization can therefore take place such that, the high density component serves as a template on which the low density component can crystallize to form lamellae in the form of kebabs emerging from a shish core [54]. An outcome of any crystallization processes in LLDPEs is the formation of tie chains that connect crystalline lamellae. The presence of butyl SCBs in chains of high molecular weight contributes towards an enhanced tie chain formation. Specifically, unbranched segments of high molecular weight chains can crystallize while the SCBs cannot. This creates a scenario where unbranched portions of chains crystallize into multiple lamellae that are connected by sections of chains with branches leading to an enhanced formation of tie chains.

Crystallization is fast when the melt is pulled rapidly in order to produce thin blown films due to the effect of higher undercooling. Crystallization is slower when the end product of film blowing is a thick film. Consequently, the lower rate of cooling during the blowing of thick films can also cause annealing effects. The WAXS data confirm this since the thickest films i.e. 75 μm are also the most crystalline, exhibiting a systematic rise in X_c by approximately 8% over the 20 μm films. The crystalline unit cell of the LLDPEs in the as made films is the stable orthorhombic crystal. These typically orient such that their a and b axes are loosely aligned along the MD and TD respectively. Lamellae are comprised of these orthorhombic unit cells and as a result of the oriented crystallization process are preferentially stacked normal to the MD-ND plane. A schematic of the this generic structure of the crystalline and non crystalline morphology is shown in Figure 63. With applied MD or TD strain, the a and c axes rotate around the b axis. Simultaneously, the lamellar size is reduced and the alignment of amorphous domains along the strain direction is initiated. These changes along with others are shown in Figure 64

9.1.2 LLDPE$_3$

The fractional content of the high density component is the highest in LLDPE$_3$ at 16% of chains (obtained from the fractional area under population A from Figure

9.1.3 LLDPE$_2$

LLDPE$_2$ is similar in its molecular architecture to LLDPE$_3$ except for a lower fractional content of high density component at 5% of the chains and higher branch content in the low density component. The effect of these changes is explained by the SAXS and WAXS data as follows. The values of LAR, F_{lam} and F_a particularly for the thin films of LLDPE$_2$ suggest that high levels of orientation can be imparted to LLDPE$_2$ films. The low density component of LLDPE$_2$ has a greater branch content than the corresponding LLDPE$_3$ polymer. The crystallizable ethylene sequence length for LLDPE$_2$ are therefore shorter and the corresponding L_{SAXS} values for LLDPE$_2$ films are less than those from LLDPE$_3$. Shorter average ethylene sequence lengths are also responsible for the lowering of d_a values.

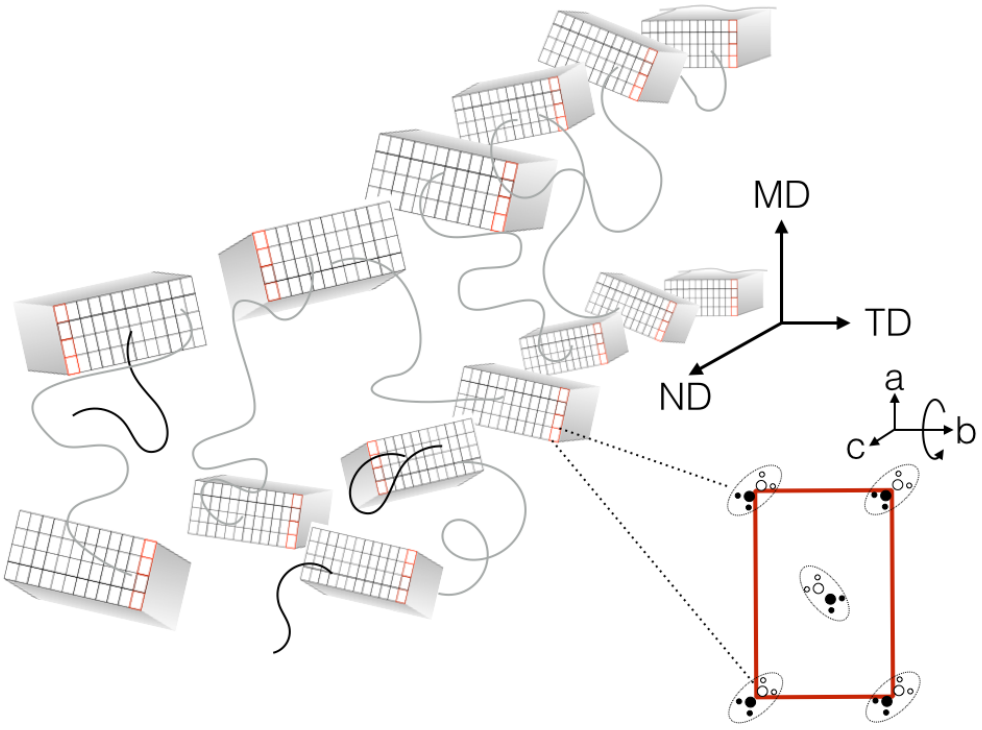

Figure 63: The representative morphology of blown films in their as made condition. The Figure illustrates the distributions of lamellar and unit cell orientations with respect to the film orientation directions MD, TD and ND. The inset shows a typical $a-b$ plane of the orthorhombic unit cell. The c axis is perpendicular to the plane of the paper and to the $a-b$ plane. Solid black lines represent loops and cilia. Grey lines represent connective tie chains.

9.1.4 LLDPE$_1$

The architecture of LLDPE$_1$ is different from LLDPE$_2$ and LLDPE$_3$. As the bivariate distribution suggests, the high density component of LLDPE$_1$ (about 3% of chains) consists of high molecular weight chains along with substantial SCB incorporation. A significant outcome of incorporating this branching in the high density component is the inability of the chains elongate in the melt. Consequently, the probability of having a template consisting of elongated shish-like nucleation sites (such as in LLDPE$_3$ or LLDPE$_3$) on which highly oriented crystallization proceeds is lowered. Without such a template structure, crystallization from the melt fails to impart significant orientation in thick films and more importantly, even the thin films. This is evident from substantially lower values of LAR,

F_{lam} and F_a for $LLDPE_1$ in comparison with $LLDPE_2$ and $LLDPE_3$. The low density component of $LLDPE_1$ is also highly branched and incorporates more branching than the low density component of $LLDPE_2$ and $LLDPE_3$. Correspondingly the ethylene sequence lengths are much lower and these are reflected in the values of both L_{SAXS} and d_a.

9.2 Blown Film Morphology Evolution Under Strain

Application of tensile strain on blown films along the MD or the TD of films causes the original morphology of films to evolve. The pathway of morphology evolution itself is dependent on the direction in which the strain is applied producing different features under MD and TD strain. The significant feature in TD deformation is the complete disruption of the original blown film morphology followed by the growth of a new lamellar superstructure plausibly due to strain induced crystallization. This new structure is persistent in its dimensionality over a large strain range of nearly 200% strain and is continuously being formed from the remnants of the original superstructure arranged into a new highly stable morphology. In order to create a generic morphological model for uniaxial tensile deformation for blown films, some of the significant features reported in Chapters 5, 6 and 7 need to be viewed collectively. Composite plots representing the collection of significant events that take place during the application of tensile strain are shown in Figure 65 to 66.

9.2.1 $LLDPE_1$

Figure 65 shows the salient features of tensile deformation observed in specimens of $LLDPE_1$ in this case by the 20μm thick films with a 2.5 BUR.

In the small strain region before the first yield point, the increase of d_{ac} from 124Å to 132Å is accompanied by a rise of the value of F_{am} from 0 to 0.1. The corresponding rise in the value of F_{am} confirms that the 8Å increase in d_a as well as d_{ac} occurs preferentially within the amorphous domains causing a partial ordering of amorphous chains. However, the c axis of the crystalline unit cells shows a slight change in its orientation, i.e. F_c becomes more positive suggesting that even within the regime of affine deformation some lamellae undergo orientational changes. The structure of the lamellae themselves is unaffected since

both L_{SAXS} and χ i.e. the tilt angle remain fixed in value. The change in the c axis orientation most probably results from the displacement and reorientation of loosely connected lamellae into the strain direction. Although only partial alignment of inter lamellar amorphous chains is achieved, the limit of strain that can be accommodated by the morphology without any loss in crystallinity is reached at the first yield point, i.e. at $\varepsilon_{0.1}$.

Beyond the first yield point, at $\varepsilon_{0.3}$, the value of χ, i.e. the tilt angle, increases abruptly from 0° to 20° and simultaneously the value of L_{SAXS} begins to decrease from an initial value of 112Å . This suggests that the stability of lamellae has been compromised and fragmentation is initiated. Correspondingly, the value of total crystallinity begins to decrease at the first yield point from approximately 40% in the as made condition. The value of d_{ac} continues to rise up to 142 Å suggesting that the average spacing between the fragmenting lamellae is still increasing. Increments in strain improve the ordering of amorphous chains increasing the value of F_{am} from 0.1 at the first yield to 0.3 at $\varepsilon_{0.3}$. Simultaneously the c axis continues to rotate towards the strain direction.

Further strain up to the second yield point causes the amorphous chains to continue to orient into the strain direction with F_{am} increasing up to 0.5. Simultaneously, the c axis of the crystalline unit cells continues to rotate towards the strain direction with F_c reaching a value of 0.4 at the second yield point. This suggests that at the second yield point the amorphous chains are more oriented towards the strain than the crystalline unit cells. Continual fragmentation occurs such that the value of L_{SAXS} drops to 85Å at the second yield point. Since the tilt angle at the second yield point has a value of 60° it can be inferred that lamellae are tilted with respect to each other subtending an obtuse angle of 120° (or 60°) on average. The characteristic dimension d_{ac} increases to a maximum of 147Å . Monoclinic crystals have begun to form beyond the first yield point. However the orthorhombic to monoclinic ratio is nearly indeterminate at low strains since the fractional content of monoclinic crystals is still less than 1%. The monoclinic content increases beyond the first yield point and is clearly captured at closer to the second yield point. The presence of monoclinic content signifies that taut tie chains (which need not necessarily be fully extended) have begun to form regions of localized stress concentration

on the surfaces of stable lamellae of which the tie chain is a part of, and which may or may not have fragmented. The total crystallinity has dropped marginally at this point to 37%. Beyond the second yield point the value of F_{am} shows a small drop along with the reducing crystallinity. The combination of these observations suggest that disordered amorphous domains are formed from the continued fragmentation of lamellae.

Beyond the second yield point, typically around strains values of 0.6, F_{am} begins to increase. This suggests that the amorphous chains are constantly under tension beyond the second yield point. These stretched amorphous chains of which some are fully extended, cannot be drawn further and hence cause previously stable lamellae to start fragmenting. Tie chains formed due to SCBs play an important role here. Specifically, branch points in extended tie chains lock at the lamellar surface. Further application of strain (and stress) creates zones of local stress concentration on the lamellar surface which finally causes lamellae to fragment at defects points, i.e. branch point locations. These fragments rotate quickly into the strain direction which is evident from the increase in the F_c values beyond the second yield point. Since the stress on lamellae has been released by the fragmentation process, monoclinic crystals which are stable only under sustained load revert back to their orthorhombic form which is observed as the drop in the orthorhombic to monoclinic ratio. As the fragmentation continues greater numbers of smaller lamellae are constantly formed. As a result, the average measured values of L_{SAXS} reduces as does the value of d_{ac} since presence of a number of fragmented lamellae causes average interlamellar distances to fall. Crystallinity at the same time does not seem to fall appreciably suggesting that the total crystallinity in the morphology remains nearly the same.

Beyond $\varepsilon_{1.6}$ the value of L_{SAXS} reaches its minimum and stays constant at 54Å for the duration of additional strain. The d_{ac} is nearly constant as well at 126Å over a strain range of 20%. The lamellar structure that contributes to the scattering in this strain range grows from the continuously strained system. Interestingly the F_c value never supersedes the value of F_{am} suggesting that the molecular axis within the crystals is not perfectly aligned along the strain but is held at some intermediate angle. This remarkable tendency of the film to form a single stable morphology across the entire specimen over a large strain range

suggests that some inherent molecular level factor is dictating the dimension of the average lamella-amorphous repeat structure. It is shown that this highly stable feature is related to the architecture of $LLDPE_1$ in particular to the low density component which makes up nearly all of the polymer. It is indeed the shortest to average lengths of crystallizable ethylene that are responsible for this highly persistent structure.

9.2.2 $LLDPE_2$ and $LLDPE_3$

$LLDPE_2$ and $LLDPE_3$ show many of the same features as $LLDPE_1$ under strain as shown in Figures 66 and 67 respectively. The significant differences in the morphological evolution under strain are as follows. Due to the longer average crystallizable length of ethylene in this polymer, the as made value of d_{ac} in $LLDPE_2$ and $LLDPE_3$ is larger than $LLDPE_1$ at 137Å and 145Å , respectively. The corresponding L_{SAXS} in the as made film is also higher than films of $LLDPE_1$ at 160Å and 180Å , respectively. Values of crystallinity for the $LLDPE_2$ and $LLDPE_3$ films are systematically higher than for $LLDPE_1$ as well. Application of strain produces similar effects as described in Section 9.2.1. The most noticeable feature in the stress-strain plots is the systematic increase in yield stress. This increase is expected as these polymers have on average larger lamellar thickness than $LLDPE_1$. The decrease in L_{SAXS} between the application of strain and the onset of the persistent structure for $LLDPE_2$ and $LLDPE_3$ is 90Å and 120Å , respectively. These values decrease rapidly prior to the onset of the persistent morphology evolution which itself is the same for the three polymers at $\varepsilon_{1.6}$. This phenomenon suggests that a critical strain point exists beyond which the original lamellar superstructure is not stable. It is proposed that a semicrystalline morphology dictated by and reflective of purely the architecture of an LLDPE alone exists. Such a morphology is therefore inherent to each LLDPE and can be accessed by the application of TD strain beyond the second yield point in the stress-strain plot for blown films.

9.3 Structure Property Relationships

In Section 2.1.2 the tear and puncture properties of a blown films were the reported as the typical standards in the identification of blown film performance. In this section the relationships between tear and puncture and the various variables extracted from the SAXS

and WAXS are investigated. The tear and puncture data for the films investigated in this work were provided by EMCC. The values are reported in Table 8. Also, the two processing parameters i.e. BUR and film thickness are combined into a single parameter known as the MD Draw Ratio. The values for MD Draw Ratio were provided by EMCC and are reported in Table 9. The MD Draw ratio is relates the film thickness and BUR and depends on the temperature of the melt as well as the die gap during extrusion. In the case of these films, the melt temperature and the die gap were the same.

Table 8: Tear and Dart Drop values provided by EMCC on blown films of the three LLDPE resins. All values are measured in gms/μm.

Resin	Film Label	Dart Drop	Elmendorf TD	Elmendorf MD
$LLDPE_1$	$LLDPE_1$.1a	24.80	13.69	6.34
	$LLDPE_1$.1b	42.99	11.59	7.86
	$LLDPE_1$.1c	54.33	11.97	9.84
	$LLDPE_1$.2a	26.69	12.61	5.77
	$LLDPE_1$.2b	54.33	11.32	8.36
	$LLDPE_1$.2c	54.33	12.18	10.45
$LLDPE_2$	$LLDPE_2$.1a	17.80	15.94	8.19
	$LLDPE_2$.1b	27.24	14.17	10.12
	$LLDPE_2$.1c	no break	13.54	11.57
	$LLDPE_2$.2a	26.65	14.33	8.39
	$LLDPE_2$.2b	31.08	13.78	9.49
	$LLDPE_2$.2c	no break	13.39	11.77
$LLDPE_3$	$LLDPE_2$.1a	5.31	20.76	9.63
	$LLDPE_3$.1b	9.33	18.17	11.09
	$LLDPE_3$.1c	25.28	16.16	11.15
	$LLDPE_3$.2a	6.85	17.09	10.04
	$LLDPE_3$.2b	11.57	16.38	9.61
	$LLDPE_3$.2c	31.18	15.31	12.83

Table 9: MD Draw Ratio for any of the programmatic films

Resin	Film Label	BUR	Thickness(μm)	MD Draw Ratio
$LLDPE_i$	$LLDPE_i$.1a	2.5	20	32
	$LLDPE_i$.1b	2.5	30	20
	$LLDPE_i$.1c	2.5	75	8
	$LLDPE_i$.2a	3.0	20	27
	$LLDPE_i$.2b	3.0	30	17
	$LLDPE_i$.2c	3.0	75	7

Specifically, Elemendorf Tear test values along MD and TD as well as dart drop values are examined for the films of the three resins. The mechanical failure of a film is understood from the perspective of two length scales at different stages of uniaxial deformation. Since the film performance is dictated by the semicrystalline morphologies encountered during the duration of tear and dart tests, any correlation between the morphology and performance must in principle account for the evolving morphology. It is a reasonable assumption that some combination of states observed during the pathway of morphology evolution during controlled uniaxial studies, are encountered during the standard tests for mechanical performance of blown films. Tear and puncture properties of films are therefore expected to depend on the initial morphology, the final morphology at the end of uniaxial strain and the pathway connecting the two. However since the trends observed in the morphology changes between initial and final morphology in all films are rather similar, for the three polymers it is proposed that the initial state of films provides a stronger case for an investigation of correlations between morphology and film performance.

In order to determine the structure-property relationships between the the mechanical properties viz. Tear (TD and MD Elmendorf) and Puncture (Dart Drop) the following method is employed. First, a master spreadsheet of all the variables extracted from SAXS and WAXS is constructed. The SAXS and WAXS variables are classified into two categories - dimension and orientation. The exhaustive list of dimensional variables is L_{SAXS}, d_{ac}, d_c, d_a and X_c. The exhaustive list of orientational variables is LAR, F_{lam} and the F_a, F_b, F_c values relative to MD and TD both. The full list of these values are tabulated in Tables 5 and 7. Second, linear models are constructed between the dimensional and orientational variables and each of the three mechanical datasets in an exhaustive manner. Third, non-contributing variables are systematically eliminated from the linear model in order to determine the structure-property relationships which depend on the least number of parameters. The approach in step 3 is made possible through the use of the statistical software R, specifically using the library MASS. Within this library the function stepAIC [129] is utilized to systematically examine the contribution of each dimensional and orientational variable to the constructed linear model. The goal of the stepAIC algorithm is to minimize

the value of the metric 'AIC'. The AIC value itself depends on two factors - the number of variables in the linear model and the relative contribution of each of those variables to the constructed linear model. The algorithm inherently penalizes every added variable in the linear model by raising the AIC value. It also raises the AIC values for variables whose contributions to the model are low relative to other variables. In this way the stepAIC algorithm identifies the minimum number of dimension and orientation variables using which, values of tear and dart can be accurately predicted. The prediction accuracy is reported as an R^2 value.

9.4 Structure - Property Correlations

The following quantitative relationships are obtained that predict tear and puncture properties in units of gms/μm.

$$TD = 3.5263 + 0.1351 L_{SAXS} - 6.2592 F_b^{TD} - 0.1676 d_c \tag{48}$$

$$\begin{aligned} MD = -1.5594 + 0.13882(\%X_c) + 0.0531 d_{ac} \\ - 0.14547(MD\ Draw\ Ratio) - 18.93206 F_b^{MD} + 11.9279 F_c^{TD} \end{aligned} \tag{49}$$

$$Dart = 192.704 - 1.577 d_a - 1.025(MD\ Draw\ Ratio) \tag{50}$$

The relative importance of each of these parameters towards the regressed data are highlighted in Figures 68 to 72. The data suggests that TD tear is dependent on dimensional and orientational parameters both. Specifically it is 60% dependent on L_{SAXS}, 20% on d_c and 10% on F_b (TD). These dependencies can be explained as follows. The ease of rotating any object in any given medium is directly related to the size of the object and how far it has to rotate. By extension therefore there is likely to be a relationship between the dimension and orientation of lamellae and the tear properties. The data suggests that dimensionally L_{SAXS} and d_c are relevant while F_b (TD) is relevant from an orientational standpoint. The

relationship predominantly suggests that increasing the value of L_{SAXS} will increase the TD tear strength.

The correlation patterns suggest that TD tear properties can be manipulated by influencing the average size and orientation of their lamellae. In the case of $LLDPE_2$ and $LLDPE_3$ the incorporation of comonomer in the high density component for both these polymers is below 2.5% and in the low density component is less than 6% and less than 7% respectively. In comparison, $LLDPE_1$ incorporates up to 9% comonomer content into both the high molecular weight and low molecular weight components. Increased comonomer addition systematically reduces the probability of finding wide lamellae as branches are more frequently encountered by the nucleating lamellae and lamellar growth fronts. Therefore, reducing the comonomer content incorporated in the low density component should increase the average lateral size of lamellae. Consequently films made from such polymers should also exhibit improved TD tear behavior.

In addition to the correlations studied by the stepAIC methodology, we also investigated the possibility of single parameter correlations between TD Tear and some dimensional and orientational variables. In addition to L_{SAXS} and F_{lam} a third parameter called 'orientability' and defined as F_a (MD) - F_a (TD) by Chum *et al* [17] were used in single parameter correlation estimations. The entire dataset is shown in Figure 69. The data shown in this figure qualitatively supports the quantitative relationships from Equation 48. These data suggest that TD tear is indeed dependent on both orientation and dimensional factors.

The relative importance of the regressor variables for predicting MD tear strength is shown in Figure 70. The MD tear predictions are more complicated to interpret than for TD due to the nearly similar weighted dependencies (between 25 and 30% of the variance) for $\%X_c$, d_{ac} and the MD draw ratio. The quantitative relationship in Equation 49 suggest that increasing the $\%X_c$ and the d_{ac} would work towards improving the MD tear strength. In order to achieve this experimentally, the average branch content in any polymer will have to be reduced from the current. Interestingly, L_{SAXS} is not captured by the AIC algorithm as relevant to MD tear suggesting a physical mechanism of MD tear which does not depend on the average size of lamellae but only on the number density of lamellae (provided lamellar

size remains the same) and the average spacing between lamellae. A comparison of MD and TD tear values as a function of MD draw ratio (see Figure 71) interestingly showed a clear orientational dependence as well. At low MD draw ratio, i.e. lowest anisotropy in films, MD and TD tear values were similar while at high MD draw ratios i.e. highest anisotropy in films, the MD-TD tear imbalance was pronounced. Clearly, by manipulating the extent of anisotropy in the films specifically with regards to F_{lam} (see Figure **??**) films with different MD-TD tear balance might be produced. Presumably, less ordered lamellae will create a more tortuous tear path preventing preferred direction tear from taking place. Interestingly, the least oriented films i.e. where F_{lam} is less than 0.10 show on average lower values of L_{SAXS} suggesting that lamellar width and orientation are inversely related. Conversely large values of L_{SAXS} such as for 20μm films are accompanied by relatively high values of LAR and F_{lam}. This suggests that films with less lamellar ordering also have less wide lamellae and ultimately exhibit a better balance for MD-TD tear.

Since L_{SAXS} pertains to the size of lamellae it is plausible that the orientation of lamellae with respect to either the MD or TD could also relate with the TD Elmendorf tear. Correspondingly, Figure 69 describes the relationship between Elmendorf tear and F_{lam} i.e. the Herman's orientation parameter of the lamellae with respect to the MD. A better correlation is produced when the data are examined in the context of F_{lam}. Once again, films of $LLDPE_2$ and $LLDPE_3$ exhibit a variety of orientations thereby suggesting that different processing conditions are able to impart a range of orientation values in these two resins. Films of $LLDPE_1$ however for the same processing conditions are unable to orient to the same extent as films of $LLDPE_2$ and $LLDPE_3$ at the same processing conditions. Correspondingly, the TD Elmendorf tear follows the trend suggesting that better orientation of the lamellae about the MD improves the TD tear.

The effect of WAXS derived orientation parameters of a film on its tear properties have been investigated by Register *et al.* [10] and Chum *et al.* [17] by observing the orientation of the a, b and c unit cell axes. Our findings agree with them to a certain extent especially where dependence of MD and TD tear on orientation is concerned. However, the disagreement between the work by these authors and the current work stems primarily due to the

lack of multiple regression parameters in the cited work. The authors regress mechanical properties using specific variables (in this case F_a (MD) - F_a) only. Although our work also suggests that this 'orientability' parameter is likely to be important, it is definitely not the only important parameter as suggested by Chum *et al.* [17].

Figure 72 shows the fit between the predicted and measured values of dart drop. Equation 50 suggests that the puncture properties, i.e. dart drop values, can be predicted using purely the MD Draw ratio and d_a as the regression variables. The relative importance of these variables is 33% and 55% respectively. The MD Draw ratio provides a measure of how oriented a film is while d_a is a dimensional parameter describing the average amorphous domain size. The relationship itself suggests that reducing the values of d_a and MD Draw ratio are likely to provide films with the best puncture resistance. Indeed the values of dart drop are the highest for the films with the least anisotropy i.e. low MD Draw Ratio.

The dart drop test is an example of multi-axial deformation wherein the response of the film to a non-uniform stress field is tested. The dependence on d_a is likely to also be related to the response rate of chains within amorphous domains. The rate at which amorphous chains can entangle and disentangle is likely to influence how a film deforms in such an environment. While the relationship determined in Equation 50 was shown to be a good predictor, certain additional statements about the dart drop results and their relationship to the molecular architecture can be made. Firstly, films with a higher crystallinity are stiffer and generally show poor dart stability. This suggests that improving the puncture resistance in a polymer is possible by reducing its inherent crystallinity by adding more branching and lowering the density. From the high values of puncture resistance for the $LLDPE_1$ films, it is inferred that smaller lamellae and possibly a more isotropic arrangement of lamellae might hold the key to improving the response in films to dart drop. These can be achieved in $LLDPE_2$ and $LLDPE_3$ by replacing the high density component of the polymer with more branched lower density material. This replacement should prevent the growth of large and ordered lamellae by reducing the elongation of the high molecular weight chains in the melt.

Similar results might also be accomplished by converting low density LLDPEs into films

of intermediate thickness at large blow up ratios. The presence of tie chains greatly improves the mechanical properties of a system by improving the tendency of a film to undergo ductile failure. The presence of a greater number of tie chains connecting lamellae might result in a better response to complex loading such as in a dart drop test by increasing the number of local ductile deformation events taking place in the film. The number of tie chains can be increased by utilizing higher molecular weight chains in the high density component of the bivariate distribution. Lastly, the rate of mechanical response in the amorphous chains might play a role in how a film undergoes multi-axial deformation prior to failure in a dart drop test. For instance, if the chains present in the entangled amorphous domains can respond to loading quickly then the energy from the impact of the dart might be preferentially dissipated by the disentanglement of these chains. Consequently, ductile deformation can proceed throughout the film preventing a crack from forming and propagating through the film. The rate of amorphous response can be probed by WAXS by observing the rate at which the amorphous orientation changes in response to a increasing deformation rates. In the experiments performed in the current work, the rate of deformation was fixed due to the limited rate at which SAXS/WAXS data could be collected. With improved detector capabilities, the above set of measurements might be undertaken to target preferentially the response of the amorphous chains

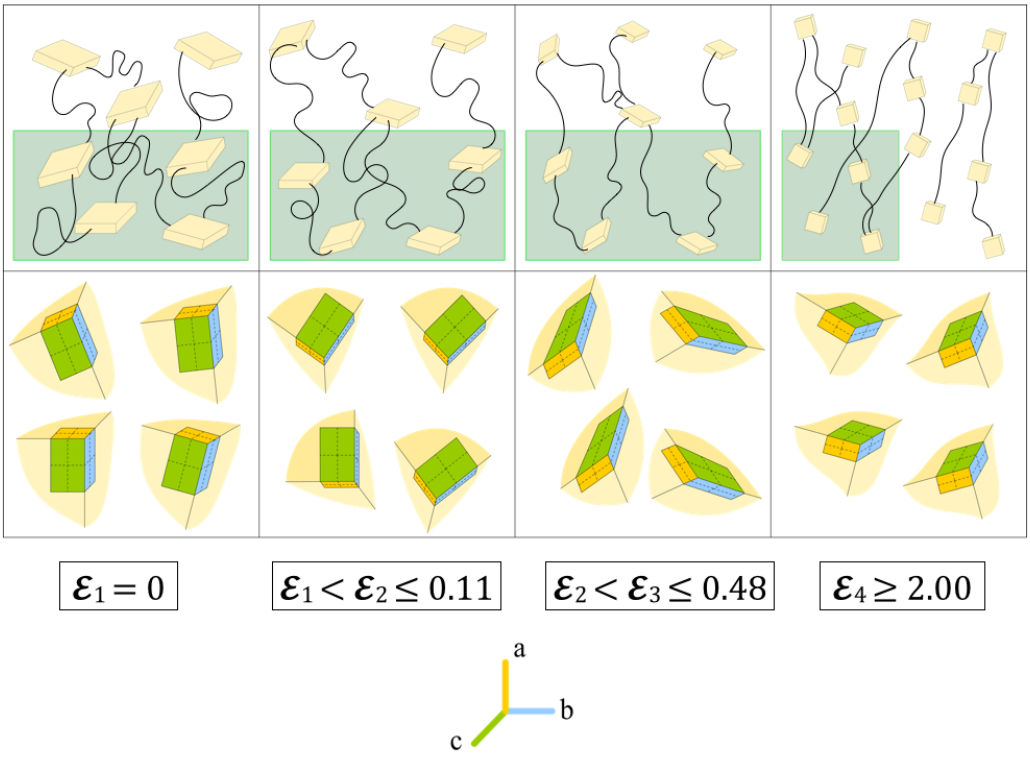

Figure 64: The generic morphology of MD deformation in blown films under four strain regions - zero strain, between zero strain and the first yield, between the first and second yield and at strains much greater than the second yield are shown. The upper rows highlight the behavior that is captured by SAXS data while the lower row shows the behavior captured in the WAXS data. The orientation of the unit cells in lamellae present within the light green boxes in the upper row are shown by the tricolor boxes in the bottom row. In the tricolor boxes, the green face is perpendicular to the c axis, yellow to the a axis and b to the blue axis. Between the first and second yield point, only monoclinic unit cells are shown to signify the orthorhombic to monoclinic transformation. The changes to d_a, L_{SAXS}, F_a, F_b, F_c and F_{am} under are implicitly captured in the deformation model. In the plane of the paper, MD is vertical while TD is horizontal. The ND is perpendicular to the plane of the paper

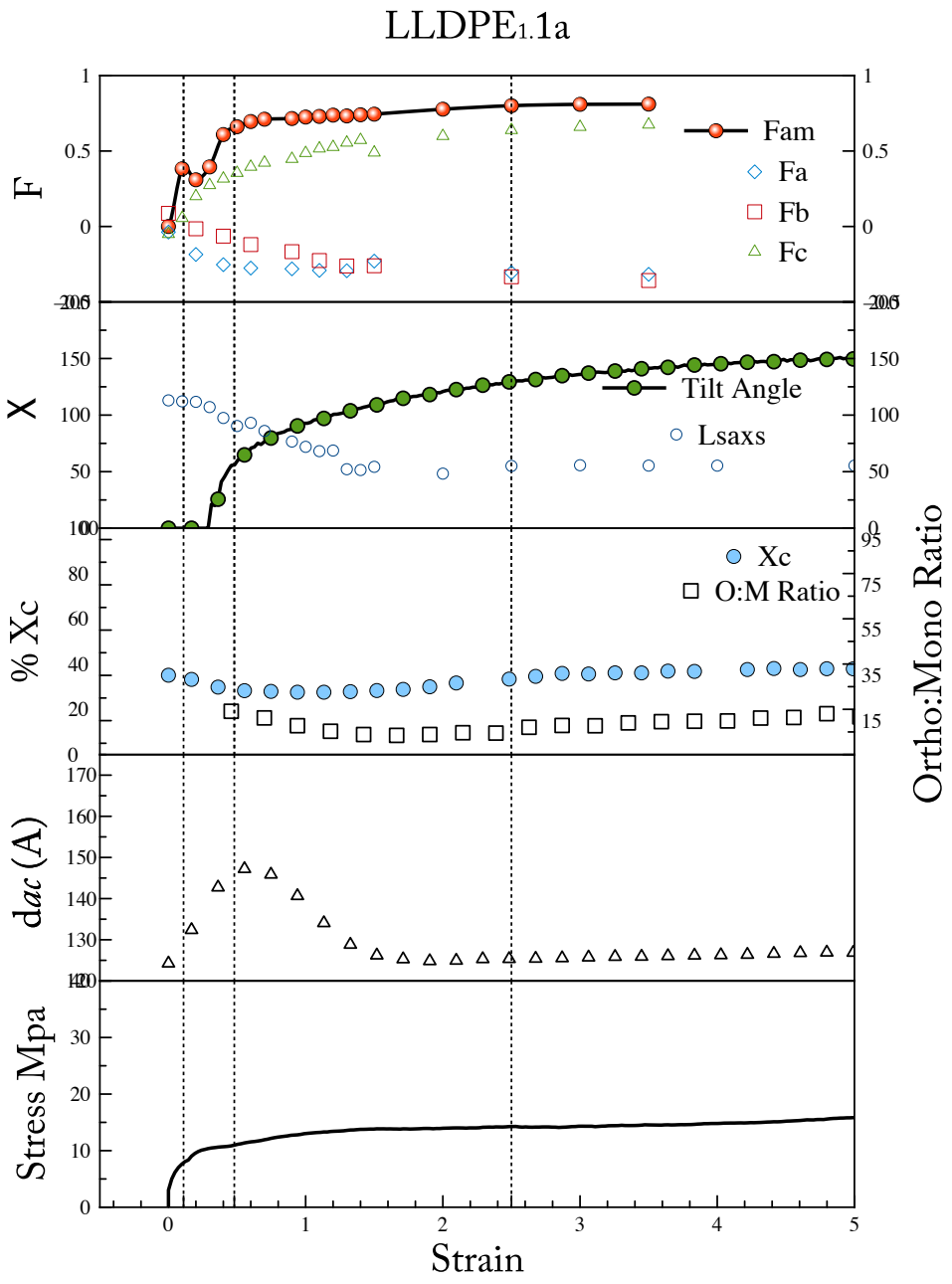

Figure 65: SAXS/WAXS analysis of LLDPE$_1$.1a under uniaxial tensile deformation showing the change in the various extracted parameters. All the data shown on this plot is for TD strain with the exception of L_{SAXS} and χ variations. These data are for an MD strained sample of LLDPE$_3$.1a

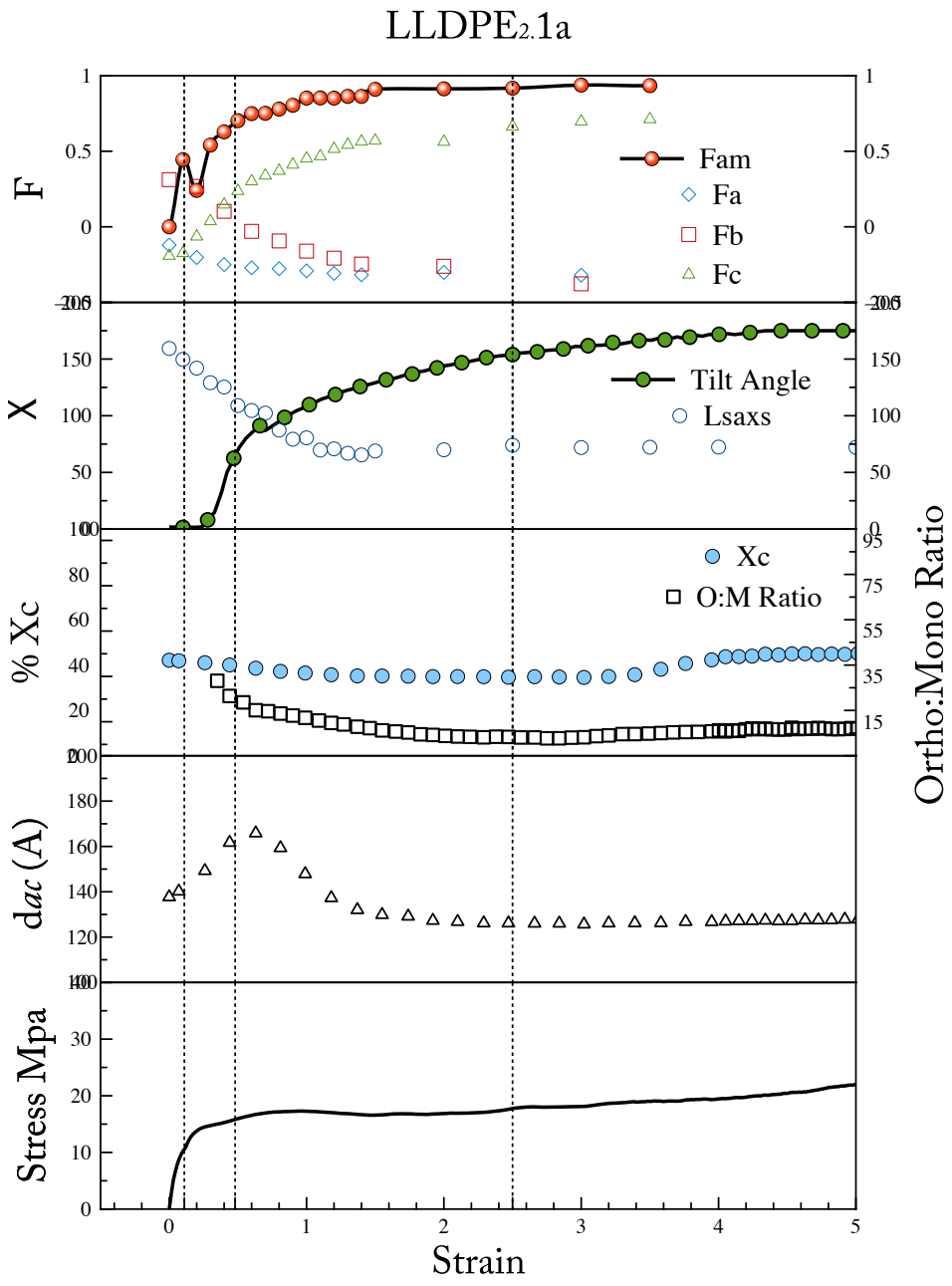

Figure 66: SAXS/WAXS analysis of LLDPE$_2$.1a under uniaxial tensile deformation showing the change in the various extracted parameters. All the data shown on this plot is for TD strain with the exception of L_{SAXS} and χ variations. These data are for an MD strained sample of LLDPE$_3$.1a

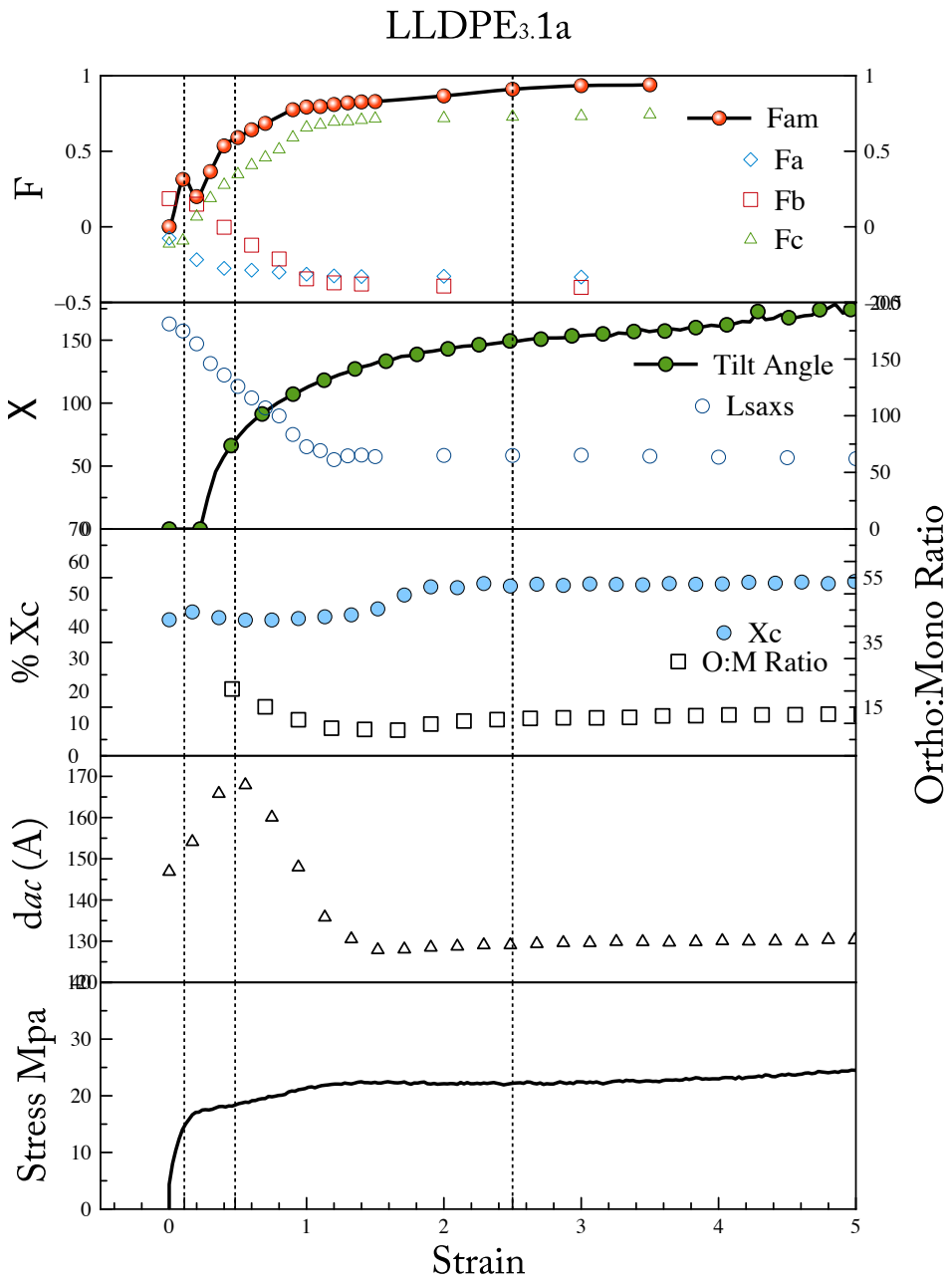

Figure 67: SAXS/WAXS analysis of LLDPE$_3$.1a under uniaxial tensile deformation showing the change in the various extracted parameters. All the data shown on this plot is for TD strain with the exception of L_{SAXS} and χ variations. These data are for an MD strained sample of LLDPE$_3$.1a

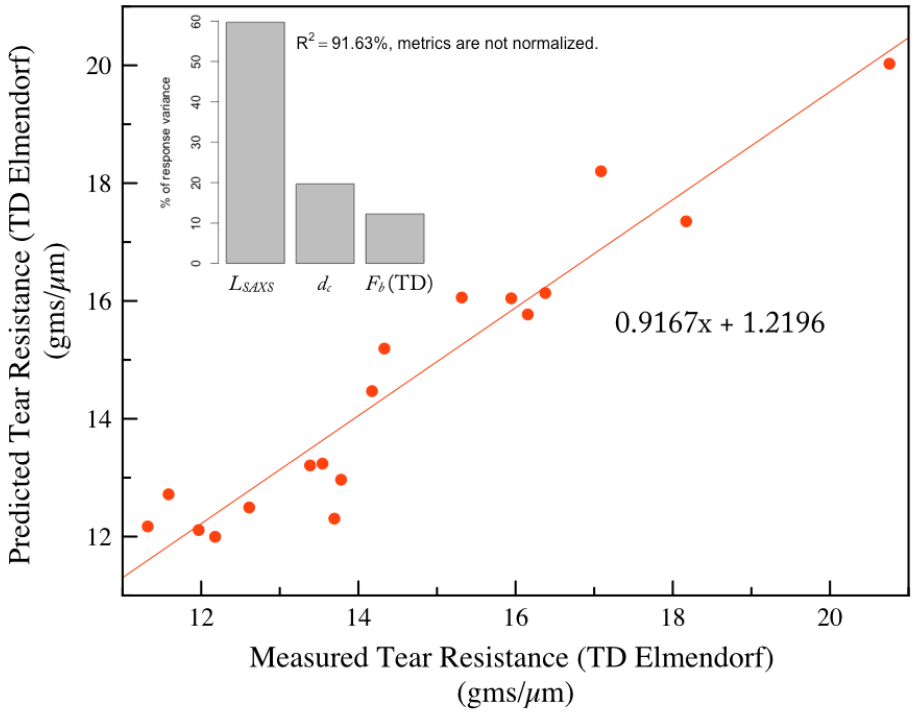

Figure 68: TD Elmendorf tear is predicted using Equation 48. The fit between the predicted and measured values is represented by the solid line. The inset plot shows the relative contribution of each of the predictor variables towards the best fit.

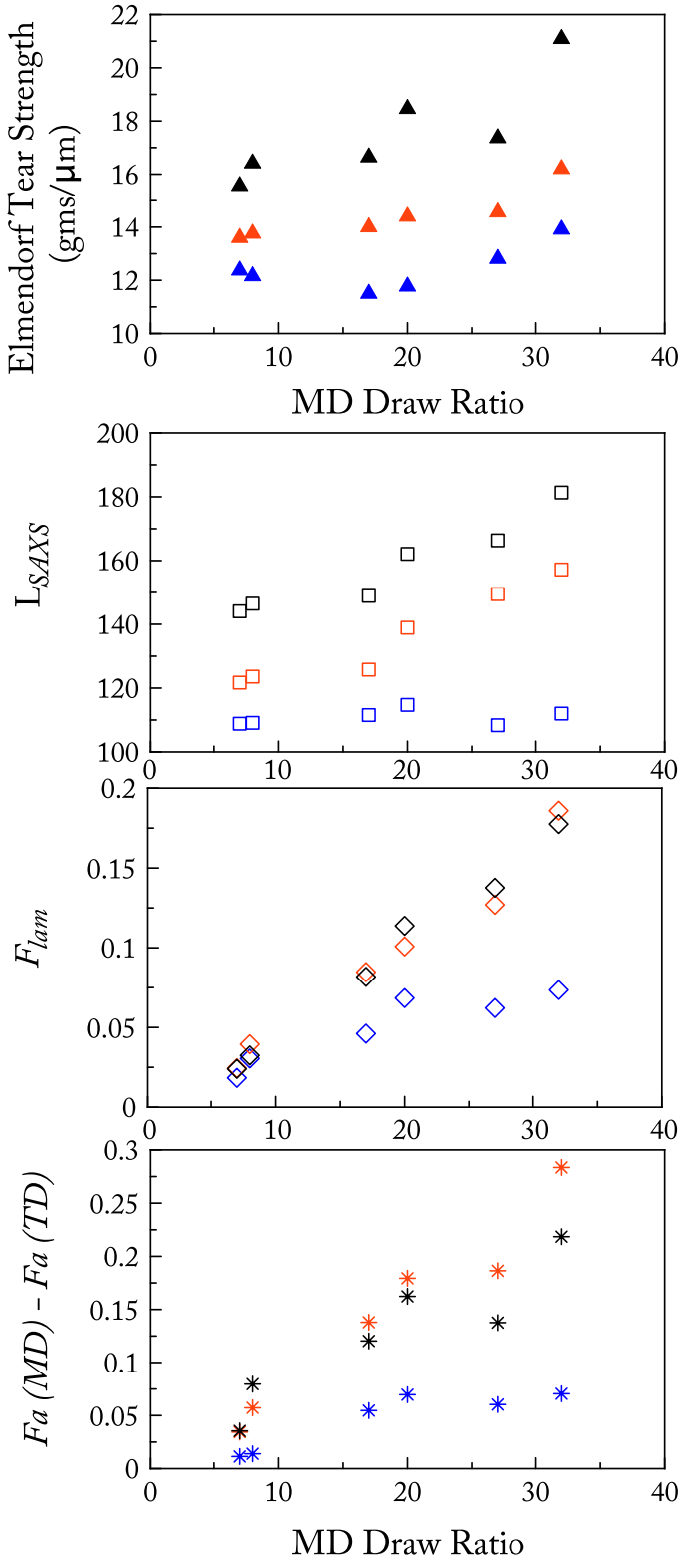

Figure 69: Single Parameter correlation estimation for Elmendorf Tear along TD. Blue, orange and black markers represent $LLDPE_1$, $LLDPE_2$ and $LLDPE_3$ respectively.

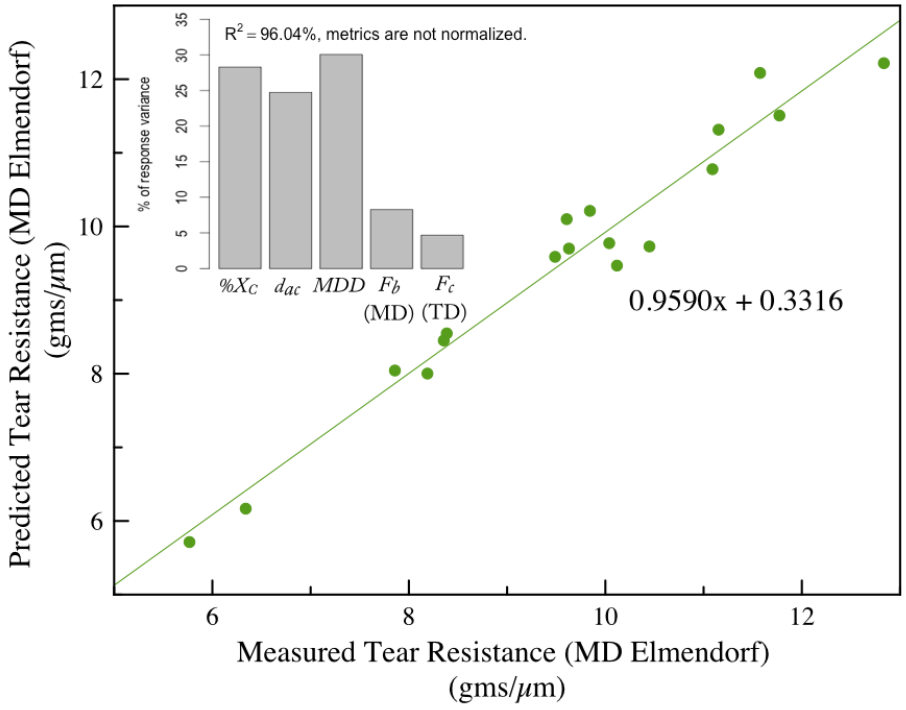

Figure 70: MD Elmendorf tear is predicted using Equation 49. The fit between the predicted and measured values is represented by the solid line. The inset plot shows the relative contribution of each of the predictor variables towards the best fit. MD draw ratio is abbreviated to MDD

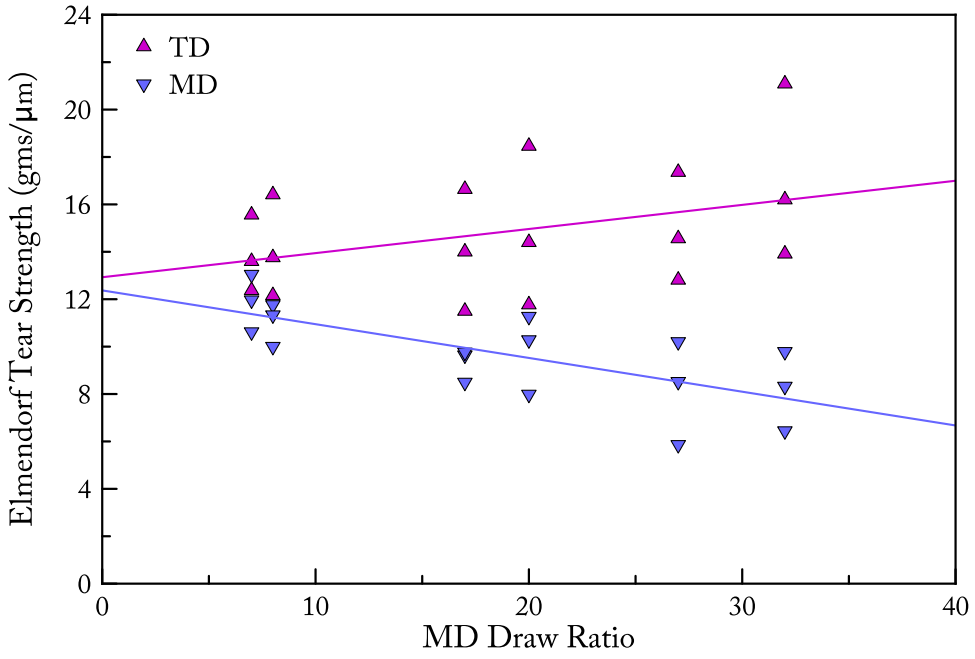

Figure 71: MD Elmendorf tear and TD Elmendorf tear values are shown as a function of the MD Draw Ratio. Solid lines represent fits to the data.

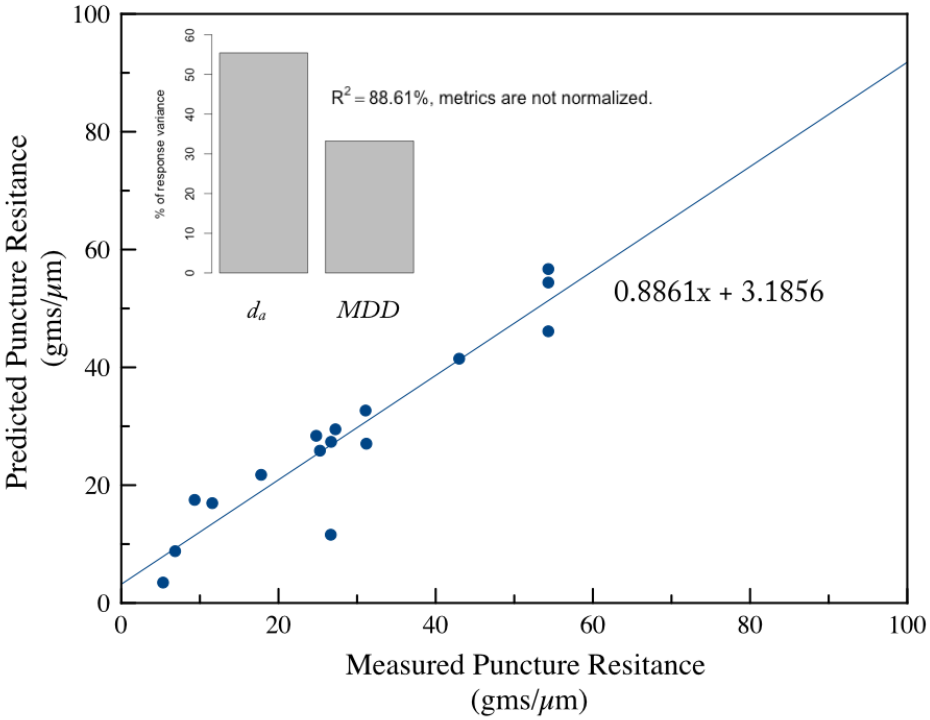

Figure 72: Dart Drop is predicted using Equation 50. The fit between the predicted and measured values is represented by the solid line. The inset plot shows the relative contribution of each of the predictor variables towards the best fit.

CHAPTER X

CONCLUSIONS

10.1 MD - TD Deformation

- When considering the stress strain behavior alone, MD strain is shown to be similar to TD strain, when considering the strain regime between strain onset and the second yield point. More obvious differences between MD deformation and TD deformation appear only after the onset of strain hardening. Under MD strain, thin films display a lower strain to failure than thick films. Under TD strain, strain to failure is independent of film thickness. It can be concluded that applying strain along TD elicits a processing independent response from blown films.

- SAXS demostrates that the morphological evolution in blown films is indeed different between MD and TD strain and these differences exist at low and high values of strain. This inference cannot be made simply by observing the stress strain behavior alone. The mechanism of monotonically increasing lamellar tilting under strain is observed only for MD strained samples. The onset of lamellar tilting occurs at the first yield point since the limit of amorphous extensibility is reached. The tilting is observed only for MD strained specimens as majority of the lamellae in blown films have their lamellar normals oriented preferentially along MD. The tilting mechanism rotates lamellae into the strain direction so as to prolong lamellar (crystal) stability while preventing abrupt changes in crystallinity. Tilting is accompanied by a breakdown of lamellae into smaller lamellar fragments. Under TD strain, since the majority of the lamellae are pre-aligned with their largest dimensions along the strain direction. This negates the need for tilting and rotation of most but not all lamellae. As a result only a smaller relative proportion of lamellae tilt and rotate under TD strain. The quadralobe scattering is therefore noticeably absent in TD strain.

- Beyond the second yield point the fibrillar morphology achieved in both MD and TD

modes is similar. Tracking of d_{ac} over the strain range reveals a process independent dimension at high strain beyond the second yield point under TD strain, but not in MD strain. This observation agrees with the behavior at high strains captured in the stress-strain plots. It reinforces the hypothesis that under TD strain, the original morphology of films is completely destroyed before strain induced recrystallization creates a new morphology from the available environment of amorphous and fragmented crystal components that is purely dependent on the architecture of the statistical LLDPE copolymer. Under MD strain, although a constant dimension of d_{ac} is achieved, the original morphology is not entirely destroyed and therefore the final morphology is process dependent.

- Objective 1 highlighted in the introduction is achieved. The following dimension and orientation parameters are extracted from the scattering patterns and these are utilized subsequently to establish quantitative structure property relationships

	Dimension	Orientation
SAXS	d_{ac} d_c d_a L_{SAXS}	LAR F_{lam}
WAXS	Domain Size Xc	F_a F_b F_c F_{am}

10.2 Mesoscale Morphology Evolution

- SAXS on the as made films of the three polymer families shows that the branching architecture of the polymer, i.e. the short chain branching content and the run length distribution in the polymer, plays an important role in governing the morphology. The trend in d_{ac} follows the trend in density, i.e. comonomer content and branching, systematically increasing from $LLDPE_1$ to $LLDPE_2$ and to $LLDPE_3$. The d_c values across the three polymers in the as made samples are very similar suggesting that increasing the average branch content increases the average spacing between lamellae but not the average thickness of the lamellae themselves. It is entirely plausible and

highly probable that the head and tail of the branching distribution i.e. chains with no branching and chains with extensive branching affect correspondingly the lamellar thickness distribution, i.e. the thinnest and thickest lamellae, and their relative populations.

- The bivariate distributions of the three polymers clearly illustrate their architectural differences. Following the shish - kebab model of crystallization it is hypothesized that chains, where upwards of 1-2% hexene comonomer is incorporated control the average lamellar thickness. Highly branched low molecular weight chains are expected to form thinner lamellae since they possess shorter crystallizable lengths of ethylene backbone. Unbranched high molecular weight chains are theoretically expected to form thick lamellae but in reality the formation of thick lamellae is likely to be suppressed due to the preferential elongation of these chains into extended chain precursors under flow followed by the co-crystallization of branched chains onto the precursor which further limits long chain relaxation.

- Theoretical considerations show that the NMR derived average values of branching and run length correlate poorly with the average lamellar thickness. It is infact the shorter run lengths that determine the average thickness of lamellae while the longer run lengths are more likely to be incorporated into the amorphous domain. The increase in d_a systematically from $LLDPE_1$ to $LLDPE_2$ and to $LLDPE_3$ supports this hypothesis.

10.3 Morphology at the Atomistic Scale

- The F_a, F_b and F_c values for as made films show that the a axis tends to align along the MD while the b axis aligns along the TD. Thin films routinely show higher levels of orientation and alignment along the MD and TD compared to thicker films. Comparing between the three polymers, $LLDPE_1$ shows weak orientation tendencies due to the prominence of short crystallizable ethylene sequences which don't elongate under flow. In fact, the orientability of $LLDPE_1$ even under highly orienting processing conditions, i.e. when achieving a BUR of 3, is quite poor. By comparison, orientation

in $LLDPE_2$ and $LLDPE_3$ films is three and two times more oriented respectively. The LAR calculated previously for the as made condition supports this conclusion since $LLDPE_1$ shows a maximum LAR of 1.6 while the maximum LAR for $LLDPE_2$ and $LLDPE_3$ is more than double, at 3.7 and 3.4, respectively. Clearly, orientability is dependent on both processing condition as well as the bivariate distribution but more so on the latter.

- The through thickness strucure of films is not represented accurately by existsing 2D lamellar models. β rotation measurements show that the orientation of lamellae through the films cannot be described by flat lamellae. Although the explanation for the through thickness structural features might be provided by invoking twisted lamellar structures, it is shown by 2D and 3D modeling efforts that this explanation is not a unique solution since the same scattering patterns can be explained differently. While a clear preference exists for the lamellar orientation scheme, the observations of β rotation can be explained by a model where lamellae are randomly oriented with respect to each other but possess a preferred global arrangement scheme.

- The evolution of the F_a, F_b and F_c values with strain is similar for all films. At high strains the c axis rotates into the strain direction with the a and b axes perpendicular to the strain. This trend occurs in both MD and TD strained films. The crystallinity associated with the different films displays a similar trend with strain experiencing on average a 10% drop between the start of strain and the second yield point. The crystallinity increases again beyond the second yield point but typically plateaus at high strains in the strain hardening regime. The reduction in L_{SAXS} suggests that the crystallinity should continue dropping. In fact it is the alignment of amorphous chains beyond the second yield point that account for the rapid increase in crystallinity between the second yield point and the onset of strain hardening. This hypothesis is suitably supported by the change in F_{am} with strain which shows a maximum value of 0.8. The presence of longer average run lengths in the amorphous domains of $LLDPE_3$ which in a highly strained environment are likely to show better alignment at lower

strains is a plausible reason for the F_{am} to attain its maximum at lower strains in this polymer.

- The orthorhombic to monoclinic transition takes place beyond the first yield point. This transformation takes place in all three polymers but is more likely to be pronounced in films with a larger fraction of thick and stable lamellae. While a direct link between the monoclinic content and the polymer architecture could not be established it is hypothesized that the potential for maximizing the monoclinic content might be realized by annealing specimens prior to straining. By annealing, the average crystal thickness can be increased which inturn is likely to force branching defects to accumulate at the crystal surface. These defects can enhance the density of impingement effects at the surface of a lamella under strain and thereby contribute additionally to the orthorhombic to monoclinic transition.

10.4 Structure - Property Relationships

- Elemendorf Tear and Dart Drop values for the three polymers are compared against the dimensional and orientational parameters derived from both SAXS and WAXS data. Firstly it is clear that dart and tear performance are competing properties. Films that exhibit high dart resistance also exhibit poor tear properties. For TD elmendorf tear, correlations with L_{SAXS} and F_{lam} are the strongest suggesting that the SAXS based dimensionality and orientation of the microstructure is directly related to the tear strength of the films. By increasing the average run lengths of the polymers, it is expected that the L_{SAXS} will be increased, which will distort further the balance of directional tear properties. To improve the overall tear strength while maintaining the balance between TD - MD tear behavior, our data indicate that this can be best achieved by using high density material in a film with little or no orientation.

- Puncture resistance correlates with well with d_a and Md Draw Ratio. It is anticipated that the established correlation can be further improved by further expeiments on an additional set of film from a fourth polymer. Based on the results, some important conclusions can be infered - firstly, there is a tendency for poorly oriented film to

exhibit increased dart drop values. This implies that a higher density polymer with a tailored fractional content of branched chains might provide the same dart drop response from a low density polymer without experiencing deterioration of tear properties. Secondly, the initial response of a film to the dart drop test could depend on the rate at which displacement of lamellae relative to each other takes place i.e. the rate at which the amorphous domains can respond to the applied stress. The latter might be studied by observnig the rate of change of amorphous orientation under different strain rates of deformation.

APPENDIX A

THE APPLICATION OF FOURIER TRANSFORMS IN SCATTERING

A.1 Autocorrelation Function

In section 2.4.1.1 the 'scattering square' describes the interdependence between the electron density distribution, the scattering amplitude, the scattering intensity and the autocorrelation function of the electron density distribution. The autocorrelation function $\Gamma_\rho(r)$ of the electron density distribution $\rho(r)$, is mathematically described as the inverse Fourier transform of the scattering intensity $I(q)$. Equation 51 states that

$$I(q) = |A(q)|^2 = \Big| \int_V \rho(r) e^{-iqr} dr \Big|^2 \tag{51}$$

Accordingly, autocorrelation function $\Gamma_\rho(r)$ can be defined based on $I(q)$ as

$$\Gamma_\rho(r) = \Big| \int_V I(q) e^{iqr} dq \Big|^2 \tag{52}$$

The autocorrelation function can be derived from $I(q)$ in the following manner. Recall that $I(q)$ is defined as the square of the scattering amplitude $A(q)$. In reality $I(q)$ is a real quantity whereas $A(q)$ is complex. The magnitude of $I(q)$ is mathematically obtained from $A(q)$ via its complex conjugate

$$I(q) = A(q) \cdot A\star(q) \tag{53}$$

$$I(q) = \left[\int_V \rho(u') e^{-iqu'} du \right] \left[\int_V \rho(u) e^{-iqu} du \right] \tag{54}$$

Substituting $r = u' - u$,

$$I(q) = \int \left[\int_V \rho(u)\rho(u+r) du \right] e^{-iqr} dr \tag{55}$$

$$I(q) = \int \Gamma_\rho(r) e^{-iqr} dr \tag{56}$$

Here, $\Gamma_\rho(r) = \int \rho(u)\rho(u+r)du$.

Additionally, $\Gamma_\rho(r)$ is directly related to the average of the value $\rho(u)\rho(u')$ taken through the whole sample space when $u' - u = r$. When $r = 0$, the value of the autocorrelation $\Gamma_\rho(0) = \langle\rho^2\rangle V$. The autocorrelation function is also referred to as the Patterson Function.

APPENDIX B

BIAXIAL STRETCHING

The fabrication of blown films is a biaxial deformation event subjecting the polymer melt to deformation along two orthogonal directions i.e. MD and TD. The resulting morphology is therefore dependent on the crystallization of polymer chains under biaxial stress and strain. Additionally, the dart drop test which measures the puncture resistance of films is also subjects films to a complex stress field bearing some resemblance to a biaxial deformation event. The evolution of film morphology under biaxial strain is therefore of significant relevance. Capturing these changes *in situ* using X-rays is however a non trivial experiment to conduct primarily due to the bulky nature of standard biaxial stretching equipment. Typical biaxial stretching devices sold by vendors such as Instron have a large footprint and as such their use as sample environments at synchrotrons is not feasible. An example of a commercially available biaxial stretching unit is provided in Figure 73. Since beamline 5-IDD at the APS has ready access to a dual headed Instron it is evident that only an Instron compatible sample environment capable of transforming unidirectional strain into biaxial strain may be utilized to perform perform *in situ* biaxial strain measurements. It is indeed desirable to have equipment that might facilitate such a conversion of uniaxial deformation to biaxial deformation. Therefore as part of this dissertation an Instron compatible biaxial strain device with the capacity for *in situ* biaxial strain measurements has been designed, fabricated and commissioned. The schematic of the device is provided in Figure 74. The device is designed to fit into any standard Instron Universal Testing Machine (UTM). The cam plate converts uniaxial force imparted by the Instron into a torsional force. The two orthogonal forces act in a synchronized manner imparting biaxial strain to a film specimen which is held by the clamps of the concertina frame. At maximum extension in either of the deformation directions the dimensions of the concertina frame are 300 mm. The cam plate has a central orifice which is expected to remain stationery in a dual headed

Figure 73: Commercially available biaxial stretching device. The large footprint of such a device obfuscates incorporation into a synchrotron beamline.

instron. The incident X-ray beam can pass through this orifice and data can be recorded at the SAXS and WAXS detectors. While the design specifications were adjusted so that the scattered X-rays could pass through to the SAXS and WAXS detectors without obstruction, *in situ* measurements have not been undertaken yet and as such it is difficult to ascertain whether this is true. Nevertheless, it is anticipated that the any obstruction might affect the WAXS data more than the SAXS data. Figure 75a shows a loaded specimen of film $LLDPE_2$.1c with its MD in the vertical direction. Figure 75b shows the same specimen under biaxial strain. Figure 75c shows the corresponding load - extension plots for single ply specimens of $LLDPE_2$.1c tested at a uniaxial deformation rate of 25.4 and 50.8 mm per minute. Although, the extension reported here is uniaxial extension, since the stretching is equi-biaxial, the extension in the orthogonal direction is the same. The discontinuities in the load strain plots occur when the uniaxial to biaxial force transformation is not smooth. The specimens loaded here had original dimensions of 101.6 mm in length as well as breadth

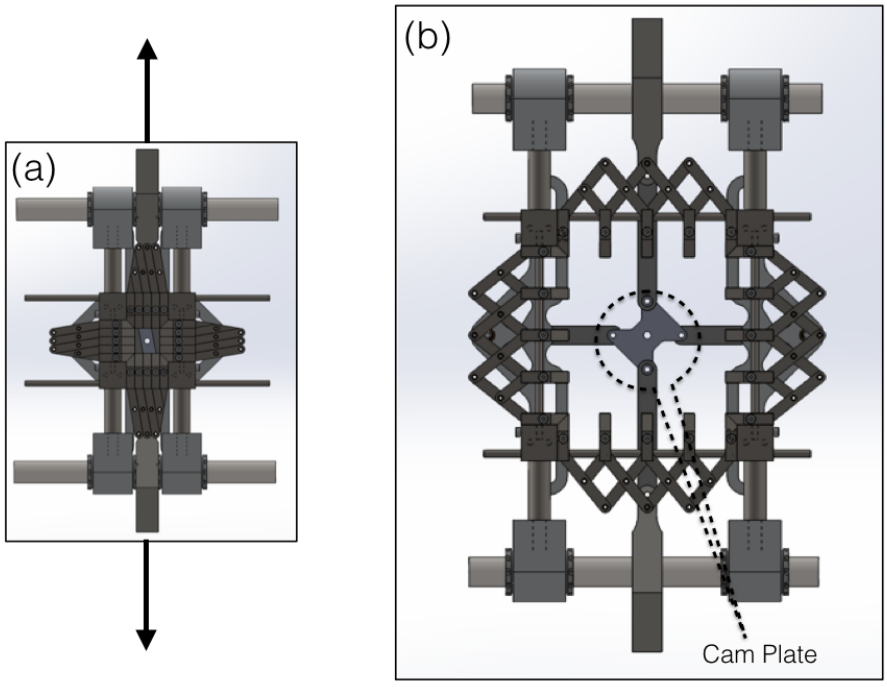

Figure 74: Schematic of the custom made Instron compatible biaxial stretching equipment showing (a) the device in the fully collapsed state where the arrows indicate the direction of deformation with respect to the instron (b) the fully expanded state. The perforated cam plate is marked

and were stretched to 171.6 mm in length and breadth. Over this 70% strain regime the load - extension plots did not show the clear presence of yield points.

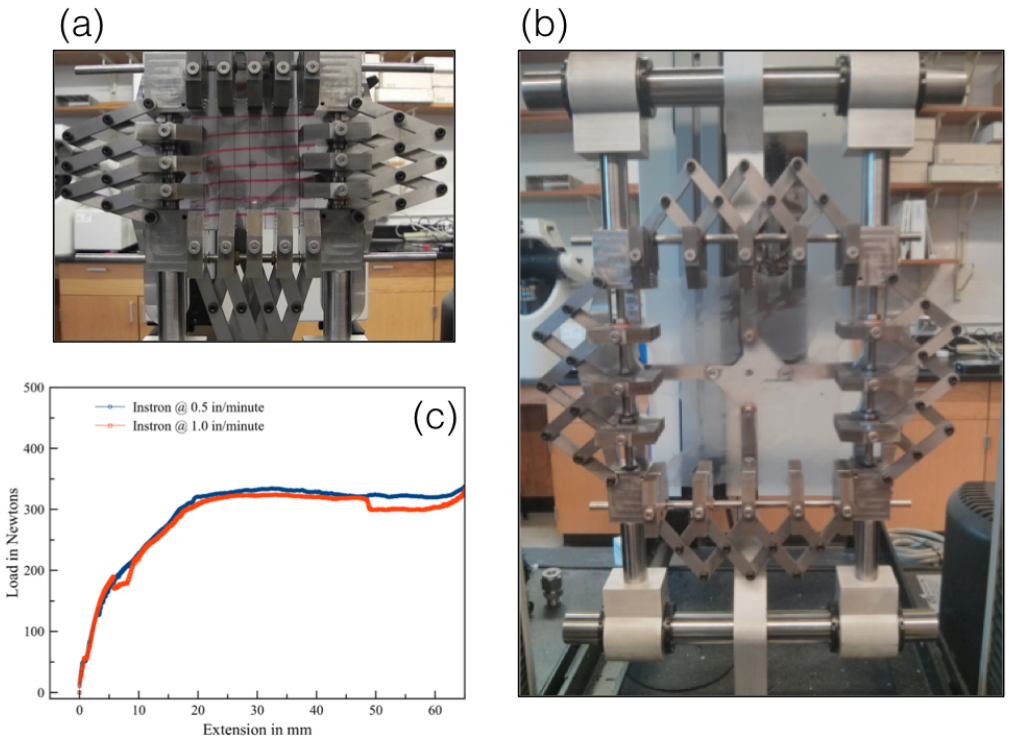

Figure 75: Biaxial deformation of single ply of LLDPE$_2$.1c with MD in the vertical direction at 25.4 mm per minute in either direction. (a) 0% uniaxial strain (b) 70% uniaxial strain (c) Load - Extension plot displayed between between 0 and 70% elongation

APPENDIX C

PRINCIPAL COMPONENTS ANALYSIS

X-ray scattering which was first used to determine the structure of DNA in 1952 [130] continues to hold great promise in materials science. Improvements in technology have made it possible to extend beyond the collection of purely static scattering images. Dynamic datasets solving in time can now be obtained resulting in what might be termed as X Ray Scattering Movies (scattering). It is expected that scattering movies will provide materials scientists with the feedback necessary to develop new materials faster than the traditional trial and error approach because it can offer information about material behavior under dynamic and evolving conditions which was previously not possible. Additionally, the scattering experimental technique is an integral part of the Materials Genome Initiative (MGI) instituted by the White House in 2011. As such the MGI aims to reduce development times for new materials as well as expedite the commercialization potential of novel materials. While the primary focus of this dissertation is to solve challenges specific to PE blown films, the opportunity to benchmark the dynamic datasets through the tools of 'materials informatics' is quite valuable and as such has been explored here.

C.1 Challenges in the analysis of large time resolved datasets

In chapters 4 to 8 the various analysis methods and results based on SAXS and WAXS data for a number of different polymer materials are reviewed so as to find variations between the three polymers to explain their mechanical properties. The 2D scattering data from these polymers are visually so similar that it is difficult for the human eye to explicitly differentiate between them. The qualitative similarities between the data are likely to influence user bias based errors in the quantitative analysis by the line profile and fitting methodology. The dimensional parameters including but not limited to d_{ac}, L_{SAXS}, d_c and d_a are likely to experience this error associated with user bias. Additionally, while the analysis of static

data is rapid, analysis of dynamic datasets following methods outlined in Chapter 4 are time intensive and require constant monitoring by a user which in turn increases the tendency to bias the results themselves.

One way to help eliminate this bias is to use an appropriate computational tool to statistically uncover and quantify differences between datasets. Further, the availability of a visualization method to display the results from the computational tool might aid scientists to expedite analysis times particularly when a large dataset (multiple polymers, various processing conditions etc) of a time resolved nature might become available.

C.2 Proposed solution to mitigate user bias and time to results

In order to eliminate the need for software monitoring by end users, reduce user bias in the analysis of scattering data, and to expedite overall analyses times, we create a tool to perform dimensionality reduction and supervised learning directly on the scattering images and then visualize the results. This approach is made possible primarily by the use of Principal Components Analysis (PCA). For a detailed understanding of PCA and similar techniques readers are directed to any advanced statistics textbooks. PCA emphobserves data and maximizes the variance between the data by an orthogonal transformation to convert observations from possibly correlated variables into linearly uncorrelated variables called principal components.

This approach of applying PCA to scattering data is in stark contrast to the current work and the work of most other groups where the scattering data are analyzed based on an understanding of a pre-defined model of scattering. While the latter is an irreplaceable aspect of the science (and art) of scattering, the former is an approach designed to take large amounts of scattering data from a variety of samples and provide a qualitative understanding of the behavior between samples.

Recently, some authors have attempted to use PCA with 1D scattering data. In the case of isotropic scattering, a 1D line profile along any ψ is conveniently representative of the full 2D pattern. This is not the case for anisotropic scattering patterns where the ψ dependence of the scattering cannot be accurately captured in reduced 1D data. Moreover,

by feeding 1D line profiles to PCA, the authors have not made full use of their 2D data. Our method of applying PCA to 2D datasets does not discard any data since we avoid reducing the 2D scattering data prior to PCA. Figure 76 shows the relative time spent analyzing scattering datasets and the extent of user bias incorporated into the results based on the different methods described.

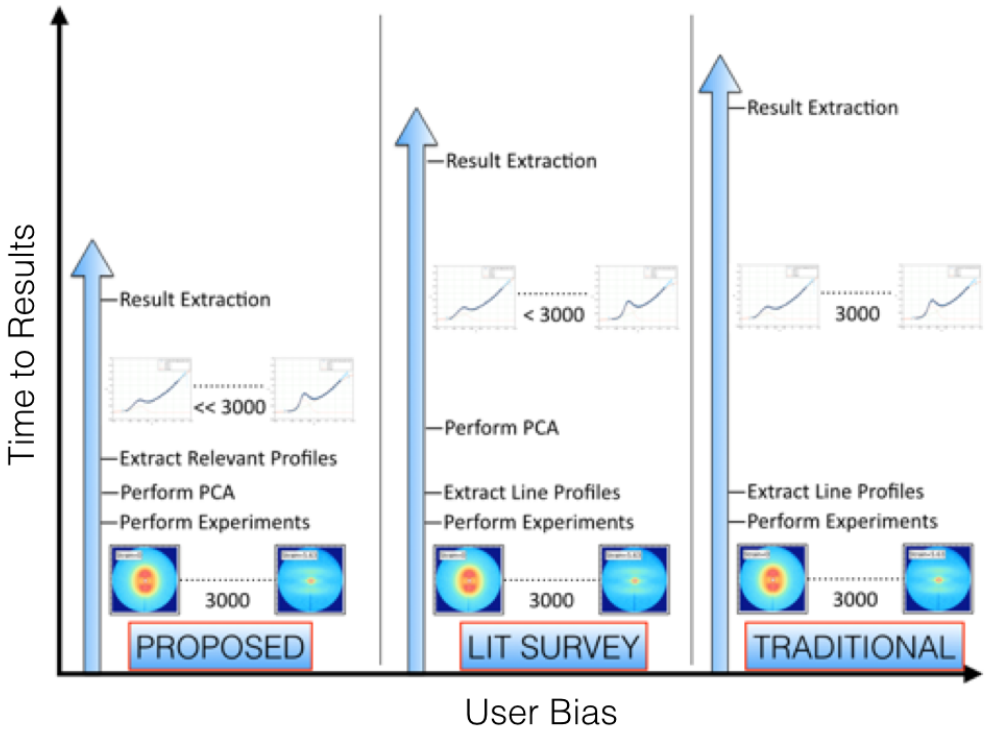

Figure 76: Schematic showing the performance of different analysis strategies as a function of user bias and time investment until results are obtained. The traditional method proposed by Tang et al is the most time consuming and prone to user bias. Methods based on PCA demonstrated by groups in the recent past have reduced analysis times but dont utilize all the scattering data. The proposed method greatly reduces user bias as well as time to results.

Since the inputs going into the PCA are sets of image sequences, the expectation is that the PCA will result in a unique trajectory of points for each strained sample. There will be as many trajectories as there are image sets. Each trajectory will be constituted by a certain number of points. The number of points per trajectory will equal the number of frames in the corresponding scattering data set. Once the PCA analysis is computed we will visualize the results. The visualization scheme constructed in D3 (a javascript based

interactive environment) will allow a user to *mouseover* points in any trajectory and 'see' the 2D images that are tied to those mouseovered points. When this tool is deployed industrially, we expect scientists to be able to use PCA to create a spread of trajectories, and the visualization tool to assist in identifying similarities and differences faster and with more precision than beofre.

C.3 Experiments and Evaluation of Method

C.3.1 Preliminary Results

In this project the scattering datasets from all the films of polymer samples $LLDPE_1$ and $LLDPE_3$ as provided in Table 2 are used to test the effectiveness of our toolkit. Data sets 1 to 6 correspond in order of film thickness and BUR to $LLDPE_1$ whereas 7 to 12 correspond to $LLDPE_3$. The preliminary work is performed on data set 1. First we successfully applied PCA to a single scattering data set and obtained a trajectory for the polymer sample as it was being mechanically strained. Each 960 x 960 image in the image series was converted from a 2D array to a 1D vector with length 921,600. Thus, there were as many vectors as there were frames (250).

Principal components (PCs) were calculated in Python. Originally PCA was used on the entire X-ray scattering image to do dimensionality reduction. This turned out to be somewhat slow because of the size of the images and because of some of the data structures were initially being used in our code. Later the *dimenion reducer* class was created that would allow for flexibility in selecting a dimensionality reduction technique. This class was designed to integrate well with machine learn python package *scikit learn*. After trying several variations on PCA, we found that kernel PCA with a linear kernel gave us the same reduced representation an order of magnitude faster than PCA. We also explored sparse PCA and found that is gave similar results to PCA and kernel PCA, but we not as fast as kernel PCA.Because the signal strength for each image is very low, the log of every pixel was used. In order to account for the variation in X-ray scattering intensity due to sample in thickness, we divided each image by the mean intensity value in each image.

A plot of the eigenvalues associated with each calculated eigenvector is shown in Figure

??. The decay of eigenvalues is expected since typically within PCA, PC1¿PC2¿PC3 and so on. We examine this decay curve and determine that PC1, PC2, and PC3 are probably the most important PCs. However in the final visualization demo, we exhibit 7 PCs since further testing showed salient features present in PCs 4,5,6, and 7.

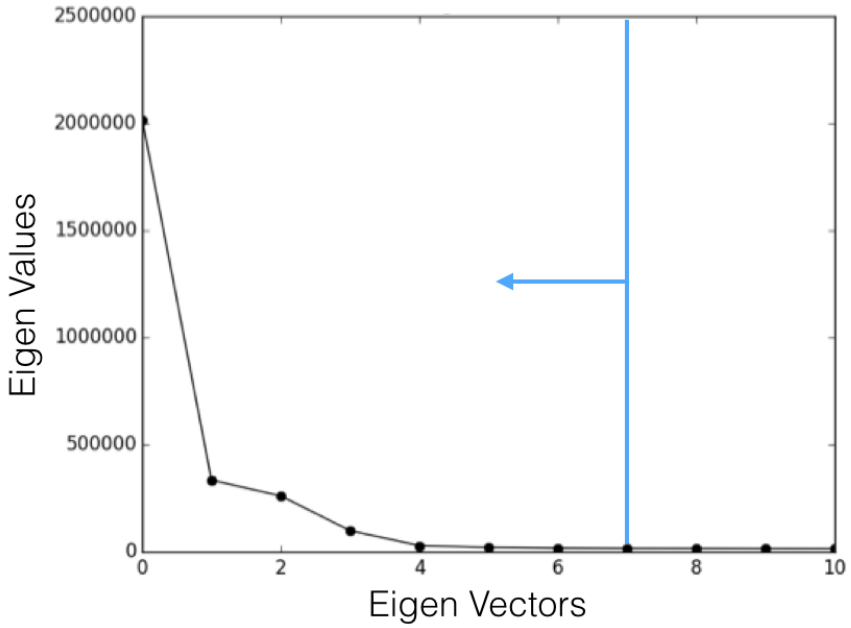

Figure 77: The decay of Eigen values of the different Eigen vectors associated with PCA suggest that the first 7 Principal Components are of relative importance. The blue arrow indicates the same.

C.3.2 Detailed Results

Once we have shown that a processing dependent pathway can be generated using PCA for a single dataset of scattering data we applied the same PCA code to all 12 data sets. The entire set of scattering data consisted of 3200 tif images corresponding to a size of approximately 6 GB. We were able to condense this data set into 1 MB after PCA. The final PCA of 12 samples provided us with 12 very similar trajectories in PC1 vs. PC2 vs. PC3. This was expected from the data set. The results of the PCA were visualized in D3. The D3 tool was created in three linked parts. In part 1 we visualized the PCA data. In

part 2 we visualized the stress/strain data under which the scattering data were collected. Finally in part 3 we showed the XRS image data associated with every strain point for which PCA data was calculated. Since we worked with multiple sample sets, we introduced a filtering mechanism to select the data. The filtering was based on data labels we created within the JSON file.

Essentially, a user can interactively select the samples he/she wishes to compare. Once the samples of interest are 'checked', the user selects which PCs of the chosen data sets he/she wishes to analyze. Selecting 'Update plot' will plot the corresponding data. Trajectories associated with samples will now be seen in the PCA space while stress strain data from the selected samples will populate the stress/strain plot. A mouseover is set up for the PCA plot such that hovering on a point in PCA space will highlight the strain values at those PCA points as well as on the stress strain plot of the corresponding sample. Clicking a point on the PCA space will bring up the black and white scattering image at the corresponding strain. This is shown in the screen shot in Figure 78.

C.3.3 Discussion

C.3.3.1 Effect of Processing Condition

Sample 2 and Sample 4 are polymer samples having the same density and thickness. They are however made via different processing conditions. In our visualization selecting samples 2 4 and then observing the different PCs should provide insight into the differences in strain evolved microstructure due to differences in processing conditions alone. The screenshot of this comparison is provided in Figure **??**. Clearly, the stress strain plots are highly similar. PCA plots are different in values although being similar in trends.

C.3.3.2 Effect of Density

Selecting samples 2,4 8,10 now provides the comparison between density related effects. Since the densities are different, microstructural differences are expected as well. These are shown in Figure **??**. While the trajectories of in PCA space for samples of lower density (i.e. samples 2,4) show smooth regions, the corresponding trajectories of the more dense materials (i.e. samples 8,10) show discontinuities. These jumps are related to microstructural

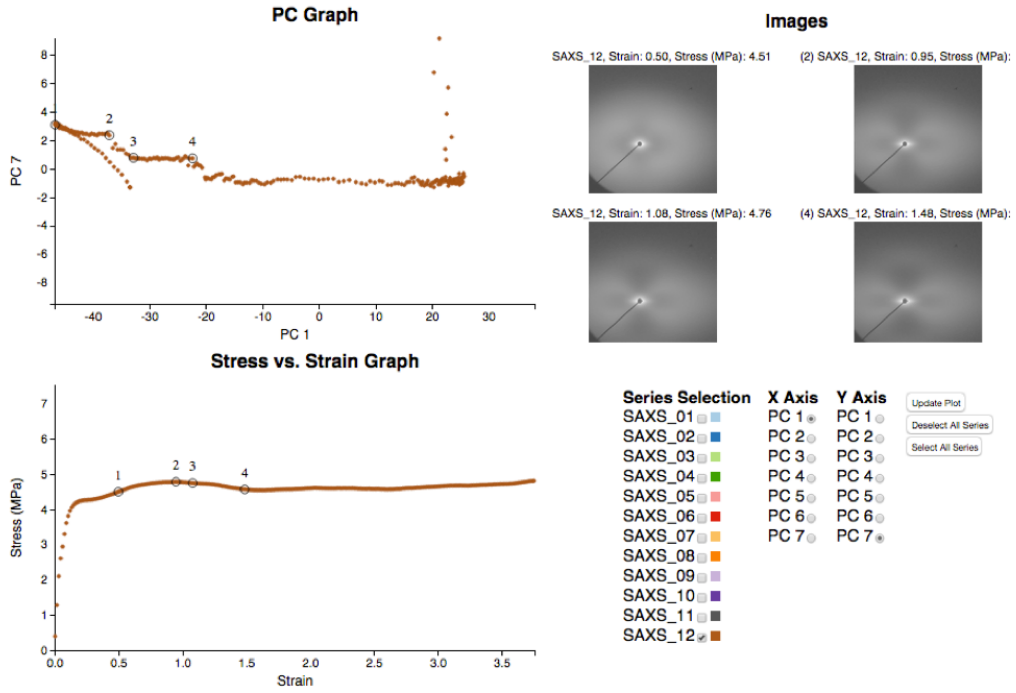

Figure 78: The stress strain plot, corresponding PCA dependencies and scattering data are shown in the visualization tool. Checking/Unchecking the selection boxes and pressing the button labeled Update Plot refreshes the page as well as updates the plot. Four points indicated by the numbers 1,2,3 and 4 show the points of interest selected here. Top left plot shows PC7 vs PC1 for sample 12. Bottom left plot shows the stress strain plot for sample 12. Highlighted are points are (1) Strain = 0.50, (2) Strain = 0.95, (3) Strain = 1.08, (4) Strain = 1.48 and the respective scattering images at these strains for objective comparison.

effects that are not present in the low density materials. PCA thus provides very useful information without the user having to analyze a single image by the traditional means.

C.3.3.3 Effect of Thickness

Selecting samples 4,5, and 6 provides the comparison between thickness related effects in Figure 6C. In PCA space the trajectories of the thin films (30 microns) although similar in trend show different values as compared to the slightly thicker films. This observation leads us to believe that thinner films have vastly different microstructures than the thicker films.

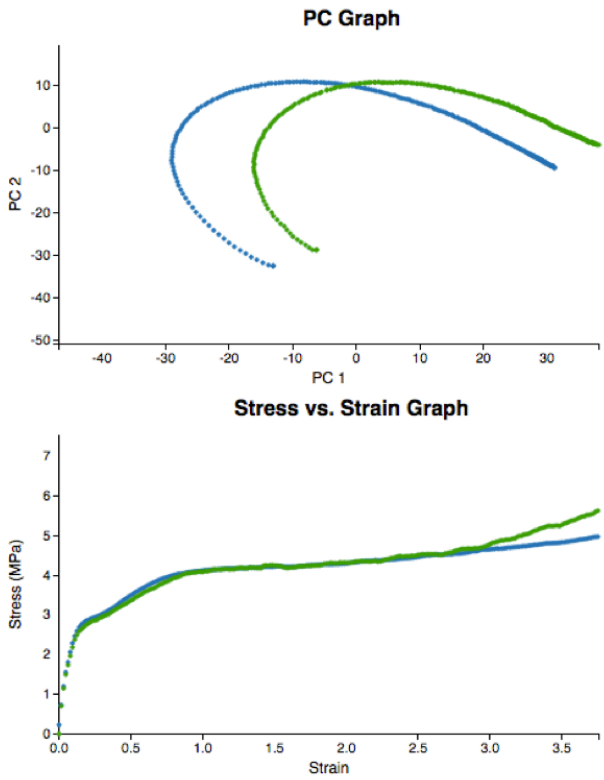

Figure 79: Visualization of the effect of processing condition on PCA

C.4 Conclusions

We present the first of a kind materials science focused toolkit to allow scientists to observe dynamic X ray scattering datasets objectively in PCA space. This toolkit permits a user to compare multiple scattering data sets objectively such that subsequent data analysis is free from user bias. The utilization of PCA space provides salient features of the microstructure data to stand out. These features have not been picked up by traditional analysis methods. The visualization tool allows a user to compare scattering data while observing the behavior of PCs. This helps determine which particular images need to be analyzed by traditional means. No longer is it required to manually fit each and every frame of each and every sample in order to obtain useful information. The toolkit created here need not be restricted to strain resolved data alone. The same approach could be very easily extended to other types of dynamic data for example in the case of microstructural evolution as a result of temperature, cyclic strain etc.

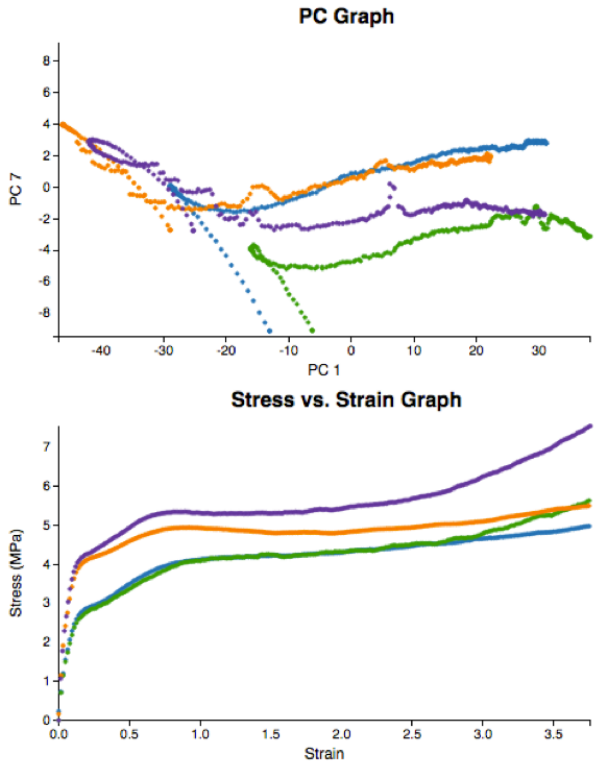

Figure 80: Visualization of the effect of polymer density on PCA

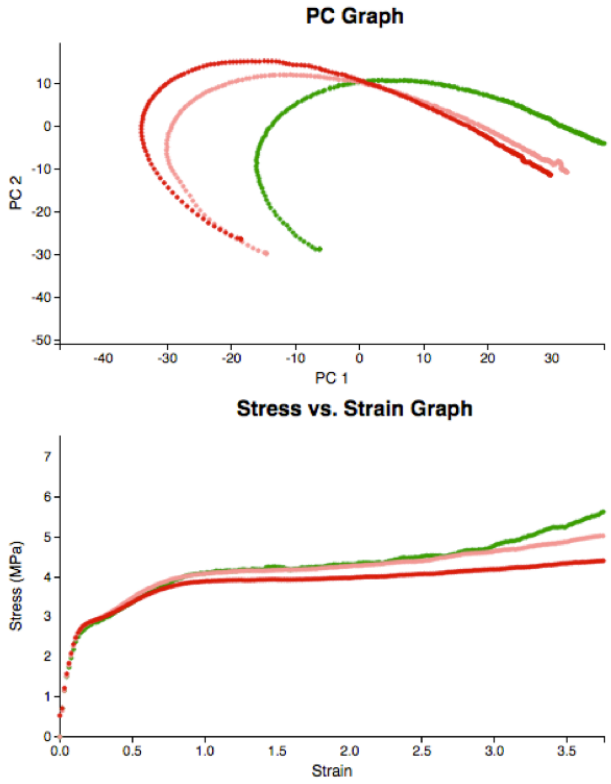

Figure 81: Visualization of the effect of film thickness on PCA

REFERENCES

[1] M. F. Butler and A. M. Donald, "Realtime in situ light scattering and xray scattering studies of polyethylene blown film deformation," *Journal of Applied Polymer Science*, vol. 67, no. 2, pp. 321–339, 1998.

[2] A. J. Peacock, *The Handbook of Polyethylene*. Marcel Dekker, 2000.

[3] T. Kanai and J. L. White, "Kinematics, dynamics and stability of the tubular film extrusion of various polyethylenes," *Polymer Engineering & Science*, vol. 24, no. 15, pp. 1185–1201, 1984.

[4] X. M. Zhang, S. Elkoun, A. Ajji, and M. A. Huneault, "Oriented structure and anisotropy properties of polymer blown films: Hdpe, lldpe and ldpe," *Polymer*, vol. 45, no. 1, pp. 217–229, 2004.

[5] R. J. Pazur and R. E. Prud'homme, "X-ray pole figure and small angle scattering measurements on tubular blown low-density poly(ethylene) films," *Macromolecules*, vol. 29, pp. 119–128, 1996.

[6] W. F. Maddams and J. E. Preedy, "Xray diffraction orientation studies on blown polyethylene films. i. preliminary measurements," *Journal of Applied Polymer Science*, vol. 22, no. 10, pp. 2721–2737, 1978.

[7] W. F. Maddams and J. E. Preedy, "Xray diffraction orientation studies on blown polyethylene films. iii. highstress crystallization orientation," *Journal of Applied Polymer Science*, vol. 22, no. 10, pp. 2751–2759, 1978.

[8] W. F. Maddams and J. E. Preedy, "Xray diffraction orientation studies on blown polyethylene films. ii. measurements on films from a commercial blowing unit," *Journal of Applied Polymer Science*, vol. 22, no. 10, pp. 2739–2749, 1978.

[9] P. H. Lindenmeyer and S. Lustig, "Crystallite orientation in extruded polyethylene film," *Journal of Applied Polymer Science*, vol. 9, no. 1, pp. 227–240, 1965.

[10] L. W. Lee, R. A. Register, and D. M. Dean, "Tear anisotropy in films blown from polyethylenes of different macromolecular architectures," *Journal of Polymer Science Part B: Polymer Physics*, vol. 43, no. 4, pp. 413–420, 2005.

[11] T. H. Kwack, C. D. Han, and M. E. Vickers, "Development of crystalline structure during tubular film blowing of lowdensity polyethylene," *Journal of Applied Polymer Science*, vol. 35, no. 2, pp. 363–389, 1988.

[12] R. K. Krishnaswamy, "A method to characterize the biaxial orientation of the crystalline phase in polyethylene blown films," *Journal of Polymer Science Part B: Polymer Physics*, vol. 38, no. 1, pp. 182–193, 2000.

[13] A. Gupta, D. M. Simpson, and I. R. Harrison, "A morphological study of hdpeblown films using smallangle xray scattering," *Journal of Applied Polymer Science*, vol. 50, no. 12, pp. 2085–2093, 1993.

[14] O. Guichon, R. Séguéla, L. David, and G. Vigier, "Influence of the molecular architecture of lowdensity polyethylene on the texture and mechanical properties of blown films," *Journal of Polymer Science Part B: Polymer Physics*, vol. 41, no. 4, pp. 327–340, 2003.

[15] M. van Drongelen, D. Cavallo, L. Balzano, G. Portale, I. Vittorias, W. Bras, G. C. Alfonso, and G. W. M. Peters, "Structure development of lowdensity polyethylenes during film blowing: A realtime wideangle xray diffraction study," *Macromolecular Materials and Engineering*, vol. 299, no. 12, pp. 1494–1512, 2014.

[16] K. Choi, J. E. Spruiell, and J. L. White, "Orientation and morphology of highdensity polyethylene film produced by the tubular blowing method and its relationship to process conditions," *Journal of Polymer Science: Polymer Physics Edition*, vol. 20, no. 1, pp. 27–47, 1982.

[17] H. Y. Chen, M. T. Bishop, B. G. Landes, and S. P. Chum, "Orientation and property correlations for lldpe blown films," *Journal of Applied Polymer Science*, vol. 101, no. 2, pp. 898–907, 2006.

[18] A. Bafna, G. Beaucage, F. Mirabella, G. Skillas, and S. Sukumaran, "Optical properties and orientation in polyethylene blown films," *Journal of Polymer Science Part B: Polymer Physics*, vol. 39, no. 23, pp. 2923–2936, 2001.

[19] H. Ashizawa, J. E. Spruiell, and J. L. White, "An investigation of optical clarity and crystalline orientation in polyethylene tubular film," *Polymer Engineering & Science*, vol. 24, no. 13, pp. 1035–1042, 1984.

[20] E. S. Sherman, "Plastic deformation and tearing in high density polyethylene blown films," *Polymer Engineering Science*, vol. 24, no. 11, pp. 895–907, 1984.

[21] R. M. Patel, T. I. Butler, K. L. Walton, and G. W. Knight, "Investigation of processingstructureproperties relationships in polyethylene blown films," *Polymer Engineering & Science*, vol. 34, no. 19, pp. 1506–1514, 1994.

[22] M. Vadlamudi, G. Subramanian, S. Shanbhag, R. G. Alamo, M. VarmaNair, D. M. Fiscus, G. M. Brown, C. Lu, and C. J. Ruff, "Molecular weight and branching distribution of a high performance metallocene ethylene 1hexene copolymer filmgrade resin," *Macromolecular Symposia*, vol. 282, no. 1, pp. 1–13, 2009.

[23] M. Gahleitner, L. Resconi, and P. Doshev, "Heterogeneous ziegler-natta, metallocene, and post-metallocene catalysis: Successes and challenges in industrial application," *MRS Bulletin*, vol. 38, no. 03, pp. 229–233, 2013.

[24] J. P. Claverie and F. Schaper, "Ziegler-natta catalysis: 50 years after the nobel prize," *MRS Bulletin*, vol. 38, no. 03, pp. 213–218, 2013.

[25] A.-C. Albertsson, H. Knuuttila, A. Lehtinen, and A. Nummila-Pakarinen, "Advances in polymer science," *springer*, vol. 169, pp. 13–27, 2004.

[26] F. Zuluaga, B. İnci, Y. Nozue, S. Hosoda, and K. B. Wagener, "Reducing branch frequency in precision polyethylene," *Macromolecules*, vol. 42, no. 14, pp. 4953–4955, 2009.

[27] A. H. Windle, "Wide angle x-ray diffraction study of the microstructure of chain-folded polyethylene crystals," *Journal of Materials Science*, vol. 10, no. 2, pp. 252–268, 2001.

[28] P. R. Swan, "Polyethylene unit cell variations with branching," *Journal of Polymer Science*, vol. 56, no. 164, pp. 409–416, 1962.

[29] F. J. Stadler, C. Gabriel, and H. Münstedt, "Influence of shortchain branching of polyethylenes on the temperature dependence of rheological properties in shear," *Macromolecular Chemistry and Physics*, vol. 208, no. 22, pp. 2449–2454, 2007.

[30] A. Romo-Uribe, A. Manzur, and R. Olayo, "Synchrotron small-angle x-ray scattering study of linear low-density polyethylene under uniaxial deformation," *Journal of Materials Research*, vol. 27, no. 10, pp. 1351–1359, 2012.

[31] R. Popli, M. Glotin, L. Mandelkern, and R. S. Benson, "Dynamic mechanical studies of and relaxations of polyethylenes," *Journal of Polymer Science: Polymer Physics Edition*, vol. 22, no. 3, pp. 407–448, 1984.

[32] K. Moorthi, K. Kamio, J. Ramos, and D. N. Theodorou, "Monte carlo simulation of short chain branched polyolefins: Structure and properties," *Macromolecules*, vol. 45, no. 20, pp. 8453–8466, 2012.

[33] K. Matsui, S. Seno, Y. Nozue, Y. Shinohara, Y. Amemiya, E. B. Berda, G. Rojas, and K. B. Wagener, "Influence of branch incorporation into the lamella crystal on the crystallization behavior of polyethylene with precisely spaced branches," *Macromolecules*, vol. 46, no. 11, pp. 4438–4446, 2013.

[34] P. Gupta, G. L. Wilkes, A. M. Sukhadia, R. K. Krishnaswamy, M. J. Lamborn, S. M. Wharry, C. C. Tso, P. J. DesLauriers, T. Mansfield, and F. L. Beyer, "Does the length of the short chain branch affect the mechanical properties of linear low density polyethylenes? an investigation based on films of copolymers of ethylene/1-butene, ethylene/1-hexene and ethylene/1-octene synthesized by a single site metallocene catalyst," *Polymer*, vol. 46, no. 20, pp. 8819–8837, 2005.

[35] C. S. Few, K. B. Wagener, and D. L. Thompson, "Systematic studies of morphological changes of precision polyethylene," *Macromolecular Rapid Communications*, vol. 35, no. 2, pp. 123–132, 2014.

[36] M. Vadlamudi, *Effect Of Branching Architecture On The Crystallization Behavior Of Random Ethylene Effect of Branching architecture on the crystallization behavior of Random Ethylene Copolymers*. PhD thesis, The Florida State University, 2010.

[37] L. Mandelkern, "Relation between properties and molecular morphology of semicrystalline polymers," *Faraday Discussions of the Chemical Society*, vol. 68, no. 0, pp. 310–319, 1979.

[38] M. D. Failla and L. Mandelkern, "Tensile properties of mixtures of linear polyethylene and random ethylene copolymers having similar molecular weights," *Macromolecules*, vol. 26, pp. 7167–7175, 1993.

[39] M. A. Kennedy, A. J. Peacock, M. D. Failla, J. C. Lucas, and L. Mandelkern, "Tensile properties of crystalline polymers: Random copolymers of ethylene," *Macromolecules*, vol. 28, pp. 1407–1421, 1995.

[40] J. C. Lucas, M. D. Failla, F. L. Smith, L. Mandelkern, and A. J. Peacock, "The double yield in the tensile deformation of the polyethylenes," *Polymer Engineering Science*, vol. 35, no. 13, pp. 1117–1123, 1995.

[41] S. Hosoda, "Structural distribution of linear low-density polyethylenes," *Polymer Journal*, vol. 20, no. 5, pp. 383–397, 1988.

[42] S. Zhang, N. Zhao, Y. Wu, Q. Dong, Q. Wang, Y. Tang, Y. Yu, J. Da, X. He, R. Cheng, and B. Liu, "Short chain branches distribution characterization of ethylene/1hexene copolymers by using tref + 13cnmr and tref + sc methods," *Macromolecular Symposia*, vol. 312, no. 1, pp. 63–71, 2012.

[43] B. Monrabal, "Crystallization analysis fractionation: A new technique for the analysis of branching distribution in polyolefins," *Journal of Applied Polymer Science*, vol. 52, no. 4, pp. 491–499, 1994.

[44] L. Hubert, L. David, R. Séguéla, G. Vigier, C. Degoulet, and Y. Germain, "Physical and mechanical properties of polyethylene for pipes in relation to molecular architecture. i. microstructure and crystallisation kinetics," *Polymer*, vol. 42, no. 20, pp. 8425–8434, 2001.

[45] W. W. Adams, D. Yang, and E. L. Thomas, "Direct visualization of microstructural deformation processes in polyethylene," *Journal of Materials Science*, no. 21, pp. 2239–2253, 1986.

[46] V. Petraccone, I. C. Sanchez, and R. S. Stein, "The orientation of amorphous chains in spherulites," *Journal of Polymer Science: Polymer Physics Edition*, vol. 13, pp. 1991–2029, 1975.

[47] H. P. Wang, S. P. Chum, A. Hiltner, and E. Baer, "Deformation of elastomeric polyolefin spherulites," *Journal of Polymer Science Part B: Polymer Physics*, vol. 47, no. 13, pp. 1313–1330, 2009.

[48] H.-R. Yang, J. Lei, L. Li, Q. Fu, and Z.-M. Li, "Formation of interlinked shish-kebabs in injection-molded polyethylene under the coexistence of lightly cross-linked chain network and oscillation shear flow," *Macromolecules*, vol. 45, no. 16, pp. 6600–6610, 2012.

[49] R. H. Somani, L. Yang, L. Zhu, and B. S. Hsiao, "Flow-induced shish-kebab precursor structures in entangled polymer melts," *Polymer*, vol. 46, no. 20, pp. 8587–8623, 2005.

[50] G. Portale, D. Cavallo, G. C. Alfonso, D. Hermida-Merino, M. van Drongelen, L. Balzano, G. W. M. Peters, J. G. P. Goossens, and W. Bras, "Polymer crystallization studies under processing-relevant conditions at the saxs/waxs dubble beamline

at the esrfthis article will form part of a virtual special issue of the journal, presenting some highlights of the 15th international small-angle scattering conference (sas2012). this special issue will be available in late 2013/early 2014.," *Journal of Applied Crystallography*, vol. 46, no. 6, pp. 1681–1689, 2013.

[51] I. Dukovski and M. Muthukumar, "Langevin dynamics simulations of early stage shish-kebab crystallization of polymers in extensional flow," *Journal of Chemical Physics*, vol. 118, no. 14, pp. 6648–6654, 2003.

[52] S. Kimata, T. Sakurai, Y. Nozue, T. Kasahara, N. Yamaguchi, T. Karino, M. Shibayama, and J. A. Kornfield, "Molecular basis of the shish-kebab morphology in polymer crystallization," *Science*, vol. 316, pp. 1014–1017, May 2007.

[53] J. K. Keum, C. Burger, F. Zuo, and B. S. Hsiao, "Probing nucleation and growth behavior of twisted kebabs from shish scaffold in sheared polyethylene melts by in situ x-ray studies," *Polymer*, vol. 48, no. 15, pp. 4511–4519, 2007.

[54] T. Kanaya, G. Matsuba, Y. Ogino, K. Nishida, H. M. Shimizu, T. Shinohara, T. Oku, J. Suzuki, and T. Otomo, "Hierarchic structure of shish-kebab by neutron scattering in a wideqrange," *Macromolecules*, vol. 40, no. 10, pp. 365–03654, 2007.

[55] B. S. Hsiao, L. Yang, R. H. S. andCarlos A. Avila-Orta, and L. Zhu, "Unexpected shish-kebab structure in a sheared polyethylene melt," *Physical Review Letters*, vol. 94, 2005.

[56] Y. Tang, Z. Jiang, Y. Men, L. An, H.-F. Enderle, D. Lilge, S. V. Roth, R. Gehrke, and J. Rieger, "Uniaxial deformation of overstretched polyethylene: In-situ synchrotron small angle x-ray scattering study," *Polymer*, vol. 48, pp. 5125–5132, 2007.

[57] L. Lu, R. G. Alamo, and L. Mandelkern, "Lamellar thickness distribution in linear polyethylene and ethylene copolymers," *Macromolecules*, vol. 27, pp. 6571–6576, 1994.

[58] J. M. Lagarón, S. López-Quintana, J. C. Rodriguez-Cabello, J. C. Merino, and J. M. Pastor, "Comparative study of the crystalline morphology present in isotropic and uniaxially stretched "conventional"and metallocene polyethylenes," *Polymer*, vol. 41, no. 8, pp. 2999–3010, 2000.

[59] N. Stribeck, R. G. Alamo, L. Mandelkern, and H. G. Zachmann, "Study of the phase structure of linear polyethylene by means of small-angle x-ray scattering and raman spectroscopy," *Macromolecules*, vol. 28, no. 14, pp. 5029–5036, 1995.

[60] A. J. Ryan, W. Bras, G. R. Mant, and G. E. Derbyshire, "A direct method to determine the degree of crystallinity and lamellar thickness of polymers: application to polyethylene," *Polymer*, vol. 35, no. 21, pp. 4537–4544, 1994.

[61] H. Zhou and G. L. Wilkes, "Comparison of lamellar thickness and its distribution determined from d.s.c., saxs, tem and afm for high-density polyethylene films having a stacked lamellar morphology," *Polymer*, vol. 38, no. 23, pp. 5735–5747, 1997.

[62] G. R. Strobl and M. Schneider, "Direct evaluation of the electron density correlation function of partially crystalline polymers," *Journal of Polymer Science: Polymer Physics Edition*, vol. 18, no. 6, pp. 1343–1359, 1980.

[63] G. R. Strobl, M. J. Schneider, and I. G. VoigtMartin, "Model of partial crystallization and melting derived from small angle xray scattering and electron microscopic studies on lowdensity polyethylene," *Journal of Polymer Science: Polymer Physics Edition*, vol. 18, no. 6, pp. 1361–1381, 1980.

[64] A. Keller, "Perpendicular orientations in polyethylene," *Nature*, vol. 174, no. 4437, pp. 926–927, 1954.

[65] A. Keller and M. Machin, "Oriented crystallization in polymers," *Journal of Macromolecular Science, Part B: Physics*, vol. 1, no. 1, pp. 41–91, 1967.

[66] Y. Fujiwara, "The superstructure of meltcrystallized polyethylene. i. screwlike orientation of unit cell in polyethylene spherulites with periodic extinction rings," *Journal of Applied Polymer Science*, vol. 4, no. 10, pp. 10–15, 1960.

[67] C. G. VONK, "Effect of a second crystalline modification in polyethylene on x-ray crystallinity measurements," *Nature*, vol. 186, pp. 962–963, 1960.

[68] K. T. Tsuneo Seto, Tetsuhiko Hara, "Phase transformation and deformation processes in oriented polyethylene," *Japanese Journal of Applied Physics*, vol. 7, no. 1, pp. 31–42, 1968.

[69] J. L. Pezzutti and R. S. Porter, "Uniaxial orientation of linear low density polyethylene," *Journal of Applied Polymer Science*, vol. 30, no. 11, pp. 4251–4259, 1985.

[70] M. F. Butler, A. M. Donald, and A. J. Ryan, "Time resolved simultaneous small- and wide-angle x-ray scattering during polyethylene deformation: 1. cold drawing of ethylene--olefin copolymers," *Polymer*, vol. 38, no. 22, pp. 5521–5538, 1997.

[71] R. Seguela, "On the straininduced crystalline phase changes in semicrystalline polymers: Mechanisms and incidence on the mechanical properties," *Journal of Macromolecular Science, Part C: Polymer Reviews*, vol. 45, no. 3, pp. 263–287, 2005.

[72] T. Yemni and R. L. McCullough, "Energetics of phase transformations in polyethylene," *Journal of Polymer Science: Polymer Physics Edition*, vol. 11, no. 7, pp. 1385–1411, 1973.

[73] M. Rubenstein and R. H. Colby, *Polymer Physics*. Oxford University Press, 2003.

[74] A. Lustiger and R. L. Markham, "Importance of tie molecules in preventing polyethylene fracture under long-term loading conditions," *Polymer*, vol. 24, no. 12, pp. 1647–1654, 1983.

[75] H. Kiho, A. Peterlin, and P. H. Geil, "Polymer deformation. vi. twinning and phase transformation of polyethylene single crystals as a function of stretching direction," *Journal of Applied Physics*, vol. 35, no. 5, pp. 1599–1605, 1964.

[76] H. Kiho, A. Peterlin, and P. H. Geil, "Polymer deformation. ix. deformation of polyethylene crystals at large strain," *Journal of Polymer Science Part B: Polymer Letters*, vol. 3, no. 4, pp. 257–262, 1965.

[77] K. Sakaoku and A. Peterlin, "Deformation of extremely thin polyethylene films," *Die Makromolekulare Chemie*, vol. 108, no. 1, pp. 234–240, 1967.

[78] R. Corneliussen and A. Peterlin, "The influence of temperature on the plastic deformation of polyethylene," *Die Makromolekulare Chemie*, vol. 105, no. 1, pp. 193–203, 1967.

[79] A. Peterlin, "Molecular model of drawing polyethylene and polypropylene," *Journal of Materials Science*, vol. 6, no. 6, pp. 490–508, 1971.

[80] G. Meinel and A. Peterlin, "Plastic deformation of polyethylene ii. change of mechanical properties during drawing," *Journal of Polymer Science Part A2: Polymer Physics*, vol. 9, no. 1, pp. 67–83, 1971.

[81] L. Lin and A. S. Argon, "Structure and plastic deformation of polyethylene," *Journal of Materials Science*, vol. 29, no. 2, pp. 294–323, 1994.

[82] A. Galeski, "Strength and toughness of crystalline polymer systems," *Progress in Polymer Science*, vol. 28, no. 12, pp. 1643–1699, 2003.

[83] B. A. G. Schrauwen, R. P. M. Janssen, L. E. Govaert, and H. E. H. Meijer, "Intrinsic deformation behavior of semicrystalline polymers," *Macromolecules*, vol. 37, no. 16, pp. 6069–6078, 2004.

[84] R. Seguela and F. Rietsch, "Double yield point in polyethylene under tensile loading," *Journal of Materials Science Letters*, vol. 9, no. 1, pp. 46–47, 1990.

[85] V. Gaucher-Miri and R. Séguéla, "Tensile yield of polyethylene and related copolymers: Mechanical and structural evidences of two thermally activated processes," *Macromolecules*, vol. 30, no. 4, pp. 1158–1167, 1997.

[86] R.-J. Roe, "Methods of x-ray and neutron scattering in polymer science," 1999.

[87] N. Stribeck, *X-ray scattering of soft matter*. Springer Science & Business Media, 2007.

[88] P. Cebe, B. S. Hsiao, and D. J. Lohse, "Scattering from polymers; characterization by x-rays, neutrons, and light/; peggy cebe, editor, benjamin s. hsiao, editor, david j. lohse, editor.," in *ACS symposium series; 0097-6156; 739*, Washington, DC; American Chemical Society, 1999., 1999.

[89] M. F. Butler, A. M. Donald, W. Bras, G. R. Mant, G. E. Derbyshire, and A. J. Ryan, "A real-time simultaneous small- and wide-angle x-ray scattering study of in-situ deformation of isotropic polyethylene," *Macromolecules*, vol. 28, no. 19, pp. 6383–6393, 1995.

[90] M. F. Butler, A. M. Donald, and A. J. Ryan, "Time resolved simultaneous small- and wide-angle x-ray scattering during polyethylene deformation—ii. cold drawing of linear polyethylene," *Polymer*, vol. 39, no. 1, pp. 39–52, 1998.

[91] S. J. Weigand and D. T. Keane, "Dnd-cat's new triple area detector system for simultaneous data collection at multiple length scales," *Nuclear Instruments and Methods in Physics Research Section A: Accelerators, Spectrometers, Detectors and Associated Equipment*, vol. 649, no. 1, pp. 61–63, 2011.

[92] J. Ilavsky, "Nika: software for two-dimensional data reduction," *Journal of Applied Crystallography*, vol. 45, pp. 324–328, 2012.

[93] Y. Tian, C. Zhu, J. Gong, S. Yang, J. Ma, and J. Xu, "Lamellae break induced formation of shish-kebab during hot stretching of ultra-high molecular weight polyethylene precursor fibers investigated by in situ small angle x-ray scattering," *Polymer*, vol. 55, no. 16, pp. 4299–4306, 2014.

[94] B. Crist and N. Morosoff, "Small-angle x-ray scattering of semicrystalline polymers. ii. analysis of experimental scattering curves," *Journal of Polymer Science: Polymer Physics Edition*, vol. 11, no. 6, pp. 1023–1045, 1973.

[95] F.Cser, "About the lorentz correction used in the interpretation of small angle x-ray scattering data of semicrystalline polymers," *Journal of Applied Polymer Science*, vol. 80, pp. 2300–2308, 2001.

[96] Y. D. Lee, P. J. Phillips, and J. S. Lin, "The influence of crystallinity distribution on smallangle xray scattering from semicrystalline polymers," *Journal of Polymer Science Part B: Polymer Physics*, vol. 29, no. 10, pp. 1235–1254, 1991.

[97] E. Dalton and M. N. Collins, "Lamella alignment ratio: a saxs analysis technique for macromolecules," *Journal of Applied Crystallography*, vol. 47, no. 3, pp. 847–851, 2014.

[98] A.Guinier, *X-Ray Diffraction In Crystals, Imperfect Crystals, and Amorphous Bodies*. W.H Freeman and Company, 1963.

[99] Z. Wilchinsky, "Measurement of orientation in polypropylene film," *Journal of Applied Physics*, vol. 31, no. 11, pp. 1969–1972, 1960.

[100] T. Albrecht and G. Strobl, "Temperature dependent crystalline-amorphous structures in linear polyethylene: Surface melting and the thickness of the amorphous layers," *Macromolecules*, vol. 28, no. 17, pp. 5827–5833, 1995.

[101] N. W. J. Brooks, "Modeling of double yield points in polyethylene: Temperature and strain-rate dependence," *Journal of Rheology*, vol. 39, no. 2, pp. 425–436, 1995.

[102] N. W. Brooks, R. A. Duckett, and I. M. Ward, "Investigation into double yield points in polyethylene," *Polymer*, vol. 33, no. 9, pp. 1872–1880, 1992.

[103] A. Prasad, R. Shroff, S. Rane, and G. Beaucage, "Morphological study of hdpe blown films by saxs, sem and tem: a relationship between the melt elasticity parameter and lamellae orientation," *Polymer*, vol. 42, no. 7, pp. 3103–3113, 2001.

[104] L.-Z. Liu, B. S. Hsiao, B. X. Fu, S. Ran, S. Toki, B. Chu, A. H. Tsou, and P. K. Agarwal, "Structure changes during uniaxial deformation of ethylene-based semicrystalline ethylenepropylene copolymer. 1. saxs study," *Macromolecules*, vol. 36, no. 6, pp. 1920–1929, 2003.

[105] R. K. Krishnaswamy, Q. Yang, L. Fernandez-Ballester, and J. A. Kornfield, "Effect of the distribution of short-chain branches on crystallization kinetics and mechanical properties of high-density polyethylene," *Macromolecules*, vol. 41, no. 5, pp. 1693–1704, 2008.

[106] S. Hosoda, Y. Nozue, Y. Kawashima, S. Utsumi, T. Nagamatsu, K. Wagener, E. Berda, G. Rojas, T. Baughman, and J. Leonard, "Perfectly controlled lamella thickness and thickness distribution: A morphological study on admet polyolefins," *Macromolecular Symposia*, vol. 282, no. 1, pp. 50–64, 2009.

[107] S. Hosoda, Y. Nozue, Y. Kawashima, K. Suita, S. Seno, T. Nagamatsu, K. B. Wagener, B. Inci, F. Zuluaga, G. Rojas, and J. K. Leonard, "Effect of the sequence length distribution on the lamellar crystal thickness and thickness distribution of polyethylene: Perfectly equisequential admet polyethylene vs ethylene/-olefin copolymer.," *Macromolecules*, vol. 44, no. 2, pp. 313–319, 2011.

[108] S. Gautam, S. Balijepalli, and G. C. Rutledge, "Molecular simulations of the interlamellar phase in polymers: Effect of chain tilt," *Macromolecules*, vol. 33, no. 24, pp. 9136–9145, 2000.

[109] S. Lee and G. C. Rutledge, "Plastic deformation of semicrystalline polyethylene by molecular simulation," *Macromolecules*, vol. 44, no. 8, pp. 3096–3108, 2011.

[110] A. Ghazavizadeh, G. C. Rutledge, A. A. Atai, S. Ahzi, Y. Rémond, and N. Soltani, "Hyperelastic characterization of the interlamellar domain and interphase layer in semicrystalline polyethylene," *Journal of Polymer Science Part B: Polymer Physics*, vol. 51, no. 23, pp. 1692–1704, 2013.

[111] A. Ghazavizadeh, G. C. Rutledge, A. A. Atai, S. Ahzi, Y. Rémond, and N. Soltani, "Micromechanical characterization of the interphase layer in semicrystalline polyethylene," *Journal of Polymer Science Part B: Polymer Physics*, vol. 51, no. 16, pp. 1228–1243, 2013.

[112] J. Che, C. R. Locker, S. Lee, G. C. Rutledge, B. S. Hsiao, and A. H. Tsou, "Plastic deformation of semicrystalline polyethylene by x-ray scattering: Comparison with atomistic simulations," *Macromolecules*, vol. 46, no. 13, pp. 5279–5289, 2013.

[113] J. M. Kim, R. Locker, and G. C. Rutledge, "Plastic deformation of semicrystalline polyethylene under extension, compression, and shear using molecular dynamics simulation," *Macromolecules*, vol. 47, no. 7, pp. 2515–2528, 2014.

[114] D. Bassett and A. Hodge, "On the morphology of melt-crystallized polyethylene. iii. spherulitic organization," in *Proceedings of the Royal Society of London A: Mathematical, Physical and Engineering Sciences*, vol. 377, pp. 61–71, The Royal Society, 1981.

[115] D. Bassett, A. Hodge, and R. Olley, "On the morphology of melt-crystallized polyethylene ii. lamellae and their crystallization conditions," in *Proceedings of the Royal Society of London A: Mathematical, Physical and Engineering Sciences*, vol. 377, pp. 39–60, The Royal Society, 1981.

[116] D. Bassett and A. Hodge, "On the morphology of melt-crystallized polyethylene. iii. spherulitic organization," in *Proceedings of the Royal Society of London A: Mathematical, Physical and Engineering Sciences*, vol. 377, pp. 61–71, The Royal Society, 1981.

[117] D. Y. Yoon and P. J. Flory, "Chain packing at polymer interfaces," *Macromolecules*, vol. 17, no. 4, pp. 868–871, 1984.

[118] D. Bassett, A. Hodge, and R. Olley, "On the morphology of melt-crystallized polyethylene ii. lamellae and their crystallization conditions," in *Proceedings of the Royal Society of London A: Mathematical, Physical and Engineering Sciences*, vol. 377, pp. 39–60, The Royal Society, 1981.

[119] D. Bassett and A. Hodge, "On lamellar organization in certain polyethylene spherulites," in *Proceedings of the Royal Society of London A: Mathematical, Physical and Engineering Sciences*, vol. 359, pp. 121–132, The Royal Society, 1978.

[120] H. Wang, P. Ansems, S. Chum, A. Hiltner, and E. Baer, "Amorphous phase of propylene/ethylene copolymers characterized by positron annihilation lifetime spectroscopy," *Macromolecules*, vol. 39, no. 4, pp. 1488–1495, 2006.

[121] T. Tagawa and K. Ogura, "Piledlamellae structure in polyethylene film and its deformation," *Journal of Polymer Science: Polymer Physics Edition*, vol. 18, no. 5, pp. 971–979, 1980.

[122] Y. Sun, S. Fischer, Z. Jiang, T. Tang, S. S. Funari, R. Gehrke, and Y. Men, "Morphological changes of linear, branched polyethylenes and their blends during crystallization and subsequent melting by synchrotron saxs and dsc," *Macromolecular Symposia*, vol. 312, no. 1, pp. 51–62, 2012.

[123] B. A. G. Schrauwen, L. C. A. v Breemen, A. B. Spoelstra, L. E. Govaert, G. W. M. Peters, and H. E. H. Meijer, "Structure, deformation, and failure of flow-oriented semicrystalline polymers," *Macromolecules*, vol. 37, no. 23, pp. 8618–8633, 2004.

[124] I. Noda, G. M. Story, and C. Marcott, "Pressure-induced transitions of polyethylene studied by two-dimensional infrared correlation spectroscopy," *Vibrational Spectroscopy*, vol. 19, no. 2, pp. 461–465, 1999.

[125] R. Hiss, S. Hobeika, C. Lynn, and G. Strobl, "Network stretching, slip processes, and fragmentation of crystallites during uniaxial drawing of polyethylene and related copolymers. a comparative study," *Macromolecules*, vol. 32, no. 13, pp. 4390–4403, 1999.

[126] D. Stoyan, W. S. Kendall, J. Mecke, and L. Ruschendorf, *Stochastic geometry and its applications*, vol. 2. Wiley New York, 1987.

[127] S. R. Kline, "Reduction and analysis of sans and usans data using igor pro," *Journal of Applied Crystallography*, vol. 39, no. 6, pp. 895–900, 2006.

[128] R. L. Cook, "Stochastic sampling in computer graphics," *ACM Transactions on Graphics (TOG)*, vol. 5, no. 1, pp. 51–72, 1986.

[129] R. Dimitris, "Bootstrap stepaic. r package version 1.2-0," 2009.

[130] W. J.D. and C. F.H.C., "Molecular structure of nucleic acids," *Nature*, vol. 171, no. 737-738, 1953.